University of Southampton

Faculty of Engineering and Physical Sciences

Chemistry

Molecular orientation and reactions probed via SERS

by

Alexander John Keeler

Thesis for the degree of Doctor of Philosophy

April 2019

University of Southampton

Abstract

Faculty of Engineering and Physical Sciences

Chemistry

Thesis for the degree of Doctor of Philosophy

Molecular orientation and reactions probed via SERS

By

Alexander John Keeler

Surface enhanced Raman spectroscopy (SERS) can be combined with electrochemical techniques (EC-SERS) to allow the *in situ* analysis of electrode surfaces, including understanding the fundamental interactions between the electrode and adsorbed molecules, and identifying the intermediates, products and mechanisms of electrochemical reactions. In this work, the potential dependent orientation of *ortho-, meta-* and *para-* nitrile substituted benzenethiol self assembled monolayers (SAMs) has been investigated on Au sphere segment void (SSV) substrates by analysis of the in plane and out of plane SERS vibrational band intensities, peak positions and the selection rules. The electroreduction of *p*-nitrothiophenol (PNTP) and electrooxidation of *p*-aminothiophenol (PATP) SAMs have also been probed. By using density functional theory (DFT) calculated Raman spectra evidence of new intermediate species has been discovered for both reactions, including a different oxidation mechanism for PATP in acidic and alkaline media. Furthermore, the adsorption and orientation of thioamide terminated molecular wires, an interesting new species for molecular electronics, has been investigated by examining both the absence of expected vibrations and the most intense SERS bands. Finally, further understanding of glycerol electrooxidation has important applications in direct liquid fuel cells (DLFCs), but has a complex reaction mechanism with many intermediates. By careful analysis of the peak pattern of *in situ* SERS spectra, intermediate species have been identified and the reaction mechanism uncovered.

Table of Contents

Research Thesis: Declaration of Authorship

Print name:	ALEXANDER JOHN KEELER
Title of thesis:	MOLECULAR ORIENTATION AND REACTIONS PROBED VIA SERS

I declare that this thesis and the work presented in it are my own and has been generated by me as the result of my own original research.

I confirm that:

1. This work was done wholly or mainly while in candidature for a research degree at this University;
2. Where any part of this thesis has previously been submitted for a degree or any other qualification at this University or any other institution, this has been clearly stated;
3. Where I have consulted the published work of others, this is always clearly attributed;
4. Where I have quoted from the work of others, the source is always given. With the exception of such quotations, this thesis is entirely my own work;
5. I have acknowledged all main sources of help;
6. Where the thesis is based on work done by myself jointly with others, I have made clear exactly what was done by others and what I have contributed myself;
7. Parts of this work have been published as:

[1] A.J. Keeler, A.E. Russell, Mechanistic insights into electrocatalytic reactions provided by SERS, Curr. Opin. Electrochem. Submitted (2019).

[2] A.J. Keeler, A.E. Russell, Potential dependent orientation of sulfanylbenzonitrile monolayers monitored by SERS, Electrochim. Acta. 305 (2019) 378–387. doi:10.1016/j.electacta.2019.03.044.

[3] A.J. Keeler, A.E. Russell, SERS investigation into the mechanism of p-nitrothiophenol electroreduction in the absence of photo-induced effects, Electrochim. Acta. Submitted (2019).

[4] A.J. Keeler, A.E. Russell, An in situ SERS study of the effect of pH on the products of p-aminothiophenol monolayer electrooxidation, Phys. Chem. Chem. Phys. Submitted (2019).

Signature:		Date:	

Acknowledgements

I would like to thank my supervisor Professor Andrea Russell for all her help, expertise, advice and support throughout my years as a PhD student. Your enthusiasm, knowledge and ability to motivate has been an inspiration and I have learnt more than I ever thought I would as your student. I would also like to acknowledge my advisor Professor Phil Bartlett for his additional expertise on everything SERS related. Furthermore, I would like to thank Dr Danai Panagoulia for teaching me the very basics of the entire project, specifically the manufacture of the Au SSV substrates and how to operate the Raman spectrometers. I am also exceptionally grateful to Alastair Clarke and Nikolay Zhelev who made the majority of my Au coated microscope slides, and to a former MSc and now PhD student Tammy Nimmo who allowed me to use her fantastic diagrams of both Au SSV manufacture and the spectroelectrochemical cell (Figures 1.4, 1.5, 2.2 and 2.4). I must also thank Ian Hayward at Renishaw for not only great spectroscopy support, but also for his great help in setting up the automated EC-SERS system. In addition, great thanks must also go to all the other members of the Russell group: Dr Andrew Leach, Dr David Inwood, Dr Turgut Sonmez, (soon to be Dr) Haoliang ‘Howard, HHH’ Huang and entirety of the Electrochemistry department at the University of Southampton for their fierce friendship and great discussions on all things electrochemistry and otherwise. Finally, I would like to thank my parents, John and Valerie, for their unwavering support, love and passion for me. I wouldn’t have been able to do it without you.

Abbreviations and Definitions

Below are, in chronological order, the abbreviations and definitions used in this thesis.

SERS	Surface enhanced Raman spectroscopy
EC-SERS	Electrochemical surface enhanced Raman spectroscopy
TERS	Tip enhanced Raman spectroscopy
EM	Electromagnetic
CT	Charge Transfer
SSV	Sphere segment void
SHIN	Shell Isolated Nanoparticles
GC	Glassy carbon
SAM	Self assembled monolayer
PANQ	poly(5-amino-1,4-napthoquinone)
44bpy	4,4’-bipyridine
ORR	Oxygen reduction reaction
TTF	Tetrathiafulvalene
OER	Oxygen evolution reaction
Kel-F®,	Polychlorotrifluoroethylene
DMSO	Dimethyl sulfoxide
4-SBN	4-sulfanylbenzonitrile
3-SBN	3-sulfanylbenzonitrile
2-SBN	2-sulfanylbenzonitrile
PNTP	*p*-nitrothiophenol
PATP	*p*-aminothiophenol
I	Current
E	Potential
t	time
TLC	Thin layer cell
SCE	Saturated calomel electrode
DMF	Dimethylformamide
CE	Counter electrode
WE	Working electrode
QRE	Quasi reference electrode

CV	Cyclic voltammetry
WiRE	Windows Raman Environment
SEM	Scanning electron microscope
TP	Thiophenol
EF	Enhancement factor
DFT	Density functional theory
ECP	Effective core potential
PCM	polarisation continuum model
XPS	X-ray photoelectron spectroscopy
IP	In plane
OOP	Out of plane
PNSTP	*p*-nitrosothiophenol
PHATP	*p*-hydroxylaminothiophenol
DMAOB	*p-p'*-dimercaptoazoxybenzene
DMAB	*p-p*'-dimercaptoazobenzene
DMHAB	*p-p'*-dimercaptohydrazobenzene
ATR	Attenuated total reflectance
SECM	Scanning electrochemical microscopy
NPQDI	4'-mercapto-N-phenyl-1,4-quinone diimine
NPQDA	4'-mercapto-N-phenyl-1,4-quinone diamine
NPQMI	4'-mercapto-N-phenyl-1,4-quinone monoimine
NQPMA	4'-mercapto-N-phenyl-1,4-quinone monoamine
SEIRAS	Surface enhanced infrared absorption spectroscopy
SFG	Sum frequency generation
MW	Molecular wire
BDTA	1,4-benzenedicarbothioamide
EDBDTA	4,4'-(ethyne-1,2-diyl)dibenzodicarbothioamine
DLFC	Direct liquid fuel cell
PEMFC	Polymer exchange membrane fuel cell
HPLC	High performance liquid chromatography

Chapter 1: Introduction

Surface enhanced Raman spectroscopy (SERS) offers the ability to study species adsorbed on electrode surfaces and follow their electrochemical reactions *in situ*. In this thesis, five such electrochemical SERS (EC-SERS) studies will be presented, including the potential dependence of monolayer orientation, intermediate identification and mechanism elucidation.

1.1 Raman Spectroscopy

The change in frequency of radiation after scattering was first theoretically predicted in 1923 by A. Smekal [1]. In his paper explaining dispersion (how the velocity of light in different media changes according to the index of refraction of the media and the wavelength of said light), he assumed that light itself has a quantum structure and showed that scattered monochromatic light consists of both its original wavelength and small amounts of both longer and shorter wavelengths. While not directly influenced by this work, C.V Raman and his junior colleague K.S Krishnan experimentally confirmed Smekal's theory in 1928 with their discovery of Raman spectroscopy [2]. They focused sunlight on common laboratory solvents and observed that most of the collected light was elastically scattered by the liquids. However, a very small amount of the sunlight was scattered inelastically and had a different wavelength to the incident beam [3]. By comparing the results from different solvents, it was determined that the shift in wavelength of the inelastically scattered light was dependent on the chemical structure of the molecules responsible for scattering. This evidence was then used to determine molecular vibrations and provide information regarding the structure, symmetry, electronic environment and bonding of the molecule. This, in turn, allows quantitative and qualitative analysis of the individual compounds [4]. This phenomenon was dubbed 'The Raman Effect' and resulted in C.V Raman being awarded the Nobel Prize for Physics in 1930 [5] and by the end of the decade the Raman Effect was the principal method of non-destructive chemical analysis [6]. In the present day, Raman spectroscopy is used in a very broad range of disciplines, it requires very little sample preparation (most samples are 'as is') and has a fast acquisition time. Potential Raman applications include: forensic science [7,8],

biology [9], medical diagnostics [10,11], surface science [12,13], pharmaceuticals [14,15] and nanotechnology [16].

To collect a Raman spectrum, light is focused onto a sample. The molecules within the sample scatter the impinged light resulting in different vibrations of bonds within the molecule. These scattered photons are collected and their energies calculated as follows:

$$\boldsymbol{h\nu_{in} = h\nu_{out} \pm h\nu_{vib}} \qquad \text{Equation 1.1}$$

where $h\nu_{in}$ is the energy of the incident photon, $h\nu_{out}$ is the energy of the scattered photons and $h\nu_{vib}$ is the energy of the molecular vibration.

The scattering occurs in three ways, resulting in Rayleigh, Stokes and anti-Stokes photons. Rayleigh photons are the most common, with the light being scattered with no change in wavelength. Stokes and anti-Stokes scattering are the result of the Raman Effect, with Stokes scattered photons (Δv = +1) having a lower frequency and anti-Stokes photons (Δv = -1) a higher frequency. This is a result of excitation of molecules to a short-lived virtual state from the impinged light; the molecules then relax back to their original electronic state and release a photon. If the vibrational energy state does not change then the resulting photons are Rayleigh photons. If the vibrational energy state increases (e.g. v = 0 to v = 1) then the resulting photon is a Stokes photon, similarly if the vibration energy state decreases then the resulting photon is an anti-Stokes photon. These concepts are visualized in Figure 1.1.

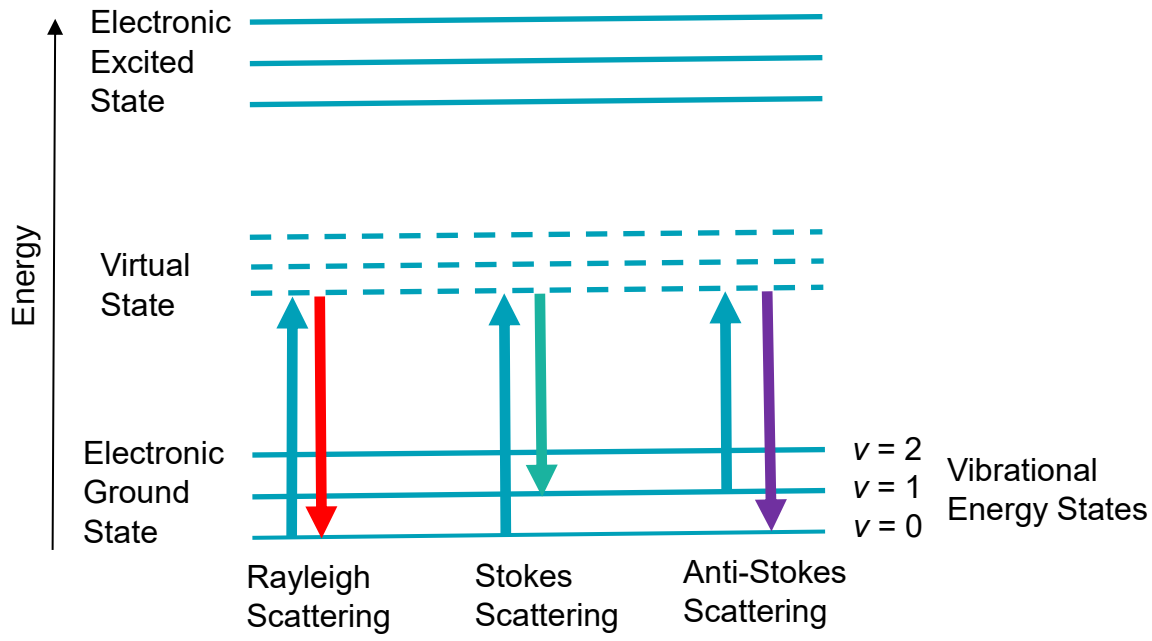

Figure 1.1 Energy level diagram for Raman scattering.

Like all spectroscopies, Raman has its own selection rules. The gross selection rule for vibrational Raman transitions is that the molecular polarizability must change as the molecule vibrates. The specific selection rule, as seen above, is that the vibrational energy level must change as $\Delta v = \pm 1$ upon vibration [17]. Raman Spectroscopy is exceedingly insensitive, with approximately only 1 in 10^7 photons being scattered inelastically, thus the spectra are dominated by Rayleigh scattered light and distinguishing Raman signals from noise can be difficult. The spectrum produced by Raman scattered light is unique to each molecule and serves as a 'fingerprint' from which said molecules can be identified, with spectral band intensities related to the amount of substance present in a sample. It can be applied to liquids, solids and gases and unlike other techniques is successful in aqueous environments [18].

However, even with all these advantages, the subsequent advances in electronics and detectors from the Second World War meant that Raman usage was surpassed by infrared (IR) spectroscopy in the 1940s. IR spectroscopy could be performed quickly and easily, without the need for dark rooms or highly trained operators [6]. Fortunately, Raman spectroscopy was revived in the 1960s with the advent of the laser [19]. This more intense light source was able to amplify the Raman Effect and increase the amount of detectable scattered light. This success continued in the early 1970s when a new branch of the

technique was born in the form of SERS, which results in up to a 10^6-10^8-fold increase in Raman signal intensities.

1.2 Surface Enhanced Raman Spectroscopy

SERS was first discovered by Fleischmann *et al.* [20] in 1974. Fleischmann and his colleagues adsorbed pyridine on an electrochemically roughened silver electrode and upon acquisition of the Raman spectrum discovered a 10^6-fold enhancement in Raman scattering intensities when compared to pyridine in solution. The enhancement observed with a roughened Ag electrode [21] was orders of magnitude greater than that expected and was later attributed to electromagnetic [22] and chemical [21] effects, with the former now understood to provide most of the typically 10^6-fold enhancement. In the many years since the initial discovery there have been over 19,000 SERS papers published, most of which describe the development of new or improved SERS substrates [23], further study of the SERS mechanism [24], and the development of advanced SERS techniques, such as tip-enhanced Raman spectroscopy (TERS), as evidenced by the two most recent Faraday Discussions on SERS [25,26] and some very recent review articles [27–29].

1.2.1 SERS selection rules

SERS probes vibrational energy levels of molecules in the same way as Raman spectroscopy described earlier. However, due to the nature of the surface adsorption of molecules there are some additional selection rules when compared to conventional Raman. When a molecule vibrates that is adsorbed (or close to) a SERS active surface it creates an oscillating molecular dipole that induces a second oscillating dipole in the metal surface. This is called an image dipole and depending on the relative orientation of the molecular and image dipoles they can either reinforce or cancel each other out, as shown in Figure 1.2.

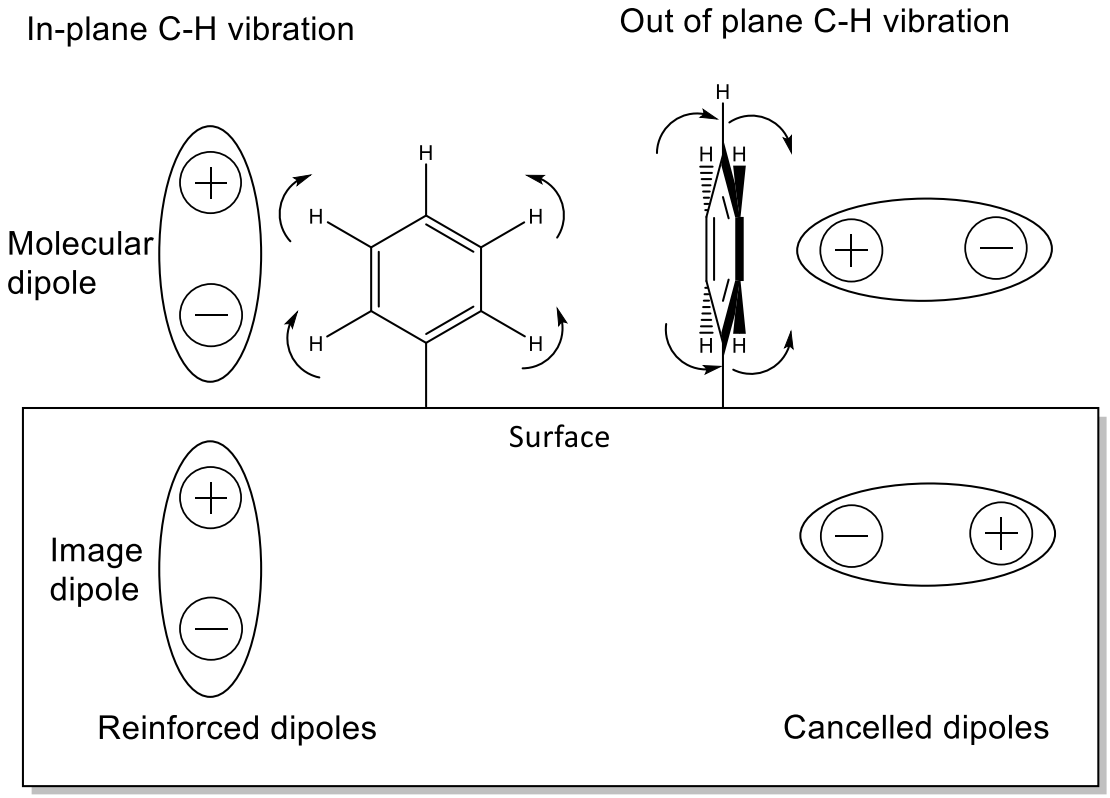

Figure 1.2: A C-H in plane vibration, which would generate a reinforcing image dipole and be more enhanced by the surface and a C-H out of plane vibration, which would generate a cancelled dipole and be less enhanced less by the surface.

However, in SERS the scattering intensity is dependent on the anisotropic polarizability of the molecule and thus, the induced dipole produced by the vibration may be in a different direction to that of the driving electromagnetic field, resulting in the surface selection rule breaking down somewhat. Metals are also less reflective in the visible region of the spectrum, resulting in weaker image dipoles and incomplete cancellation. Overall, this means that SERS spectra follow a loose set of guidelines rather than firm selection rules [30], which can be summarised as follows. Vibrations involving atoms directly bonded to metal atoms are more pronounced in SERS spectra, while vibrations involving atoms that are close to the metal surface will also be more enhanced. Furthermore, vibrations with larger components of dipole moment in a direction normal to the surface will be enhanced more. For example, when molecules are adsorbed parallel to the metal surface the out of plane (of the molecule) vibrational modes are more enhanced. Similarly, perpendicular adsorption results in the in plane (of the molecule) modes being more enhanced. If both in plane and out of plane bending modes are equally

enhanced then this indicates that the molecule is adsorbed in a tilted orientation or in mixed adsorption sites, the latter being less likely.

1.2.2 SERS enhancement mechanism

Fleischmann *et al.* [20] initially concluded that the increased surface area from the roughened electrode meant a greater number of the adsorbate molecules in the laser spot. This resulted in more molecules at the surface to scatter incident light to produce a greater Raman signal. However, this was discounted when the currently accepted mechanism of the enhancement was elucidated by two separate groups in 1977; both Jeanmarie and Van Duyne [31] and Albrecht and Creighton [20] proved that the increase in surface area could not explain the Raman signal enhancement. They independently determined that the enhancement was due to electromagnetic (EM) and charge transfer effects (CT). It is now understood that the EM provides the majority ($\approx 10^4$ out of the 10^6 enhancement) of the increased signal intensities due to SERS [20,32]. This mechanism arises from the excitation of collective oscillations of electrons at the rough metal surface, called surface plasmons, when a light source is shone onto the metal surface. Surface plasmons can either be localized to particular points, such as being trapped in the features of the metal surface, or be delocalized and propagate along the surface [33], as shown in Figure 1.3. These coupled plasmons create an enhanced electric field (E) at the metal surface. Both the incident light from the laser source and the light scattered by molecules on the surface are influenced by E giving a total Raman signal intensity enhancement proportional to E^4. This occurs as the electric field creates a large local dipole at the surface, which in turn creates an induced dipole in the molecule at the surface. This large induced dipole in the molecules means that the impinging radiation is more likely to be scattered and result in greater Raman scattering signal intensities [24].

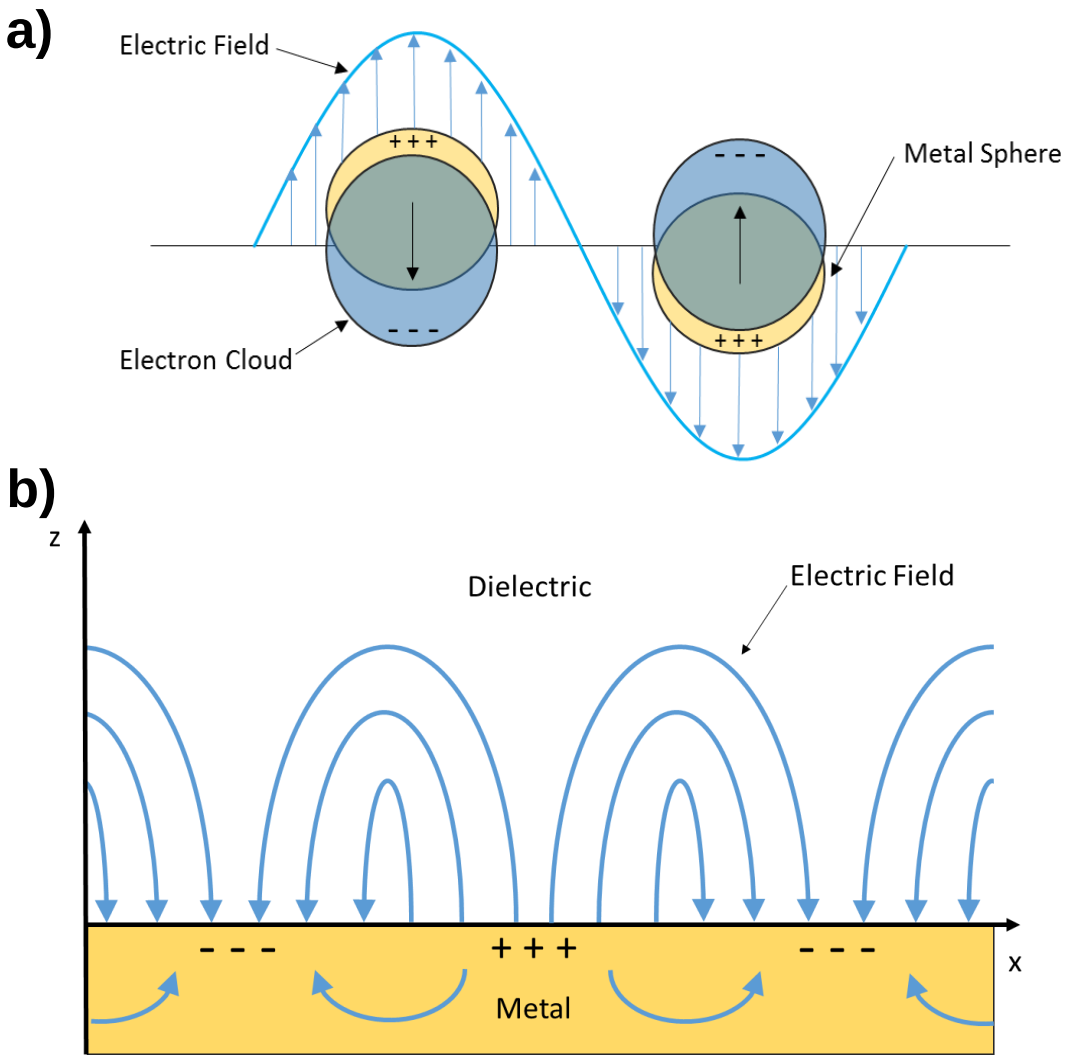

Figure 1.3: a) a plasmon fixed at a point on the surface, called a localized surface plasmon, b) a plasmon that can propagate across a surface, called a surface plasmon. Figure adapted from Willets *et al*. [34].

The remainder of the enhancement (≈10^2) is due to the CT, or chemical, effect. This arises from chemisorption-induced molecular resonance effects, by either altering the adsorbate electronic states or creating new states upon adsorption. The resulting transfer of electrons between chemisorbed molecules and the surface results in a change in polarizability of the bonds of the adsorbed molecule. This results in an increase in the induced dipole in molecules, resulting in more intense scattering. Although such chemical enhancement does not necessarily require rough surfaces, for most SERS studies it usually operates in conjunction with EM enhancement [24].

1.2.3 SERS Substrates

SERS substrates have advanced considerably from the highly roughened/disordered metal surfaces characteristic of the original discovery. Although such highly disordered surfaces are still used, as understanding of the role of plasmonics and the (optical) electric field strength in achieving the enhancement has improved, so has the number of new substrates being manufactured. Many materials have been tested for SERS but the coinage metals Au, Ag and Cu have been found to be the most popular due to the easy excitement of surface plasmons by visible or near IR light to provide large SERS signal enhancement [23]. Other plasmonic materials have been investigated, such as the alkali metals (Li, Na, K *etc.*) and Al, Ga, In, Pt, Rh and metal alloys [23,35], but as their enhancements are generally poor and therefore these are rarely used.

This understanding has enabled the design of nanostructured substrates in which the plasmons are focussed (e.g. sharp tips [34] or dendrites [36]) or confined (e.g. sphere segment voids (SSV) [18,33,37]) as well as the development of SERS probes (e.g. shell isolated nanoparticles (SHIN) [38–40]) that can be used to study non-SERS active surfaces as depicted in Figure 1.4a.

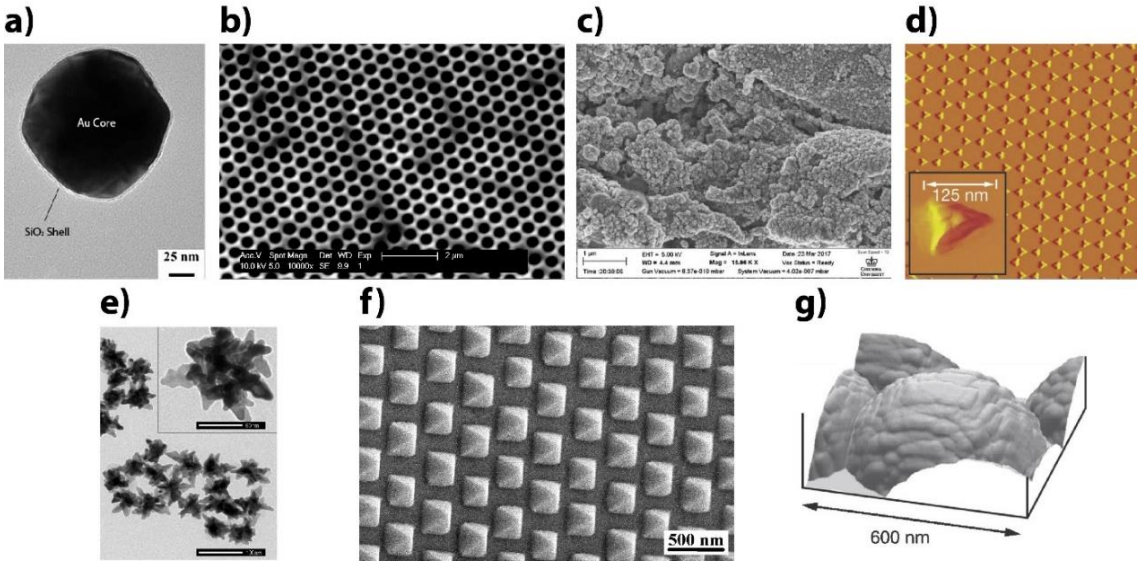

Figure 1.4: A selection of SERS substrates: a) Au@SiO_2 SHINERS particles [41], b) Au sphere segment voids, c) roughened Cu [42], d) Au nanotriangles [34], e) Au nanostars [36], f) Au nanopyramids [43] and g) Ag film-over-nanospheres [34]. Adapted with permission from original content authors.

1.2.3.1 Sphere Segment Void Substrates

SSV nanostructured substrates have been developed within the last decade [18,44]. These are plasmonic substrates that contain a hexagonally close packed array of half spheres, called voids, across the surface. These are robust, easily reproducible and provide approximately 10^6 fold enhancement of Raman signals. They are produced by loading a hexagonally close packed layer of polystyrene spheres onto a flat gold surface, then electrodepositing more gold (or another metal of interest) through the layer. These spheres can then be dissolved, leaving behind the void surface structure. This process is briefly shown in Figure 1.5, and will be described in detail in Chapter 2.

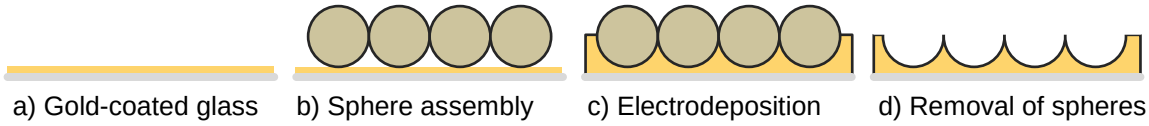

Figure 1.5: An overview of the main SSV substrate preparation method.

SSV substrates provide good enhancements to SERS signals because they can support both localised plasmons, trapped in the voids of the surface structure, and delocalized plasmons that move on the flat surface of the substrate that encompass the voids, represented in Figure 1.6.

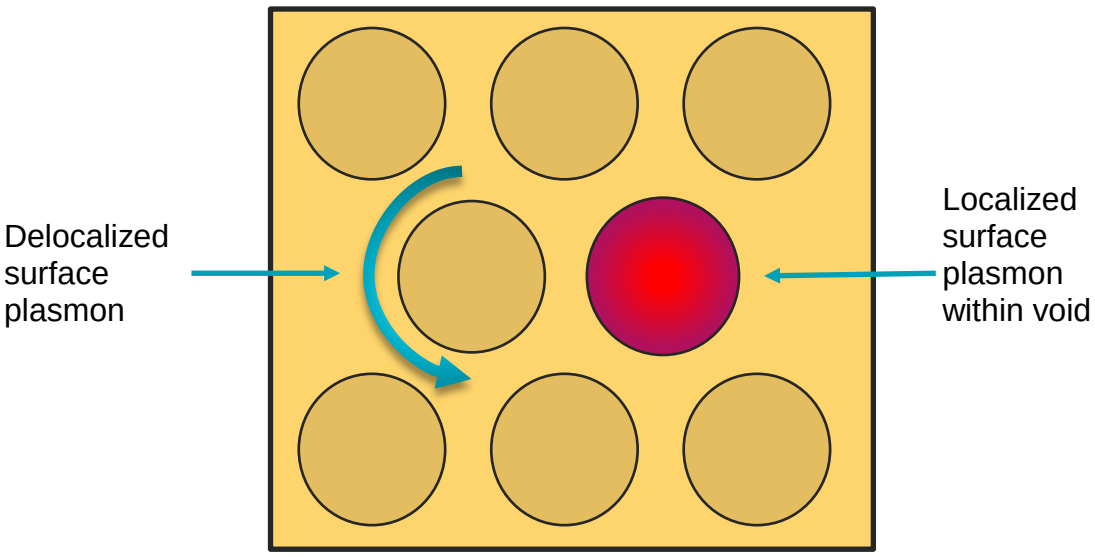

Figure 1.6: The two different types of surface plasmons present on an SSV surface. The darker gold regions represent the void structure. Figure based on work from Abdelsalam *et al*. [18].

The majority of the SERS enhancement is caused by the localized plasmons in the voids of the structure. By varying the amount of gold deposited and the

diameter of the spheres, the depth of the voids can be adjusted. Therefore, it is possible to tune the plasmonic properties of the metal surface via the void geometry and provide the best enhancements for the particular laser wavelength in use or media in which the samples are investigated [37].

Alongside these developments in SERS substrates, there has been improved understanding that the structure of electrode surfaces can affect the outcome of electrode reactions through the study of single crystal surfaces and nanoparticles. Thus, it may be inappropriate to assume that the structure of the SERS substrate (roughened or otherwise intentionally nanostructured) can be treated as an insignificant parameter. The use of SHIN particles provides a means of achieving enhancement on non-active surfaces such as smooth single crystal metal surfaces [40] or highly absorbing (black electrode) surfaces such as glassy carbon (GC) [45]. However, casting SHIN particles on an electrode surface may also cause a perturbation to the reaction by restricting mass transport.

1.3 Electrochemical SERS

EC-SERS is a combination of SERS and electrochemical techniques that allows *in situ* analysis of electrode surfaces, including understanding the fundamental interactions between the electrode surface and adsorbed molecules, and identifying the mechanism of electrochemical reactions. Here, I present an overview of the recent literature in these areas, with specific interest where the authors have ensured that, at least some, of the electrochemical data that is presented is obtained using the same electrodes as those used for the SERS measurements.

SERS offers several advantages over other vibrational spectroscopic probes of electrode surfaces such as IR. The enhancement is strongest for molecules at or on the surface of substrate [46,47] and the metal-adsorbate vibrations are readily observed, whereas these would be in the far-IR region for IR studies, where the strong absorbance by the solvent obscures the rather weak signals, causing experimental difficulties [48]. Water and many other solvents used in electrochemistry do not have strong Raman signals and thus thin-layer cells with micron-scale pathlengths are not necessary. Additionally,

molecules such as O_2 can be observed by Raman, making SERS particularly useful in the study of the oxygen reduction and evolution reactions.

1.3.1 Studies of Self-Assembled Monolayers

SERS has traditionally been used to study the fundamental properties of molecules at, or close to, metal surfaces. These molecules can either be physisorbed or chemisorbed as self assembled monolayers (SAMs) to provide uniform, well defined environments at metal surfaces [49]. SAMs are arrays of molecules that spontaneously arrange themselves into crystalline structures on solid or liquid surfaces [50], shown in Figure 1.7.

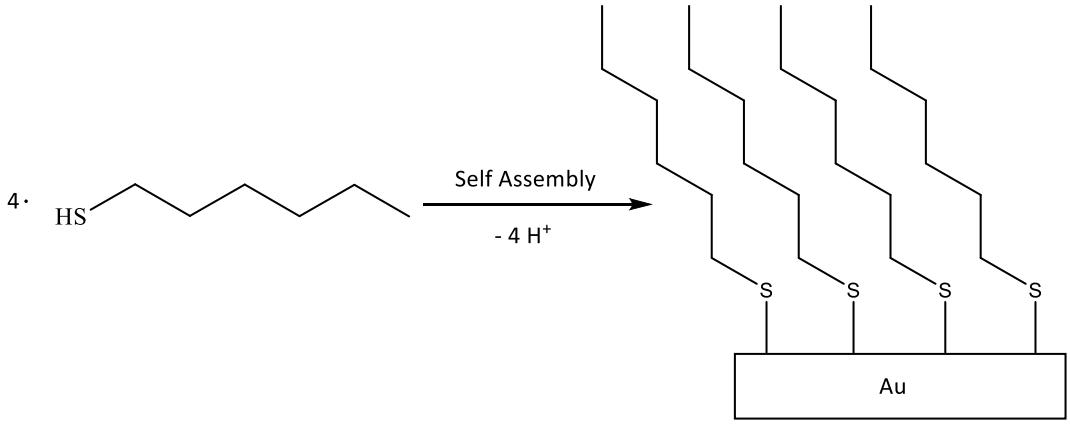

Figure 1.7: Formation of a 1-hexanethiolate SAM on an Au surface from 1-hexanethiol via self-assembly.

The high affinity of thiols for gold (and other metal surfaces) and their ability to replace molecules on the surface (an important cleaning effect) have made this combination the most popular in SAM research [50]. They have gained much attention due to their ease of formation on a variety of surfaces (including graphene) and their ability to modify the properties of the surface even after adsorption. SAM modified metal electrodes have applications across a range of areas such as corrosion protection [51], as mediators providing more facile electron transport between the electrode surface and species in solution [52], and in the design of electrochemical sensors [53,54], electrochemical transistors [55], molecular junctions [56] and rectifying devices [57]. In recent years, the most popular EC-SERS studies of this type have fallen into three main categories. Investigations into: a) redox inactive molecules, b) redox active

molecules and c) how bound molecules influence external electrochemical reactions.

Firstly, when investigating surface bound redox inactive molecules, additional information about the molecule-surface interaction can be gathered from the collected SERS spectra, including information regarding SAM orientation [40,58–68], which is of particular interest due to its ability to control electrode catalytic activity, electron transfer, and the binding of additional molecules [69]. For example, in 2016 Cabello *et al.* investigated thiocyanate adsorbed on Au surfaces, revealing the binding atom changed from S to N as the potential was moved positive [40]. Similarly, the binding atom can remain constant but the molecular orientation can change with potential. Huang *et al.* showed that Au bound hypoxanthine moved from tilted to upright as the potential was moved negative [60], while Zdaniauskiene *et al.* displayed how positively charged pyridinium terminated monolayers laid flat at more negative potentials, due to an electrostatic attraction to the surface [68].

Secondly, following redox active molecules *in situ* can provide new insights into reaction mechanisms and possible intermediates. Recent EC-SERS studies on such systems have led to greater understanding of the redox processes of viologen at different crystal faces of Au [70] and of the role of surface plasmons in the electrochemical hydrogenation of p-ethynylaniline [39]. Furthermore, in 2016 Bailey and Schultz investigated the redox processes of riboflavin, confirming a two-step two electron reaction pathway via the appearance of bands specific for a semi-quinone intermediate species [71]. In 2017, Aouzal *et al.* explored poly(5-amino-1,4-napthoquinone) (PANQ) binding on metal surfaces and followed a reversible electrochemical interaction with Li species in solution, opening up the possibility of using PANQ as a cathode in rechargeable batteries [72]. Additionally, Meneghello *et al.* have used EC-SERS to study the redox behaviour the clinically used drug mitoxantrone bound to DNA, rather than a model species such as methylene blue. Mitoxantrone has applications in treating cancer [73].

Finally, in recent years SERS articles investigating how molecules at electrode surfaces influence, or monitor, additional electrochemical reactions, rather than their own redox processes have become ever more popular.

For example, the observation that 3-amino-1,2,3-triazole inhibits Cu corrosion [74], but imidazole has no such effect [63]. Similarly, how cyanide ligands [75] and picolinic acid [76] aid Ag electrodeposition, or that 4-mercaptobenzoic acid can be used as a pH probe for Ni electrodeposition [77]. In addition, in 2017 Yonezawa *et al.* investigated how 4,4'-bipyridine (44bpy) accelerated the hydrogen evolution reaction on Au, proposing 44bpy reorientation via a surface-molecule interaction that increases the reaction rate [78].

1.3.2 Studies of oxygen electrochemistry

The electrochemical reactions of oxygen are both technologically important, with applications in fuel cells, water electrolysers and air-batteries, and well suited to study by SERS as the species involved are Raman active. In particular, SERS has proved useful in the study of the oxygen reduction reaction (ORR) in the aprotic solvents used in lithium-air (oxygen) batteries, which may be a promising power source for electric vehicles if the barriers such as low cycle life and the formation of undesirable byproducts can be overcome.

Galloway and Hardwick [45] employed SHIN particles to study the ORR in DMSO at smooth Au, Pt, Pd, and GC, and in acetonitrile at GC electrode surfaces. In DMSO they showed that the interaction of the superoxide O_2^- intermediate with the electrode surface was dependent on the nature of that surface. The SHINERS results suggest that O_2^- lies flat on Pt at more positive potentials, switching to an end-on orientation as the potential is made more negative, whilst the end-on orientation is preferred at all potentials for Au and Pd, as evidenced by peaks observed between 400 and 550 cm^{-1} (Figure 1.8a). In contrast, no peaks were observed for the surface-O_2^- interaction at GC and only peaks attributed to O_2^- in solution were observed. Other peaks were observed at GC attributed to HO_2 and LiO_2, the latter observed in the presence of 0.5 mol dm^{-3} $LiClO_4$ (Figure 1.8b). LiO_2 can decompose to produce Li_2O_2, which is insulating and is, thus, an undesirable byproduct. Qiao and Ye [79] used SERS at sputtered Au electrodes, employed for both the electrochemical and Raman measurements, to investigate the use of tetrathiafulvalene (TTF) as a redox mediator, designed to facilitate the oxidation of Li_2O_2 during the oxygen evolution reaction (OER) in dimethyl sulfoxide (DMSO) and thus improve the cycle life of the Li-O_2 battery. Their results showed that at the Au electrode the TTF^+ ions produced were mainly consumed by the oxidative decomposition of

LiO_2 during ORR/OER cycles in contrast to the desired action (Figure 1.8c). In contrast, at porous carbon electrodes, for which they were unable to obtain SERS, the *ex situ* Raman data supported TTF mediated oxidation of Li_2O_2, but also showed that the excess TTF^+ formed during round trip ORR/OER cycles correlated with the amount of a Li_2CO_3 by-product, which similarly suggested that TTF would not be a good redox mediator at this surface. The insights provided by SERS in both of these studies are highly valuable, enabling identification of by-products and furthering understanding of how the nature of the electrode surface influences their interactions with that surface.

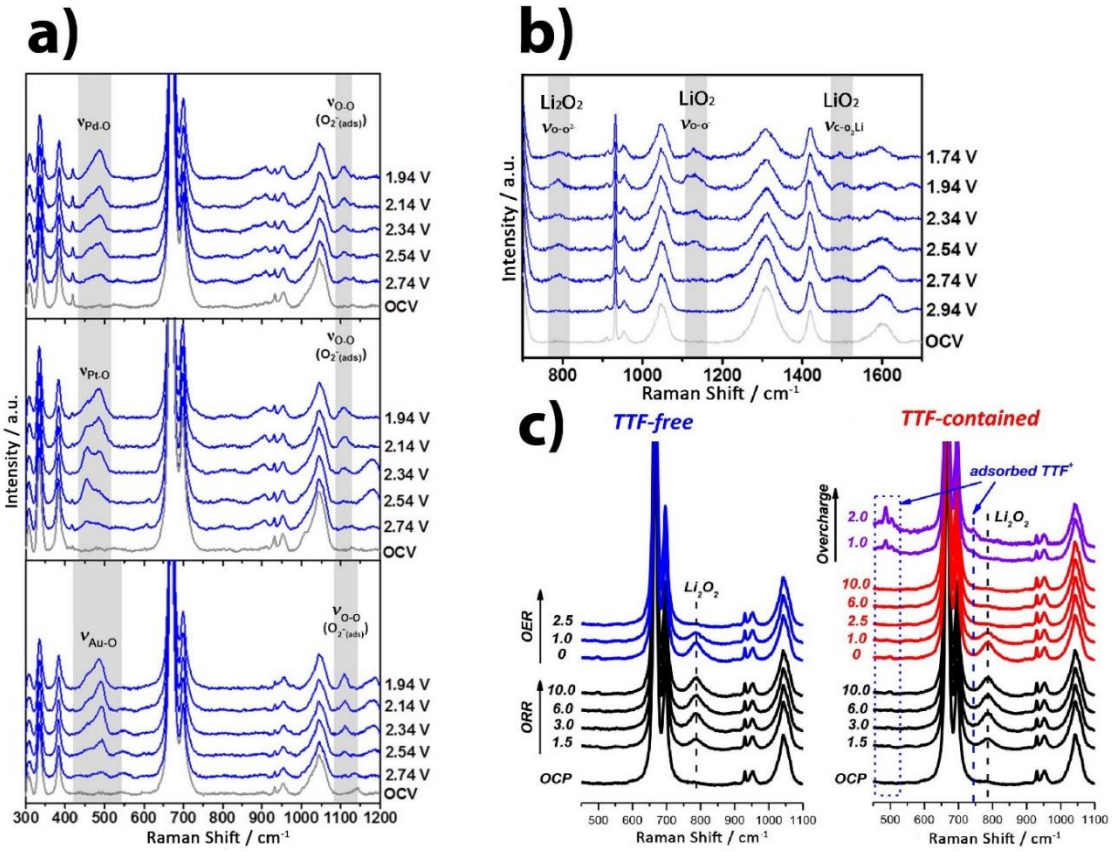

Figure 1.8: In situ SERS spectra of a) the ORR with SHIN's on the surface of polycrystalline Pd, Pt and Au in O_2 saturated 0.1 M $TBAClO_4$/DMSE electrolyte. Potentials *vs.* Li/Li^+. [45] b) the ORR with SHIN's on a GC electrode in an electrolyte of 0.5 M $LiClO_4$ in DMSO. Potentials *vs.* Li/Li^+. [45] c) the ORR and OER on sputtered Au electrodes in O_2 saturated 0.5 M $LiClO_4$ in DMSO [79] Adapted and reproduced with permission of Galloway and Hardwick and Qiao and Ye.

The borrowed SERS strategy, in which a SERS active substrate is coated with a thin layer of another material, thereby transferring the enhancement to the new surface, was utilised by Diaz-Morales *et al.* [80] to study OER on nickel oxyhydroxide (NiOOH) surfaces. Approximately 5

monolayers of Ni were plated on to an electrochemically roughened Au SERS substrate. The pH dependent $Ni(OH)_2$/NiOOH redox couple is clearly visible in the cyclic voltammograms of this surface obtained in alkaline to neutral pH $NaOH/NaClO_4$ electrolytes. The SERS show peaks associated with the Ni hydroxide and oxyhydroxide species as well as an active oxygen species with a peak between 800-1150 cm^{-1}, which was identified as the superoxo O-O vibration of $NiOO^-$. They go on to suggest that this species acts as the O_2 precursor when the pH > 11.

1.3.3 Electrochemistry of carbon monoxide and carbon dioxide

The concept of using the electrochemical reduction of CO_2 to produce a variety of fuels and commodity chemicals is an increasing research area in electrocatalysis [81]. CO is both a product (via partial reduction) and proposed intermediate in this process and in the electrocatalytic oxidation of organic compounds, such as methanol. SERS measurements are able to probe the metal-adsorbate vibrations providing information that is complementary to that obtained using IR and, where the catalyst is a roughened electrode surface or nanoparticles, directly study the working catalyst. Two studies of CO_2 reduction and one of CO oxidation are highlighted below.

Chernyshova and coworkers [42] studied the CO_2 reduction at roughened Cu electrodes, obtaining the electrochemical and SERS data using the same surfaces and combining these with density functional theory (DFT) and isotope exchange experiments to provide further information regarding the reaction mechanism. In particular they were able to show that the first intermediate of CO_2 conversion to formate on Cu is a carboxylate anion $*CO_2^-$ coordinated to the surface through one of its C–O bonds with the $\eta^2(C,O)$-CO_2^- structure (Figure 1.9, $\eta^2(C,O)$ indicates the CO_2^- anion binds to the surface via both metal-C and metal-O bonds). Consequently, the authors validated Hori's hypothesis [82,83] that CO_2 electroreduction starts with a common first intermediate. The $\eta^2(C,O)$-CO_2^- structure was also observed at potentials much more anodic than the onset of the CO_2 electroreduction. This suggests a critical role of additional cooperative effects such as surface defects, residual surface oxide, and co-adsorbed electron donors, which are yet to be understood. Finally, it was concluded that the electrocatalytic activity of the metal is related to the strengths of the metal–C and metal–O bonds of $\eta^2(C,O)$-CO_2^-.

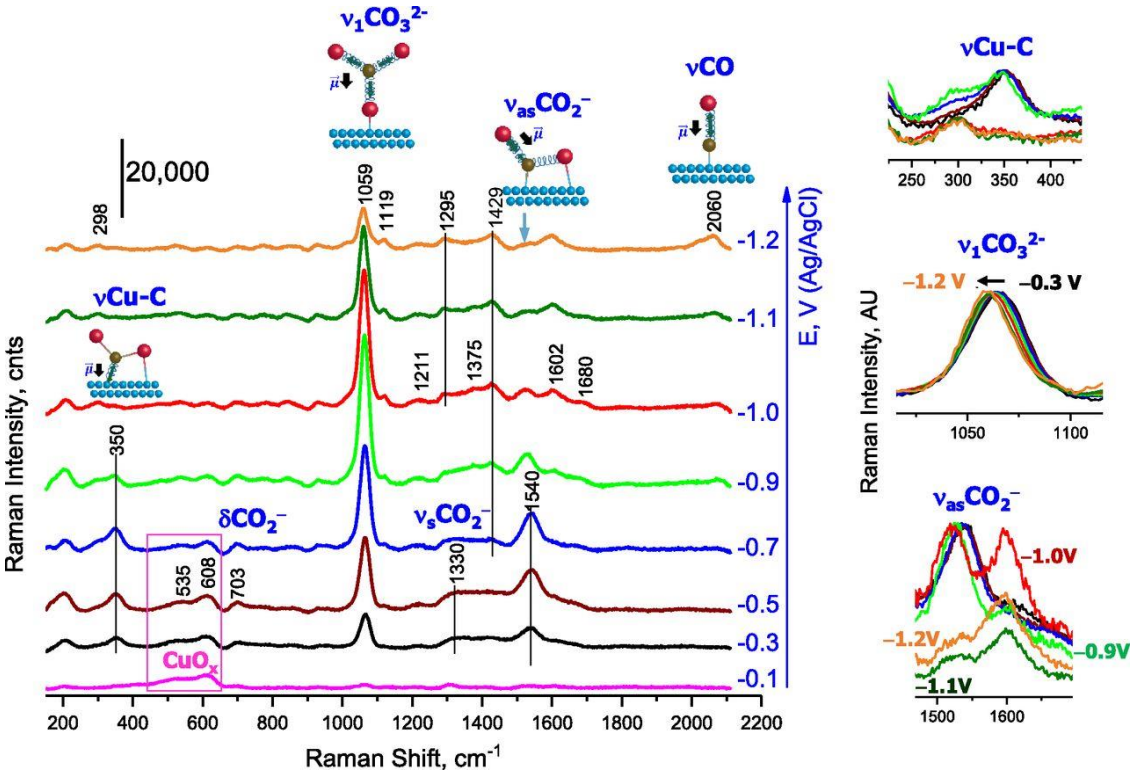

Figure 1.9: Potential dependant SERS spectra of roughened Cu in CO_2 saturated 0.1 M $NaHCO_3$ Reproduced with permission from Chernyshova *et al.* [42].

Whilst CO_2 reduction at Cu produces the most hydrocarbons, reduction at Ag and Au electrodes yields the greatest Faradaic efficiency for CO production [84], which is attributed to the weaker binding of CO to these surfaces. Modification of Ag electrode surfaces by N-containing additives had been shown to enhance CO_2 conversion [85] and Oberst *et al.* [86] extended this work to Au surfaces, studying the adsorption of the modifiers (benzotriazole and ethanolamine) and CO adsorption using SERS at roughened Au electrodes in alkaline electrolytes. In contrast to their earlier findings on Ag, addition of benzotriazole was found to have little effect on both the CO_2 activity and product distribution, which they attribute to the fact that CO adsorption on Au is much weaker than that on Ag (ca 0.28 eV *vs.* ca 0.40 eV, respectively) [87]. Modification of the surface by ethanolamine, which is a CO_2 scavenger did enhance the activity on Au, which they attributed to a local increase in the local CO_2 availability at the Au electrode surface.

Fuel cell electrocatalysts are typically nanoparticle in nature, which poses difficulties for SERS characterisation, especially for non-SERS active Pt-based alloy nanoparticles, which are the more common electrocatalysts for the H_2

anode reaction in reformate fuelled cells. Liang and coworkers [88] have taken an innovative approach to the study of such alloy nanoparticles by anchoring the Pt-based nanocrystals onto the SiO_2 shell of SHIN particles. The modified SHIN particles were then used to study catalytic CO electrooxidation on Pt and PtFe bimetallic nanoparticles. The modified SHIN particles were deposited on to a GC electrode for both the voltammetric and SERS measurements and the Pt_1Fe_x (x = 0, 0.5, 1, 1.5) particles were activated by cycling from -0.25 V to 1.0 V *vs.* SCE in 0.1 mol dm^{-3} $HClO_4$, which resulted in dissolution of some of the Fe to produce a Pt rich surface. Spectra were collected in a CO saturated solution, with peaks corresponding to the Pt–CO and C–O stretching modes being observed, with greater intensities observed for those catalysts which contained Fe. The frequency of the Pt-CO stretching peak was found to decrease with increasing Fe content, indicating a change to the electronic state of the Pt (d-band centre), which weakens the Pt-CO bond and enhances the electrocatalytic activity beyond that accounted for by the increased surface area of the particles upon leaching of Fe from the surface.

1.3.4 Formic acid oxidation

The electrooxidation of formic acid is of interest both as an intermediate in the oxidation of other small organic molecules and as fuel itself for direct formic acid fuel cells [89]. Pt monolayers coated Au nanoparticles (Au@Pt) have been shown to be active electrocatalysts for formic acid oxidation at room temperature [90]. Two recent mechanistic SERS studies have been reported. The first by Jeong and Kim [91] used Au@Pt substrates that were prepared by self-terminating electrodeposition of Pt onto dendritic Au rod (DAR) structures and both the electrochemical and SERS data were obtained using the same electrodes. The electrocatalytic activity of formic acid was found to be dependent on the Pt coverage and thickness. CO was used as a probe to determine the number of potential step cycles required to fully cover the Au surface with Pt through observation of the characteristic Pt-CO modes between 380-490 cm^{-1} and the C-O stretching mode on Au at 2094 cm^{-1}. Surfaces with island-type Pt layers on Au (low Pt coverage) exhibited electrochemical behaviour attributed to the direct oxidation of formic acid, whilst the indirect pathway, wherein CO_{ads} is as an intermediate, was observed as the Pt coverage increased. In contrast, CO_{ads} was observed in the SERS of the low Pt

coverage surfaces, indicating that the indirect electrooxidation of formic acid occurs.

In a more recent paper, Xie *et al.* [92] combined EC-SERS and high-frequency heating technology using a thermocouple microelectrode loading with round Au@Pt nanoparticles which also served as the SERS substrate to investigate the formic acid electrooxidation at different temperatures. The cyclic voltammetry data (from 25 ^{o}C to 100 ^{o}C) indicated that formic acid oxidation was enhanced significantly as the temperature increased. The SERS data showed that CO oxidative desorption from the Pt shell was promoted at higher temperatures, accounting for the improved catalytic activity, but did not support any change in the mechanism of the formic acid oxidation reaction.

1.4 Summary and thesis overview

45 years after its discovery, SERS remains a valuable tool for the study of electrode processes and mechanistic insights can be achieved, particularly for electrocatalytic reactions in which the reactants or intermediates are bound to the electrode surface. However, given the need to nanostructure the surface or use invasive probes to achieve enhancement, continued care needs to be taken when comparing electrochemical data obtained on SERS and non-SERS electrodes. As illustrated by several of the studies presented above, the nanostructures required for SERS or to achieve the electrocatalytic activity can in fact have the same effect, making SERS an excellent method for the mechanistic study of electrocatalytic reactions. This thesis aims to build upon the existing literature to further the understanding of the fundamental interactions between electrode surfaces and molecular adsorbates, as well as to elucidate intermediates in and mechanisms of electrochemical redox processes.

The literature presented in the current chapter has introduced EC-SERS and provided examples of some recent advancements in the field. This has also been recently submitted as a review article titled ‘Mechanistic insights into electrocatalytic reactions provided by SERS’ [93]. In Chapter 2, the chemicals, equipment and experimental and computation methods used for the

experiments of this thesis are described, including an analysis of the properties of the Au SSV substrates used for SERS.

Chapters 3-6 contain the main results of this thesis and all use a combination of SERS and DFT calculated Raman spectra. In Chapter 3, the potential dependent orientations of 4-sulfanylbenzonitrile (4-SBN), 3-SBN and 2-SBN SAMs are investigated, achieved by analysis of aromatic and nitrile in plane and out of plane vibrational band intensities, peak positions and the SERS selection rules. The information in this chapter was recently published as the journal article 'Potential dependent orientation of sulfanylbenzonitrile monolayers monitored by SERS' [94]. In Chapter 4, the electroreduction of *p*-nitrothiophenol (PNTP) and electrooxidation of *p*-aminothiophenol (PATP) are presented, including how the orientation of PNTP changed upon reduction and intermediate and product identification for both reactions. This chapter forms the basis of two submitted journal articles 'SERS investigation in the electroreduction of *p*-nitrothiophenol in the absence of photo-induced effects' [95] and 'An *in situ* SERS study of the effect of pH on the products of *p*-aminothiophenol monolayer electrooxidation' [96]. In Chapter 5, the orientation of thioamide terminated molecular wires are explored and in Chapter 6, glycerol electrooxidation is investigated, identifying intermediates of the reaction and thus providing additional information regarding its mechanism.

Chapter 7 provides the conclusions to this thesis and the results of the previous chapters are discussed with regards to the insight gained into adsorbate-surface interactions and redox mechanism elucidation. In addition, proposals for future work in these areas are here presented.

1.5 References

[1] A. Smekal, Zur Quantentheorie der Dispersion, Naturwissenschaften. 11 (1923) 873–875. doi:10.1007/BF01576902.

[2] C. V. Raman, K.S. Krishnan, A New Type of Secondary Radiation, Nature. 121 (1928) 501–502. doi:10.1038/121501c0.

[3] R. Singh, C. V. Raman and the Discovery of the Raman Effect, Phys. Perspect. 4 (2002) 399–420. doi:10.1007/s000160200002.

[4] R.S. Das, Y.K. Agrawal, Raman spectroscopy: Recent advancements, techniques and applications, Vib. Spectrosc. 57 (2011) 163–176. doi:10.1016/j.vibspec.2011.08.003.

[5] N. Dombey, The Nobel prize in physics, Nature. 300 (1982) 106–107. doi:10.1038/300106a0.

[6] American Chemical Society International Historic Chemical Landmarks. The Raman Effect., (1998). http://www.acs.org/content/acs/en/education/whatischemistry/landmarks/ramaneffect.html (accessed December 1, 2015).

[7] S.D. Harvey, M.E. Vucelick, R.N. Lee, B.W. Wright, Blind field test evaluation of Raman spectroscopy as a forensic tool, Forensic Sci. Int. 125 (2002) 12–21. doi:10.1016/S0379-0738(01)00615-6.

[8] C.M. Hodges, J. Akhavan, The use of Fourier Transform Raman spectroscopy in the forensic identification of illicit drugs and explosives, Spectrochim. Acta Part A Mol. Spectrosc. 46 (1990) 303–307. doi:10.1016/0584-8539(90)80098-J.

[9] R. Manoharan, Y. Wang, M.S. Feld, Histochemical analysis of biological tissues using Raman spectroscopy, Spectrochim. Acta Part A Mol. Biomol. Spectrosc. 52 (1996) 215–249. doi:10.1016/0584-8539(95)01573-6.

[10] N.J. Kline, P.J. Treado, Raman Chemical Imaging of Breast Tissue, J. Raman Spectrosc. 28 (1997) 119–124. doi:10.1002/(SICI)1097-4555(199702)28:2/3<119::AID-JRS73>3.3.CO;2-V.

[11] A.C. Williams, H.G.M. Edwards, B.W. Barry, Fourier transform Raman spectroscopy a novel application for examining human stratum corneum, Int. J. Pharm. 81 (1992) R11–R14. doi:10.1016/0378-5173(92)90022-T.

[12] K. Prasad, D.T. Grubb, Deformation behavior of Kevlar fibers studied by Raman spectroscopy, J. Appl. Polym. Sci. 41 (1990) 2189–2198. doi:10.1002/app.1990.070410923.

[13] H.G.M. Edwards, M. Gniadecka, S. Petersen, J.P. Hart Hansen, O. Faurskov Nielsen, D.H. Christensen, et al., NIR-FT Raman spectroscopy as a diagnostic probe for mummified skin and nails, Vib. Spectrosc. 28

(2002) 3–15. doi:10.1016/S0924-2031(01)00141-2.

[14] C. Eliasson, P. Matousek, Noninvasive authentication of pharmaceutical products through packaging using spatially offset Raman spectroscopy, Anal. Chem. 79 (2007) 1696–1701. doi:10.1021/ac062223z.

[15] A. Torreggiani, G. Fini, Drug-antiserum molecular interactions: a Raman spectroscopic study, J. Raman Spectrosc. 30 (1999) 295–300. doi:10.1002/(SICI)1097-4555(199904)30:4<295::AID-JRS376>3.0.CO;2-N.

[16] M.S. Amer, Raman spectroscopy and molecular simulation investigations of adsorption on the surface of single-walled carbon nanotubes and nanospheres, J. Raman Spectrosc. 38 (2007) 721–727. doi:10.1002/jrs.1689.

[17] H.G. Karge, E. Geidel, Vibrational Spectroscopy, in: Vib. Spectrosc., 3rd ed., Oxford University Press, 2004: pp. 1–200. doi:10.1007/b94235.

[18] M.E. Abdelsalam, P.N. Bartlett, J.J. Baumberg, S. Cintra, T.A. Kelf, A.E. Russell, Electrochemical SERS at a structured gold surface, Electrochem. Commun. 7 (2005) 740–744. doi:10.1016/j.elecom.2005.04.028.

[19] T.H. Maiman, Stimulated Optical Radiation in Ruby, Nature. 187 (1960) 493–494. doi:10.1038/187493a0.

[20] M. Fleischmann, P.J. Hendra, A.J. McQuillan, Raman spectra of pyridine adsorbed at a silver electrode, Chem. Phys. Lett. 26 (1974) 163–166. doi:10.1016/0009-2614(74)85388-1.

[21] M.G. Albrecht, J.A. Creighton, Anomalously Intense Raman Spectra of Pyridine at a Silver Electrode, J. Am. Chem. Soc. 99 (1977) 5215–5217. doi:10.1021/ja00457a071.

[22] D.L. Jeanmaire, R.P. Van Duyne, Surface raman spectroelectrochemistry, J. Electroanal. Chem. Interfacial Electrochem. 84 (2006) 1–20. doi:10.1016/s0022-0728(77)80224-6.

[23] B. Sharma, R.R. Frontiera, A.I. Henry, E. Ringe, R.P. Van Duyne, SERS: Materials, applications, and the future, Mater. Today. 15 (2012) 16–25. doi:10.1016/s1369-7021(12)70017-2.

[24] P.L. Stiles, J.A. Dieringer, N.C. Shah, R.P. Van Duyne, Surface-Enhanced Raman Spectroscopy, Annu. Rev. Anal. Chem. 1 (2008) 601–626. doi:10.1146/annurev.anchem.1.031207.112814.

[25] Surface enhanced Raman Spectroscopy, Faraday Discuss. 132 (2006).

[26] Surface Enhanced Raman Spectroscopy, Faraday Discuss. 205 (2017).

[27] Ji-Yang, J.C. Dong, V.V. Kumar, J.F. Li, Z.Q. Tian, Probing electrochemical interfaces using shell-isolated nanoparticles-enhanced Raman spectroscopy, Curr. Opin. Electrochem. 1 (2017) 16–21. doi:10.1016/j.coelec.2016.12.009.

[28] T. Touzalin, S. Joiret, E. Maisonhaute, I.T. Lucas, Capturing electrochemical transformations by tip-enhanced Raman spectroscopy, Curr. Opin. Electrochem. 6 (2017) 46–52. doi:10.1016/j.coelec.2017.10.016.

[29] J.H.K. Pfisterer, K.F. Domke, Unfolding the versatile potential of EC-TERS for electrocatalysis, Curr. Opin. Electrochem. 8 (2018) 96–102. doi:10.1016/j.coelec.2018.03.023.

[30] G. Aruldhas, Molecular structure and spectroscopy, 2nd ed., PHI Learning, Delhi, 2007.

[31] D.L. Jeanmaire, R.P. Van Duyne, Surface raman spectroelectrochemistry, J. Electroanal. Chem. Interfacial Electrochem. 84 (1977) 1–20. doi:10.1016/S0022-0728(77)80224-6.

[32] A.J. McQuillan, The discovery of surface-enhanced Raman scattering, Notes Rec. R. Soc. 63 (2009) 105–109. doi:10.1098/rsnr.2008.0032.

[33] T.A. Kelf, Y. Sugawara, R.M. Cole, J.J. Baumberg, M.E. Abdelsalam, S. Cintra, Localized and delocalized plasmons in metallic nanovoids, Phys. Rev. B - Condens. Matter Mater. Phys. 74 (2006) 245415. doi:10.1103/PhysRevB.74.245415.

[34] K.A. Willets, R.P. Van Duyne, Localized Surface Plasmon Resonance Spectroscopy and Sensing, Annu. Rev. Phys. Chem. 58 (2006) 267–297. doi:10.1146/annurev.physchem.58.032806.104607.

[35] R.P. Van Duyne, J.C. Hulteen, D.A. Treichel, Atomic force microscopy

and surface-enhanced Raman spectroscopy. I. Ag films and Ag film over polymer nanosphere surfaces supported on glass, J. Chem. Phys. 99 (1993) 2101–2115. doi:10.1063/1.465276.

[36] C.G. Khoury, T. Vo-Dinh, Gold nanostars for surface-enhanced Raman scattering: synthesis, characterization and optimization, J. Phys. Chem. C. 112 (2008) 18849–18859. doi:10.1021/jp8054747.

[37] S. Mahajan, R.M. Cole, B.F. Soares, S.H. Pelfrey, A.E. Russell, J.J. Baumberg, Relating SERS intensity to specific plasmon modes on sphere segment void surfaces, J. Phys. Chem. C. 113 (2009) 9284–9289. doi:10.1021/jp900661u.

[38] J.F. Li, Y.F. Huang, Y. Ding, Z.L. Yang, S.B. Li, X.S. Zhou, Shell-isolated nanoparticle-enhanced Raman spectroscopy, Nature. 464 (2010). doi:10.1038/nature08907.

[39] B.W. Mao, M.M. Xu, J.F. Li, J.C. Dong, Y. Wang, J. Yang, In situ SERS and SHINERS study of electrochemical hydrogenation of p-ethynylaniline in nonaqueous solvents, Electrochem. Commun. 78 (2017) 16–20. doi:10.1016/j.elecom.2017.03.015.

[40] G. Cabello, X.J. Chen, R. Panneerselvam, Z.Q. Tian, Potential dependent thiocyanate adsorption on gold electrodes: a comparison study between SERS and SHINERS, J. Raman Spectrosc. 47 (2016) 1207–1212. doi:10.1002/jrs.4944.

[41] X.D. Tian, B.J. Liu, J.F. Li, Z.L. Yang, B. Ren, Z.Q. Tian, SHINERS and plasmonic properties of Au Core SiO_2 shell nanoparticles with optimal core size and shell thickness, J. Raman Spectrosc. 44 (2013) 994–998. doi:10.1002/jrs.4317.

[42] I. V Chernyshova, P. Somasundaran, S. Ponnurangam, On the origin of the elusive first intermediate of CO_2 electroreduction., Proc. Natl. Acad. Sci. U. S. A. 115 (2018) E9261–E9270. doi:10.1073/pnas.1802256115.

[43] T.H. Lin, N.C. Linn, L. Tarajano, B. Jiang, P. Jiang, Electrochemical SERS at periodic metallic nanopyramid arrays, J. Phys. Chem. C. 113 (2009) 1367–1372. doi:10.1021/jp809363m.

[44] A.E. Russell, S.H. Pelfrey, J. Speed, S. Mahajan, P.N. Bartlett, J.J.

Baumberg, Sphere Segment Void Structures: a Reproducible SERS Substrate for Electrochemical Studies, in: 41st Am. Chem. Soc. Cent. Reg. Meet., 2009.

[45] T.A. Galloway, L.J. Hardwick, Utilizing In Situ Electrochemical SHINERS for Oxygen Reduction Reaction Studies in Aprotic Electrolytes, J. Phys. Chem. Lett. 7 (2016) 2119–2124. doi:10.1021/acs.jpclett.6b00730.

[46] M. Shanthil, R. Thomas, R.S. Swathi, T.K. George, Ag@SiO_2 core-shell nanostructures: Distance-dependent plasmon coupling and SERS investigation, J. Phys. Chem. Lett. 3 (2012) 1459–1464. doi:10.1021/jz3004014.

[47] R.A. Hackler, N. Large, S.S. Masango, M.O. McAnally, G.C. Schatz, P.C. Stair, et al., High-Resolution Distance Dependence Study of Surface-Enhanced Raman Scattering Enabled by Atomic Layer Deposition, Nano Lett. 16 (2016) 4251–4259. doi:10.1021/acs.nanolett.6b01276.

[48] A.E. Russell, L. Rubasingham, T.H. Ballinger, P.L. Hagans, Thin layer effects in in situ far-infrared spectroscopy, J. Electroanal. Chem. 422 (1997) 197–200. doi:10.1016/S0022-0728(96)04891-7.

[49] J.C. Love, L.A. Estroff, J.K. Kriebel, R.G. Nuzzo, G.M. Whitesides, Self-assembled monolayers of thiolates on metals as a form of nanotechnology, Chem. Rev. 105 (2005) 1103–1169. doi:10.1021/cr0300789.

[50] L. Newton, T. Slater, N. Clark, A. Vijayaraghavan, Self assembled monolayers (SAMs) on metallic surfaces (gold and graphene) for electronic applications, J. Mater. Chem. C. 1 (2013) 376–393. doi:10.1039/C2TC00146B.

[51] Y. Xia, X.M. Zhao, G.M. Whitesides, Pattern transfer: Self-assembled monolayers as ultrathin resists, Microelectron. Eng. 32 (1996) 255–268. doi:10.1016/0167-9317(95)00174-3.

[52] B. Liu, A.J. Bard, M. V. Mirkin, S.E. Creager, Electron Transfer at Self-Assembled Monolayers Measured by Scanning Electrochemical Microscopy, J. Am. Chem. Soc. 126 (2004) 1485–1492. doi:10.1021/ja038611p.

[53] R.G. Bozic, A.C. West, R. Levicky, Square wave voltammetric detection of 2,4,6-trinitrotoluene and 2,4-dinitrotoluene on a gold electrode modified with self-assembled monolayers, Sensors Actuators, B Chem. 133 (2008) 509–515. doi:10.1016/j.snb.2008.03.017.

[54] S. Yang, B. Xu, J. Zhang, X. Huang, J. Ye, C. Yu, Controllable adsorption of reduced graphene oxide onto self-assembled alkanethiol monolayers on gold electrodes: Tunable electrode dimension and potential electrochemical applications, J. Phys. Chem. C. 114 (2010) 4389–4393. doi:10.1021/jp911760b.

[55] P. Marmont, N. Battaglini, P. Lang, G. Horowitz, J. Hwang, A. Kahn, et al., Improving charge injection in organic thin-film transistors with thiol-based self-assembled monolayers, Org. Electron. Physics, Mater. Appl. 9 (2008) 419–424. doi:10.1016/j.orgel.2008.01.004.

[56] H.B. Akkerman, P.W.M. Blom, D.M. de Leeuw, B. de Boer, Towards molecular electronics with large-area molecular junctions, Nature. 441 (2006) 69–72. doi:10.1038/nature04699.

[57] C.A. Nijhuis, W.F. Reus, A.C. Siegel, G.M. Whitesides, A molecular half-wave rectifier, J. Am. Chem. Soc. 133 (2011) 15397–15411. doi:10.1021/ja201223n.

[58] L.Q. Dong, J.Z. Zhou, L.L. Wu, P. Dong, Z.H. Lin, SERS studies of self-assembled DNA monolayer - Characterization of adsorption orientation of oligonucleotide probes and their hybridized helices on gold substrate, Chem. Phys. Lett. 354 (2002) 458–465. doi:10.1016/S0009-2614(02)00163-X.

[59] D.A. Nelson, Z.D. Schultz, Influence of Optically Rectified Electric Fields on the Plasmonic Photocatalysis of 4-Nitrothiophenol and 4-Aminothiophenol to 4,4-Dimercaptoazobenzene, J. Phys. Chem. C. 122 (2018) 8581–8588. doi:10.1021/acs.jpcc.8b00662.

[60] W. Huang, J.Z. Jiang, L. Chen, B.Q. Zhang, S.F. Deng, J.J. Sun, et al., Density functional theory and surface enhanced Raman spectroscopy studies of tautomeric hypoxanthine and its adsorption behaviors in electrochemical processes, Electrochim. Acta. 164 (2015) 132–138.

doi:10.1016/j.electacta.2015.02.220.

[61] K.T. Carron, L.G. Hurley, Axial and azimuthal angle determination with surface-enhanced Raman spectroscopy: thiophenol on copper, silver, and gold metal surfaces, J. Phys. Chem. 95 (1991) 9979–9984. doi:10.1021/j100177a068.

[62] B. Ren, R.A. Gu, J.L. Yao, X.M. Fan, Z.Q. Tian, Y.X. Yuan, The reorientation of benzonitrile on platinum electrode probed by surface enhanced Raman spectroscopy, J. Electroanal. Chem. 624 (2008) 129–133. doi:10.1016/j.jelechem.2008.08.004.

[63] E.F. Silva, M.C.E. Bandeira, W.A. Alves, O.R. Mattos, Surface-Enhanced Raman Scattering and Electrochemical Investigations on the Adsorption of Imidazole: Imidazolium Couple and Its Implications on Copper Corrosion Inhibition, J. Electrochem. Soc. 165 (2018) C375–C384. doi:10.1149/2.0841807jes.

[64] I. Brand, J. Juhaniewicz-Debinska, L. Wickramasinghe, C.N. Verani, An: In situ spectroelectrochemical study on the orientation changes of an [FeiiiLN2O3] metallosurfactant deposited as LB Films on gold electrode surfaces, Dalt. Trans. 47 (2018) 14218–14226. doi:10.1039/c8dt00333e.

[65] Z.Q. Tian, B. Ren, D.Y. Wu, Surface-enhanced Raman scattering: From noble to transition metals and from rough surfaces to ordered nanostructures, J. Phys. Chem. B. 106 (2002) 9463–9483. doi:10.1021/jp0257449.

[66] J.E. Pemberton, M.A. Bryant, R.L. Sobocinski, S.L. Joa, A Simple Method for Determination of Orientation of Adsorbed Organics of Low Symmetry Using Surface-Enhanced Raman Scattering, J . Phys. Chem. 96 (1992) 3716–3182. doi:10.1021/j100188a039.

[67] C.A. Szafranski, W. Tanner, P.E. Laibinis, R.L. Garrell, Surface-enhanced Raman spectroscopy of aromatic thiols and disulfides on gold electrodes, Langmuir. 14 (1998) 3570–3579. doi:10.1021/la9702502.

[68] A. Zdaniauskiene, T. Charkova, I. Matulaitiene, O. Eicher-Lorka, A. Matijoška, M. Skapas, et al., Electrochemical Shell-Isolated Nanoparticle-Enhanced Raman Spectroscopy: Bonding, Structure, and Ion-Pairing of

the Positive Charge Bearing Pyridinium Ring Terminated Monolayer at Smooth Gold Electrode, J. Phys. Chem. C. 122 (2018) 1234–1242. doi:10.1021/acs.jpcc.7b09970.

[69] Y. Chao, Q. Zhou, Y. Li, Y. Yan, Y. Wu, J. Zheng, Potential dependent surface-enhanced Raman scattering of 4-mercaptopyridine on electrochemically roughened silver electrodes, J. Phys. Chem. C. 111 (2007) 16990–16995. doi:10.1021/jp0760051.

[70] B.Y. Wen, J. Yi, Y.H. Wang, K. Madasamy, H. Zhang, M. Kathiresan, In-situ monitoring of redox processes of viologen at Au(hkl) single-crystal electrodes using electrochemical shell-isolated nanoparticle-enhanced Raman spectroscopy, Electrochem. Commun. 72 (2016) 131–134. doi:10.1016/j.elecom.2016.08.026.

[71] M.R. Bailey, Z.D. Schultz, SERS speciation of the electrochemical oxidation–reduction of riboflavin, Analyst. 141 (2016) 5078–5087. doi:10.1039/C6AN01054G.

[72] R. Wang, Z. Aouzal, M. Bazzaoui, M. Bouabdallaoui, S. Ben Jadi, E.A. Bazzaoui, In situ surface-enhanced Raman scattering investigation of poly(5-amino-1,4-naphthoquinone) using roughened electrodes and metal colloids, Synth. Met. 231 (2017) 80–88. doi:10.1016/j.synthmet.2017.06.019.

[73] M. Meneghello, E. Papadopoulou, P. Ugo, P.N. Bartlett, Using Electrochemical SERS to Measure the Redox Potential of Drug Molecules Bound to dsDNA - A Study of Mitoxantrone, Electrochim. Acta. 187 (2016) 684–692. doi:10.1016/j.electacta.2015.11.121.

[74] Y. Wan, Z. Qin, Q. Xu, M. Chen, Y.L. Min, M. Li, Corrosion inhibition activity and adsorption behavior of 3-amino-1, 2, 4-triazole on copper, Int. J. Electrochem. Sci. 12 (2017) 10701–10713. doi:10.20964/2017.11.68.

[75] V. Caramia, B. Bozzini, Potential-dependent reactivity of adsorbed cyanide during the electrodeposition of silver from cyanocomplexes: a study based on in-situ surface-enhanced Raman spectroscopy , Trans. IMF. 93 (2014) 82–88. doi:10.1179/0020296714z.000000000207.

[76] C.I. Vázquez, G.F.S. Andrade, M.L.A. Temperini, G.I. Lacconi,

Spectroelectrochemical study of picolinic acid adsorption during silver electrodeposition, Electrochim. Acta. 156 (2015) 154–162. doi:10.1016/j.electacta.2015.01.034.

[77] T. Homma, M. Kunimoto, M. Sasaki, T. Hanai, M. Yanagisawa, Surface enhanced Raman spectroscopy measurement of surface pH at the electrode during Ni electrodeposition reaction, J. Appl. Electrochem. 48 (2018) 561–567. doi:10.1007/s10800-017-1139-1.

[78] Y. Yonezawa, H. Minamimoto, F. Nagasawa, M. Takase, S. Yasuda, K. Murakoshi, In-situ electrochemical surface-enhanced Raman scattering observation of molecules accelerating the hydrogen evolution reaction, J. Electroanal. Chem. 800 (2017) 7–12. doi:10.1016/j.jelechem.2017.04.049.

[79] Y. Qiao, S. Ye, Spectroscopic Investigation for Oxygen Reduction and Evolution Reactions with Tetrathiafulvalene as a Redox Mediator in Li-O2 Battery, J. Phys. Chem. C. 120 (2016) 15830–15845. doi:10.1021/acs.jpcc.5b11692.

[80] O. Diaz-Morales, D. Ferrus-Suspedra, M.T.M. Koper, The importance of nickel oxyhydroxide deprotonation on its activity towards electrochemical water oxidation, Chem. Sci. 7 (2016) 2639–2645. doi:10.1039/c5sc04486c.

[81] J.E. Bercaw, J.N.H. Reek, G.L. Waldrop, R. Hille, T.B. Rauchfuss, H. Dobbek, Frontiers, Opportunities, and Challenges in Biochemical and Chemical Catalysis of CO_2 Fixation , Chem. Rev. 113 (2013) 6621–6658. doi:10.1021/cr300463y.

[82] Y. Hori, Electrochemical CO2 Reduction on Metal Electrodes, in: Mod. Asp. Electrochem., Springer New York, New York, NY, 2008: pp. 89–189. doi:10.1007/978-0-387-49489-0_3.

[83] Y. Hori, H. Wakebe, T. Tsukamoto, O. Koga, Electrocatalytic process of CO selectivity in electrochemical reduction of CO_2 at metal electrodes in aqueous media, Electrochim. Acta. 39 (1994) 1833–1839. doi:10.1016/0013-4686(94)85172-7.

[84] H.A. Hansen, J.B. Varley, A.A. Peterson, J.K. Nørskov, Understanding

trends in the electrocatalytic activity of metals and enzymes for CO_2 reduction to CO, J. Phys. Chem. Lett. 4 (2013) 388–392. doi:10.1021/jz3021155.

[85] C.E. Tornow, M.R. Thorson, S. Ma, A.A. Gewirth, P.J.A. Kenis, Nitrogen-based catalysts for the electrochemical reduction of CO_2 to CO, J. Am. Chem. Soc. 134 (2012) 19520–19523. doi:10.1021/ja308217w.

[86] J.L. Oberst, H.R. “Molly” Jhong, P.J.A. Kenis, A.A. Gewirth, Insight into the electrochemical reduction of CO_2 on gold via surface-enhanced Raman spectroscopy and N-containing additives, J. Solid State Electrochem. 20 (2016) 1149–1154. doi:10.1007/s10008-015-2874-z.

[87] Y. Santiago-Rodríguez, J.A. Herron, M.C. Curet-Arana, M. Mavrikakis, Atomic and molecular adsorption on Au(111), Surf. Sci. 627 (2014) 57–69. doi:10.1016/j.susc.2014.04.012.

[88] M.M. Liang, Y.H. Wang, R. Shao, W.M. Yang, H. Zhang, H. Zhang, et al., In situ electrochemical surface-enhanced Raman spectroscopy study of CO electrooxidation on PtFe nanocatalysts, Electrochem. Commun. 81 (2017) 38–42. doi:10.1016/j.elecom.2017.05.022.

[89] K. Jiang, H.X. Zhang, S. Zou, W. Bin Cai, Electrocatalysis of formic acid on palladium and platinum surfaces: From fundamental mechanisms to fuel cell applications, Phys. Chem. Chem. Phys. 16 (2014) 20360–20376. doi:10.1039/c4cp03151b.

[90] M.D. Obradović, A. V. Tripković, S.L. Gojković, The origin of high activity of Pt-Au surfaces in the formic acid oxidation, Electrochim. Acta. 55 (2009) 204–209. doi:10.1016/j.electacta.2009.08.038.

[91] H. Jeong, J. Kim, Insights into the Electrooxidation Mechanism of Formic Acid on Pt Layers on Au Examined by Electrochemical SERS, J. Phys. Chem. C. 120 (2016) 24271–24278. doi:10.1021/acs.jpcc.6b08611.

[92] W. Chang Xie, Y. Ling, Y.Z. Zhang, H. Pan, G.K. Liu, J. Tang, In-situ electrochemical surface-enhanced Raman spectroscopy study of formic acid electrooxidation at variable temperatures by high-frequency heating technology, Electrochim. Acta. 281 (2018) 323–328. doi:10.1016/j.electacta.2018.05.167.

[93] A.J. Keeler, A.E. Russell, Mechanistic insights into electrocatalytic reactions provided by SERS, Curr. Opin. Electrochem. Submitted (2019).

[94] A.J. Keeler, A.E. Russell, Potential dependent orientation of sulfanylbenzonitrile monolayers monitored by SERS, Electrochim. Acta. 305 (2019) 378–387. doi:10.1016/j.electacta.2019.03.044.

[95] A.J. Keeler, A.E. Russell, SERS investigation into the mechanism of p-nitrothiophenol electroreduction in the absence of photo-induced effects, Electrochim. Acta. Submitted (2019).

[96] A.J. Keeler, A.E. Russell, An in situ SERS study of the effect of pH on the products of p-aminothiophenol monolayer electrooxidation, Phys. Chem. Chem. Phys. Submitted (2019).

Chapter 2: Experimental and theoretical methods

The experimental and theoretical methods used throughout this work are described here.

2.1 Materials and Chemicals

The materials and chemicals used in this thesis, alongside their suppliers and any further details are shown in Table 2.1.

Chemical Name	Supplier
2-sulfanylbenzonitrile, 95 %	Enamine
3-sulfanylbenzonitrile. 95 %	Enamine
4-aminothiophenol, 97 %	Sigma-Aldrich
4-nitrothiophenol, 96 %	Alfa Aesar
4-sulfanylbenzonitrile, 98 %	Enamine
Acetone, >99.5 %	Sigma-Aldrich
Argon gas, compressed, oxygen free	BOC
Benzenethiol, >98 %	Sigma-Aldrich
Chromium Chips, 99.9 %	Agar Scientific
Clear nail varnish	Rimmell
Ethanol, absolute, > 99.8 %	Sigma-Aldrich
Ethanol, anhydrous, >99.5 %	Sigma-Aldrich
Glass cover slip, 24x24 mm, 0.14 – 0.19 mm thick	Thermo Scientific
Glycerol, >99.5 %	Sigma-Aldrich
Gold brightener additive (E3)	Metalor
Gold plating solution, cyanide free, MetGold ECF 60	Metalor
Gold surface cleaning solution, H_2O >90 %, H_2SO_4 <10 %	Sigma-Aldrich
Gold wire for evaporation, 0.2 mm diameter, 99.99 %	Agar Scientific
Gold wire, 1 mm diameter, 99.9 %	Alfa Aesar
Micro-90 cleaning solution, concentrated	Sigma-Aldrich
Microscope Slides, 76x26 mm, 1 mm thick	Thermo Scientific
N,N-Dimethylformamide, anhydrous, 99.8 %	Sigma-Aldrich
Nitrogen gas, compressed, oxygen free	BOC
Parafilm	Bemis
Platinum wire, 1 mm diameter, 99.9 %	Alfa Aesar
Polystyrene Sphere solution, 600 nm diameter, 1.8 %	Thermo-Scientific
Potassium chloride, >99.5 %	Sigma-Aldrich
Potassium Hydroxide, >90 %	Sigma-Aldrich
Pyridine, >99 %	Sigma-Aldrich
Silicon wafer, 5x5 mm, 1 mm thick	Renishaw
Stainless steel wire, 1 mm diameter, Fe:Ni:Cr 90:19:11 wt%	Alfa Aesar
Tetrabutylammonium tetrafluoroborate, >99.0 %	Sigma-Aldrich
1,4-benzenedicarbothioamide	Synthesized in house
4,4'-(ethyne-1,2-diyl)dibenzodicarbothioamine	Synthesized in house

Table 2.1: List of the materials and chemicals used and their suppliers.

All water used for preparing solutions was ultra-pure (Suez Select, 18.4 MΩ cm) and any glassware and the spectroelectrochemical cell were both

cleaned with acetone and ultra-pure water before use. In addition, the electrolytes in Chapter 3 were made up with non-aqueous solvents and thus, any equipment used here was dried at 105 ^{o}C for an additional 12 hours (Thermo Scientific) before being transferred to a nitrogen filled glove box (Belle Technology).

2.2 Sphere Segment Void Substrates

Sphere segment void (SSV) substrates were first developed at the University of Southampton in 2004 [1] and later discovered to provide a reproducible alternative to traditional roughened metal surface enhanced Raman spectroscopy (SERS) substrates [2–6]. They provide a reusable and tuneable surface that is stable in a variety of electrolytes and under high intensity laser illumination. Therefore, they are excellent substrates for electrochemical SERS (EC-SERS). All SERS spectra in this thesis were recorded using Au SSV substrates unless explicitly stated. The following instructions state how these were manufactured [2], with a schematic shown in Figure 2.2.

2.2.1 SSV Manufacture

Microscope slides were cleaned by sonicating for 30 minutes in each of: dilute Micro-90 solution (25: 1, water: Micro-90), deionised water, ethanol and acetone before being dried with an argon flow. Onto these cleaned slides a 10 nm adhesion layer of chromium (chromium chips) then 200 nm of gold (gold wire for evaporation) were deposited using vacuum evaporation, before being cut into 8 equally sized pieces to be used as a base to create a thin layer cell (TLC). Parafilm was cut into an inverse trapezium shape and placed onto each gold piece, before a glass cover slip was stacked on top and the complete structure heated to approximately 55 ^{o}C on a hot plate to begin melting the parafilm. The structure was then lightly pressed, enabling the parafilm to act as a glue to attach the gold piece and the glass cover slip and the TLC region to form. 10 µL of polystyrene sphere solution (1.8 %, 600 nm) was then injected into the TLC region and the pieces left to dry tilted at an angle of approximately 30 ^{o} in a 14 ^{o}C fridge for 48 hours.

During the drying process, the water evaporated slowly and resulted in a monolayer of self-assembled polystyrene spheres in a hexagonal array on the gold surface. The formation of the array was caused by both attractive hydrodynamic and lateral capillary forces, causing the spheres to move from solution onto the surface and then become packed [7,8]. This process is shown in Figure 2.1.

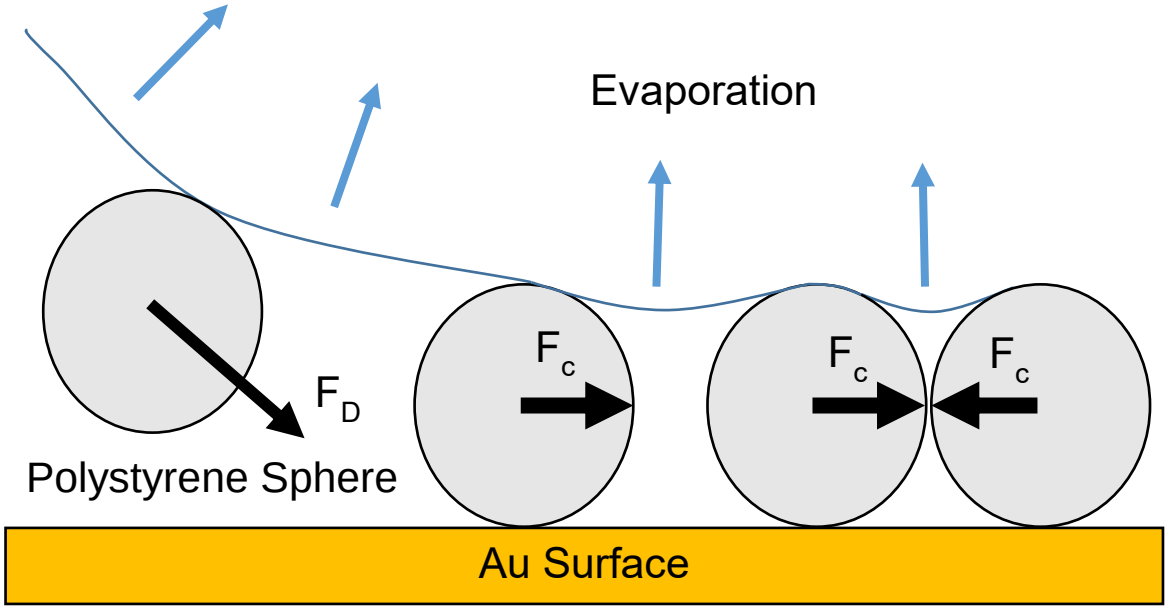

Figure 2.1: Representation of the formation of a polystyrene sphere monolayer, on an gold surface, from the evaporation of a water / polystyrene sphere suspension. F_D is a hydrodynamic force driving the movement of the spheres to the edges of the evaporating area, F_c is a lateral capillary force from the overlap of water menisci between spheres.

After 48 hours the TLC was disassembled by re-heating and the glass cover slip and parafilm were removed and the non-polystyrene sphere region then insulated using clear nail varnish. The Au SSV structure was then formed by electrodeposition through the array from a gold plating solution (1000:1, Au Plating solution: brightener, Metalor) using an Autolab PGSTAT101 to control a three electrode cell (Au piece working electrode, platinum wire counter electrode and saturated calomel electrode (SCE) reference electrode at -0.72 V *vs.* SCE. The amount of Au deposited was controlled by monitoring the charge passed (see 2.2.2 Void Height Calculation) and was approximately 480 nm thick, corresponding to 0.8 times the diameter of the polystyrene spheres, giving a total gold layer of 680 nm. After this, the substrates were rinsed with ethanol, dried under nitrogen flow for at least 5 minutes and left to soak in N,N-dimethylformamide (DMF) for 24 hours to remove the spheres. Depending on

the size of the area of successful nanostructuring, each substrate was then cut into as many as four separate pieces, taking the total possible substrates from one microscope slide to be 32. The properties of Au SSV substrates are described and discussed in ‘2.6 Properties of SSV substrates’

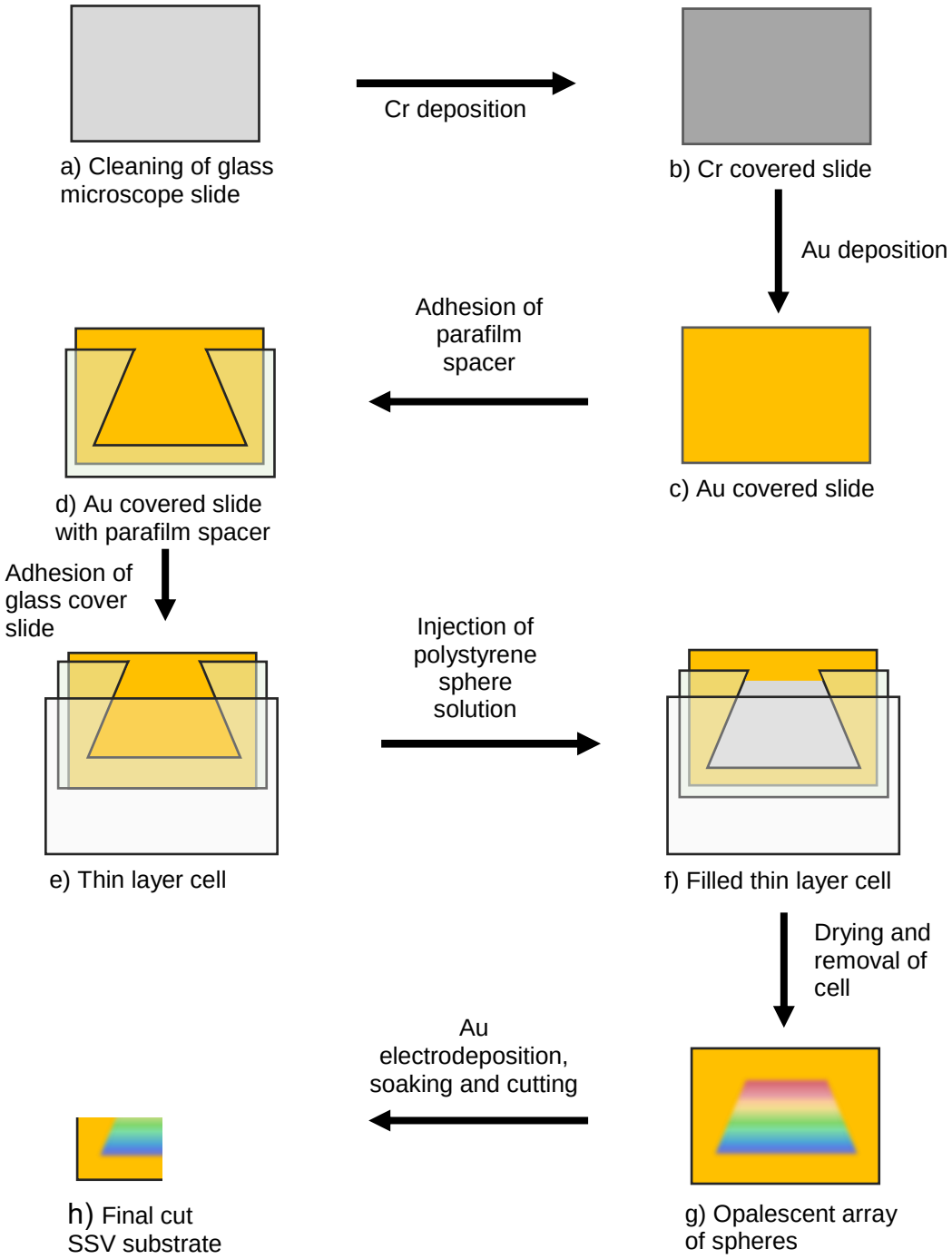

Figure 2.2: Scheme for SSV manufacture.

2.2.2 Void Height Calculation

When using Au SSV substrates and a 785 nm laser for SERS the maximum signal intensity is achieved when using 600 nm voids with a film thickness of 480 nm [5], this was therefore the void size used in all experiments in this thesis.

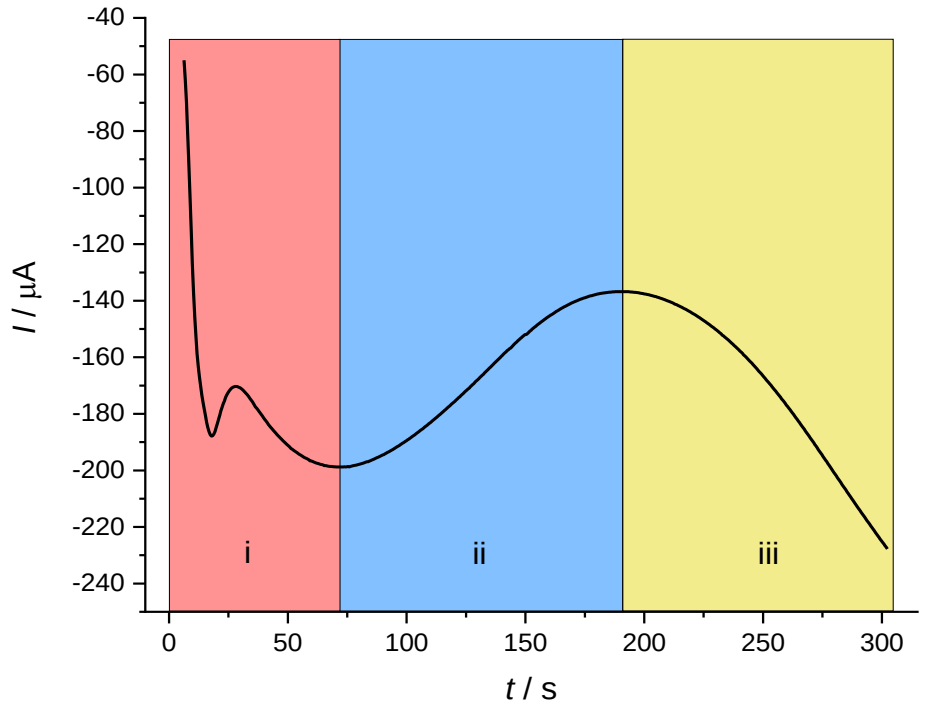

Figure 2.3: Chronoamperometric response waveform of the electrodeposition of gold through a hexagonally close packed array of 600 nm polystyrene spheres, where i) = nucleation and growth of metal centres, ii) = film growth up the lower half of the spheres and iii) film growth upward from the middle of the spheres.[9] The experiment was stopped at the point where the gold had plated 465 nm though the spheres.

Figure 2.3 shows the chronoamperometric response of electrodeposition of Au through 600 nm polystyrene spheres, where in i) the current becomes more negative as the initial metal surface area for deposition increases. In ii) the current becomes less negative due to a reduction in available metal surface area for electrodeposition as the deposited film fills the gaps in the sphere array, up to the middle of the spheres. In iii) the current becomes more negative again due to an increase in available metal surface for electrodeposition as the deposited film moves up the top half of the sphere. The electrodeposition was stopped at the point where the film height reached 480 nm up the spheres and can be derived from Faraday's law as follows:

According to Faradays law:

$$Q = nzF \qquad \text{Equation 2.1}$$

Where Q is the amount of charged passed when depositing n moles of gold, z is the number of electrons involved in the electrodeposition of one gold atom and F is the Faraday constant.

$$n = \frac{m}{M} \qquad \text{Equation 2.2}$$

$$m = \rho V \qquad \text{Equation 2.3}$$

m is the mass of gold deposited, M is the gold atomic weight, ρ is the density of gold and V is the volume of gold deposited. Combining Equation 1, 2 and 3 gives:

$$Q = \frac{\rho zF}{M} V \qquad \text{Equation 2.4}$$

The charge passed point at which the deposited gold film reaches the half way point up the spheres ($h_{1/2}$) is $Q_{1/2}$, therefore:

$$Q_{1/2} = \frac{\rho zF}{M} V_{1/2} \qquad \text{Equation 2.5}$$

Similarly, the point at which the deposition was stopped and had reached the required height of 465 nm (h_f) is Q_f:

$$Q_f = \frac{pzF}{M} V_f \qquad \text{Equation 2.6}$$

By dividing Equation 2.6 by Equation 2.5:

$$\frac{Q_f}{Q_{1/2}} = \frac{V_f}{V_{1/2}} \qquad \text{Equation 2.7}$$

The volume of gold deposited at film height h is equal to the deposition across the whole area (*i.e.* if no spheres were present) minus the volume occupied by the spheres themselves at height h.

$$V = V_t - N_s V_s \qquad \text{Equation 2.8}$$

$$V = A_t h - N_s V_s \qquad \text{Equation 2.9}$$

Where V is volume deposited with spheres present, V_t is the volume deposited across the area if no spheres were present, A_t is the total deposition area, N_s is the number of spheres and V_s is the volume of each sphere at height h. Assuming the spheres are touching and hexagonally packed, the packing density, η, is:

$$\eta = \frac{N_s A_s}{A_t} = \frac{\pi\sqrt{3}}{6} \qquad \text{Equation 2.10}$$

$$A_t = \frac{6N_s A_s}{\pi\sqrt{3}} \qquad \text{Equation 2.11}$$

Where A_s is the area of a circle with radius r_s.

$$A_s = \pi {r_s}^2 \qquad \text{Equation 2.12}$$

Substitution of Equation 2.12 into Equation 2.11 gives:

$$A_t = \frac{6N_s {r_s}^2}{\sqrt{3}} \qquad \text{Equation 2.13}$$

The volume of a sphere, V_s, at height h, with a radius of r_s is:

$$V_s = \frac{\pi h^2(3r_s - h)}{3} \qquad \text{Equation 2.14}$$

By substituting Equation 2.13 and Equation 2.14 into Equation 2.9, the volume of gold deposited is:

$$V = N_s \left[\frac{6h{r_s}^2\sqrt{3} - \pi h^2(3r_s - h)}{3}\right] \qquad \text{Equation 2.15}$$

At $h = h_{1/2} = r_s$ and $V = V_{1/2}$ Equation 2.15 becomes:

$$V_{1/2} = N_s {r_s}^3 \left[\frac{6\sqrt{3} - 2\pi}{3}\right] \qquad \text{Equation 2.16}$$

At $h = h_f$ and $V = V_f$ Equation 2.15 becomes:

$$V_f = N_s \left[\frac{6h_f {r_s}^2\sqrt{3} - \pi {h_f}^2(3r_s - h_f)}{3}\right] \qquad \text{Equation 2.17}$$

By substituting Equation 2.17 and Equation 2.16 into Equation 2.7:

$$\frac{Q_f}{Q_{1/2}} = \frac{6h_f {r_s}^2\sqrt{3} - \pi {h_f}^2(3r_s - h_f)}{2{r_s}^3(3\sqrt{3} - \pi)} \qquad \text{Equation 2.18}$$

Substituting in r_s = 300 nm and h_f = 480 nm:

$$\frac{Q_f}{Q_{1/2}} = 1.31$$

This ratio then allowed Q_f to be calculated from $Q_{1/2}$ and the experiment stopped when this charge had passed, giving a deposited film with a height of 480 nm.

2.3 Self Assembled Monolayer Formation

Self-assembled monolayers (SAMs) of thiols were prepared by immersing a clean gold SSV substrate into a dilute solution of the desired thiol, as per the recommended practice outlined by Sigma-Aldrich [10]. Firstly, substrates were submerged in thiol solution (5 mM, ethanol) for 24-48 hours; they were then removed from solution and rinsed with ethanol for 10-15 seconds before being dried thoroughly under nitrogen flow, ready for use.

2.4 Electrolyte Preparation

Electrolytes were made up by dissolving a required amount of salt in either aqueous or non-aqueous solvents. When using non-aqueous solvents the electrolyte was made up and stored in a glove box, when using aqueous solvents these were made up in the fume hood.

2.5 Analytical Techniques

Each experiment used a spectroelectrochemical cell manufactured at the University of Southampton pictured in Figure 2.4. The cell consisted of a sealed chamber (Kel-F®, polychlorotrifluoroethylene) where electrolyte was injected as well as contacts for a working electrode (a Au SSV substrate) and two platinum wires acting as the counter electrode (CE) and the platinum quasi-reference electrode (Pt QRE). In Chapter 6, this was replaced by a AuO reference electrode wire. All of this was covered by a 2 mm thick quartz window.

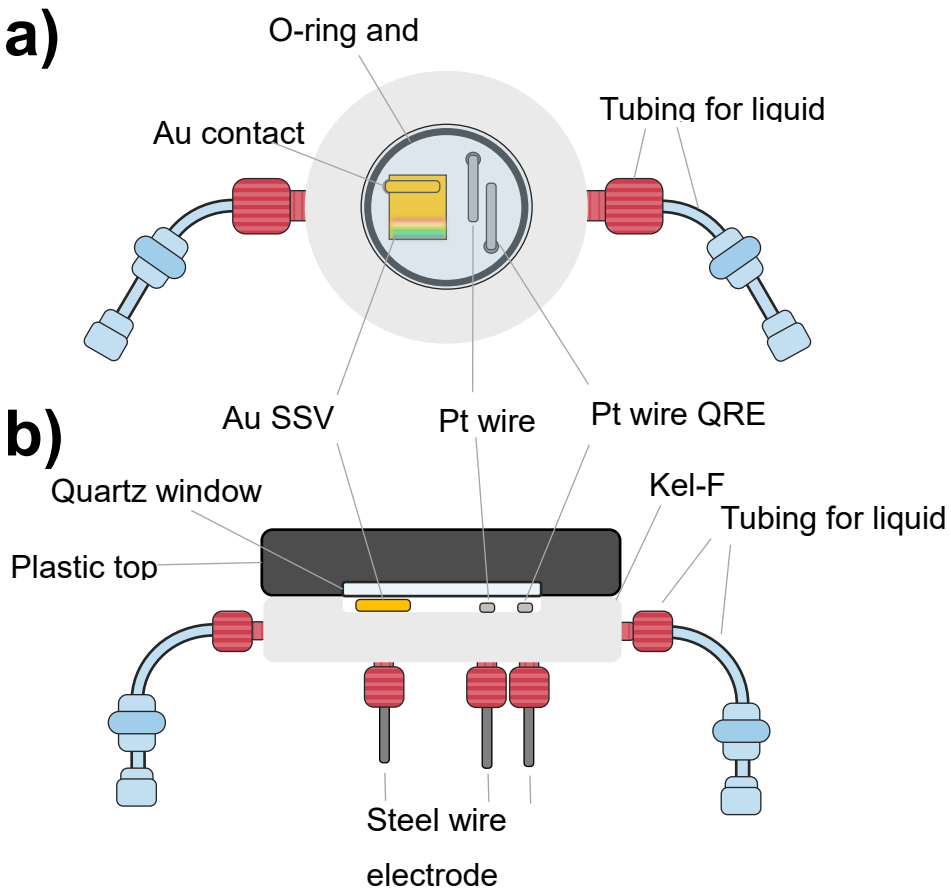

Figure 2.4: Diagram of the spectroelectrochemical cell. a) top view, b) side view.

The cell was assembled and the gold SSV substrate secured on the lab bench. If the electrolyte was aqueous, it was deoxygenated by purging with nitrogen for 15 minutes before being injected into the cell. If non aqueous, the electrolyte was injected into the cell in a glove box.

2.5.1 Cyclic Voltammetry

Cyclic voltammetry (CV) was performed using a Metrohm Autolab PGSTAT101 potentiostat and accompanying NOVA 1.11 or 2.0 software. The details of each CV can be found in the relevant figure caption.

2.5.2 Raman Spectroscopy

All Raman spectra were collected using a Renishaw inVia Raman spectrometer [11] attached to a Leica DM2500 M microscope with 50x Olympus LMPlanFL N objective, and analysed using Renishaw Windows Raman Environment (WiRE) 4.2. The spectrometer was coupled to a 785 nm diode laser light source with a power of 100 mW, calibrated using a silicon wafer to ensure the silicon peak was at 520 ± 0.5 cm^{-1}. Spectra either were taken across the maximum spectral range of the spectrometer (0-3200 cm^{-1}), or centred on a wavenumber of interest, giving a smaller spectral window of ± 600 cm^{-1}.

During a Raman measurement monochromatic light from the laser source was shone onto the sample via a series of mirrors. Here, the scattered light by the sample was collected through an aperture and separated into its component wavelengths by a diffraction grating. The separated light was then focused onto a CCD (charge coupled device) array detector where the intensity of each wavelength was measured by a pixel of the array. The CCD is then read off by a computer and plotted as Raman counts as a function of wavenumber (or Raman Shift).

2.5.2.1 Spectral background removal

The intensity of the background signal can swamp the rest of the Raman spectrum. In order to better resolve the vibrational peaks this background can be removed within WiRE 4.2. This was carried out using the ‘Remove Baseline’ tool, by fitting a polynomial to the base of the peaks and removing the area below the line. This is shown in Figure 2.5.

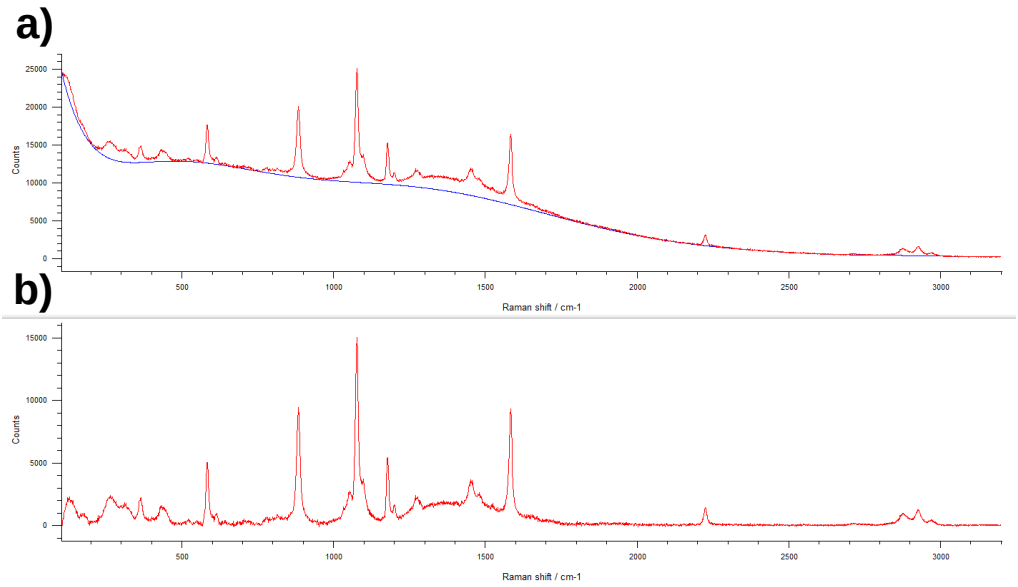

Figure 2.5: The ‘Remove Baseline’ tool in WiRE 4.2, using a SERS spectrum of 4-sulfanylbenzonitrile (4-SBN) adsorbed onto an Au SSV substrate. a) is the raw spectrum, with the blue line being the polynomial fitted as a baseline. b) is the result of the removal of the background underneath the proposed baseline.

2.5.2.2 Cosmic Ray Removal

Thin, sharp spikes can randomly appear in Raman spectra. They are natural events called cosmic rays and are detectable when using sensitive integrating detectors such as charge-coupled devices (CCDs) [12]. These peaks are characterised by their small full-width half-maximum (FWHM) size of approximately 1.5 cm^{-1}. Their appearance can interfere with the interpretation of spectra and can be removed using the Zap Data tool in WiRE 4.2, shown in Figure 2.6.

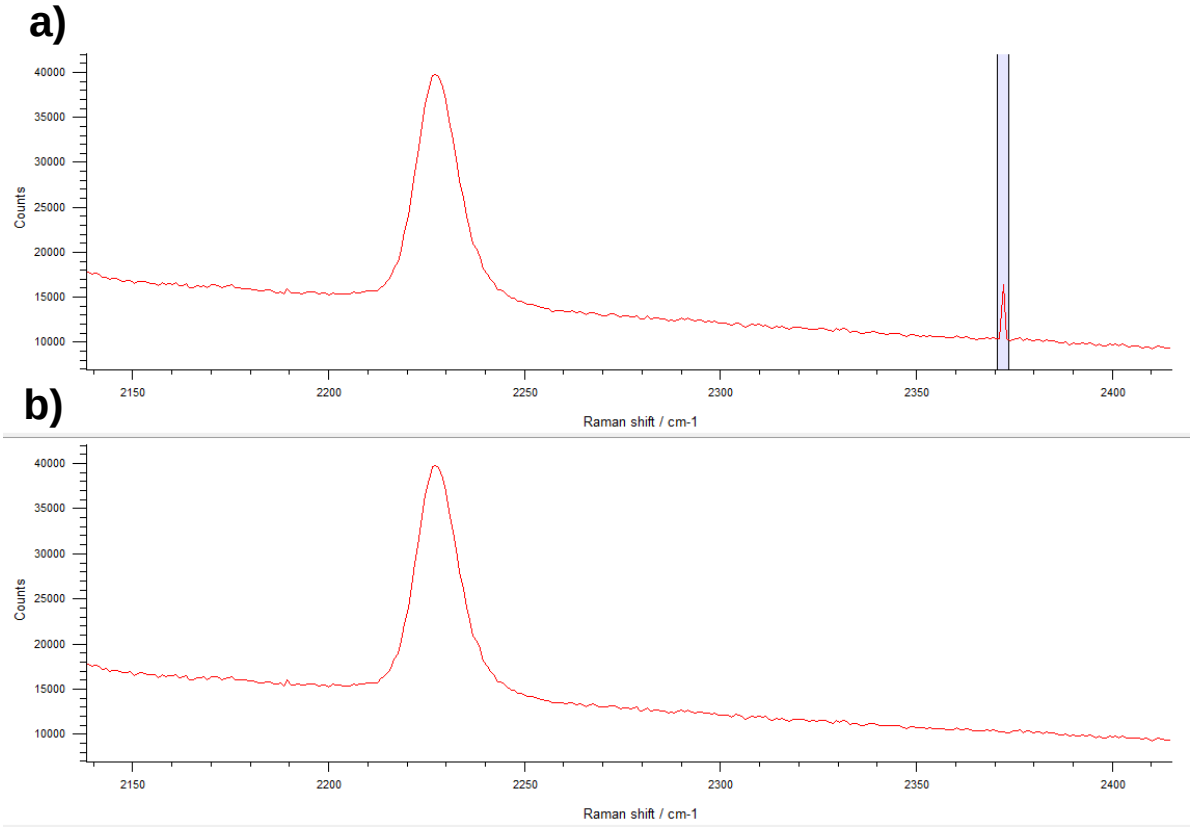

Figure 2.6: The ‘Zap Data’ tool in WiRE 4.2, using a spectrum of 4-SBN adsorbed onto an Au SSV surface. The blue highlighted region in the above spectrum, a), is an erroneous peak associated with a cosmic ray. In the bottom spectra, b), the peak has been removed by cutting out said highlighted region.

2.5.2.3 Peak Fitting

Vibrational Raman peaks each have position, height, width and area properties. Each of these characteristics provide information about the frequency, polarizability and degeneracy of bonds within the sample being investigated. Gaussian peaks were fitted to match those in the spectra and allow these parameters to be accurately extracted. This was carried out for every vibrational peak in this report using the ‘Peak Fit’ tool of WiRE 4.2 and is shown in Figure 2.7.

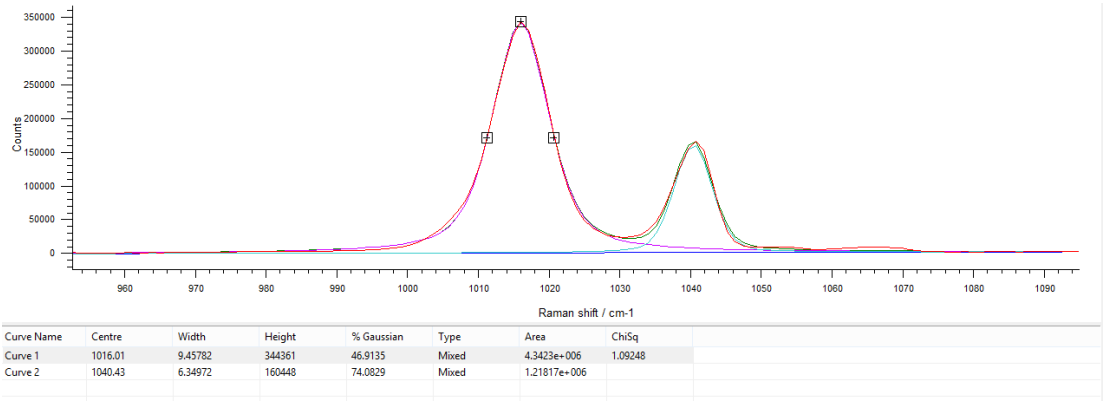

Curve Name	Centre	Width	Height	% Gaussian	Type	Area	ChiSq
Curve 1	1016.01	9.45782	344361	46.9135	Mixed	4.3423e+006	1.09248
Curve 2	1040.43	6.34972	160448	74.0829	Mixed	1.21817e+006	

Figure 2.7: The 'Peak Fit' tool in WiRE 4.2, here being used to characterize the pyridine ring breathing modes at 1016 and 1040 cm^{-1}. Gaussian curves are mathematically fitted to spectral data to provide accurate information regarding the peak position, height and area.

2.5.2.4 Intensity Conversion and Normalization

All Raman spectra were recorded as the number of counts hitting the charge-coupled device (CCD) of the spectrometer. This value was then converted (shown in Equation 2.19) to the units more commonly used in the literature: intensity in Counts (cm^{-1}) mW^{-1} s^{-1}.

$$I = \frac{C}{Pt_{acq}n_{acq}} \qquad \text{Equation 2.19}$$

Where I = intensity (Counts (cm^{-1}) mW^{-1} s^{-1}), C = Raman Counts (Counts (cm^{-1})), P = Laser intensity (mW), t_{acq} = spectral acquisition time (s) and n_{acq} = number of spectral acquisitions.

For EC-SERS where Raman intensities were investigated, the intensities were normalised to reduce the differences in focus, position, laser intensity and SERS enhancement factor between acquisitions as well as to remove variations in the background intensity between spectra. This was carried out by dividing the intensity across the whole spectrum by an intensity value at a specific wavenumber (normally 525 cm^{-1}). The same wavenumber was used in each spectrum in a data set and chosen where there is no vibrational information or spectral artefacts. This is shown in Equation 2.20:

$$I_{norm} = \frac{I}{I_{spec}} \qquad \text{Equation 2.20}$$

Where I_{norm} is the normalised intensity, I is the intensity (Counts (cm^{-1}) mW^{-1} s^{-1}) and I_{spec} is the intensity at the specified wavenumber (Counts (cm^{-1}) mW^{-1} s^{-1}).

2.5.3 Electrochemical Surface Enhanced Raman Spectroscopy

EC-SERS was carried out by sequentially stepping the potential whilst obtaining SERS spectra. The electrochemistry was controlled with a Metrohm Autolab PGSTAT101 and Nova 1.10, while the Raman acquisitions were made using the same instrument described in '2.5.2 Raman Spectroscopy'. The combined setup is shown in Figure 2.8. The first potential of each experiment was held for 300 seconds to ensure the substrate was at equilibrium before the first Raman acquisition. The potential was then held throughout this acquisition before being stepped to the next potential. Here, the potential was now held for 100 seconds before and during Raman acquisition. This 100 second cycle was repeated for the remaining potentials to be probed, details of which can be found in the relevant figure captions. In order to control both Nova 1.10 and WiRE 4.2 a script was created using Pulover's Macro Creator 5.0 [13], enabling the mouse and keyboard of the computer controlling both programs to be automated. This allowed potentials to be stepped, SERS acquisitions started and data saved without the need for an operator to be present. An example of the script at a set potential is shown in Appendix A.

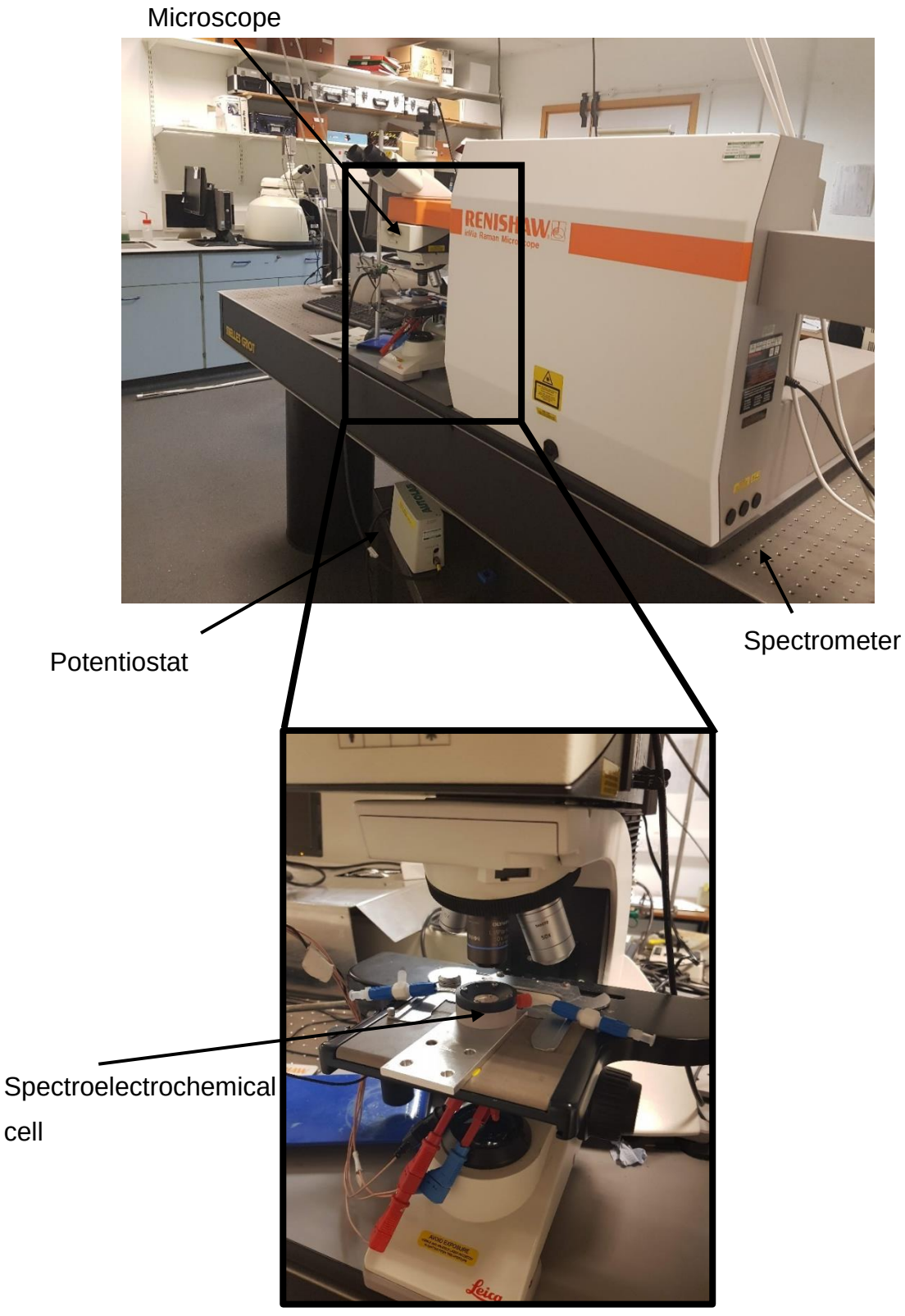

Figure 2.8: The EC-SERS equipment, a Renishaw InVia Raman spectrometer, Leica DM2500 M microscope and a Metrohm Autolab PGSTAT101 potentiostat. Inset, the position of the spectroelectrochemical cell on the microscope. The spectroelectrochemical cell electrodes were connected to the potentiostat via the crocodile clips underneath.

2.6 Properties of Sphere Segment Void substrates

Figure 2.9 shows a scanning electron microscope (SEM) image of a nanostructured gold SSV surface. The SSV surface shows hexagonally close-packed areas of circular voids on the surface.

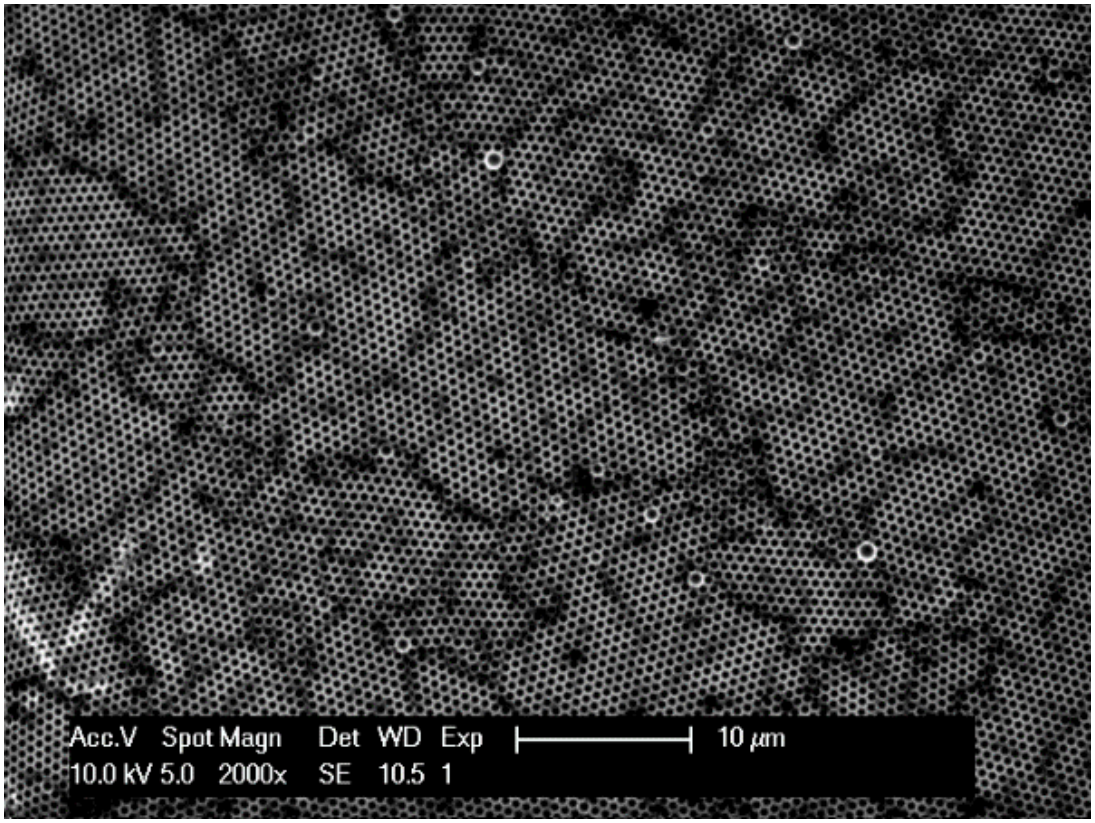

Figure 2.9: SEM image a nanostructured gold SSV surface, produced by electrodepositing gold though an array of 600 nm polystyrene spheres to give a film thickness of 465 nm.

2.6.1 SERS Enhancement

SERS enhancements are normally in the order of 10^6 or 10^8 when compared to conventional Raman signals. Figure 2.10 shows the comparison between experimentally acquired SERS spectra of a thiophenol (TP) SAM adsorbed on the SSV and the non-SSV region of a gold substrate, as well as a DFT calculated Raman spectrum of TP adsorbed on a Au_5 cluster (shown inset). The intensity of the SERS signal for the SSV region is clearly visible, while no peaks can be seen on the SSV region, illustrating the enhancement provided by the SSV structure. Comparison of the spectrum with that of calculated TP verifies that the experimental spectra is of TP and not an impurity. The assignment of SERS and DFT peaks for TP is given in Table 2.2.

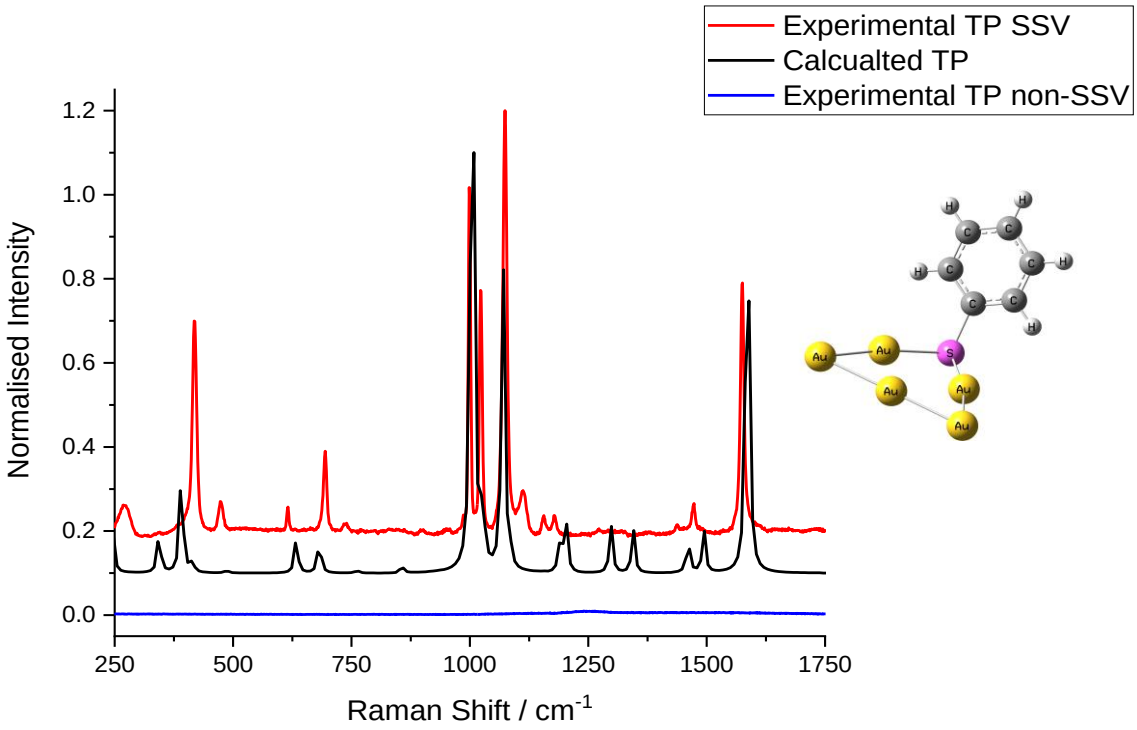

Figure 2.10: Experimental SERS and DFT calculated Raman spectra of thiophenol (TP). The SERS spectra were of TP adsorbed onto a gold SSV substrate and flat Au non-SSV substrate. The DFT spectrum was calculated from the optimised structure of a TP molecule adsorbed on an Au_5 cluster, as shown inset. Spectra have been normalised by the largest peak in each spectrum, the backgrounds removed and are offset for clarity.

Mode	Wilson Number	SERS Frequency /cm^{-1}	Calculated Frequency / cm^{-1}
ν_{C-H}	7a	419	388
ν_{C-H}	16a	472	412
δ_{C-C}	6a	694	678
δ_{C-C}	12	999	1008
δ_{C-H}	18a	1023	1024
ν_{C-C}	1	1074	1071
δ_{C-C}	9a	1160	1189
δ_{C-C}	19b	1432	1464
ν_{C-C}	8a	1575	1585

Table 2.2: SERS peaks for TP adsorbed on a gold SSV substrate. Assigned on the basis of Holze.[14], v = stretch and δ = bend.

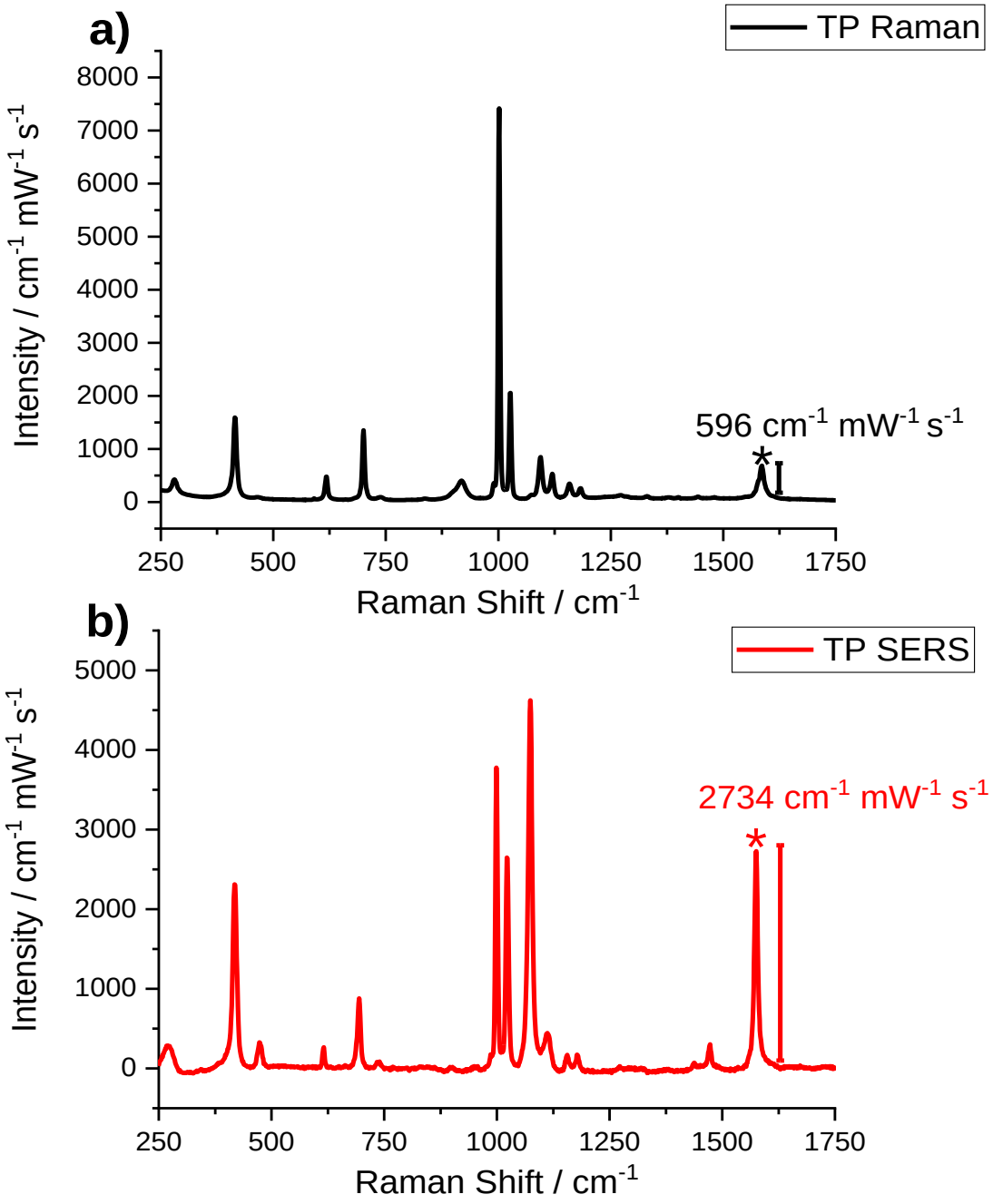

Figure 2.11: a) Raman spectrum of liquid TP b) SERS spectrum of TP adsorbed on a gold SSV substrate. The spectra were both acquired at the same laser power and acquisition time, and the backgrounds have been removed for clarity.

In order to quantitatively calculate the enhancement of the SSV surface an established method was used, which was well explained in the supporting information of Xu *et al.* [15]. There, they compared the Raman and SERS signal intensity of the C-C stretching vibration ($\nu_{C\text{-}C}$, 8a) of TP. Figure 2.11 shows the Raman spectrum of liquid TP and the SERS spectrum when adsorbed onto a gold SSV substrate, with the C-C stretching peaks marked with stars. These

peaks intensities are 596 Counts (cm^{-1}) mW^{-1} s^{-1} in Raman, and 2734 Counts (cm^{-1}) mW^{-1} s^{-1} in SERS. Assuming the same laser power and exposure time used between spectra, the enhancement factor (EF) of the SERS substrate can be calculated as a ratio between the intensity of a peak in both the SERS and Raman spectra, normalised to the number of scattering molecules.

$$EF = \frac{\frac{I_{SERS}}{N_{SERS}}}{\frac{I_{Raman}}{N_{Raman}}} \qquad \text{Equation 2.21}$$

Where I_{SERS} corresponds to SERS signal intensity, I_{Raman} the Raman signal intensity, N_{SERS} is the number of molecules in the illumination area of the laser in the SERS experiment, N_{Raman} is the number of molecules in the illumination area of the laser in the Raman experiment.

For SERS the signal only comes from a monolayer of molecules on the SSV surface. This can be assumed to be a complete monolayer, with each TP molecule encompassing a circular area (A_{TP}) of 1 nm^2, the actual SSV surface area (A_{SSV}) being 4x the geometric area and the laser spot size (A_{laser}) being 160 μm^2. The calculation of the spot size for this spectrometer is available in Appendix A.

$$A_{SSV} = 4A_{laser} \qquad \text{Equation 2.22}$$

$$A_{SSV} = 640\ \mu m^2$$

Therefore, the number of molecules on the SSV surface illuminated by the laser (N_{laser}) can be calculated as follows:

$$N_{SERS} = \frac{A_{SSV}}{A_{TP}} \qquad \text{Equation 2.23}$$

$$N_{SERS} = 256000\ molecules$$

For Raman the signal comes from a volume of illuminated solid (V_{solid}). Here, with a line focus laser this can be assumed to be a cylinder with length of 20 µm and radius of 8 µm.

$$V_{solid} = 20\ \mu m \times\ \pi(8\ \mu m)^2 \qquad \text{Equation 2.24}$$

$$V_{solid} = 1280\pi\ \mu m^3$$

The number of molecules of TP illuminated in the Raman experiment (N_{Raman}) can be calculated from Avogrado's constant (N_A) and the number of moles of thiol illuminated (n_{Raman}), which itself can be expressed as a factor the V_{solid}, the density of TP (ρ_{thiol} = 1.073 g mL^{-1}) and the molecular weight of TP (M_{thiol} = 110.18 g mol^{-1}):

$$N_{Raman} = N_A n_{Raman} \qquad \text{Equation 2.25}$$

$$n_{thiol} = \frac{V_{solid} d_{thiol}}{M_{thiol}} \qquad \text{Equation 2.26}$$

$$n_{thiol} = 1.25\pi \times 10^{-11}\ mol$$

$$N_{Raman} = 7.51\pi \times 10^{12}\ molecules$$

By substituting N_{Raman} = 7.51π x10^{12}, N_{SERS} = 640000, I_{SERS} = 2734 Counts (cm^{-1}) mW^{-1} s^{-1} and I_{Raman} = 596 Counts (cm^{-1}) mW^{-1} s^{-1} into Equation 2.21 it becomes:

$$EF = 1.06 \times 10^{8}$$

The enhancement factor of the SSV substrate was therefore determined to be 1.06 x10^8.

2.6.2 Electrochemical Stability

To investigate how the gold SSV surface responds in an electrochemical environment, spectra were recorded using adsorbed pyridine at differing potentials. This is shown in Figure 2.12.

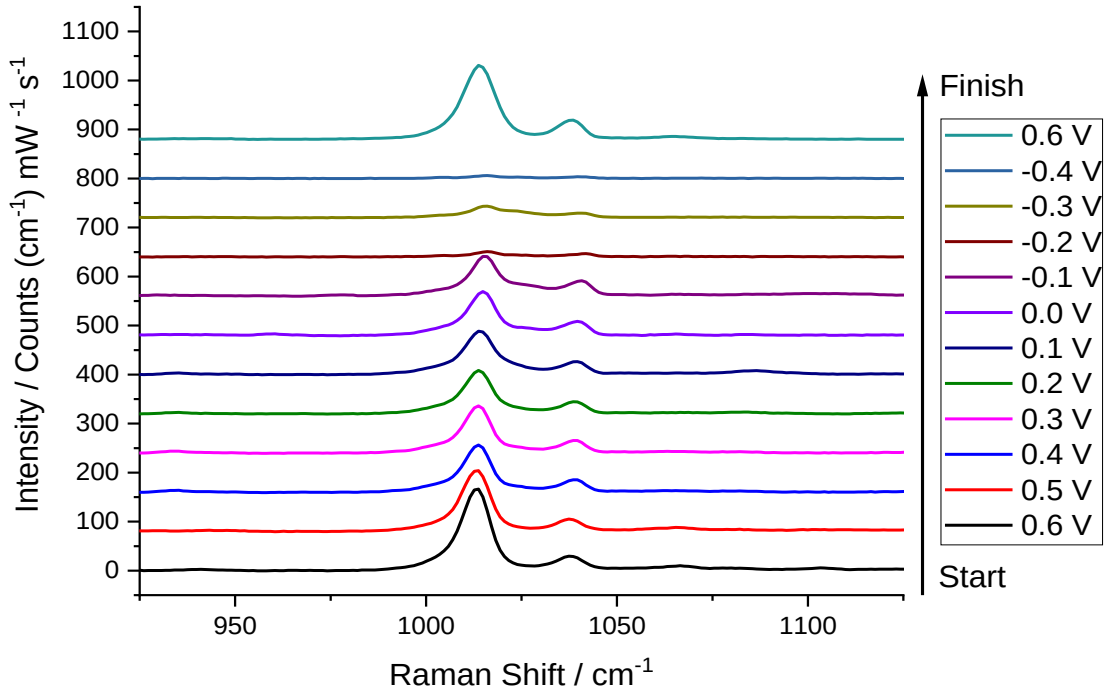

Figure 2.12: EC-SERS spectra recorded in 0.1 M KCl containing 0.05 M pyridine using a gold SSV substrate at potentials *vs.* Pt QRE. Spectra have their backgrounds removed and are offset for clarity.

As the potential was stepped from 0.60 V to -0.40 V *vs.* Pt QRE the pyridine ring breathing bands at 1014 cm^{-1} and 1039 cm^{-1} decreased until they were almost indistinguishable from the noise. However, when the potential was stepped back up to the starting point of 0.60 V the bands return to their original magnitude. By examining the SERS selection rules, it is clear that at 0.0 V and more negative potentials pyridine has reoriented to be more parallel to the surface, so the ring breathing bands are now not enhanced by the SSV surface and the band intensity reduced to zero. Once the potential was stepped back to 0.60 V the pyridine re-orientated to be more perpendicular to the surface and the re-enhanced bands again appear in the SERS spectra [2,16]. This indicates that gold SSV substrates provide an electrochemically active surface upon which reversible changes in SERS peaks can be measured without a loss of activity.

2.7 Density Functional Theory

For the last 30 years density functional theory (DFT) has been the dominant method for quantum mechanical modelling of chemical systems. It is primarily used to determine the electronic structure of the system in question by providing a solution to the many-body Schrodinger equation. Traditional methods for solving this (such as Hartree-Fock) necessitate hefty computational processing power, which in large, complex systems is prohibitive. DFT is a useful alternative as it solves for the electron density, thus reducing the many body problem, of the system from which interesting electronic properties can be easily derived [17–19].

All DFT calculations were carried out using the Gaussian 09W software package and modelled as the metal–molecule complex, on a bed of 5 gold atoms. Calculations to both optimise the geometry of the complexes and calculate their Raman spectra were carried out using the 6-311+g (d', p') basis set for the carbon, hydrogen, nitrogen, oxygen and sulfur atoms, the LANL2DZ effective core potential (ECP) for the gold inner shells and corresponding basis set for the gold valence electrons, alongside the hybrid functional B3LYP. In addition, solvation effects were modelled with the integral equation formalism polarisation continuum model (PCM), using the matching solvent as the experimental conditions. Finally, spectral frequencies were scaled by 0.981 to account for unwanted anharmonicity. These computational settings were chosen as they have been shown to provide good accuracy when compared to experimental systems, while balancing the use of computation resources [20–24].

2.7.1 Au cluster size determination

To be able to produce the most accurate DFT spectra the optimum size of the Au cluster used for the model had to be determined. By using 4-SBN as the model molecule, DFT calculated Raman spectra were generated of this molecule adsorbed onto Au clusters ranging from Au_1 (i.e. just an atom) to Au_5 and compared to experimental spectra. The DFT optimised structures of these systems and their calculated spectra are shown in Figures 2.13 and 2.14.

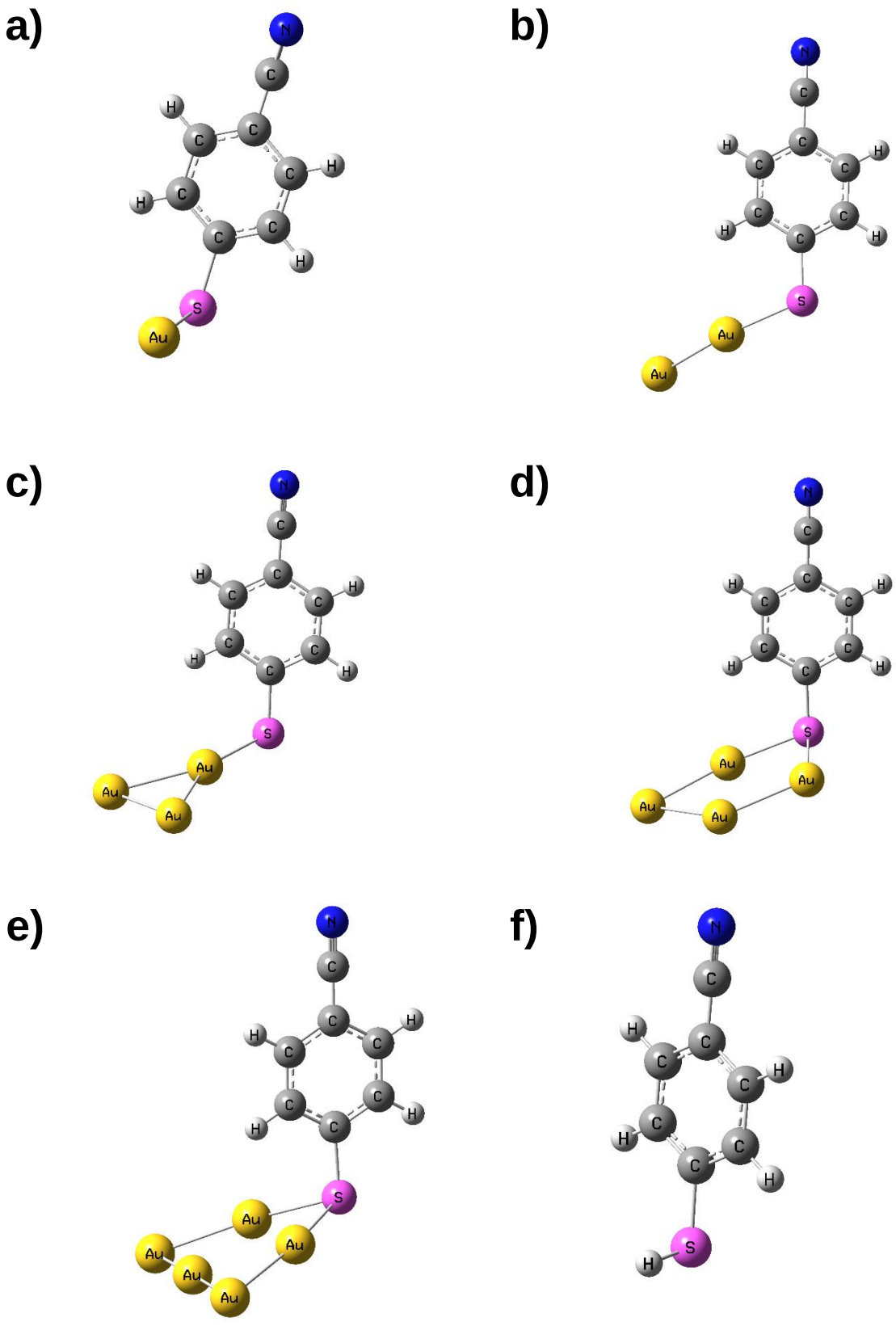

Figure 2.13: DFT optimised models of 4-SBN adsorbed on: a) Au, b) Au_2, c) Au_3, d) Au_4 e) Au_5 and f) as the gas phase molecule. These were used to calculate the DFT Raman spectra of each system.

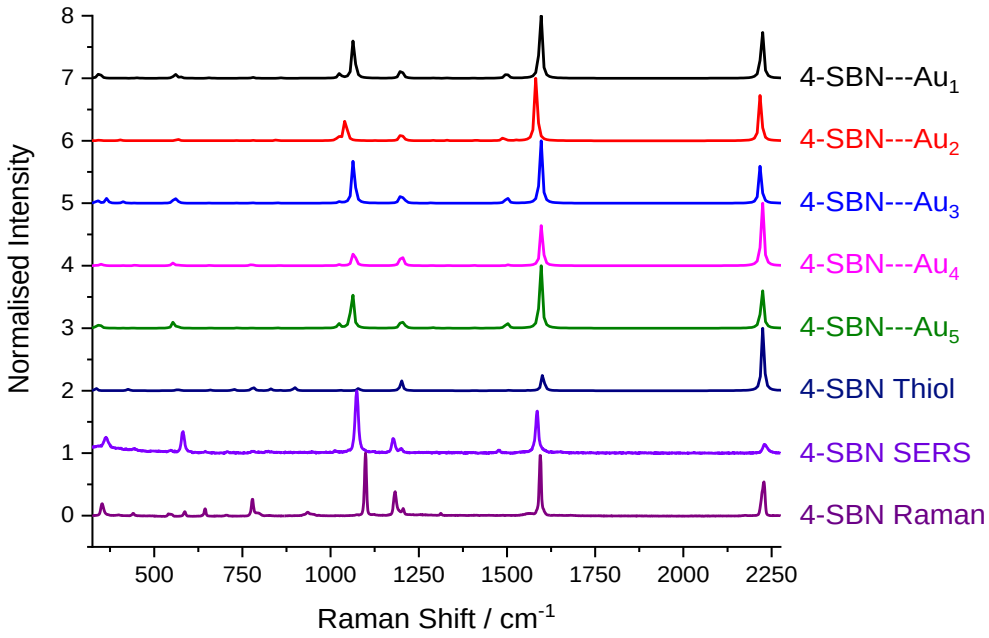

Figure 2.14: DFT calculated Raman spectra of 4-SBN adsorbed onto Au clusters ranging from 1-5 atoms and the free thiol molecule. The experimental SERS spectrum and Raman spectrum of the neat liquid are also shown for comparison. Each spectrum has been normalised to its largest peak intensity and are offset for clarity.

By comparison to the experimentally acquired SERS spectra the best agreement in peak frequency and intensity came from the 4-SBN---Au_5 system. Therefore, this was the cluster size used for all DFT calculations in this thesis. In addition, this is the preferred configuration used for similar studies in the literature [23,24].

2.7 References

[1] P.N. Bartlett, J.J. Baumberg, S. Coyle, M.E. Abdelsalam, Optical properties of nanostructured metal films, Faraday Discuss. 125 (2004) 117–132. doi:10.1039/b304116f.

[2] M.E. Abdelsalam, P.N. Bartlett, J.J. Baumberg, S. Cintra, T.A. Kelf, A.E. Russell, Electrochemical SERS at a structured gold surface, Electrochem. Commun. 7 (2005) 740–744. doi:10.1016/j.elecom.2005.04.028.

[3] A.E. Russell, S.H. Pelfrey, J. Speed, S. Mahajan, P.N. Bartlett, J.J. Baumberg, Sphere Segment Void Structures: a Reproducible SERS

Substrate for Electrochemical Studies, in: 41st Am. Chem. Soc. Cent. Reg. Meet., 2009. https://www.researchgate.net/publication/267321988_Sphere_Segment_Void_Structures_a_Reproducible_SERS_Substrate_for_Electrochemical_Studies (accessed February 19, 2016).

[4] R.P. Johnson, S. Mahajan, M.E. Abdelsalam, R.M. Cole, J.J. Baumberg, A.E. Russell, P.N. Bartlett, SERS from two-tier sphere segment void substrates., Phys. Chem. Chem. Phys. 13 (2011) 16661–16665. doi:10.1039/c1cp21126a.

[5] S. Mahajan, R.M. Cole, B.F. Soares, S.H. Pelfrey, A.E. Russell, J.J. Baumberg, P.N. Bartlett, Relating SERS intensity to specific plasmon modes on sphere segment void surfaces, J. Phys. Chem. C. 113 (2009) 9284–9289. doi:10.1021/jp900661u.

[6] S. Mahajan, R.M. Cole, J.D. Speed, S.H. Pelfrey, A.E. Russell, P.N. Bartlett, S.M. Barnett, J.J. Baumberg, Understanding the surface-enhanced Raman spectroscopy " background," J. Phys. Chem. C. 114 (2010) 7242–7250. doi:10.1021/jp907197b.

[7] P.A. Kralchevsky, N.D. Denkov, K.D. Danov, Particles with an undulated contact line at a fluid interface: Interaction between capillary quadrupoles and rheology of particulate monolayers, Langmuir. 17 (2001) 7694–7705. doi:10.1021/la0109359.

[8] A.S. Dimitrov, K. Nagayama, Steady-state unidirectional convective assembling of fine particles into two-dimensional arrays, Chem. Phys. Lett. 243 (1995) 462–468. doi:10.1016/0009-2614(95)00837-T.

[9] D. Pletcher, A first course in electrode processes, 2nd ed., Royal Society of Chemistry, Cambridge, 2009.

[10] Sigma-Aldrich, Preparing Self-Assembled Monolayers (SAMs): A Step-by-Step Guide for Solution-Based Self-Assembly, 2016. https://www.sigmaaldrich.com/content/dam/sigma-aldrich/docs/Aldrich/Instructions/1/al-266.pdf.

[11] Renishaw, InVia Confocal Raman Microscope, (n.d.). http://www.renishaw.com/en/invia-confocal-raman-microscope--6260

(accessed January 5, 2017).

[12] D. Wieboldt, Understanding Raman Spectrometer Parameters, SpectroscopyOnline. (2010) 5. http://www.spectroscopyonline.com/understanding-raman-spectrometer-parameters?id=&sk=&date=&&pageID=4 (accessed May 15, 2017).

[13] R.U. Batista, Pulover's Macro Creator – The Complete Automation Tool, (n.d.). https://www.macrocreator.com/ (accessed October 23, 2018).

[14] R. Holze, The adsorption of thiophenol on gold - A spectroelectrochemical study, Phys. Chem. Chem. Phys. 17 (2015) 21364–21372. doi:10.1039/c5cp00884k.

[15] J.L. Trotter, S.E.J. Bell, C.P. McCoy, M.P. Konrad, Y. Xu, Rapid One-Pot Preparation of Large Freestanding Nanoparticle-Polymer Films, Small. 13 (2016) 1602163. doi:10.1002/smll.201602163.

[16] M. Fleischmann, P.J. Hendra, A.J. McQuillan, Raman spectra of pyridine adsorbed at a silver electrode, Chem. Phys. Lett. 26 (1974) 163–166. doi:10.1016/0009-2614(74)85388-1.

[17] N.M. Harrison, An Introduction to Density Functional Theory, Technology. 2 (1995) 1–26. doi:10.1016/S1380-7323(05)80031-7.

[18] U. von Barth, Basic Density-Functional Theory an Overview, Phys. Scr. T109 (2004) 9. doi:10.1238/physica.topical.109a00009.

[19] R. In, C. Biology, Reviews in computational biology, John Wiley & Sons, 2013. https://books.google.co.uk/books?hl=en&lr=&id=EPS-nsT3wyUC&oi=fnd&pg=PA187&dq=An+Introduction+to+Density+Functional+Theory&ots=2PPFQKQr5q&sig=Wq0RYL-uuZqmvieI6gggA6oz5w0#v=onepage&q=An Introduction to Density Functional Theory&f=false (accessed January 9, 2018).

[20] I. Matulaitiene, Z. Kuodis, A. Matijoška, O. Eicher-Lorka, G. Niaura, SERS of the Positive Charge Bearing Pyridinium Ring Terminated Self-Assembled Monolayers: Structure and Bonding Spectral Markers, J. Phys. Chem. C. 119 (2015) 26481–26492. doi:10.1021/acs.jpcc.5b07687.

[21] G.D. Fleming, I. Golsio, A. Aracena, F. Celis, L. Vera, R. Koch, M.

Campos-Vallette, Theoretical surface-enhanced Raman spectra study of substituted benzenes: I. Density functional theoretical SERS modelling of benzene and benzonitrile, Spectrochim. Acta Part A Mol. Biomol. Spectrosc. 71 (2008) 1049–1055. doi:10.1016/J.SAA.2008.02.046.

[22] M. Muniz-Miranda, B. Pergolese, A. Bigotto, Surface-enhanced raman scattering and density functional theory study of 4-nitrobenzonitrile adsorbed on Ag and Ag/Pd nanoparticles, J. Phys. Chem. C. 112 (2008) 6988–6992. doi:10.1021/jp711745t.

[23] L. Bin Zhao, M. Zhang, B. Ren, Z.Q. Tian, D.Y. Wu, Theoretical Study on Thermodynamic and Spectroscopic Properties of Electro-Oxidation of p -Aminothiophenol on Gold Electrode Surfaces, J. Phys. Chem. C. 118 (2014) 27113–27122. doi:10.1021/jp507987x.

[24] L.B. Zhao, J.L. Chen, M. Zhang, D.Y. Wu, Z.Q. Tian, Theoretical Study on Electroreduction of p-Nitrothiophenol on Silver and Gold Electrode Surfaces, J. Phys. Chem. C. 119 (2015) 4949–4958. doi:10.1021/jp512957c.

Chapter 3: Potential dependent orientation of sulfanylbenzonitrile monolayers

The orientation of self assembled monolayers (SAMs) has been previously investigated with a variety of techniques including x-ray photoelectron (XPS) [1,2], infrared (IR) [3] and Raman [4] spectroscopies. Surface enhanced Raman spectroscopy (SERS) can also be used as it has well defined propensities [5], has excellent surface specificity and large signal enhancement of adsorbed molecules [4], with a number of studies being reported [6–12]. These selection rules have been explained more thoroughly in Chapter 1 but briefly, vibrations perpendicular to the surface are enhanced to a greater extent and signals are larger, similarly vibrations parallel to the surface are less enhanced and smaller. However, care must be taken when interpreting the results as Raman scattering is dependent on the anisotropic polarizability of the molecule and thus, the induced image dipole produced by the vibration may be in a different direction to that of the driving electromagnetic field. Therefore, it has only been possible to determine orientation with well-defined vibrations and simple molecules [13,14].

The orientation of substituted benzene thiol monolayers is defined in terms of by the tilt angle, θ, and a twist angle, χ. θ represents the angle between the surface normal and the aromatic ring and χ the orientation of the ring with respect to the surface as depicted for 4-sulfanylbenzonitrile (4-SBN) in Figure 3.1. At $\theta = 0°$ the rotational axis of the ring is perpendicular to the surface and at $\theta = 90°$ this axis is parallel to the surface. At $\chi = 0°$ the plane of the ring faces the metal surface, being parallel to this surface when $\theta = 90°$, whilst at $\chi = 90°$ and $\theta = 90°$ the plane of the ring is side on and perpendicular to the metal surface.

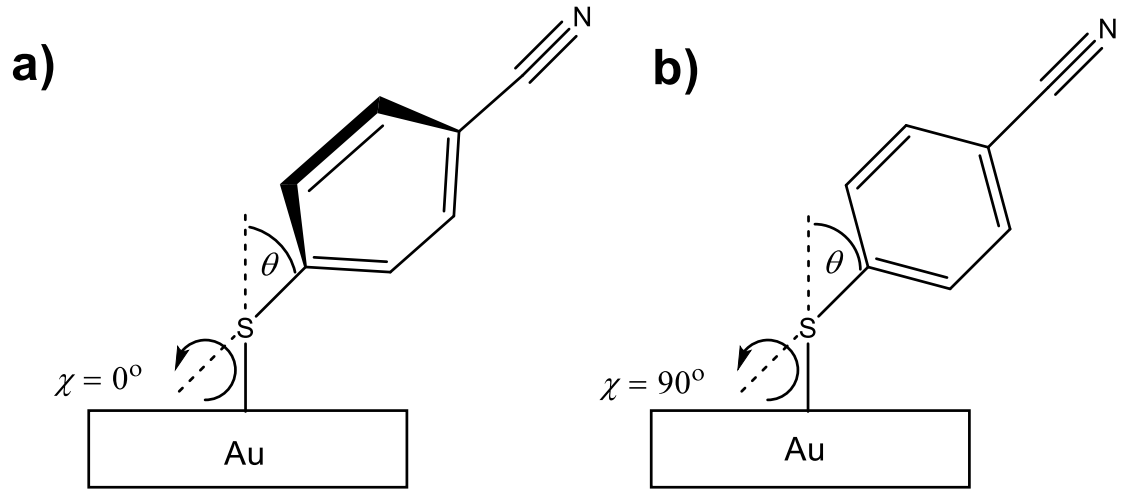

Figure 3.1: Molecular orientation of 4-sulfanylbenzonitrile is defined by the tilt angle, θ, and twist angle, χ. The tilt angle is defined as the angle between the surface normal and the S-C bond and the twist angle is defined as the angle between the plane of the surface and that of the ring. a) the ring in a face on orientation to the surface with χ = 0°, and b) shows the ring in a side on orientation with χ = 90°.

Orientation analysis studies in the literature of the unsubstituted molecule, thiophenol (TP), have provided conflicting results. Wan *et al.* [3] and Carron and Hurley [7] determined a tilt angle, θ, of 14° and twist angle, χ, of 0° using SERS and surface enhanced infrared absorption spectroscopy (SEIRAS), respectively. In contrast, a SERS study carried out by Szafranski *et al.* [14] suggested TP angles of θ = 76° and χ = 0°, with the discrepancy possibly arising from differences in the definition of θ, which is conventionally defined as shown in Figure 3.1 as the deviation from the surface normal rather than from the surface plane.

In electrochemical SERS (EC-SERS) the rate of change in frequency of a Raman mode (and thus the vibrational energy), with respect to potential, termed the electrochemical Stark effect, can also provide additional insights regarding the orientation of the adsorbate. The magnitude of the Stark effect, called the Stark shift, depends on the dynamic dipole moment of the vibrational mode and strength of the electric field at the electrode surface [15,16], shown by the Taylor expansion of Equation 3.1.

$$\Delta\nu = {}^{1}\!/_{hc}(\Delta\mu E + {}^{1}\!/_{2}\, E\Delta\alpha E + \cdots) \qquad \text{Equation 3.1}$$

Where $\Delta\nu$ is the Stark shift, h is planks constant, c is the speed of light, E is the applied electric field, μ is the dipole moment and α is the polarizability of the bond.

A larger Stark tuning indicates greater coupling and will be largest when the vibration is aligned to the direction of the electric field, i.e. perpendicular to the electrode surface. For example, Schkolnik *et al.* showed further potential dependence of the nitrile stretching frequency for 4-SBN adsorbed on roughened Au, wherein the magnitude of the Stark shift was 8 $cm^{-1} V^{-1}$ [17]. A reversible change in the intensity of the vibration was also reported and explained as an orientation change with change in applied potential. Further analysis of the effects of the potential on the orientation of the benzene ring were not presented as the aim of that study was to understand the interactions of the adsorbed monolayer with co-adsorbed species.

In this chapter a combined (density functional theory) DFT and experimental SERS approach is presented to characterise the potential dependent orientation of the para-substituted 4-SBN, ortho-substituted 3-sulfanylbenzonitrile (3-SBN), and meta-substituted 2-sulfanylbenzonitrile (2-SBN) adsorbed on gold sphere segment void (SSV) substrate electrodes [18,19]. The variations in the spectra are interpreted in terms of the combined effects of a change in the orientation of both the benzene ring and nitrile group arising from the electrostatic interactions with the metal surface.

3.1 Sulfanylbenzonitrile SERS characterisation

The experimentally obtained SERS and DFT calculated Raman spectra of 4-SBN, 3-SBN and 2-SBN SAMs are shown in Figure 3.2. These show very good agreement, but intensities between the DFT and SER spectra vary as the calculations only simulate the chemical enhancement and not the additional electromagnetic enhancement also present in SERS [20]. In addition, small shifts in peak positions are observed as an approximate effective core potential (ECP) for the Au inner shell electrons was used rather than treating every electron individually. Vibrational modes in which the polarisability changes are aligned in the plane (IP) and out of the plane (OOP) of the benzene ring are labelled as they should provide the greatest sensitivity to the orientation of 4-

SBN, 3-SBN, and 2-SBN with respect to the metal surface. These peaks are the aromatic ring C-H 9a IP and 10b OOP bends and the C≡N IP stretching vibration and C≡N OOP bending mode. Molecular coordinate diagrams of these vibrations are depicted in Figure 3.2 and are labelled according to Wilson notation based on the previously reported study by Merlin and Cornard [21].

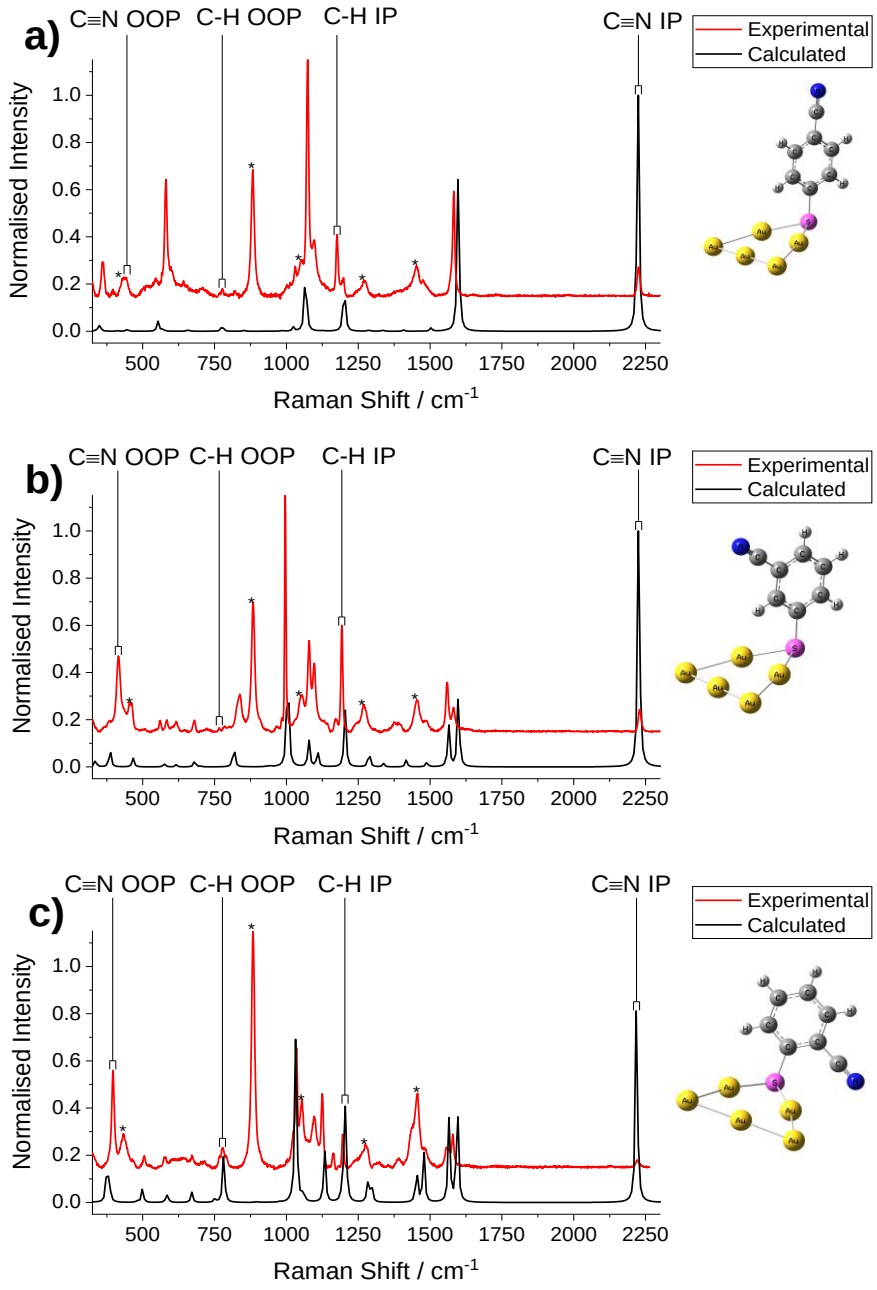

Figure 3.2: Experimental SERS and DFT calculated Raman spectra of: a) 4-SBN, b) 3-SBN and c) 2-SBN SAMs with, inset, the optimised structures. SERS spectra are of the SAMs adsorbed on Au SSV substrates held at 0.0 V *vs.* Pt QRE in 0.1 M TBATFB. Starred peaks (*) correspond to ethanol from the electrolyte. Spectra are normalised to the largest peak in each spectrum and offset for clarity.

Aromatic Ring Vibrations

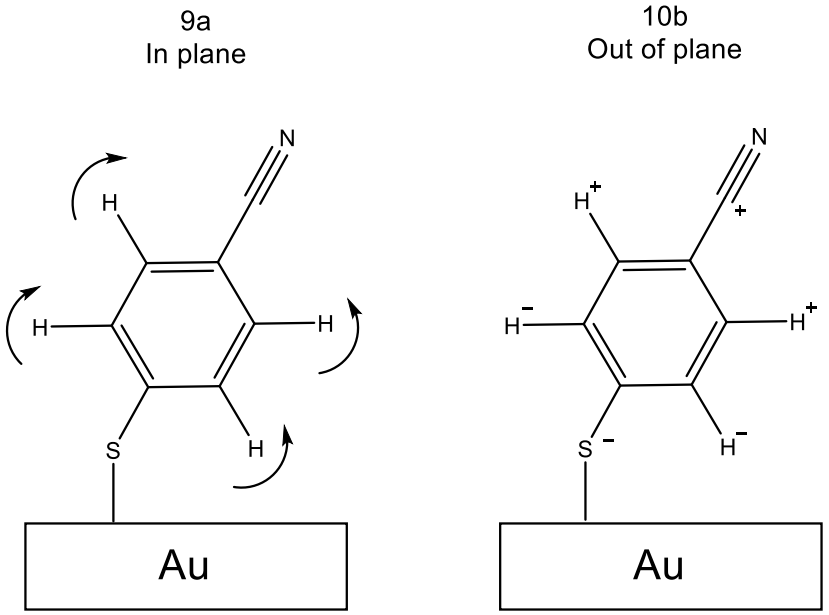

Nitrile Group Vibrations

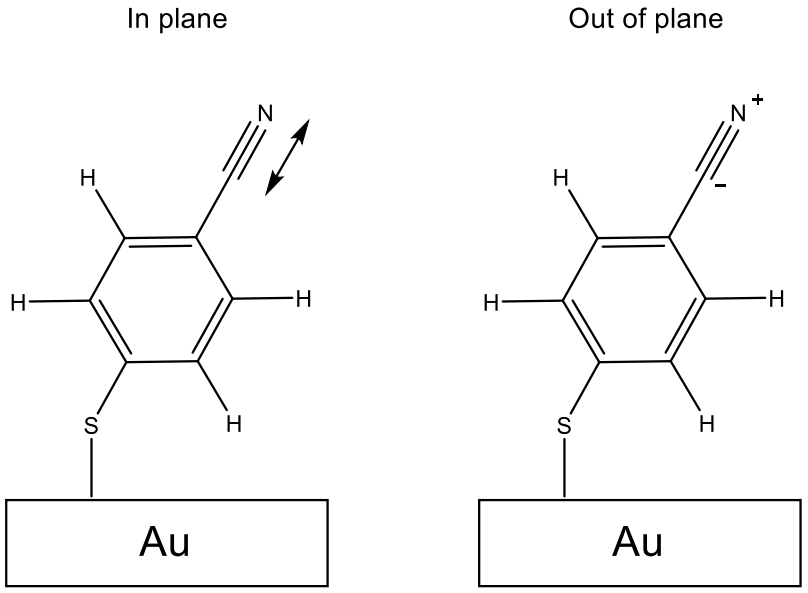

Figure 3.3: The IP and OOP aromatic ring and nitrile group vibrations for 4-SBN. The 9a and 10b vibrations are both C-H bends and the atomic coordinate changes for these were taken from Merlin and Cornard [21], the nitrile vibrations are C≡N stretches and bends respectively. Arrows indicate bond movement within the plane of the aromatic ring, + and – signs show movement into and out of the plane of the ring.

The suitability of the IP and OOP modes in providing information regarding the orientation of the SBN molecules was confirmed by examination of DFT calculated Raman spectra for the molecules bonded to an Au_5 cluster. Figure 3.4 shows the dipole derivative unit vectors for each vibration for all three monolayers and that for each complementary vibration (e.g. C-H IP:OOP) the IP and OOP vectors are indeed perpendicular to one another. A full vibrational assignment of the DFT calculated Raman and SERS spectra of 4-SBN, 3-SBN and 2-SBN is provided in Appendix B.

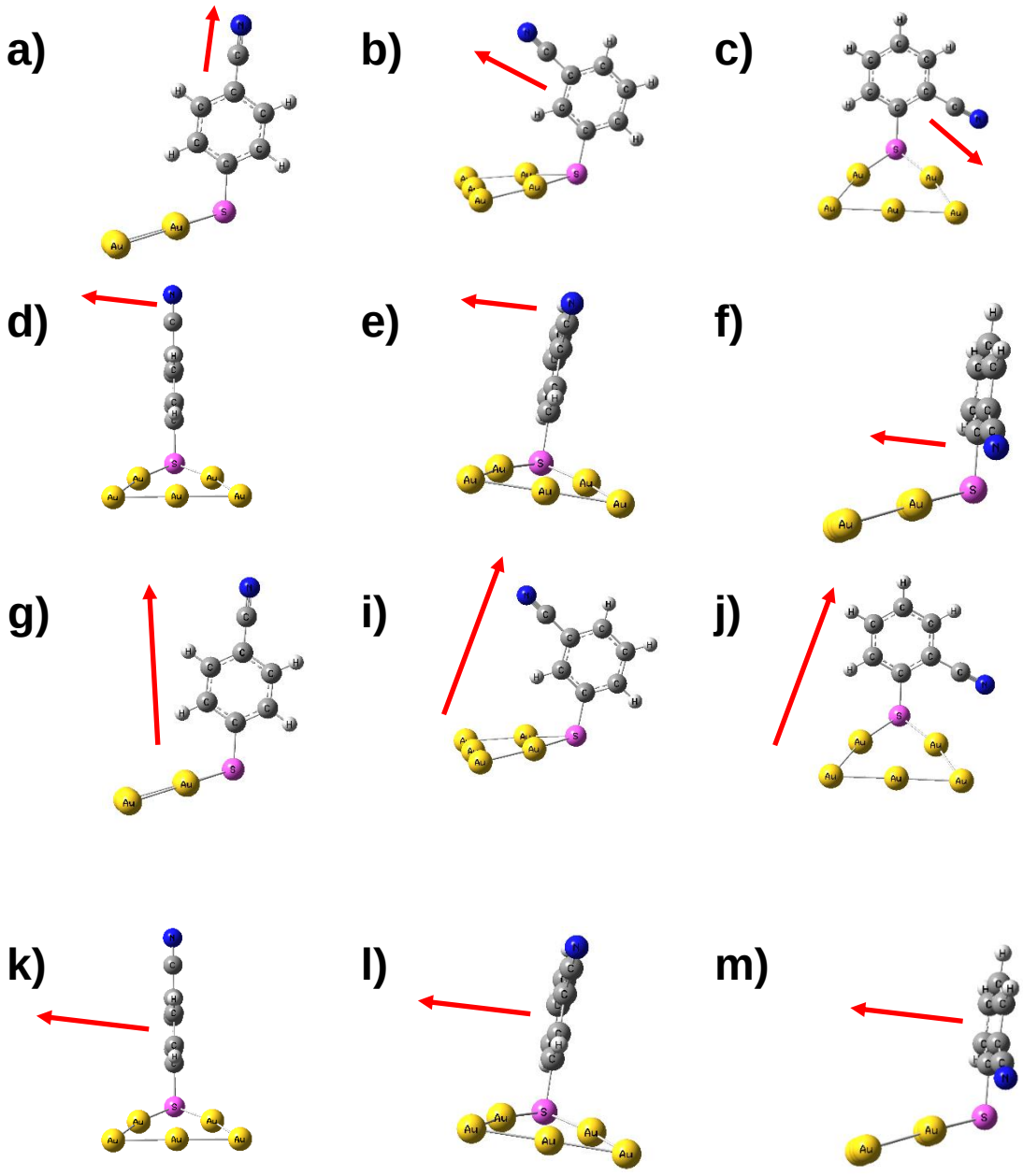

Figure 3.4: The dipole derivative unit vectors for the nitrile C≡N IP (a-c) and OOP (d-f) and the aromatic ring C-H IP (g-i) and OOP (k-m) vibrations of 4-SBN, 3-SBN and 2-SBN.

3.2 SERS potential dependence

To ensure a stable potential window in which the orientation of the three monolayers could be analysed, cyclic voltammograms were acquired and are presented in Figure 3.5. This indicates in the potential window from -0.60 V to 0.20 V *vs*. Pt QRE there are no redox processes for each of 4-SBN, 3-SBN or 2-SBN and upon multiple cycles there is no loss of coverage from monolayer desorption, as evidenced by the reproducibility of the CVs over the three cycles shown.

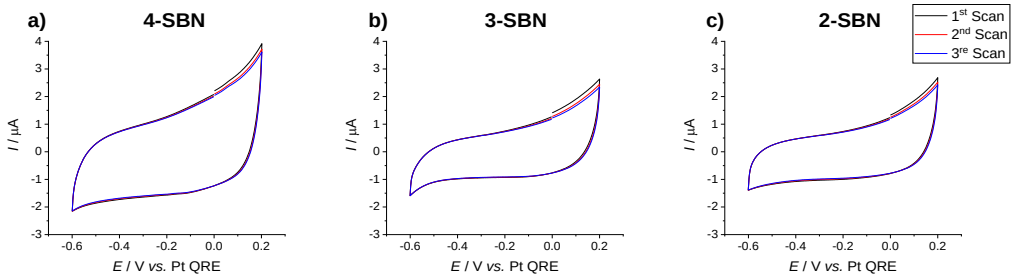

Figure 3.5: Cyclic voltammograms of a) 4-SBN, b) 3-SBN and c) 2-SBN SAMs on Au SSV substrates in 0.1 M TBATFB. Scan rate = 100 mV s^{-1}.

The SERS spectra for the C≡N IP stretching and C≡N OOP bending modes as a function of the applied potential for each of the adsorbed SBN SAMs are shown in Figure 3.6. A Stark shift is clearly observed for the C≡N stretching vibration for 4-SBN (Figure 3.6a), with smaller Stark shifts observed for 3-SBN (Figure 3.6b) and 2-SBN (Figure 3.6c). The peak positions of the C≡N band for each SBN monolayer are plotted as a function of the potential in Figure 3.7 and the Stark shifts determined from the gradient are indicated. In each case there is a break in the slope at approximately -0.1 V *vs.* Pt QRE, with the most significant difference being found for 2-SBN (Figure 3.7c). This variation in the Stark shift indicates a change in the alignment of the C≡N bond with respect to the electric field normal to the electrode surface and suggests that at potentials negative of -0.1 V the bond is in greater alignment with the electric field. For the case of 4-SBN this would correspond to an increase in θ with potential, whilst for 3-SBN and 2-SBN reorientation would require a change in both θ and χ. The error calculation for Raman shift is provided in Appendix B.

Variations in the intensities of the C≡N IP and OOP bands are also shown in Figure 3.6. Overall, for 4-SBN the C≡N IP vibration has a greater

intensity than the OOP vibration, while for 3-SBN and 2-SBN the OOP vibration peak intensity is larger. This indicates the nitrile is in a more parallel orientation to the surface in 3-SBN and 2-SBN due to its position on the benzene ring and an interaction to the Au surface. Such an interaction is visible in the DFT calculated spectra in Figure 3.2, where for 2-SBN the nitrile group is close to the Au surface and can be seen to disrupt the cluster shape, via an attraction between the nitrile group and its nearest Au atom. In 4-SBN and 3-SBN the nitrile group is further away and no change in the cluster is observable. Such an interaction may also be effected by changing the electrochemical potential.

A reversible decrease in the intensity of the C≡N IP band with increasing potential is observed for 4-SBN, In agreement with Schklonik *et al.* [22]. A similar, although smaller, effect was observed for 2-SBN, but little change was observed in the positive sweep (-0.6 to 0.2 V *vs.* Pt QRE) for 3-SBN, with an increase observed at potentials negative of -0.4 V on the negative sweep. Analysis of the OOP peak intensities for 4-SBN is more difficult as the band is much weaker (Figure 3.6g). In contrast, clearly resolved peaks are observed for the OOP modes for 3-SBN and 2-SBN (Figure 3.6h and i). However, detailed interpretation of this difference is complicated by the fact that the intensity is dependent both on the orientation of the mode with respect to the metal surface, as described above, and the distance from the surface, which must be smallest for 2-SBN, for which the most intense peaks are observed. The ratios of the intensities of the C≡N OOP bend:C≡N IP stretch increase linearly with potential (Figure 3.6m-o) for all three molecules, which may be accounted for by an increase in θ with potential for 4-SBN, but requires variation of χ for both 3-SBN and 2-SBN.

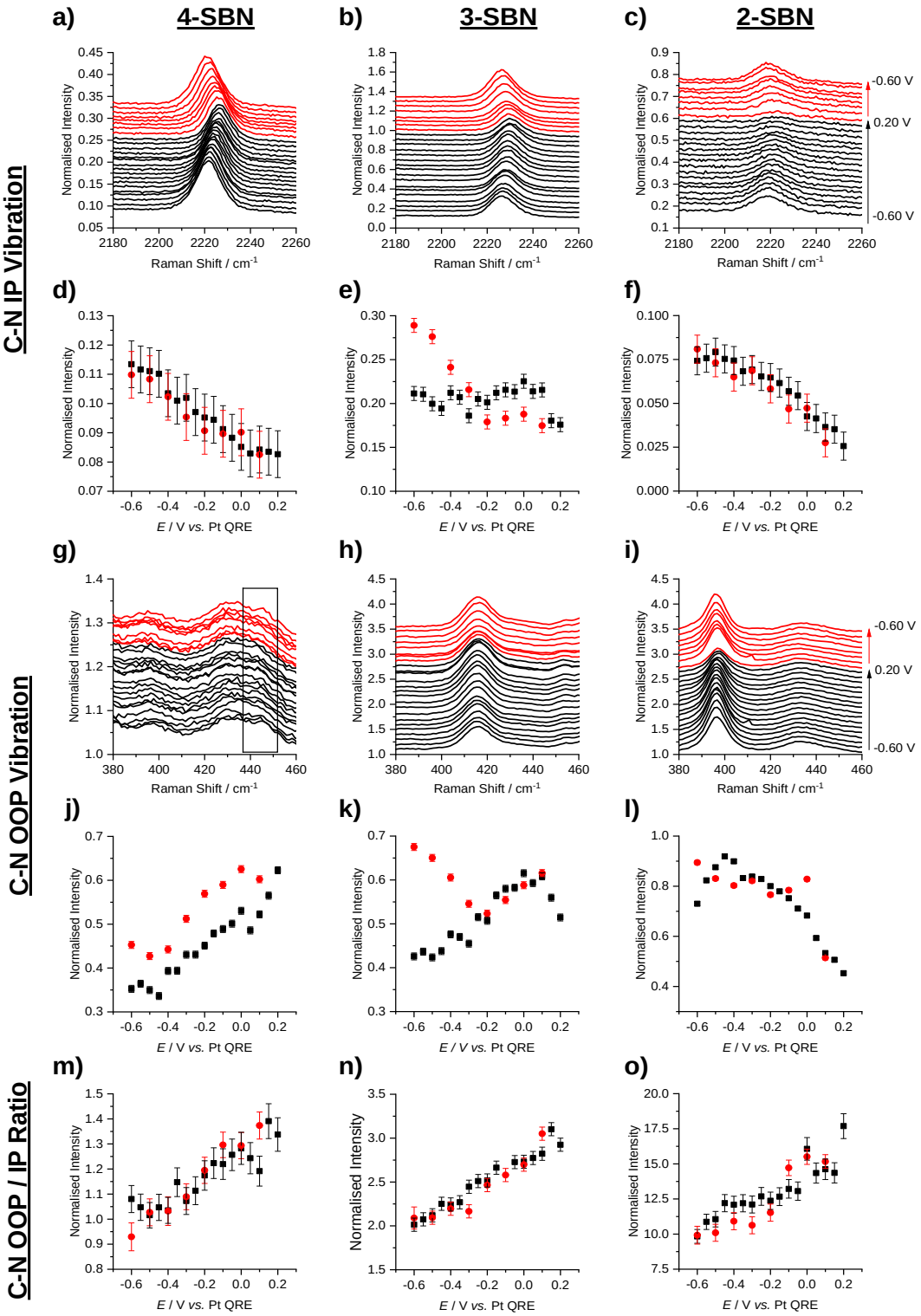

Figure 3.6: EC-SERS spectra of the nitrile C≡N IP and C≡N OOP vibrations (normalised to the background intensity at 525 cm^{-1} in each spectra and offset for clarity), the normalised intensity of each peak and the OOP / IP ratio for SAM's of 4-SBN, 3-SBN and 2-SBN adsorbed on Au SSV substrates.

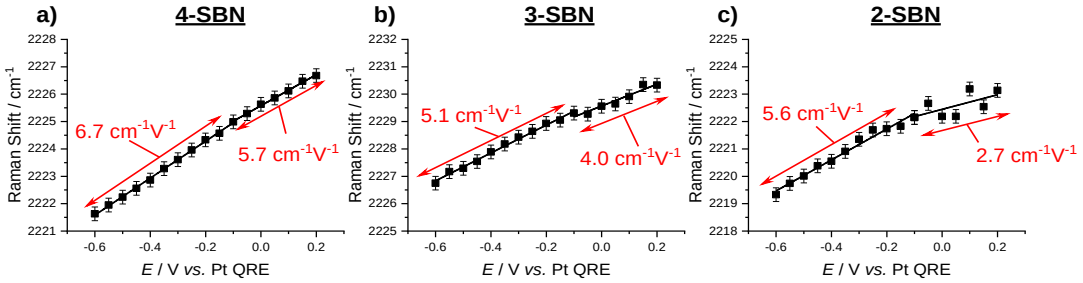

Figure 3.7: The Raman shift of the C≡N IP vibration with respect to potential for a) 4-SBN, b) 3-SBN and c) 2-SBN. The gradients shown at the Stark shifts either side of -0.1 V.

The effects of potential dependence of the orientation of the ring χ can be probed by comparison of the intensities of the IP and OOP C-H bending modes of the ring and the ratio of their intensities, as previously reported in studies of benzene and substituted benzenes on Au [14,23]. The SERS spectra corresponding to the C-H IP and OOP modes and the ratio of the OOP:IP intensities are shown in Figure 3.8 for all three SBN SAMs. The peaks associated with the IP bending vibration, mode 9a in Figure 3.3, are more intense than those for the OOP vibration, mode 10b in Figure 3.3, in agreement with the DFT calculated Raman spectra shown in Figure 3.2, as these are associated with a larger change in the polarizability. As predicted by the molecular geometry, for 4-SBN and 2-SBN the IP intensities decrease with increasing potential (Figure 3.8d and f), whilst for 3-SBN there is little potential dependence (Figure 3.8e), in agreement with the trends in the intensity of the C≡N IP stretching mode (Figure 3.6d-f). In contrast the intensities of the OOP C-H modes do not match the potential dependence of the OOP C≡N bending modes, thus providing information regarding the potential dependence of χ.

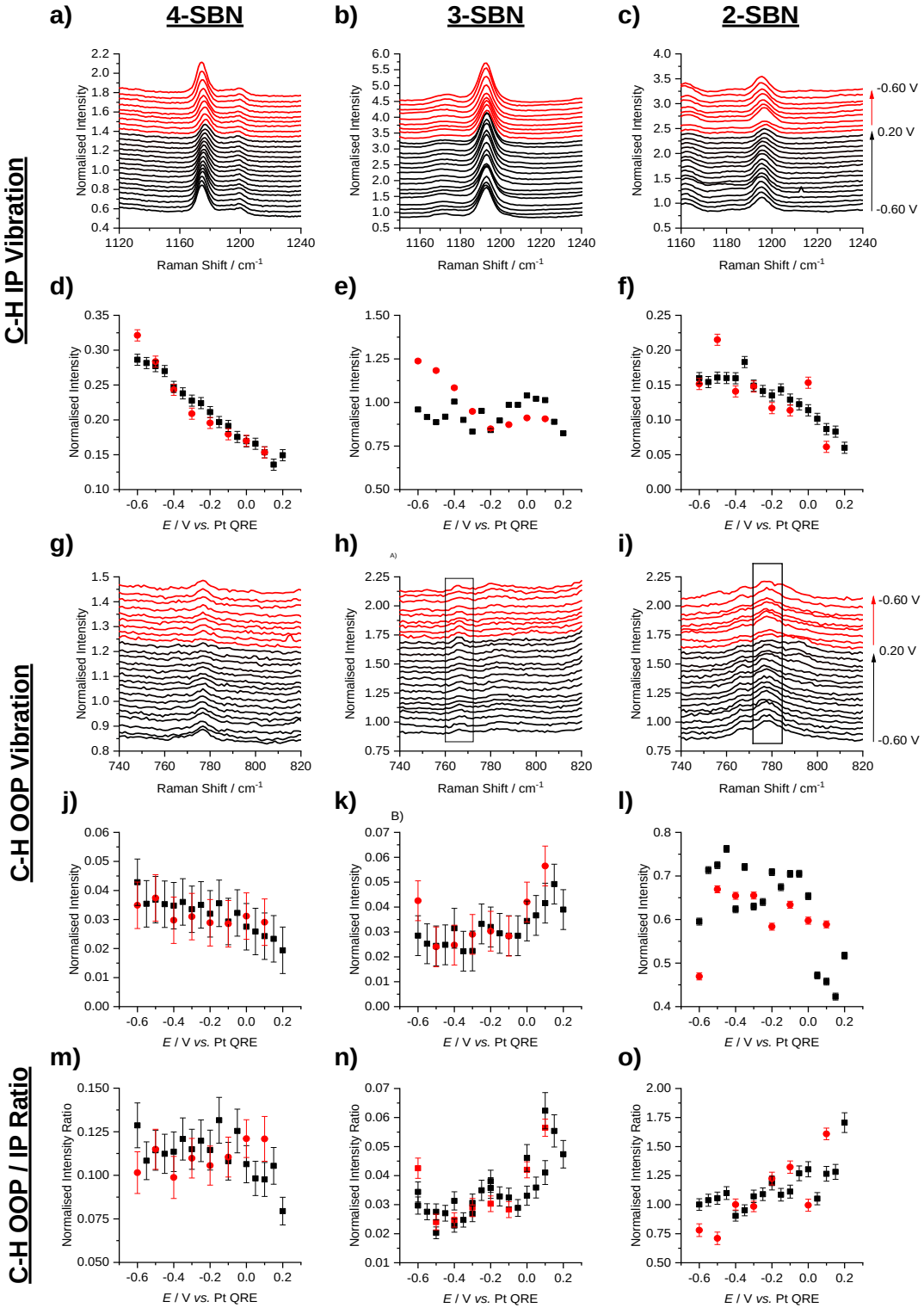

Figure 3.8: EC-SERS spectra of the aromatic C-H IP and OOP vibrations (normalised to the background intensity at 525 cm^{-1} in each spectra and offset for clarity), the normalised intensity of each peak and the OOP / IP ratio for SAM's of 4-SBN, 3-SBN and 2-SBN adsorbed on Au SSV substrate.

For 4-SBN the intensity of the OOP C-H mode (Figure 3.8j) decreases with potential, whilst that of the OOP C≡N bend increases (Figure 3.6j).

However, as seen in Figure 3.8m, the ratio of the OOP:IP C-H modes shows little potential dependence. Thus for 4-SBN the orientation change corresponds to an increase in θ, with little or no change in χ. For 3-SBN, the intensities of both the OOP C-H vibration (Figure 3.8k) and the OOP C≡N bend (Figure 3.6k) increase with potential. In addition, the ratio of the OOP:IP C-H modes shown in Figure 3.8n increases with potential, indicating a decrease in χ. However, the insensitivity of the Stark tuning rate (Figure 3.7b) and intensity of the IP C≡N and C-H modes suggests little potential dependence of θ. Finally, for 2-SBN the OOP C-H mode (Figure 3.8l) shows little potential dependence, whilst the OOP C≡N bend (Figure 3.6l) decreases with increasing potential. Similarly to that observed for 3-SBN, the ratio of the OOP:IP C-H modes for 2-SBN, shown in Figure 3.8o, increases with potential indicating an decrease in χ, which accompanies an increase in θ. These potential dependent orientation changes are depicted in Figure 3.9. Furthermore, the calculation for the error in intensity and Raman shift is provided in Appendix B. As seen in Figures 3.6, 3.7 and 3.8 the error is small, indicating that the change in Raman shift and intensity cannot be accounted for by the error alone and is therefore a result of the electrochemical potential applied.

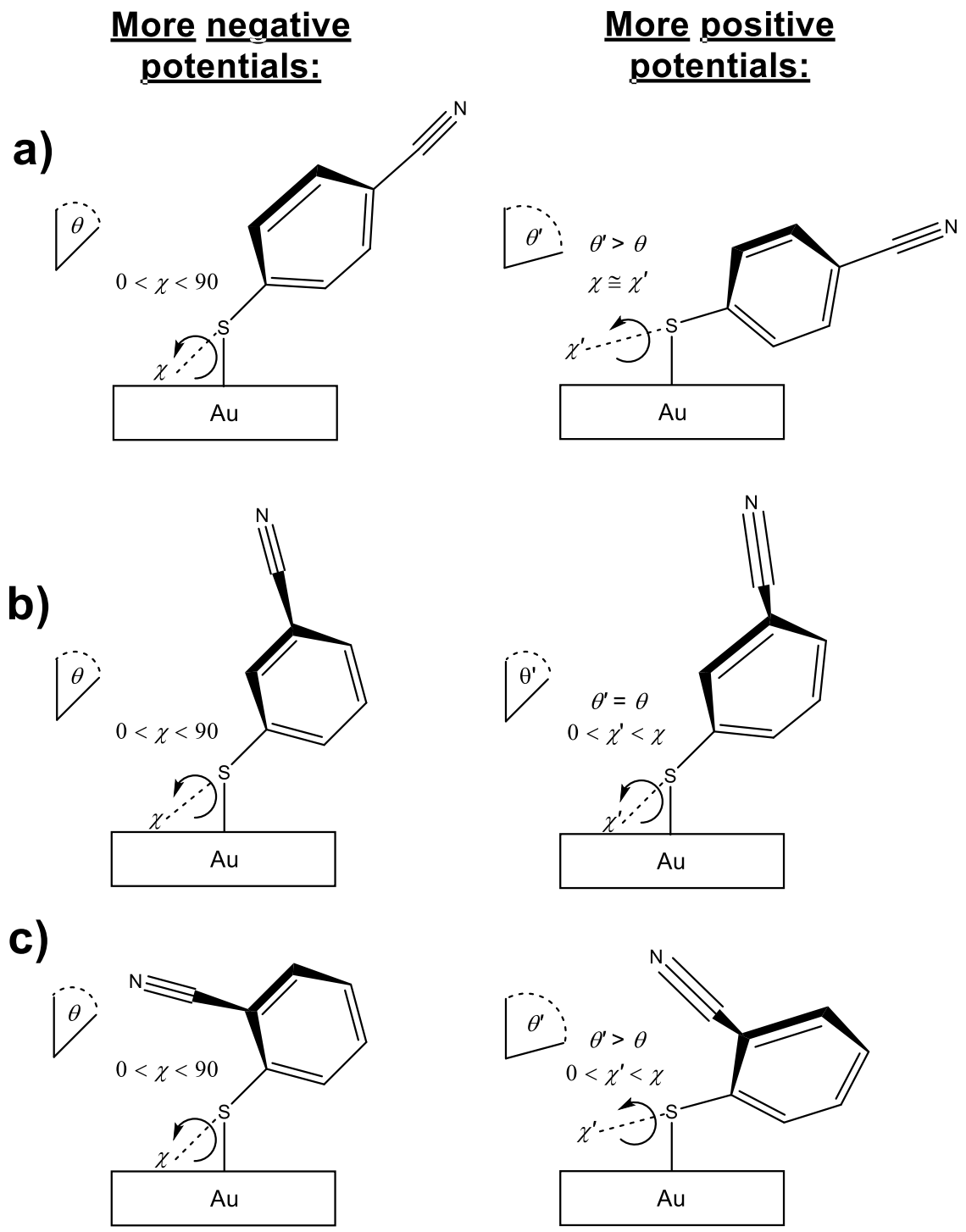

Figure 3.9: Potential dependence of the orientation of a) 4-SBN, showing the increase in θ with potential accompanied by little change to χ, b) 3-SBN showing no change in θ and a decrease in χ, and c) 2-SBN showing an increase in θ and decrease in χ. Negative potentials shown on the left and positive potentials on the right.

The potential dependences observed for the three SAMS reported in this study illustrate the relative effects of the interactions of the nitrile and the aromatic ring with the electrode surface and are in good agreement with previously reported studies of related molecules containing nitrile groups [9,24] and/or aromatic rings [23,25,26]. The effect of the nitrile group is ascribed to the interaction between the dipole moment of the nitrile group and the electrode surface, whilst that of the aromatic ring is attributed to the increased attraction of the π electrons of the benzene ring to the metal surface at positive potentials. The latter effect is evident in early SERS studies by Gao *et al.* [23,27] of benzene adsorbed at roughened gold surfaces. They found that benzene adsorbed in a flat orientation as evidenced by broadening of the ring breathing mode (Wilson number = 1) compared to the Raman spectra of the pure liquid. This broadening indicated ring-surface π orbital overlap and therefore the flat orientation. The widths of the ring breathing modes of the three SBN monolayers are as a function of the potential are plotted in Figure 3.10 (error calculation provided in Appendix B). For 4-SBN (Figure 8a), the peak width decreased as the potential was moved more positive, indicating lessening surface-ring π interactions and a reduction in the amount of back bonding. This is consistent with a change in orientation to be more side on with respect to the surface at more positive potentials and an increase in χ, confirming the small change in χ suggested by the potential dependence of the C-H modes. For 3-SBN (Figure 3.10b), the peak width increased on the forward scan (-0.60 V to 0.20 V), indicating a decrease in χ and again agreement with the analysis of the intensities of the C-H modes. The hysteresis in the peak width observed in figure 3.10b for the reverse scan (0.2 V to -0.60 V) agrees with the similar hysteresis seen in Figures 3.6e, 3.6k for the C≡N modes and 3.8e for the C-H modes, indicating that the change to χ is not reversible. For 2-SBN (Figure 8c), the peak width decreased upon moving to positive potentials, indicating a decreasing surface-ring π interaction and increase in χ. However, the interpretation of the potential dependence of the C≡N and C-H modes presented above indicated an increase in θ and decrease in χ. I account for this discrepancy by noting that the increase in θ results in

the aromatic ring being closer to the electrode surface causing a surface-ring π interaction that disrupts any influence caused by a change in χ.

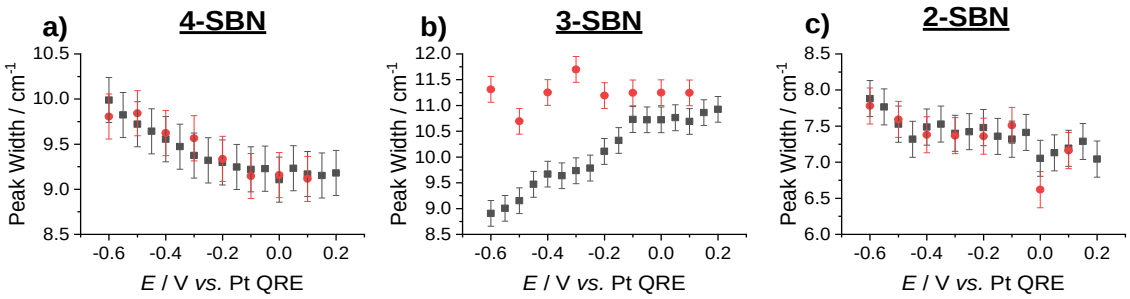

Figure 3.10: The peak width of the IP C-C ring stretching vibration (Wilson number = 1) *vs.* electrochemical potential for a) 4-SBN, b) 3-SBN and c) 2-SBN.

3.3 Summary

In this chapter the potential dependent response of the SERS band intensities, C≡N stretching vibration frequencies, and peak width of the ring breathing mode for *ortho*-, *meta*- and *para*- nitrile substituted benzenethiol SAMs have been presented. All three molecules undergo a change in orientation as the potential is increased, which is driven by the electrostatic interactions of the nitrile group (a dipole interaction) and aromatic ring (π orbital overlap) with the electrode surface. The nitrile group was found to be orientated more parallel to the surface as with increasing potential via a variation in θ and/or χ. Similarly, the orientation of the aromatic ring, defined by χ, was found to vary with potential, increasing slightly for 4-SBN and decreasing for 3-SBN and 2-SBN.

3.4 References

[1] J.U. Nielsen, M.J. Esplandiu, D.M. Kolb, 4-nitrothiophenol SAM on Au(111) investigated by in situ STM, electrochemistry, and XPS, Langmuir. 17 (2001) 3454–3459. doi:10.1021/la001775o.

[2] W. Southerland, C. Hosten, A. Vivoni, O. Bakare, N. Enwerem, M. Ukaegbu, V. Sam, Probing the adsorption and orientation of 2,3-dichloro-5,8-dimethoxy-1,4-naphthoquinone on gold nano-rods: A SERS and XPS study, J. Mol. Struct. 1114 (2016) 197–205. doi:10.1016/j.molstruc.2016.02.043.

[3] L.J. Wan, M. Terashima, H. Noda, M. Osawa, Molecular Orientation and Ordered Structure of Benzenethiol Adsorbed on Gold(111), J. Phys. Chem. B. 104 (2000) 3563–3569. doi:10.1021/jp993328r.

[4] P.L. Stiles, J.A. Dieringer, N.C. Shah, R.P. Van Duyne, Surface-Enhanced Raman Spectroscopy, Annu. Rev. Anal. Chem. 1 (2008) 601–626. doi:10.1146/annurev.anchem.1.031207.112814.

[5] G. Aruldhas, Molecular structure and spectroscopy, 2nd ed., PHI Learning, Delhi, 2007.

[6] L.Q. Dong, J.Z. Zhou, L.L. Wu, P. Dong, Z.H. Lin, SERS studies of self-assembled DNA monolayer - Characterization of adsorption orientation of oligonucleotide probes and their hybridized helices on gold substrate, Chem. Phys. Lett. 354 (2002) 458–465. doi:10.1016/S0009-2614(02)00163-X.

[7] K.T. Carron, L.G. Hurley, Axial and azimuthal angle determination with surface-enhanced Raman spectroscopy: thiophenol on copper, silver, and gold metal surfaces, J. Phys. Chem. 95 (1991) 9979–9984. doi:10.1021/j100177a068.

[8] G. Cabello, X.J. Chen, R. Panneerselvam, Z.Q. Tian, Potential dependent thiocyanate adsorption on gold electrodes: a comparison study between SERS and SHINERS, J. Raman Spectrosc. 47 (2016) 1207–1212. doi:10.1002/jrs.4944.

[9] B. Ren, R.A. Gu, J.L. Yao, X.M. Fan, Z.Q. Tian, Y.X. Yuan, The reorientation of benzonitrile on Platinum electrode probed by surface enhanced Raman spectroscopy, J. Electroanal. Chem. 624 (2008) 129–133. doi:10.1016/j.jelechem.2008.08.004.

[10] E.F. Silva, M.C.E. Bandeira, W.A. Alves, O.R. Mattos, Surface-Enhanced Raman Scattering and Electrochemical Investigations on the Adsorption of Imidazole: Imidazolium Couple and Its Implications on Copper Corrosion Inhibition, J. Electrochem. Soc. 165 (2018) C375–C384. doi:10.1149/2.0841807jes.

[11] I. Brand, J. Juhaniewicz-Debinska, L. Wickramasinghe, C.N. Verani, An In situ spectroelectrochemical study on the orientation changes of an

[$Fe^{iii}N_2O_3$] metallosurfactant deposited as LB Films on gold electrode surfaces, Dalt. Trans. 47 (2018) 14218–14226. doi:10.1039/c8dt00333e.

[12] Z.Q. Tian, B. Ren, D.Y. Wu, Surface-enhanced Raman scattering: From noble to transition metals and from rough surfaces to ordered nanostructures, J. Phys. Chem. B. 106 (2002) 9463–9483. doi:10.1021/jp0257449.

[13] J.E. Pemberton, M.A. Bryant, R.L. Sobocinski, S.L. Joa, A Simple Method for Determination of Orientation of Adsorbed Organics of Low Symmetry Using Surface-Enhanced Raman Scattering, J . Phys. Chem. 96 (1992) 3716–3182. doi:10.1021/j100188a039.

[14] C.A. Szafranski, W. Tanner, P.E. Laibinis, R.L. Garrell, Surface-enhanced Raman spectroscopy of aromatic thiols and disulfides on gold electrodes, in: F. Adar, J.E. Griffiths (Eds.), Langmuir, 1998: pp. 3570–3579. doi:10.1021/la9702502.

[15] V. Oklejas, C. Sjostrom, J.M. Harris, Surface-enhanced Raman scattering based vibrational Stark effect as a spatial probe of interfacial electric fields in the diffuse double layer, J. Phys. Chem. B. 107 (2003) 7788–7794. doi:10.1021/jp0344693.

[16] H. Lehle, J.M. Kriegl, K. Nienhaus, P. Deng, S. Fengler, G.U. Nienhaus, Probing electric fields in protein cavities by using the vibrational Stark effect of carbon monoxide, Biophys. J. 88 (2005) 1978–1990. doi:10.1529/biophysj.104.048140.

[17] G. Schkolnik, Vibrational Stark Spectroscopy as a Tool for Probing Electrostatics at Protein Surfaces and Self Assembled Monolayers, 2012. https://depositonce.tu-berlin.de/bitstream/11303/3723/1/Dokument_48.pdf (accessed May 17, 2017).

[18] A.E. Russell, S.H. Pelfrey, J. Speed, S. Mahajan, P.N. Bartlett, J.J. Baumberg, Sphere Segment Void Structures: a Reproducible SERS Substrate for Electrochemical Studies, in: 41st Am. Chem. Soc. Cent. Reg. Meet., 2009.

[19] M.E. Abdelsalam, P.N. Bartlett, J.J. Baumberg, S. Cintra, T.A. Kelf, A.E. Russell, Electrochemical SERS at a structured gold surface, Electrochem.

Commun. 7 (2005) 740–744. doi:10.1016/j.elecom.2005.04.028.

[20] L. Bin Zhao, J.L. Chen, M. Zhang, D.Y. Wu, Z.Q. Tian, Theoretical study on electroreduction of p-nitrothiophenol on silver and gold electrode surfaces, J. Phys. Chem. C. 119 (2015) 4949–4958. doi:10.1021/jp512957c.

[21] J.C. Merlin, J.P. Cornard, A Pictorial Representation of Normal Modes of Vibration Using Vibrational Symmetry Coordinates, J. Chem. Educ. 83 (2006) 1393. doi:10.1021/ed083p1393.

[22] G. Schkolnik, J. Salewski, D. Millo, I. Zebger, S. Franzen, P. Hildebrandt, Vibrational Stark Effect of the Electric-Field Reporter 4-Mercaptobenzonitrile as a Tool for Investigating Electrostatics at Electrode/SAM/Solution Interfaces, Int. J. Mol. Sci. 13 (2012) 7466–7482. doi:10.3390/ijms13067466.

[23] X. Gao, J.P. Davies, M.J. Weaver, Test of surface selection rules for surface-enhanced Raman scattering: the orientation of adsorbed benzene and monosubstituted benzenes on gold, J. Phys. Chem. 94 (1990) 6858–6864. doi:10.1021/j100380a059.

[24] Y. Sato, S. Ye, T. Haba, K. Uosaki, Potential Dependent Orientation and Oxidative Decomposition of Mercaptoalkanenitrile Monolayers on Gold. An in Situ Fourier Transform Infrared Spectroscopy Study , Langmuir. 12 (2002) 2726–2736. doi:10.1021/la950675t.

[25] I. Matulaitiene, Z. Kuodis, A. Matijoška, O. Eicher-Lorka, G. Niaura, SERS of the Positive Charge Bearing Pyridinium Ring Terminated Self-Assembled Monolayers: Structure and Bonding Spectral Markers, J. Phys. Chem. C. 119 (2015) 26481–26492. doi:10.1021/acs.jpcc.5b07687.

[26] A. Chen, D. Yang, J. Lipkowski, S. Sun, B. Pettinger, In situ FTIR studies of 4-cyanopyridine adsorption at the Au(111) electrode, Can. J. Chem. 74 (2006) 2321–2330. doi:10.1139/v96-259.

[27] M.L. Patterson, M.J. Weaver, Surface-Enhanced Raman Spectroscopy as a Probe of Adsorbate-Surface Bonding: Simple Alkenes and Alkynes Adsorbed at Gold Electrodes, J. Phys. Chem. 89 (1985) 5046–5051. doi:10.1021/j100269a032.

Chapter 4: *p*-nitrothiophenol electroreduction and *p*-aminothiophenol electrooxidation

In-depth understanding of the mechanisms of redox processes at electrode surfaces is vital in furthering the design of electrocatalysts and electrosynthetics processes, both in terms of fundamental studies and for electrochemical engineering applications. However, significant challenges lie in identifying intermediates [1]. Surface enhanced Raman spectroscopy (SERS) is an excellent technique to study such systems as it allows monolayer level chemical characterisation [2] and provides surface specificity [3].

p-nitrothiophenol (PNTP) is an important probe molecule in spectroscopic applications as it forms well packed SAMs on metal surfaces, has large Raman and IR signal intensity, and is both electrochemically and photochemically active [4–21]. These properties allow PNTP to be used as a model to help further understand the reduction of nitrobenzene [22], a process used in many applications from the syntheses of pharmaceuticals [23,24], dyes and pigments [25], to the industrial manufacture of aniline [26–28]. This latter reaction is typically environmentally unfriendly with a high E factor (defined as the weight ratio of the by-products to the desired products), however when Au is used as a catalyst the process is highly selective and no additional treatments are required [27,29]. The environmental benefits justify continued interest in ascertaining the details of the reaction mechanism, including the identification of any intermediates. In addition, PNTP has been used to probe the electronic structure of underlying metal surfaces [7,17–19] and has applications for charge transfer in molecular electronics [16,21].

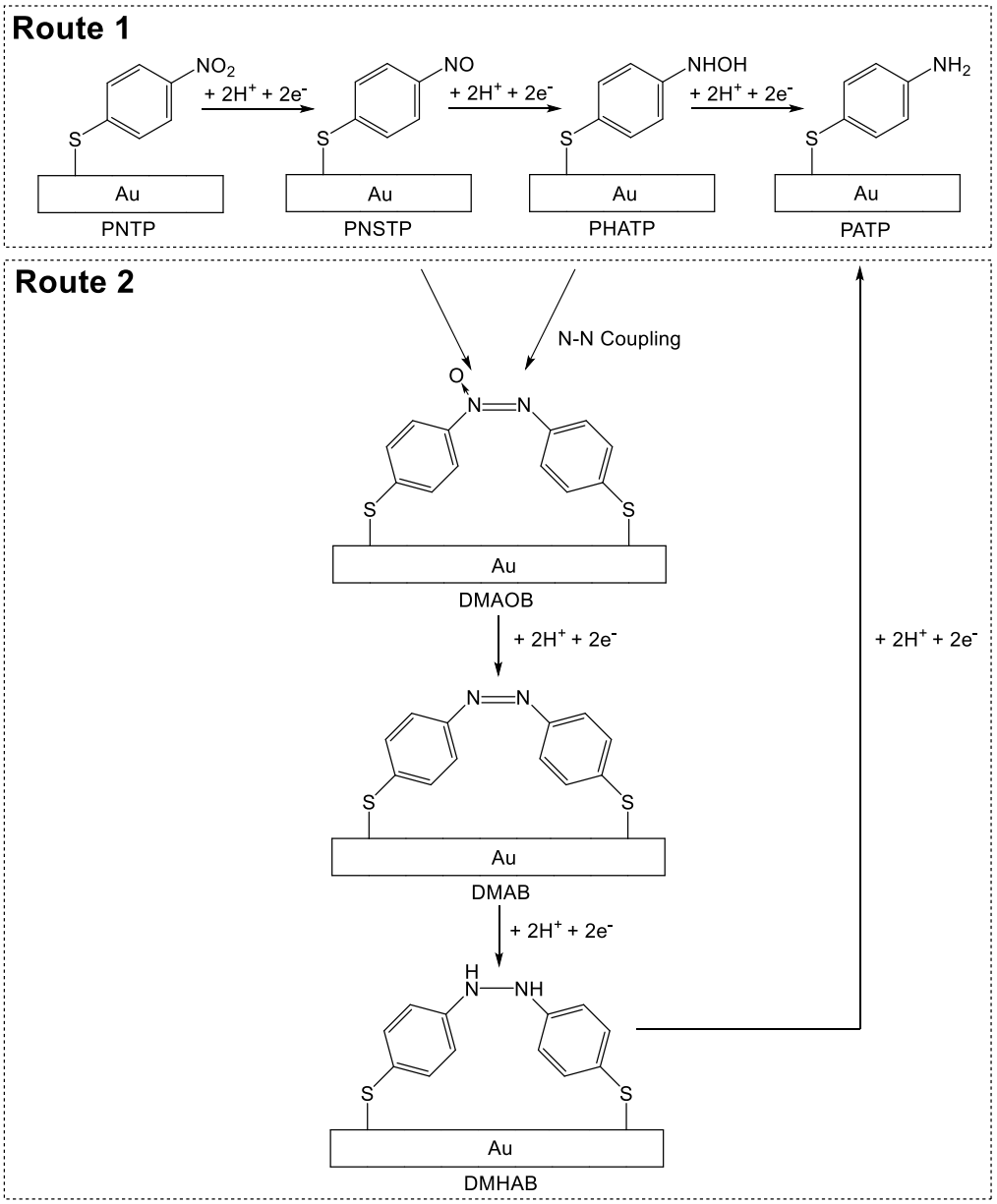

Figure 4.1: Reaction scheme for the two reduction pathways of PNTP to PATP. Route 1 is the unimolecular direct electrochemical pathway, whilst Route 2 involves the chemical coupling of the surface intermediates.

Figure 4.1 shows the generally accepted reaction scheme of PNTP electroreduction [22,29]. Two reaction routes are proposed, the first (Route 1 in Figure 4.1) is the direct unimolecular pathway, involving the reduction of PNTP to *p*-nitrosothiophenol (PNSTP), then to *p*-hydroxylaminothiophenol (PHATP) and finally, in the slowest step, to the amine PATP. The second (Route 2 in Figure 4.1) is a dimerisation pathway and involves the reaction of one PNSTP and one PHATP intermediate from the first route to form the azoxy derivative, *p-p'*-dimercaptoazoxybenzene (DMAOB). This can then be further reduced to *p-*

p'-dimercaptoazobenzene (DMAB) and *p-p'*-dimercaptohydrazobenzene (DMHAB), before finally to PATP in consecutive steps.

The reduction pathway has been investigated using SERS [4,6,7,9–11,14–22] and infrared (IR) [4,8] spectroscopies, with the Raman spectra well characterised using density functional theory (DFT) calculations [22]. However, when investigating PNTP using SERS large signals corresponding to DMAB are routinely observed, as the bimolecular reduction pathway is also photo-catalysed by the laser used in the Raman measurements. This photochemical reaction has been well studied and recent advancements have determined that hot electrons generated via the surface plasmon resonance of the SERS substrate are responsible for the catalysis. A review by Chen *et al.* explains the phenomenon well [11]. Due to this competing reduction pathway, SERS studies have provided no evidence of either PNSTP or PHATP in the unimolecular reduction pathway, although a complementary SERS study by Gao *et al*. followed the electroreduction of the nitrobenzene and found nitrosobenzene as an intermediate on Au [30]. Success has been achieved with attenuated total reflectance (ATR) IR, X-ray photoelectron spectroscopy (XPS), and scanning electrochemical microscopy (SECM), revealing the presence of PNSTP and PHATP on Au electrodes during the reduction of PNTP [8,31–33].

Figure 4.2 shows the electrooxidation products of *p*-aminothiophenol (PATP) in acid and base. These have been previously theoretically determined using DFT calculations [34], concluding that in acid the 'head to tail' species 4'-mercapto-N-phenyl-1,4-quinone diimine (NPQDI) forms via N-C4 coupling, which itself has redox properties and can be reduced to the corresponding diamine 4'-mercapto-N-phenyl-1,4-quinone diamine (NPQDA). In addition, in these conditions a hydrolysis reaction can convert NPQDI to 4'-mercapto-N-phenyl-1,4-quinone monoimine (NPQMI) which again also has redox chemistry and can be reversibly reduced to 4'-mercapto-N-phenyl-1,4-quinone monoamine (NPQMA). The formation of a surface bound quinone redox couple is especially interesting as it takes part in many biological systems [35]. In base, the N-N coupled species p-p'- dimercaptoazobenzene (DMAB) and its redox couple p-p'-dimercaptohydrazobenzene (DMHAB) are proposed.

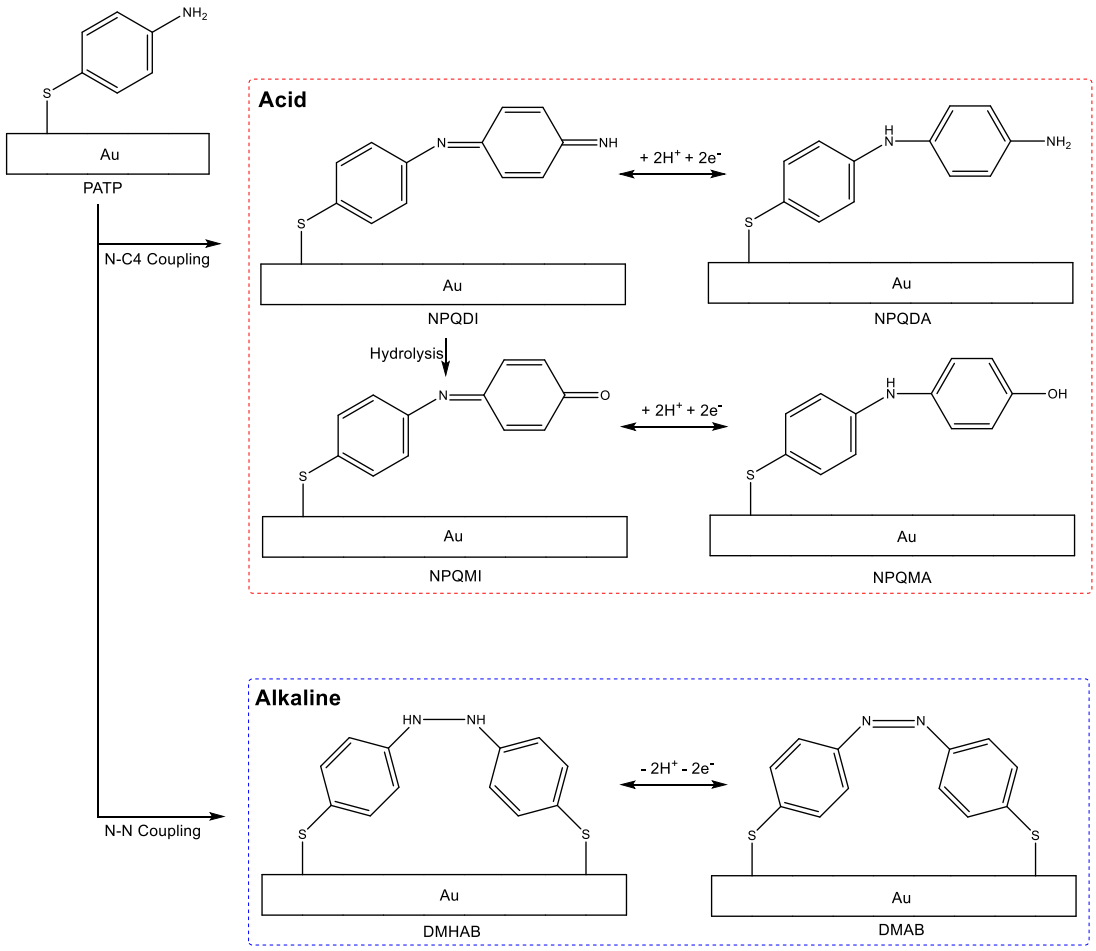

Figure 4.2: The proposed reaction products of the electrochemical oxidation of PATP in acidic, neutral and basic media. Adapted from Retna Raj *et al.*[36] and Zhao *et al.* [34].

PATP has applications in molecular junctions[37] and as a model for biological systems [35], and has been readily investigated with SERS [11,14,20,34,38–44], surface enhanced IR absorption spectroscopy (SEIRAS) [36], XPS [35,45] and electrochemistry [37,39,46]. Its rich SERS research history has also recently been well discussed in a review by Huang *et al.* [47]. The electrooxidation products in acid have been previously observed by SEIRAS [36] but a previous electrochemical SERS (EC-SERS) study concluded that the potential induced changes in PATP spectra were the result of electropolymerization reactions from additional aniline molecules present in the electrolyte [40].

As previously described in Chapter 3, alongside *in situ* mechanistic studies SERS can also provide information about the orientation of adsorbed molecules as a function of the electrode potential. The orientation is of interest

due to the effect it can have on electron transfer, molecule-surface interactions, electrode catalytic activity and the binding of additional molecules [48–51]. Previous orientation analysis studies using sum-frequency generation (SFG) spectroscopy found PNTP had a tilt angle (θ, the angle between the surface normal and benzene ring) of 59°. The same technique found θ for the unsubstituted molecule thiophenol (TP) was 49° [52], while SERS and SEIRAS studies of TP found θ to be 14° and the twist angle (χ, the angle of the benzene ring to the surface – see Chapter 3 for more details) to be 0° respectively [2,53]. I believe the tilt angle of PNTP to be small, and therefore the primary axis of the molecules is more perpendicular to the surface, on the basis of the very large SERS intensity of in plane (IP, with respect to the plane of the benzene ring) vibrations and very weak intensity of the out of plane (OOP) vibrations both reported in the literature [4,6,7,9–11,14,15,17–20] and in the results presented below.

In this chapter, I present DFT calculated Raman and experimental SERS spectra to characterise the intermediates of PNTP electroreduction and the products of PATP electrooxidation adsorbed on gold sphere segment void (SSV) substrate electrodes [54,55]. In addition, PNTP orientation changes positive and negative of the redox potential of the reaction are investigated by monitoring the intensities of IP and OOP modes and the magnitudes of any Stark shifts.

4.1 *p*-nitrothiophenol electroreduction

4.1.1 Identification of intermediates

The experimentally obtained SERS and DFT calculated Raman spectra of PNTP are shown in Figure 4.3, with the optimised structure on an Au_5 cluster shown inset. In general, there is good agreement between the experimental and calculated spectra, although there are some variations due to limitations in the DFT calculations (See ‘3.1 Sulfanylbenzonitrile SERS characterisation’ for further information). However, the similarity of the spectra provides confidence in the subsequent calculated spectra for the proposed reaction intermediates and products.

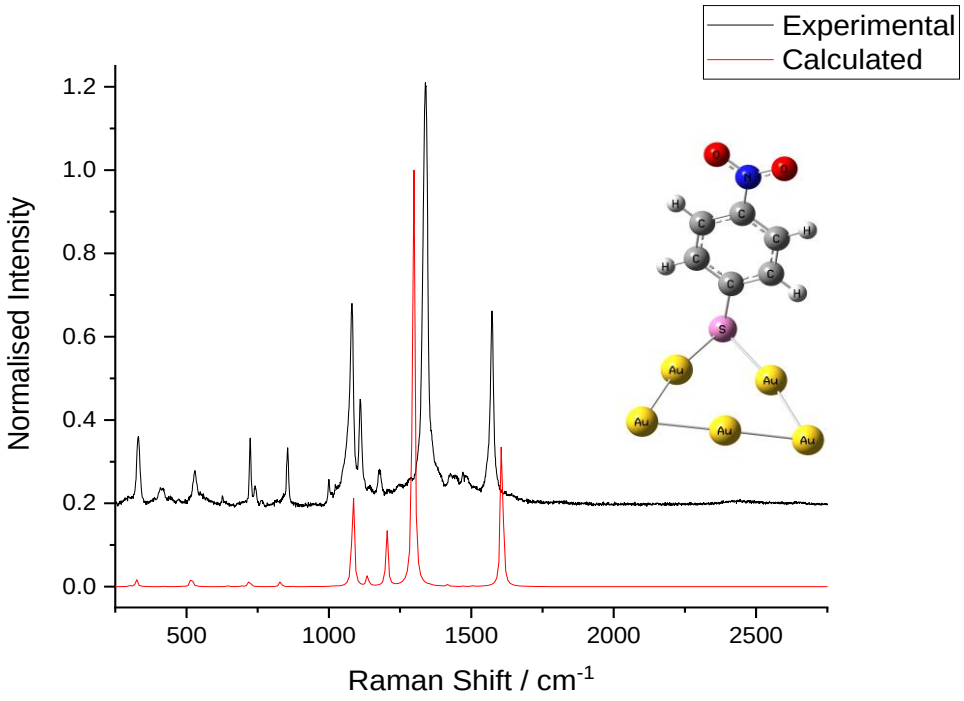

Figure 4.3: Experimental SERS and DFT calculated Raman spectra of a PNTP SAM with, inset, the optimised structure. The SERS spectrum is of PNTP adsorbed on an Au SSV substrate in 0.1 M $NaClO_4$ at the open circuit potential. Spectra are normalised to the largest peak in each spectra and offset for clarity.

Figure 4.4 shows the DFT optimised structures of these intermediates and their corresponding calculated Raman spectra. There are clear differences between the intermediates, especially in the 1000 cm^{-1} to 2000 cm^{-1} window. The direct pathway species PNSTP and PHATP have large peaks at 1077, 1160, 1398 and 1614 cm^{-1} and at 1090, 1204 and 1629 cm^{-1}, respectively. Similarly, for the dimerisation pathway there are clear peaks for DMAOB at 1087, 1263, 1480 and 1617 cm^{-1}, for DMAB at 1085, 1152, 1416, 1472 and 1611 cm^{-1}, and for DMHAB at 1090 and 1635 cm^{-1}. These spectra are very similar to those presented by Zhao *et al.* but intensities here vary [22], which is attributed to the slightly different calculation parameters used. Zhao *et al.* used a hybrid exchange-correlation functional of B3LYP and PW91PW91, whereas we used B3LYP. Full SERS and DFT vibrational assignments of these species and PNTP are available in Appendix C.

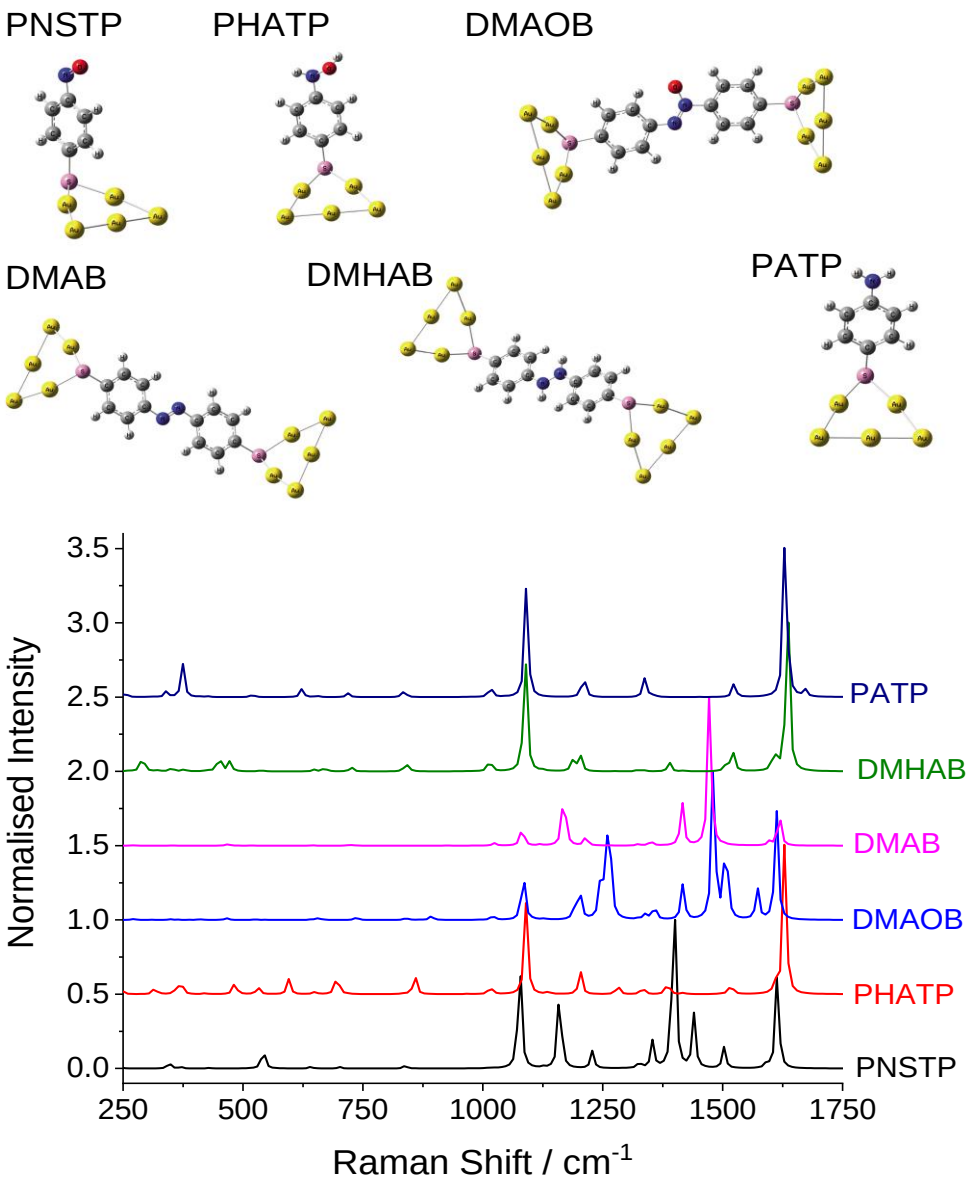

Figure 4.4: DFT optimised structures of the PNTP reduction species adsorbed on Au_5 clusters and their calculated Raman spectra. Spectra are normalised to the largest peak in each spectra and offset for clarity.

Furthermore, for DMAOB, DMAB and DMHAB where there are two Au binding sites additional binding configurations were also investigated. For example, DMAB-Au where the two S atoms were bound to one large Au cluster. However, when the resulting system was optimised and the DFT spectra calculated there were no large characteristic bands at 1416 and 1472 cm^{-1} for DMAB as seen in previous studies in the literature [11]. This suggests that these configurations were not those that form during SERS experiments, I believe due to the significant strain on the molecules seen in these configurations.

As described earlier, following the electroreduction of PNTP using SERS can be complicated by the formation of DMAB via a photo-catalysed dimerisation pathway. In many cases DMAB modes have large SERS intensities and overwhelm the spectra, making additional analysis challenging. The possible effects of the photoreaction were tested using three different laser powers: 240 mW cm^{-2}, 480 mW cm^{-2} and 1200 mW cm^{-2} and spectra were taken every 60 s for 25 acquisitions. The first and last spectra are shown in Figure 4.5. The Raman shift of peaks corresponding to DMAB at 1146, 1390 and 1426 cm^{-1} are marked in the spectra (green stars), with only the 1146 cm^{-1} peak noticeable at any laser power. Therefore, the amount of photochemically generated DMAB is small and the smooth nature of the SSV substrate appears to prevent the generation of catalytic hot electrons observed on highly roughened SERS substrates under similar experimental conditions. All other potential dependent PNTP SERS experiments reported below use the same spectral sequence, electrolyte and a laser power of 480 W cm^{-2}.

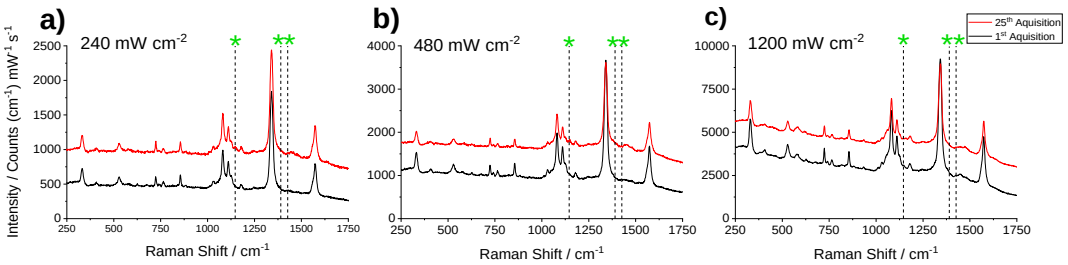

Figure 4.5: 1st and 25th SERS spectra of PNTP SAMs submerged in 0.1 M $NaClO_4$ at the open circuit potential acquired in a sequence. Spectra had an acquisition time of 10 s, with a 60 s delay between acquisitions and were taken at three different laser powers: a) 240 mW cm^{-2} (0.05 % total power), b) 480 mW cm^{-2} (0.10 %), c) 1200 mW cm^{-2} (0.50 %). Green stars correspond to the Raman shifts of peaks for photochemically produced DMAB. Spectra offset for clarity.

A cyclic voltammogram of a PNTP SAM adsorbed on an Au SSV in 0.1 M $NaClO_4$ is shown in Figure 4.6a. In the first scan there is a large reduction peak with an onset potential of -0.40 V. In subsequent scans, this is no longer present, indicating an irreversible reduction. The corresponding SERS spectra of PNTP as a function of applied potential are shown in Figure 4.6b. From 0.20 V to -0.60 V there is little change in the spectra, but at potentials more negative than -0.70 V the PNTP modes (labelled with red stars) all decreased in intensity, becoming indistinguishable from the noise by -1.30 V. In addition, at -0.60 V new peaks appeared at 389, 417, 998, 1025, 1067, 1179, 1564 and 1597 cm^{-1}

(black stars). These are characteristic of PATP [14,38,47], and are in good agreement with the DFT calculated Raman spectra. The reduction in intensity of PNTP modes and subsequent increase in intensity for peaks assigned to PATP clearly shows that PNTP has been electrochemically reduced to PATP on the SSV surface, in agreement with previously reported SERS studies [4,8,13,14].

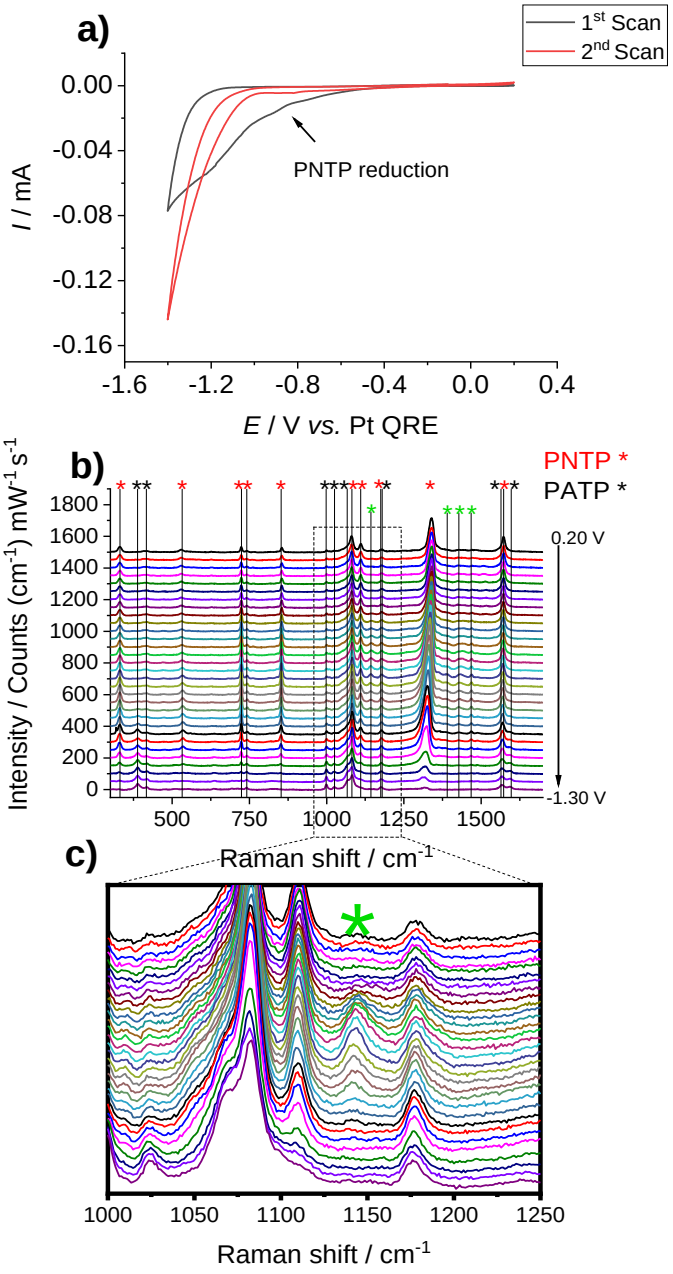

Figure 4.6: a) Cyclic voltammograms of a PNTP SAM on an Au SSV substrate in 0.1 M $NaClO_4$. Scan rate = 5 mV s^{-1}. b) EC-SERS spectra of this system where the red starred peaks are those assigned to PNTP, black starred peaks correspond to PATP and green starred peaks to intermediate species. c) spectra zoomed in from 1000-1250 cm^{-1}, with the green star marking the peak at 1427 cm^{-1}. Spectra offset for clarity.

In Figure 4.6b there are also four peaks at 1146, 1290, 1427 and 1460 cm^{-1} labelled with green stars. The modes at 1146, 1390 and 1427 cm^{-1} appeared at -0.20 V and increased in intensity as the potential was made more negative, reaching a maximum at -0.70 V, before disappearing completely by -0.85 V. Previous studies assign these to photochemically produced DMAB and also match our DFT calculated Raman spectra (Figure 4.4). However, as shown in Figure 4.5, the photochemical pathway is not active in this spectroelectrochemical system and therefore the DMAB produced here is attributed to the bimolecular electrochemical pathway.

The fourth additional peak at 1427 cm^{-1} (Figure 4.6c) initially appeared at -0.20 V and had disappeared by -1.10 V. By comparison to the DFT calculated Raman spectra of all the intermediates (Figure 4.4) this peak can be assigned to the C-C bending vibration, C-H bending vibration and C=O stretching vibration ($\delta_{C-C} + \delta_{C-H} + \nu_{C=O}$, 19b + 18b) at 1440 cm^{-1} for PNSTP. Previous studies have been unable to observe this intermediate and thus this is the first SERS evidence for this species. Together with the presence of DMAB, the observation of PNSTP indicates that the electrochemical reduction of PNTP proceeds via both the direct and dimerisation pathways on the Au SSV surface.

4.1.2 PNTP Orientation

The orientation of SAMs can be probed using SERS by comparison of the intensity of vibrational modes, as previously discussed in Chapter 3. From the SERS selection rules, vibrations perpendicular to the surface are more enhanced and the signals are larger, while parallel vibrations are less enhanced and smaller. For PNTP the aromatic ring C-H IP (in plane of the ring, Wilson number = 9a) and OOP (out of plane, 5) have orthogonal dipole orientations so are ideal for such a study, providing information about θ and χ. Ideally, a second set of orthogonal nitro group vibrations would be used to give further insight into the molecule's orientation. However, only an IP C-N stretching vibration could be characterised, providing information only regarding changes to the tilt angle θ. No peaks for the C-N OOP mode were observed above the noise level of the data. Coordinate diagrams of these vibrations are shown in Figure 4.7, with the dipole derivative unit vectors shown in Figure 4.8, confirming the vibrational direction of each mode.

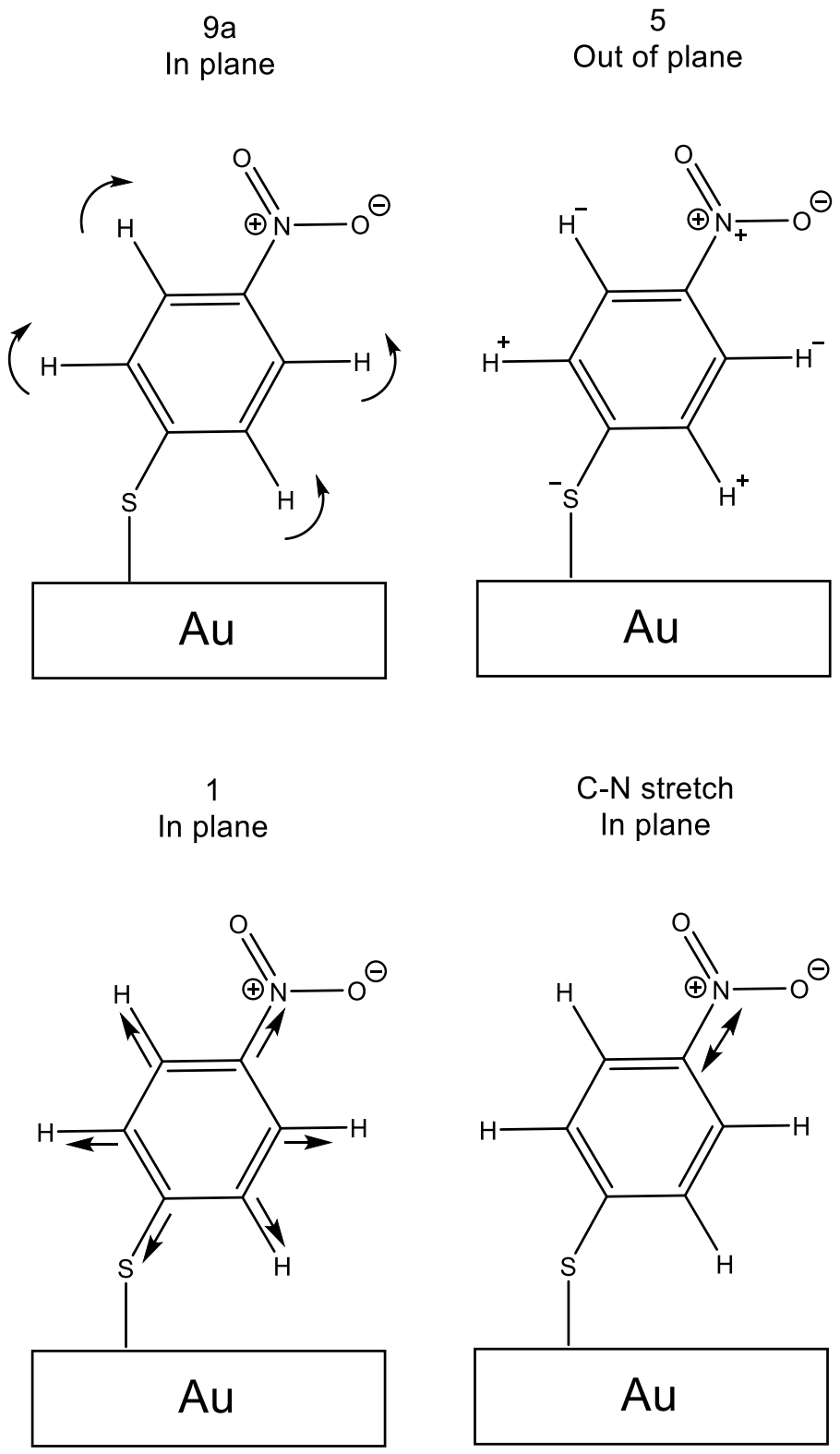

Figure 4.7: The aromatic ring and C-N vibrations analysed in this chapter. The 9a and 5 vibrations are IP and OOP C-H bends, the 1 vibration is an IP C-C stretch and the atomic coordinate changes for these are taken from Merlin and Cornard [56]. The C-N vibration is an IP stretch. Arrows indicate bond movement within the plane of the aromatic ring, + and – signs show movement into and out of the plane of the ring.

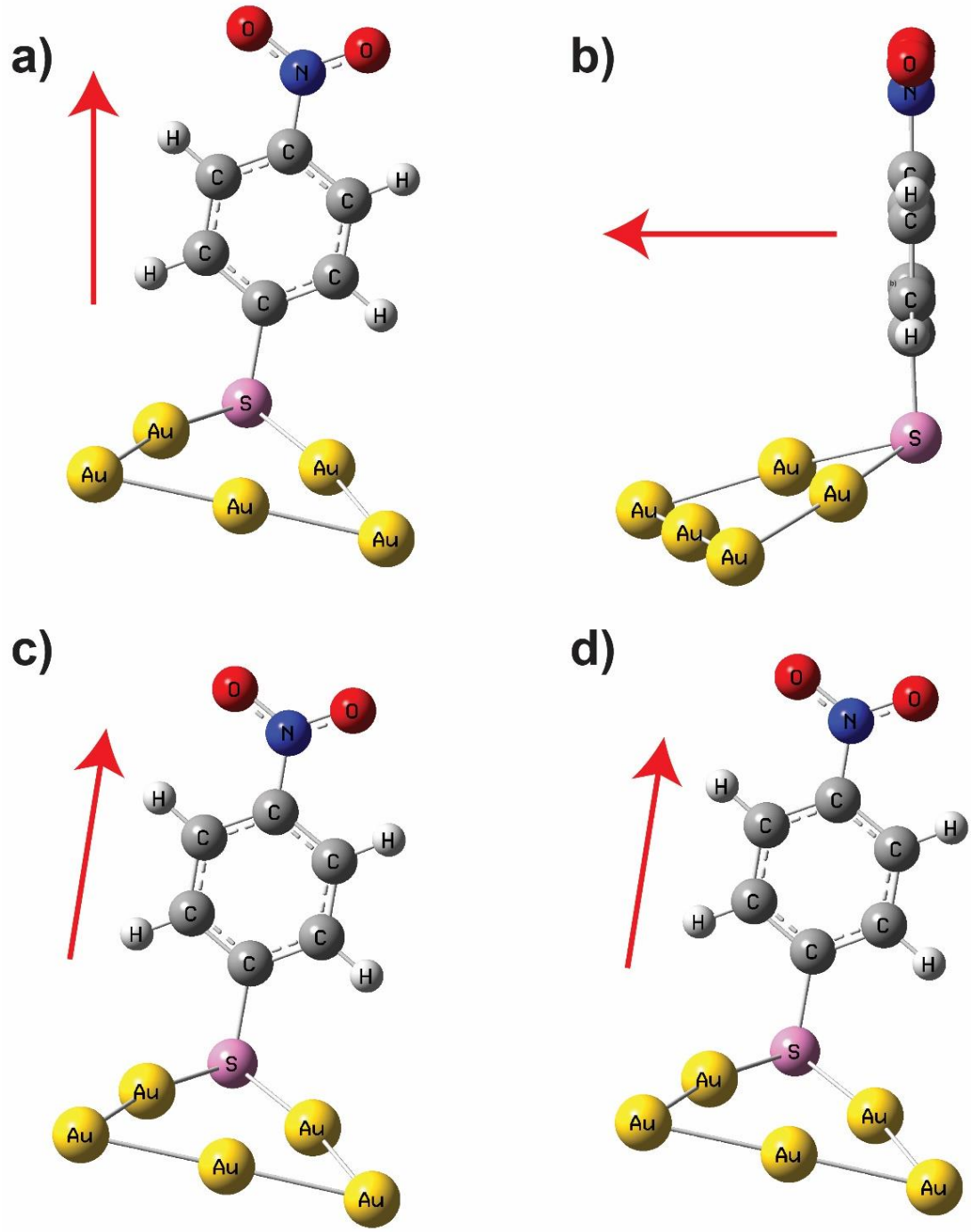

Figure 4.8: The dipole derivative unit vectors for the aromatic ring a) 9a C-H IP bend (Wilson number = 9a), b) C-H OOP bend (5), c) C-C ring breathing mode (1) and d) C-N IP stretch.

Figure 4.9 shows the effect of electrochemical potential on a) the intensity and b) the Raman shift of the C-N stretching vibration at 1339 cm^{-1}, while Figure 4.10 shows variations in the intensity of the C-H IP and OOP bands at 1181 cm^{-1} and 741 cm^{-1}, respectively. The EC-SERS spectra have been previously shown in Figure 4.6.

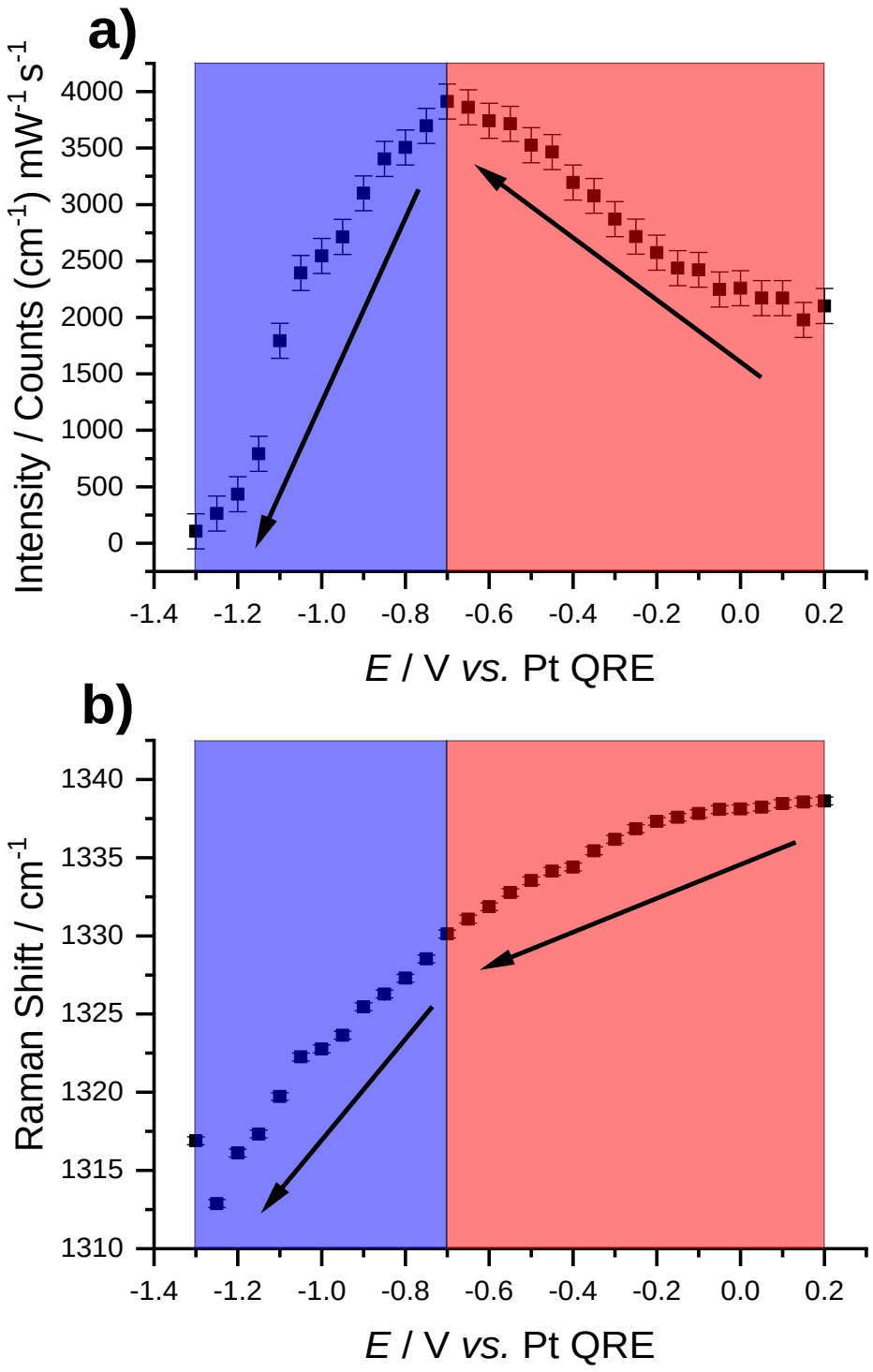

Figure 4.9: The a) normalised intensity and b) Raman shift of the PNTP C-N IP stretching vibration with respect to potential. The red region is at potentials positive of PNTP reduction, the blue region is at potentials negative of PNTP reduction.

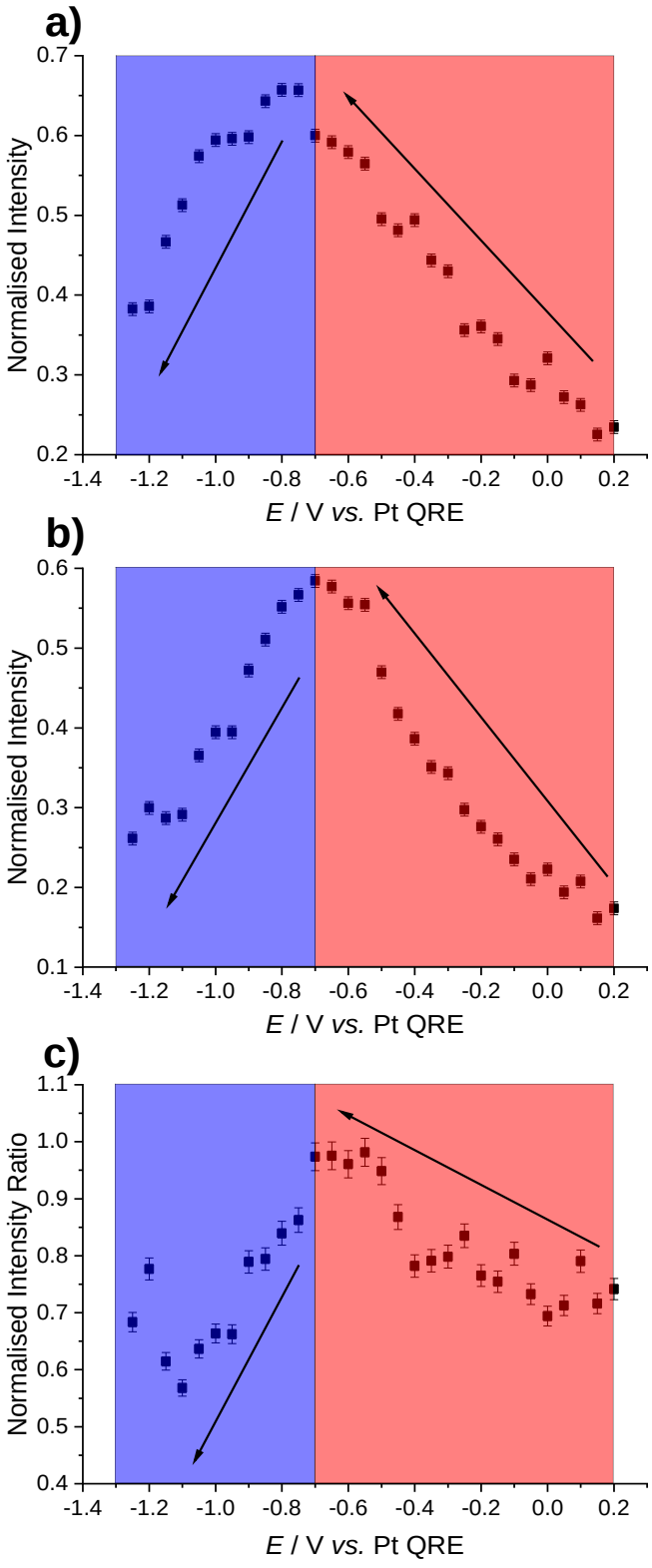

Figure 4.10: The normalised intensity of the PNTP C-H a) IP vibration, b) OOP vibration and c) the OOP:IP ratio. The red region is at potentials positive of PNTP reduction, the blue region is at potentials negative of PNTP reduction.

There are two clear regions in the intensities of all three vibrational modes, from 0.20 V to -0.70 V, which is at potentials above PNTP reduction (red area), and from -0.70 to -1.30 V, the potentials where the reduction occurs (blue area). Positive of the reduction potential, as the potential was moved negative, the intensity of the three modes and the C-H OOP:IP ratio increased. Thus, the IP vibrations both moved to a more perpendicular orientation with respect to the surface, via a decrease in θ, while the OOP vibration also moved to a more perpendicular orientation, via a decrease in χ. Similarly, the Stark shift for the C-N stretching vibration increased in this region, indicating the vibration became more aligned with the electric field, again revealing a decrease in θ. At the reduction potentials, all the vibrational intensities fell as the PNTP concentration on the surface decreased. However, the Stark shift of C-N continued to rise and the C-H OOP:IP ratio also decreased, revealing that even as PNTP was reduced, both θ and χ continued to decrease. These orientation changes are shown in Figure 4.11.

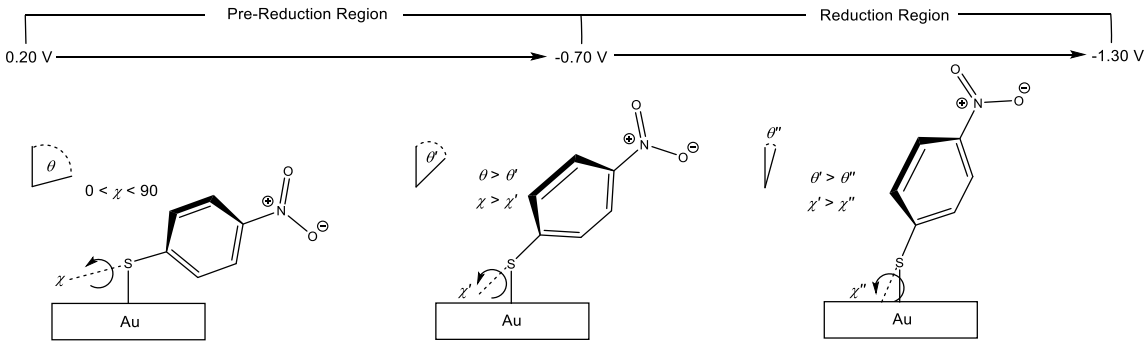

Figure 4.11: Potential dependence of the orientation of PNTP at pre-reduction and during electroreduction, showing a continual decrease in θ and χ as the potential was moved negative.

The potential dependence for PNTP reported here displays the relative effects of the interactions of both the aromatic ring and nitro group with the electrode surface. This is a similar interaction to that displayed in the literature and in Chapter 3 and is attributed to the interaction between the dipole moment of the nitrile group and the electrode surface [57,58]. Both the nitro and nitrile functional groups have a similar dipole magnitude and therefore the same interaction can be used to explain PNTP's behaviour here [59,60]. In addition, the influence of the aromatic ring-surface interaction reported in Chapter 3 and in early SERS studies [61,62] is also present here with PNTP. This interaction

can be probed by investigating the width of the PNTP ring breathing mode (Wilson number = 1), which is shown in Figure 4.12. At more negative potentials the width increases, indicating increasing surface-ring π interactions and a decrease in χ. The errors in the intensity, Raman shift and peak width for PNTP were the same as those used for Chapter 3 and indicate that the changes in these three parameters shown in Figures 4.9, 4.10 and 4.11 are outside of experimental error and can be attributed to the effect of the applied potential.

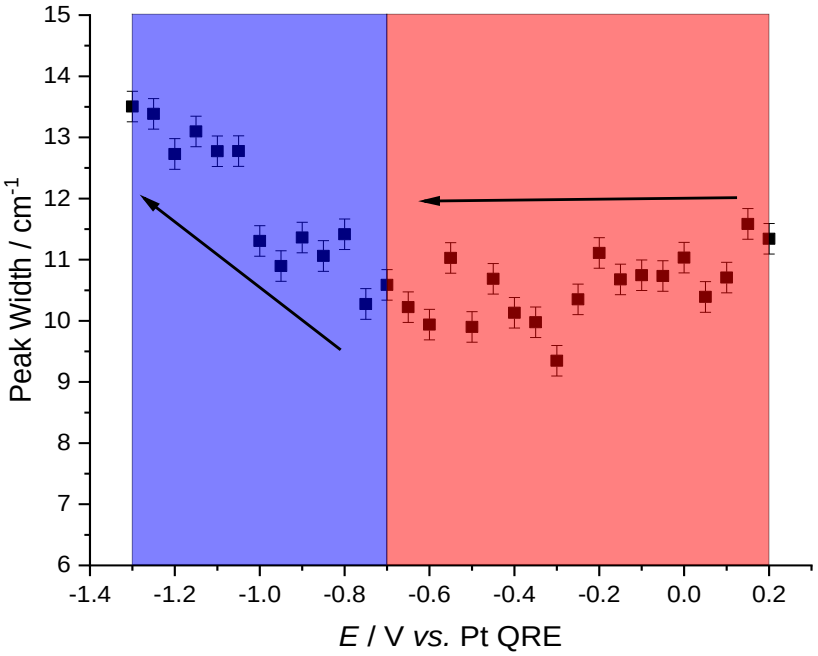

Figure 4.12: The peak width of the IP C-C stretching vibration (Wilson number = 1) *vs.* electrochemical potential for PNTP. The red region is at potentials above PNTP reduction, the blue region is at the reduction potentials.

4.2 *p*-aminothiophenol electrooxidation

The experimentally obtained SERS and DFT calculated Raman spectra of PATP are shown in Figure 4.13, with the optimised structure on an Au_5 cluster shown inset. Much like PNTP, the good agreement between the two spectra gives confidence that the subsequent DFT spectra of the oxidation products will be accurate. A laser power of 480 mW cm^{-2} was used to acquire the SERS spectra and additional peaks appeared (labelled with green stars) at 1145, 1383 and 1419 cm^{-1} that can be assigned to photochemically produced DMAB [44]. Reducing the laser power resulted in a significant reduction in

signal intensity and made species identification difficult due to the increased spectral noise. Therefore, due to the peaks for DMAB being small this larger laser power was used for the SERS acquisitions below.

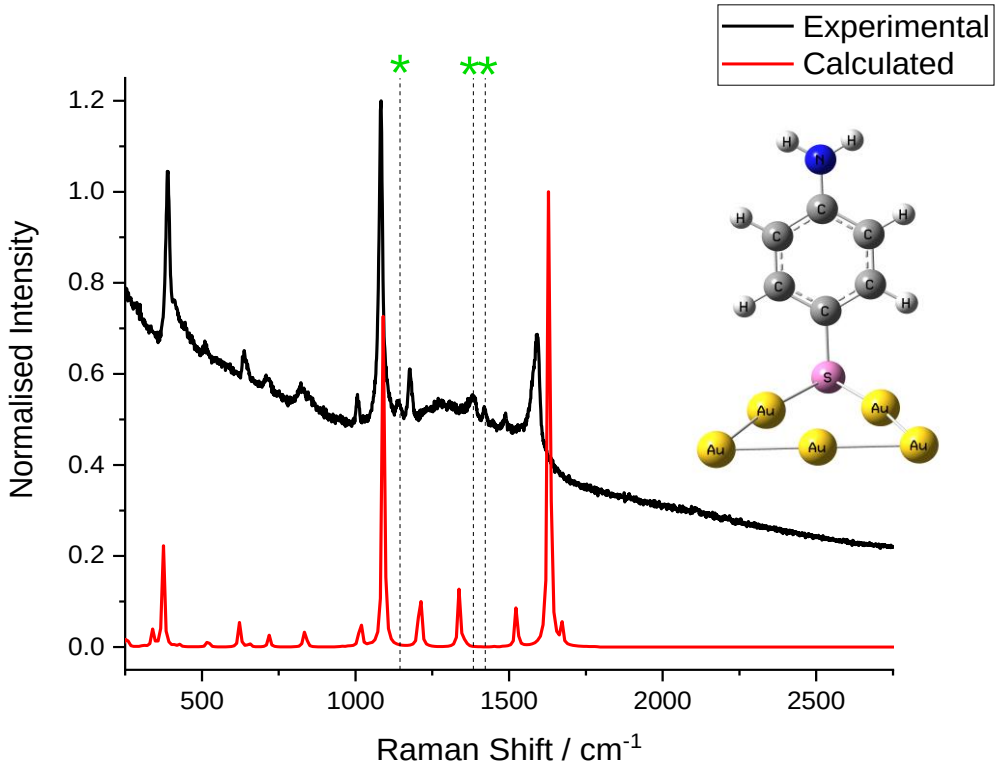

Figure 4.13: Experimental SERS and DFT calculated Raman spectra of a PATP SAM with, inset, the optimised structure. The SERS spectrum is of a PATP SAM adsorbed on an Au SSV substrate in 0.1 M KOH at the open circuit potential. The green starred peaks correspond to photochemically produced DMAB and the spectra are offset for clarity.

4.2.1 PATP electrooxidation in acidic media

From Figure 4.2 the initial PATP oxidation products in acidic media are the N-C4 coupled species NPQDI and NPQDA. In addition, a second set of products are also proposed via a hydrolysis reaction to the redox couple NPQMI and NPQMA. The DFT calculated Raman spectra and the optimised structures used for these species are shown in Figure 4.14.

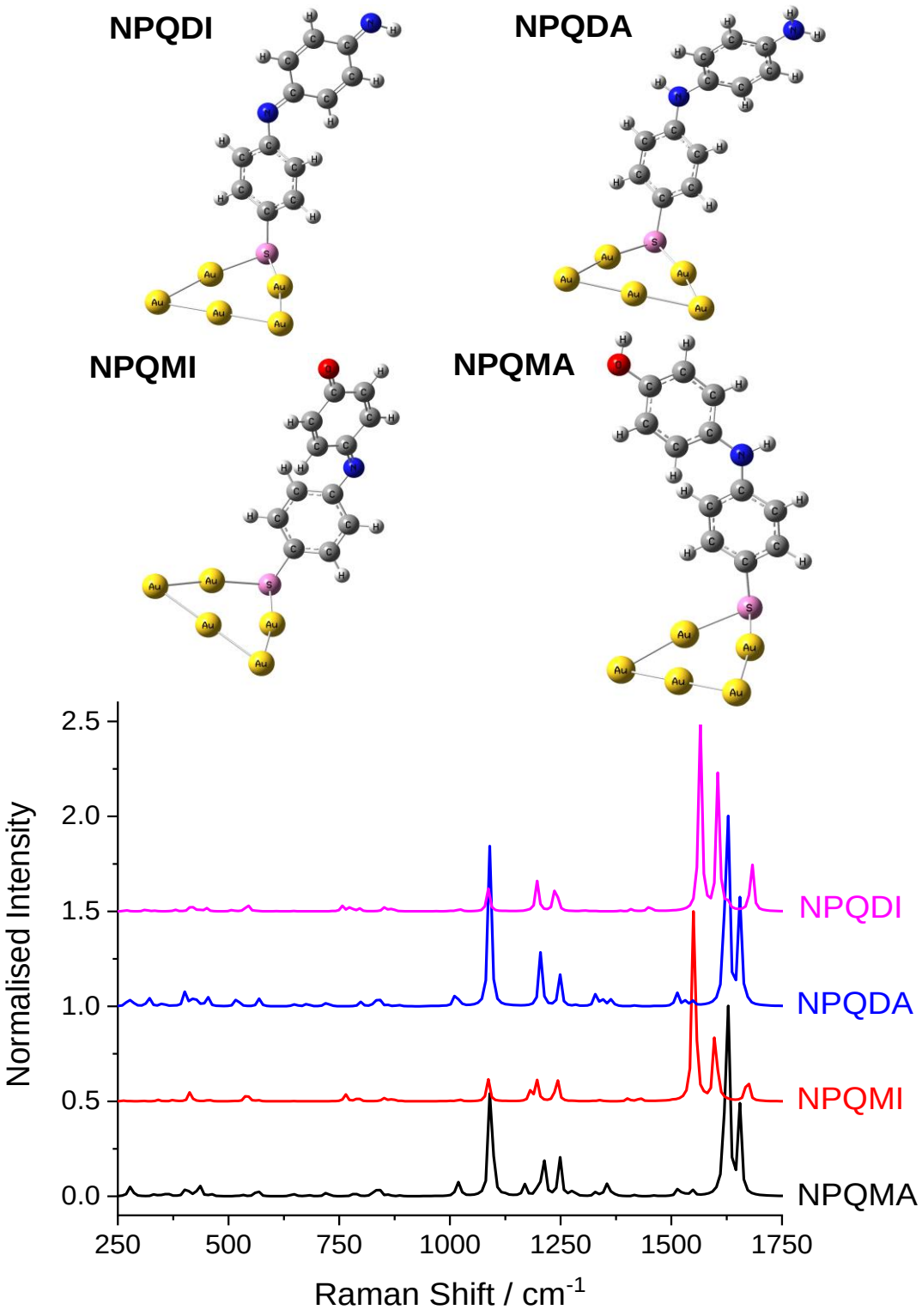

Figure 4.14: DFT optimised structures of the PATP oxidation species in acidic media adsorbed on Au_5 clusters and their calculated Raman spectra. Spectra are normalised to the largest peak in each spectra and offset for clarity.

It is apparent that there are clear spectral differences between the reactant PATP and all the possible products, most notably with 2 intense peaks for NPQDA and NPQMA and 3 intense peaks for NPQDI and NPQMI around

1600 cm^{-1}. Full DFT and SERS vibrational assignments of these species are available in Appendix C.

A CV of a PATP SAM on an Au SSV substrate, in 0.1 M $HClO_4$ is shown in Figure 4.15. In the first scan there is a large oxidation peak with an onset potential of 0.20 V, labelled X, that does not return on subsequent scans, indicating an irreversible process previously attributed to PATP oxidation to NPQDI [36]. Subsequent scans reveal a redox couple about 0.15 V (Y and Y') corresponding to both NPQDA/NPQDI and NPQMA/NQPMI, and a reduction peak that diminishes in intensity in subsequent scans at -0.10 V (Z) for NPQDA hydrolysis to NPQMA [36].

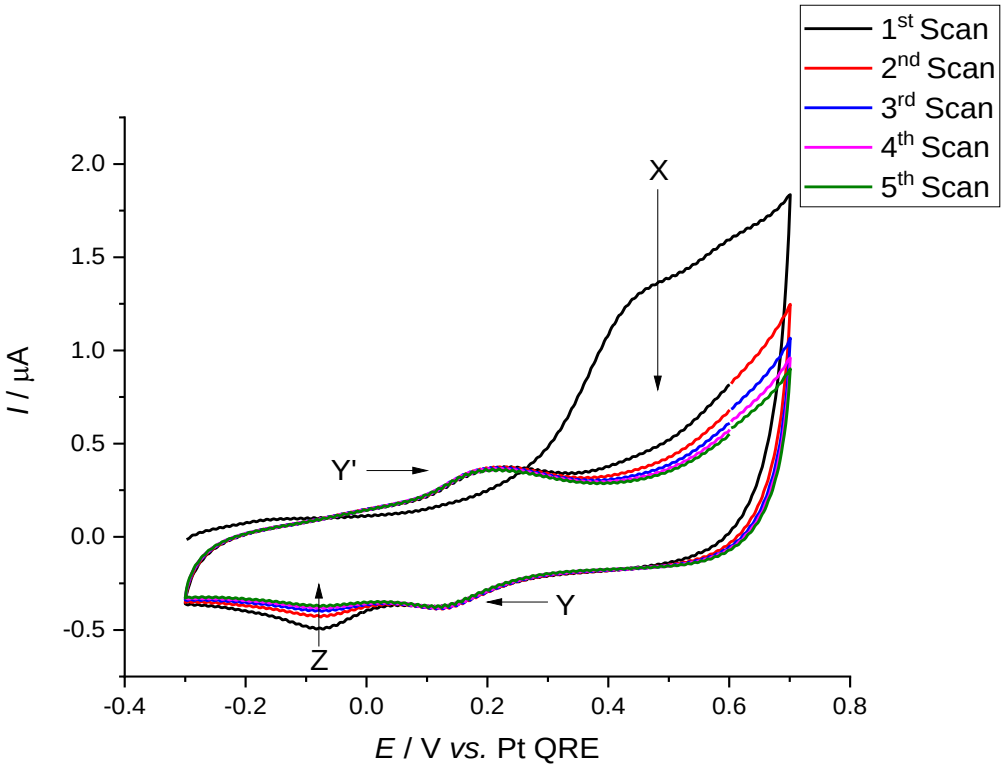

Figure 4.15: Cyclic voltammograms of a PATP SAM adsorbed on an Au SSV substrate in 0.1 M $HClO_4$. Scan rate = 5 mV s^{-1}.

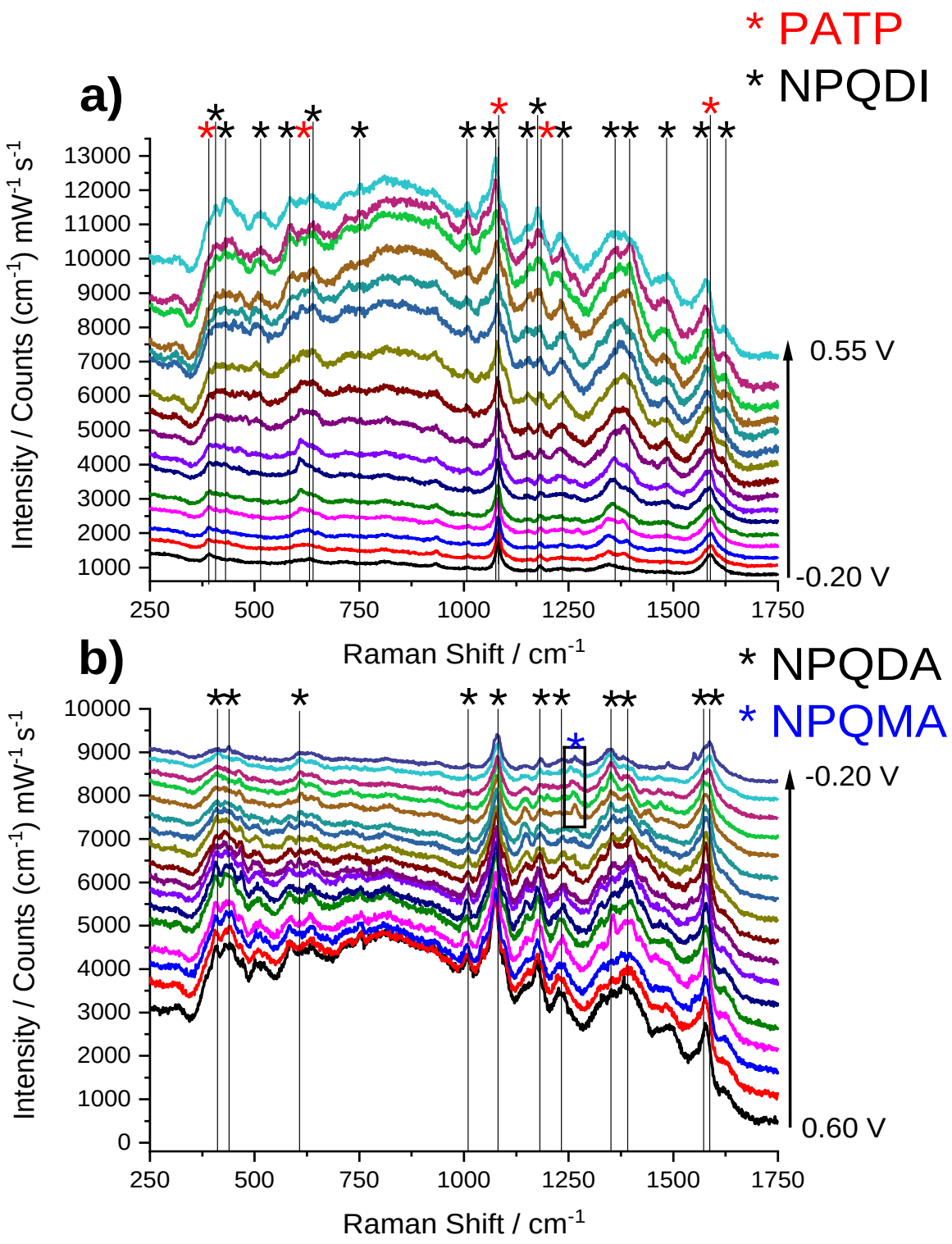

Figure 4.16: EC-SERS spectra of the first scan of a PATP SAM on Au SSV electrode, in 0.1 M $HClO_4$. a) The spectra on the positive scan with red starred peaks corresponding to PATP and black starred peaks to NPQDI. b) The spectra on the negative scan with black starred peaks corresponding to NPQDA and blue to NPQMA. Spectra offset for clarity.

Figure 4.16 shows the EC-SERS spectra of this system. In Figure 4.16a as the potential was moved from -0.20 V to 0.60 V peaks corresponding to PATP (marked with red stars) decreased in intensity. At 0.00 V, the onset potential of X, new peaks appeared and grew at 407, 431, 511, 584, 639, 751, 1007, 1076, 1151, 1176, 1235, 1322, 1361, 1396, 1484, 1581 and 1626 cm^{-1} (marked with black stars). When compared to the DFT spectra in Figure 4.14 these can be assigned to modes for NPQDI. In Figure 4.16b as the potential was moved negative, beginning at 0.15 V peaks (marked with black stars) grew at 411, 439, 607, 1010, 1081, 1181, 1351, 1391, 1573 and 1587 cm^{-1} and can be assigned to reduced species NPQDA. In addition, at potentials more negative of 0.00 V two additional peaks appeared at 1264 cm^{-1} and 1447 cm^{-1} (boxed and marked with a blue star). These peaks are not present in the DFT spectra of NPQDA, NPQDI or PATP but can be assigned to a C-O stretching vibration (ν_{C-O}) at 1273 cm^{-1} and a C-C, C-O and O-H bending vibration ($\delta_{C-C} + \delta_{C-H} + \delta_{O-H}$) at 1459 cm^{-1} in the DFT calculated Raman spectra of NPQMA. The growth of these two peaks matches the potential of the hydrolysis peak Z in Figure 4.15. Figure 4.17 shows the EC-SERS spectra of a second scan. In Figure 4.17a as the potential is moved positive very similar peaks appear as in Figure 4.16a and therefore can be initially assigned to NPQDI. However, due to the presence of NPQMA in Figure 4.16b and the similarity of the DFT calculated Raman spectra between NPQMI and NPQDI (Figure 4.14) these peaks are assigned to NPQMI. In Figure 4.17b the same peaks (marked in black) as in Figure 4.16b increased in intensity and the characteristic vibrations at 1264 cm^{-1} and 1447 cm^{-1} returned, indicating that NPQMA was again present on the electrode surface.

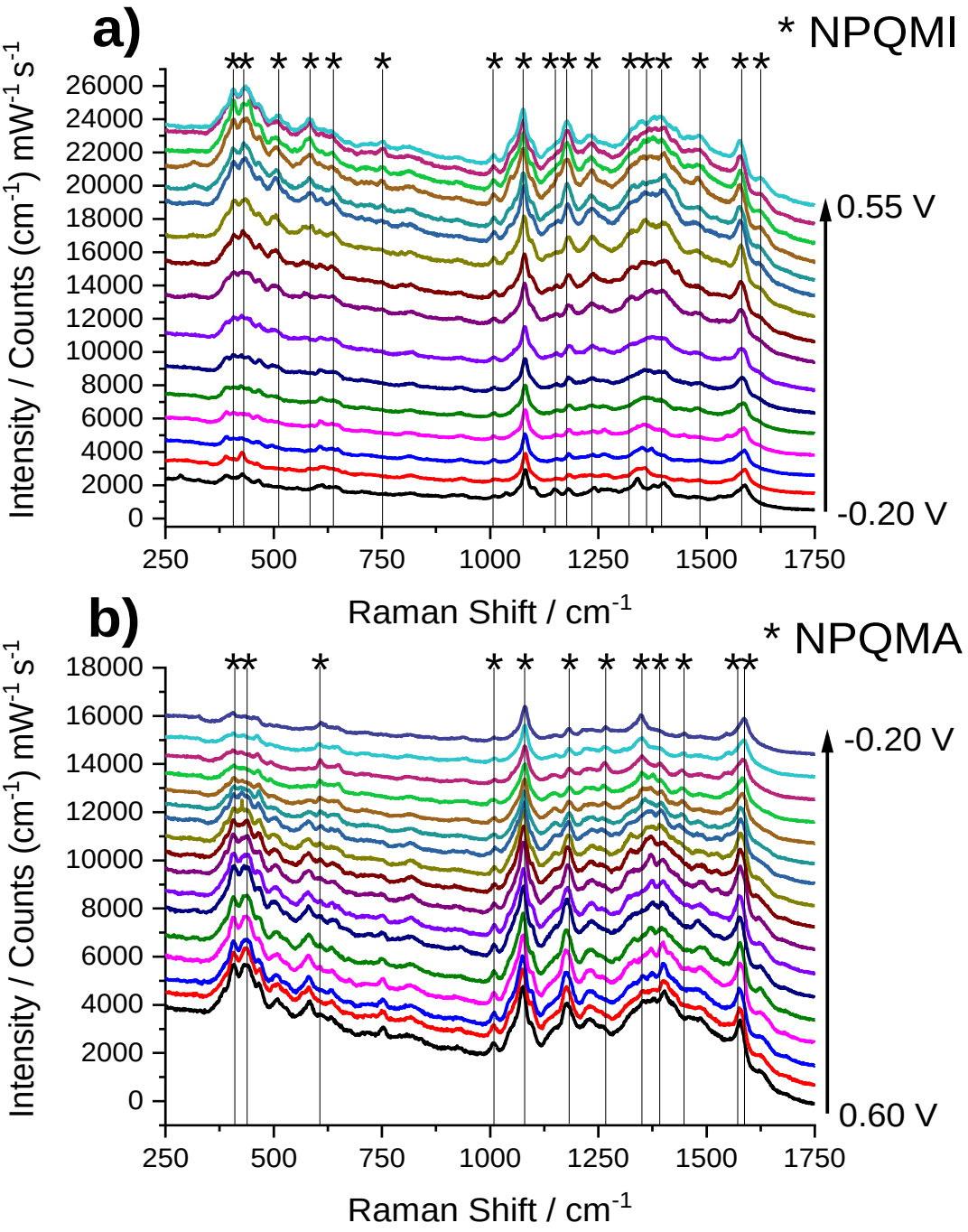

Figure 4.17: EC-SERS spectra of the second scan of a PATP SAM on Au SSV electrode, in 0.1 M $HClO_4$. a) The spectra on the positive scan with black starred peaks corresponding to NPQDI. b) The spectra on the negative scan with black starred peaks corresponding to NPQMA. Spectra offset for clarity.

4.2.2 PATP electrooxidation in alkaline media

Figure 4.18 shows the DFT optimised structure and calculated Raman spectra of the proposed PATP oxidation products in alkaline solution. When compared to the spectra for PATP (Figure 4.13) DMAB has strong distinguishable peaks at 1168, 1417 and 1472 cm^{-1}, but DMHAB and PATP are very similar. However, the most noticeable differences are that DMHAB has two peaks at 451 and 470 cm^{-1} whereas PATP only has one at 373 cm^{-1}. In addition, DMHAB has two peaks at 1187 cm^{-1} and 1201 cm^{-1}, and 1508 cm^{-1} and 1523 cm^{-1}, whereas PATP only has single peaks at 1090 cm^{-1} and 1523 cm^{-1}. Full DFT and SERS spectra vibrational characterisation for DMAB and DMHAB are provided in Appendix C.

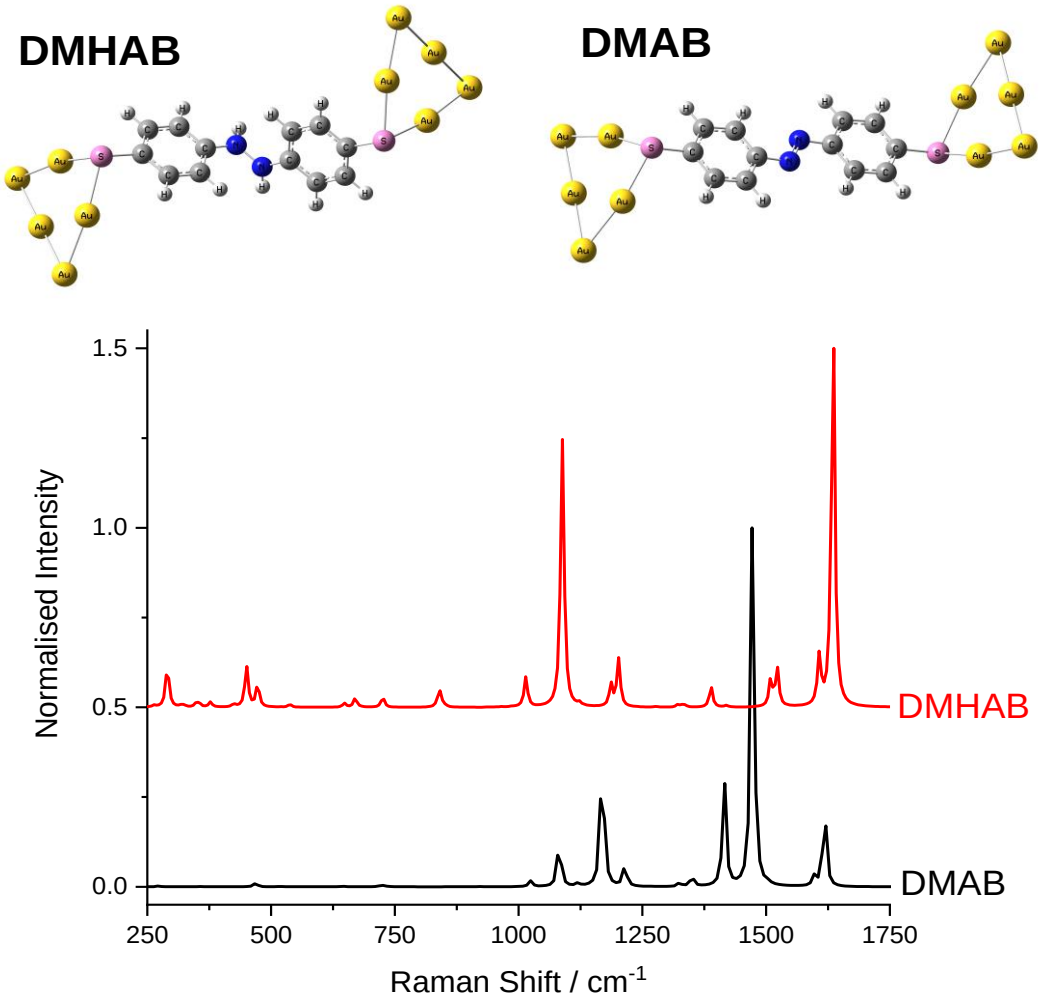

Figure 4,18: DFT optimised structures of the PATP oxidation species in basic media adsorbed on Au_5 clusters and their calculated spectra. Spectra are normalised to the largest peak and offset for clarity.

Figure 4.19 shows the CV of a PATP SAM on an Au SSV substrate, in 0.1 M KOH. As the potential is swept from -0.60 V to 0.20 V *vs.* Pt QRE there is an oxidation peak at 0.15 V, labelled A. As the potential is swept back from 0.20 to -0.60 V there is a reduction peak at -0.35 V, labelled A'.

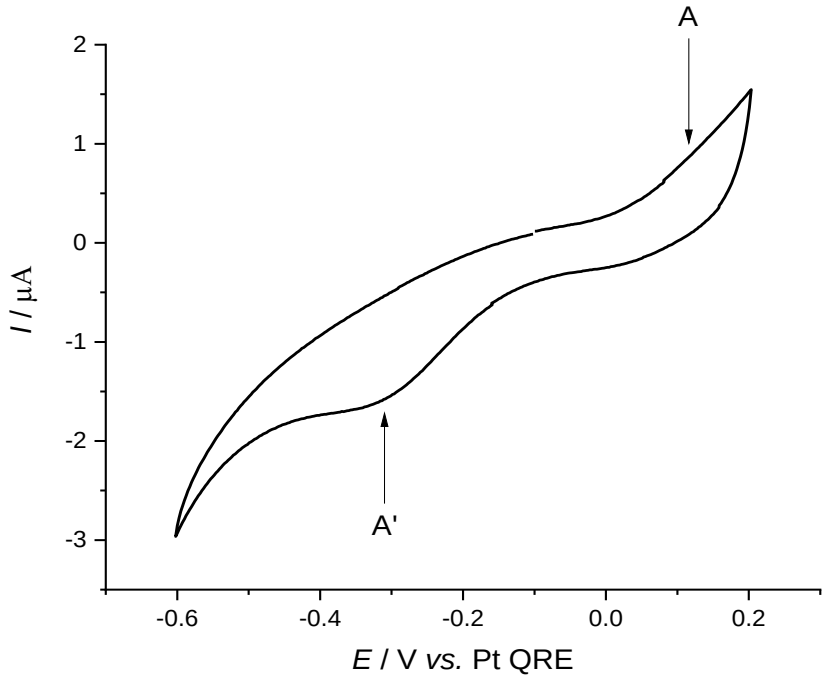

Figure 4.19: Cyclic voltammogram of a PATP monolayer adsorbed on an Au SSV substrate in 0.1 M KOH. Scan rate = 5 mV s^{-1}.

Figure 4.20 shows EC-SERS spectra of a PATP SAM in 0.1 M KOH. In Figure 4.20a when the potential was moved from -0.60 V to 0.15 V peaks that were characteristic of PATP (marked in red) at 391, 641, 1083, 1183 and 1590 cm^{-1} all decreased in intensity. In addition, peaks at 407, 441, 465, 529, 641, 718, 750, 1078, 1142, 1173, 1305, 1390, 1436, 1574 cm^{-1} (marked in black) all appeared and increased in intensity. When compared to the DFT spectra in Figure 4.18, these peaks can be assigned to DMAB. The most obvious peaks were those at 407, 529, 1390 and 1420 cm^{-1}. These are a C-C bending vibration (δ_{C-C}, 16a + δ_{C-C}, 10b), a C-C bending and C-H bending vibration (δ_{C-C}, 19b + δ_{C-C}, 18b), and an N=N stretching vibration ($\nu_{N=N}$), respectively. These peaks are present even at -0.60 V due to the photochemical oxidation of PATP and therefore their growth is attributed to both the electrochemical and photochemical pathways.

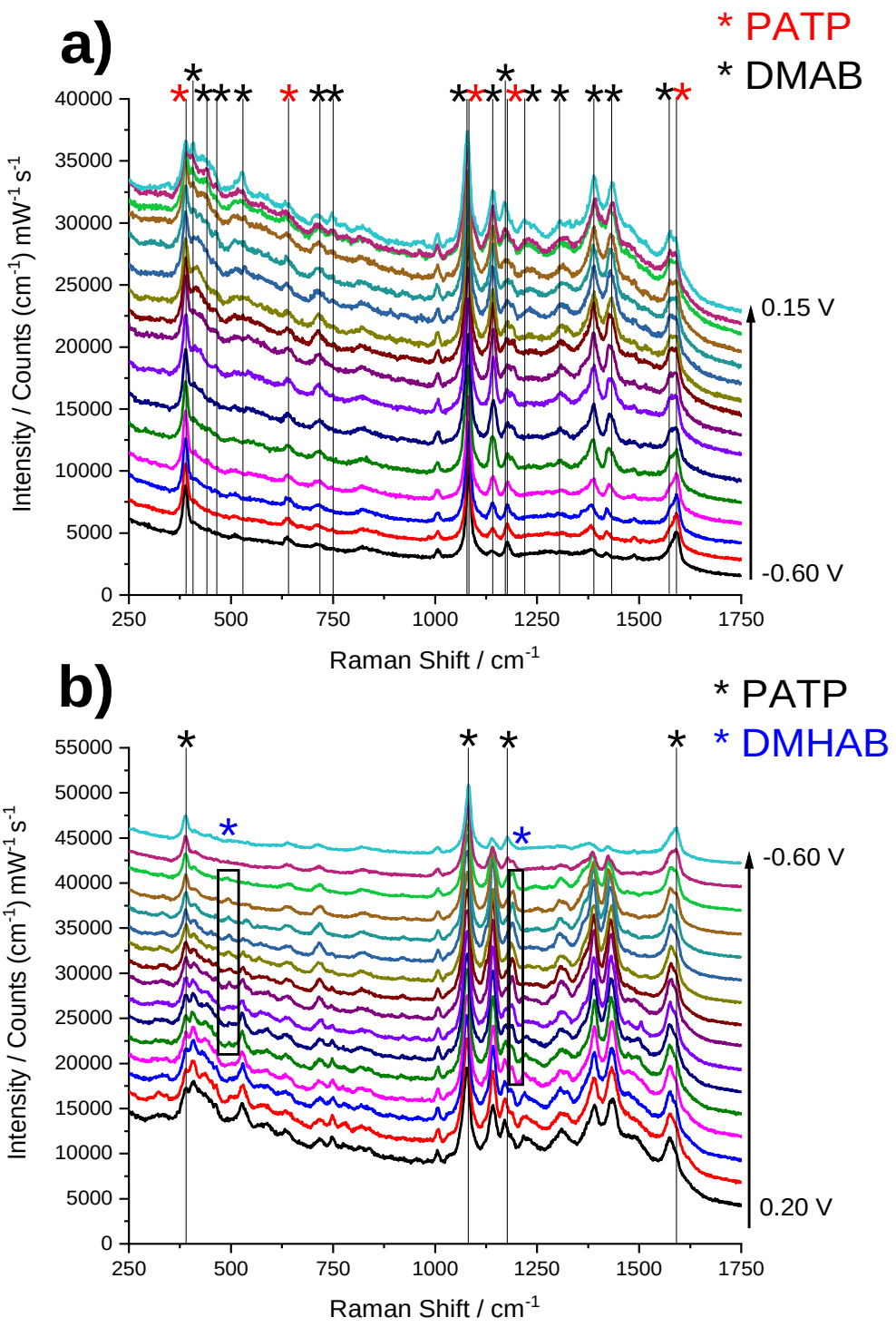

Figure 4.20: EC-SERS spectra of a PATP SAM on Au SSV electrode, in 0.1 M KOH at potentials. a) The spectra on the positive scan from -0.60 V to 0.15 V where red starred peaks are those assigned to PATP and black starred peaks correspond to DMAB. b) The spectra on the negative scan, from 0.20 V to -0.60 V where black starred peaks are those assigned to PATP and blue starred peaks are those assigned to DMDAB. Spectra offset for clarity.

In Figure 4.20b peaks for PATP (marked in black) reappeared at 390, 1081, 1176 and 1590 cm^{-1} and their intensity increased as the potential was moved negative. However, between the potentials of 0.00 V and -0.50 V two peaks at 494 and 1190 cm^{-1} (blue stars) increased in intensity to maxima at -0.35 V, before disappearing by -0.50 V. These peaks were assigned to the N-H bending vibration (δ_{N-H}) at 473 cm^{-1} and C-H bending and N-N stretching vibration (δ_{C-H}, 9a + $\nu_{N=N}$) at 1187 cm^{-1} in the DMHAB DFT spectra. The presence of these peaks indicates that A' in Figure 4.19 corresponds to DMAB reduction to DMDAB and then finally back PATP. The laser position was then moved and the potential stepped back to 0.20 V (Figure 4.21), resulting in the same peaks for DMAB reappearing (black stars). This confirms A in the CV (Figure 4.19) is the electrochemical oxidation of PATP to DMAB.

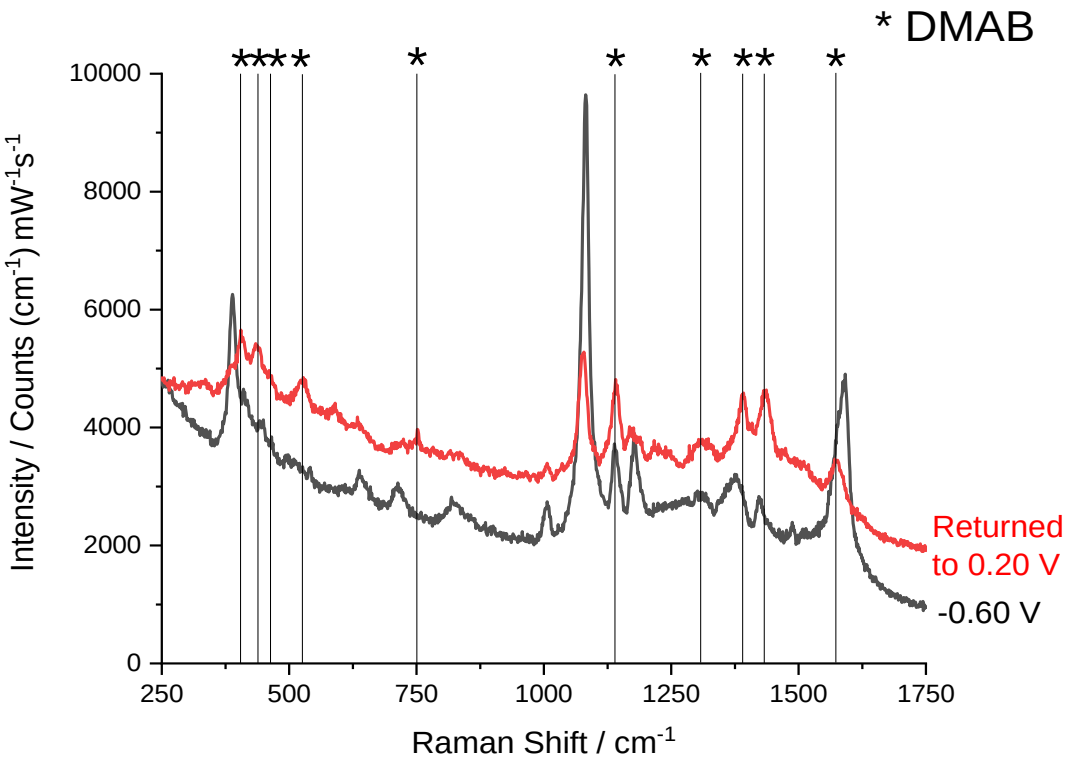

Figure 4.21: EC-SERS spectra of a PATP SAM on Au SSV electrode, in 0.1 M KOH, where the potential is stepped directly from -0.60 V to 0.20 V. Black stars indicate peaks corresponding to electrochemically produced DMAB. Spectra offset for clarity.

4.3 Summary

In this chapter, the mechanism of PNTP electroreduction to PATP has been investigated using *in situ* potential dependent SERS, while avoiding the photocatalytic formation of the dimer product DMAB. The vibrations of PNTP, its electroreduction products and any suspected intermediates were characterised using a combination of experimental and DFT calculated Raman spectra. SERS peaks were observed for the electrochemical formation of the intermediates PNSTP and DMAB, indicating that both the direct unimolecular and dimerisation pathways were active.

In addition, by carefully analysing the PNTP SERS intensities of both IP and OOP modes of the aromatic ring, and the intensity and peak position of the IP nitro group vibration, orientation changes at potentials above and during electroreduction were revealed. As the potential was moved negative, PNTP oriented to be more perpendicular to the surface, via a decrease in θ, driven by an electrostatic interaction of the nitro group and surface. The plane of the aromatic ring also twisted with a reducing χ, resulting greater ring-surface π interactions and an increase in the peak width of the C-C ring breathing mode. Both these orientation changes continued during reduction.

Furthermore, PATP electrooxidation in both acidic and alkaline electrolytes was followed using SERS. In acid, by comparison to DFT calculated Raman spectra of proposed products, SERS spectra corresponding to electrochemically generated NPQDI, NPQDA, NPQMI and NPQMA were characterised, providing evidence of an N-C4 coupling pathway and additional hydrolysis reaction. In base, DMAB formation via an N-N coupling pathway and the corresponding reduction back to PATP via the intermediate DMHAB were also observed.

4.4 References

[1] T. Hartman, C.S. Wondergem, N. Kumar, A. Van Den Berg, B.M. Weckhuysen, Surface- and Tip-Enhanced Raman Spectroscopy in Catalysis, J. Phys. Chem. Lett. 7 (2016) 1570–1584. doi:10.1021/acs.jpclett.6b00147.

[2] L.J. Wan, M. Terashima, H. Noda, M. Osawa, Molecular Orientation and Ordered Structure of Benzenethiol Adsorbed on Gold(111), J. Phys. Chem. B. 104 (2000) 3563–3569. doi:10.1021/jp993328r.

[3] B. Sharma, R.R. Frontiera, A.I. Henry, E. Ringe, R.P. Van Duyne, SERS: Materials, applications, and the future, Mater. Today. 15 (2012) 16–25. doi:10.1016/s1369-7021(12)70017-2.

[4] T. Matsue, N. Matsuda, K. Yoshii, M. Osawa, I. Uchida, K. Ataka, Surface-Enhanced Infrared and Raman Studies of Electrochemical Reduction of Self-Assembled Monolayers Formed from p-Nitrothiophenol at Silver, Chem. Lett. 21 (2006) 1385–1388. doi:10.1246/cl.1992.1385.

[5] J. Zhou, T. Zhang, H. Li, Y. Cui, J. Hu, Citrate-stabilized large Au nanoparticles: Seed-mediated synthesis and their size-optimized enhanced Raman at Pd overlayers, Chem. Phys. Lett. 628 (2015) 91–95. doi:10.1016/j.cplett.2015.03.059.

[6] E.M. Van Schrojenstein Lantman, O.L.J. Gijzeman, A.J.G. Mank, B.M. Weckhuysen, Investigation of the kinetics of a surface photocatalytic reaction in two dimensions with surface-enhanced Raman scattering, ChemCatChem. 6 (2014) 3342–3346. doi:10.1002/cctc.201402647.

[7] M. Sun, Z. Zhang, H. Zheng, H. Xu, In-situ plasmon-driven chemical reactions revealed by high vacuum tip-enhanced Raman spectroscopy, Sci. Rep. 2 (2012) 647. doi:10.1038/srep00647.

[8] M. Futamata, C. Nishihara, N. Goutev, Electrochemical reduction of p-nitrothiophenol-self-assembled monolayer films on Au(1 1 1) surface and coadsorption of anions and water molecules, in: Surf. Sci., 2002: pp. 241–248. doi:10.1016/S0039-6028(02)01636-9.

[9] H.K. Choi, W.H. Park, C.G. Park, H.H. Shin, K.S. Lee, Z.H. Kim, Metal-Catalyzed Chemical Reaction of Single Molecules Directly Probed by Vibrational Spectroscopy, J. Am. Chem. Soc. 138 (2016) 4673–4684. doi:10.1021/jacs.6b01865.

[10] L. Li, Q. Cui, M. Bargheer, A. Yashchenok, H. Möhwald, Mechanistic study on reduction reaction of nitro compounds catalyzed by gold nanoparticles using in situ SERS monitoring, Colloids Surfaces A

Physicochem. Eng. Asp. 470 (2015) 108–113. doi:10.1016/j.colsurfa.2015.01.075.

[11] X.J. Chen, G. Cabello, D.Y. Wu, Z.Q. Tian, Surface-enhanced Raman spectroscopy toward application in plasmonic photocatalysis on metal nanostructures, J. Photochem. Photobiol. C Photochem. Rev. 21 (2014) 54–80. doi:10.1016/j.jphotochemrev.2014.10.003.

[12] T. Touzalin, S. Joiret, E. Maisonhaute, I.T. Lucas, Complex Electron Transfer Pathway at a Microelectrode Captured by in Situ Nanospectroscopy, Anal. Chem. 89 (2017) 8974–8980. doi:10.1021/acs.analchem.7b01542.

[13] T. Zhu, H.Z. Yu, Y.C. Wang, Z.F. Liu, Irreversible adsorption and reduction of p-nitrothio-phenol monolayers on gold: Electrochemical in situ surface enhanced Raman spectroscopy, Mol. Cryst. Liq. Cryst. Sci. Technol. Sect. A Mol. Cryst. Liq. Cryst. 337 (1999) 241–244. doi:10.1080/10587259908023422.

[14] M. Futamata, Surface-plasmon-polariton-enhanced Raman scattering from self-assembled monolayers of p-nitrothiophenol and p-aminothiophenol on silver, J. Phys. Chem. 99 (1995) 11901–11908. doi:10.1021/j100031a018.

[15] L. Xia, C. Ma, J. Wang, S. Wu, Y. Liu, Q. Zhang, P. Song, A new strategy for effective distance regulation of the surface plasmon assisted coupling reaction of: P -nitrothiophenol to p, p ′-dimercaptoazobenzene, Chem. Commun. 53 (2017) 9582–9585. doi:10.1039/c7cc04780k.

[16] Q. Zhou, X. Li, Q. Fan, X. Zhang, J. Zheng, Charge transfer between metal nanoparticles interconnected with a functionalized molecule probed by surface-enhanced Raman spectroscopy, Angew. Chemie - Int. Ed. 45 (2006) 3970–3973. doi:10.1002/anie.200504419.

[17] P. Xu, J. Chu, H.L. Wang, X. Han, L. Kang, X. He, J. Xiong, In Situ Surface-Enhanced Raman Spectroscopy Study of Plasmon-Driven Catalytic Reactions of 4-Nitrothiophenol under a Controlled Atmosphere, ChemCatChem. 7 (2015) 1004–1010. doi:10.1002/cctc.201403032.

[18] L. Kang, P. Xu, B. Zhang, H. Tsai, X. Han, H.L. Wang, Laser wavelength-

and power-dependent plasmon-driven chemical reactions monitored using single particle surface enhanced Raman spectroscopy, Chem. Commun. 49 (2013) 3389–3391. doi:10.1039/c3cc40732b.

[19] E.M. Van Schrojenstein Lantman, T. Deckert-Gaudig, A.J.G. Mank, V. Deckert, B.M. Weckhuysen, Catalytic processes monitored at the nanoscale with tip-enhanced Raman spectroscopy, Nat. Nanotechnol. 7 (2012) 583–586. doi:10.1038/nnano.2012.131.

[20] D.A. Nelson, Z.D. Schultz, Influence of Optically Rectified Electric Fields on the Plasmonic Photocatalysis of 4-Nitrothiophenol and 4-Aminothiophenol to 4,4-Dimercaptoazobenzene, J. Phys. Chem. C. 122 (2018) 8581–8588. doi:10.1021/acs.jpcc.8b00662.

[21] D. Natelson, D.R. Ward, J.W. Ciszek, P. Nordlander, J.M. Tour, Y. Wu, N.J. Halas, Simultaneous Measurements of Electronic Conduction and Raman Response in Molecular Junctions, Nano Lett. 8 (2008) 919–924. doi:10.1021/nl073346h.

[22] L. Bin Zhao, J.L. Chen, M. Zhang, D.Y. Wu, Z.Q. Tian, Theoretical study on electroreduction of p-nitrothiophenol on silver and gold electrode surfaces, J. Phys. Chem. C. 119 (2015) 4949–4958. doi:10.1021/jp512957c.

[23] M. Jo, K. Matuso, M. Yamaguichi, S. Yoshino, K. Tanaka, K. Kawaguchi, A. Nakanishi, H. Shiota, Syntheses and antimicrobial activities of five-membered heterocycles having a phenylazo substituent., Chem. Pharm. Bull. (Tokyo). 32 (2011) 3291–3298. doi:10.1248/cpb.32.3291.

[24] A.K. Singh, J. Das, N. Majumdar, Novel bacteriorhodopsin analogues based on azo chromophores, J. Am. Chem. Soc. 118 (1996) 6185–6191. doi:10.1021/ja954286x.

[25] A.A. Fadda, H.A. Etman, F.A. Amer, M. Barghout, K.S. Mohamed, Azo disperse dyes for synthetic fibres. I: 2- Methyl- and 2-phenylquinazolone derivatives, J. Chem. Technol. Biotechnol. 61 (1994) 343–349. doi:10.1002/jctb.280610410.

[26] R.S. Downing, P.J. Kunkeler, H. Van Bekkum, Catalytic syntheses of aromatic amines, Catal. Today. 37 (1997) 121–136. doi:10.1016/S0920-

5861(97)00005-9.

[27] A. Corma, P. Serna, Chemoselective hydrogenation of nitro compounds with supported gold catalysts, Science. 313 (2006) 332–334. doi:10.1126/science.1128383.

[28] H.U. Blaser, A golden boost to an old reaction, Science. 313 (2006) 312–313. doi:10.1126/science.1131574.

[29] A. Corma, P. Concepción, P. Serna, A different reaction pathway for the reduction of aromatic nitro compounds on gold catalysts, Angew. Chemie - Int. Ed. 46 (2007) 7266–7269. doi:10.1002/anie.200700823.

[30] P. Gao, D. Gosztola, M.J. Weaver, Surface-enhanced Raman spectroscopy as a probe of electroorganic reaction pathways. 1. Processes involving adsorbed nitrobenzene, azobenzene, and related species, J. Phys. Chem. 92 (1988) 7122–7130. doi:10.1021/j100336a018.

[31] S. Schwamborn, L. Stoica, S. Neugebauer, T. Reda, H.L. Schmidt, W. Schuhmann, Local modulation of the redox state of p-nitrothiophenol self-assembled monolayers using the direct mode of scanning electrochemical microscopy, ChemPhysChem. 10 (2009) 1066–1070. doi:10.1002/cphc.200900118.

[32] H. Tsutsumi, S. Furumoto, M. Morita, Y. Matsuda, Electrochemical behavior of a 4-nitrothiophenol modified electrode prepared by the self-assembly method, J. Colloid Interface Sci. 171 (1995) 505–511. doi:10.1006/jcis.1995.1209.

[33] J.U. Nielsen, M.J. Esplandiu, D.M. Kolb, 4-nitrothiophenol SAM on Au(111) investigated by in situ STM, electrochemistry, and XPS, Langmuir. 17 (2001) 3454–3459. doi:10.1021/la001775o.

[34] L. Bin Zhao, M. Zhang, B. Ren, Z.Q. Tian, D.Y. Wu, Theoretical study on thermodynamic and spectroscopic properties of electro-oxidation of p-aminothiophenol on gold electrode surfaces, J. Phys. Chem. C. 118 (2014) 27113–27122. doi:10.1021/jp507987x.

[35] J. Lukkari, M. Meretoja, K. Kleemola, J. Kankare, T. Ollonqvist, Electrochemical Post-Self-Assembly Transformation of 4-

Aminothiophenol Monolayers on Gold Electrodes, Langmuir. 14 (2002) 1705–1715. doi:10.1021/la970931x.

[36] C.R. Raj, F. Kitamura, T. Ohsaka, Electrochemical and in situ FTIR spectroscopic investigation on the electrochemical transformation of 4-aminothiophenol on a gold electrode in neutral solution, Langmuir. 17 (2001) 7378–7386. doi:10.1021/la010746q.

[37] C. Jiang, J.M. Elliott, D.J. Cardin, S.C. Tsang, An electrochemical study of 4-aminothiophenol/Pt nanoparticle multilayers on gold electrodes, Langmuir. 25 (2009) 534–541. doi:10.1021/la802567a.

[38] Z. Zhang, D. Kinzel, V. Deckert, Photo-Induced or Plasmon-Induced Reaction: Investigation of the Light-Induced Azo-Coupling of Amino Groups, J. Phys. Chem. C. 120 (2016) 20978–20983. doi:10.1021/acs.jpcc.6b03233.

[39] L.S. Jiao, Z. Wang, L. Niu, J. Shen, T.Y. You, S.J. Dong, A. Ivaska, In situ electrochemical SERS studies on electrodeposition of aniline on 4-ATP/Au surface, J. Solid State Electrochem. 10 (2006) 886–893. doi:10.1007/s10008-005-0021-y.

[40] A. Blacha-Grzechnik, R. Turczyn, M. Burek, J. Zak, In situ Raman spectroscopic studies on potential-induced structural changes in polyaniline thin films synthesized via surface-initiated electropolymerization on covalently modified gold surface, Vib. Spectrosc. 71 (2014) 30–36. doi:10.1016/j.vibspec.2014.01.008.

[41] J. Hu, S. Chen, R.P. Johnson, X. Lin, Z. Yang, A.E. Russell, Surface-enhanced raman scattering on uniform Pd and Pt films: From ill-defined to structured surfaces, J. Phys. Chem. C. 117 (2013) 24843–24850. doi:10.1021/jp4081433.

[42] A. Merlen, M. Chaigneau, S. Coussan, Vibrational modes of aminothiophenol: a TERS and DFT study, Phys. Chem. Chem. Phys. 17 (2015) 19134–19138. doi:10.1039/c5cp01579k.

[43] M.R. Lopez-Ramirez, D. Aranda Ruiz, F.J. Avila Ferrer, S.P. Centeno, J.F. Arenas, J.C. Otero, J. Soto, Analysis of the Potential Dependent Surface-Enhanced Raman Scattering of p-Aminothiophenol on the Basis

of MS-CASPT2 Calculations, J. Phys. Chem. C. 120 (2016) 19322–19328. doi:10.1021/acs.jpcc.6b05891.

[44] H.P. Zhu, Y.F. Huang, G.K. Liu, Z.Q. Tian, D.Y. Wu, B. Ren, When the Signal Is Not from the Original Molecule To Be Detected: Chemical Transformation of para -Aminothiophenol on Ag during the SERS Measurement, J. Am. Chem. Soc. 132 (2010) 9244–9246. doi:10.1021/ja101107z.

[45] M.. Schneeweiss, D.. Kolb, V. Batz, H. Hagenström, D. Mandler, D. Kramer, Electrochemistry and structure of the isomers of aminothiophenol adsorbed on gold, J. Electroanal. Chem. 491 (2002) 55–68. doi:10.1016/s0022-0728(00)00294-1.

[46] V. Ganesh, R.R. Pandey, B.D. Malhotra, V. Lakshminarayanan, Electrochemical characterization of self-assembled monolayers (SAMs) of thiophenol and aminothiophenols on polycrystalline Au: Effects of potential cycling and mixed SAM formation, J. Electroanal. Chem. 619–620 (2008) 87–97. doi:10.1016/j.jelechem.2008.03.015.

[47] Y.F. Huang, D.Y. Wu, H.P. Zhu, L. Bin Zhao, G.K. Liu, B. Ren, Z.Q. Tian, Surface-enhanced Raman spectroscopic study of p-aminothiophenol, Phys. Chem. Chem. Phys. 14 (2012) 8485. doi:10.1039/c2cp40558j.

[48] Y. Yonezawa, H. Minamimoto, F. Nagasawa, M. Takase, S. Yasuda, K. Murakoshi, In-situ electrochemical surface-enhanced Raman scattering observation of molecules accelerating the hydrogen evolution reaction, J. Electroanal. Chem. 800 (2017) 7–12. doi:10.1016/j.jelechem.2017.04.049.

[49] I. Brand, J. Juhaniewicz-Debinska, L. Wickramasinghe, C.N. Verani, An: In situ spectroelectrochemical study on the orientation changes of an [FeiiiLN2O3] metallosurfactant deposited as LB Films on gold electrode surfaces, Dalt. Trans. 47 (2018) 14218–14226. doi:10.1039/c8dt00333e.

[50] I. Matulaitiene, Z. Kuodis, A. Matijoška, O. Eicher-Lorka, G. Niaura, SERS of the Positive Charge Bearing Pyridinium Ring Terminated Self-Assembled Monolayers: Structure and Bonding Spectral Markers, J. Phys. Chem. C. 119 (2015) 26481–26492. doi:10.1021/acs.jpcc.5b07687.

[51] Y. Chao, Q. Zhou, Y. Li, Y. Yan, Y. Wu, J. Zheng, Potential dependent surface-enhanced raman scattering of 4-mercaptopyridine on electrochemically roughened silver electrodes, J. Phys. Chem. C. 111 (2007) 16990–16995. doi:10.1021/jp0760051.

[52] M. Grunze, W. Eck, M. Zharnikov, S. Frey, B. Zeysing, V. Stadler, K. Heister, A. Terfort, Structure of Thioaromatic Self-Assembled Monolayers on Gold and Silver, Langmuir. 17 (2002) 2408–2415. doi:10.1021/la001540c.

[53] K.T. Carron, L.G. Hurley, Axial and azimuthal angle determination with surface-enhanced Raman spectroscopy: thiophenol on copper, silver, and gold metal surfaces, J. Phys. Chem. 95 (1991) 9979–9984. doi:10.1021/j100177a068.

[54] A.E. Russell, S.H. Pelfrey, J. Speed, S. Mahajan, P.N. Bartlett, J.J. Baumberg, Sphere Segment Void Structures: a Reproducible SERS Substrate for Electrochemical Studies, in: 41st Am. Chem. Soc. Cent. Reg. Meet., 2009. https://www.researchgate.net/publication/267321988_Sphere_Segment_Void_Structures_a_Reproducible_SERS_Substrate_for_Electrochemical_Studies (accessed February 19, 2016).

[55] M.E. Abdelsalam, P.N. Bartlett, J.J. Baumberg, S. Cintra, T.A. Kelf, A.E. Russell, Electrochemical SERS at a structured gold surface, Electrochem. Commun. 7 (2005) 740–744. doi:10.1016/j.elecom.2005.04.028.

[56] J.C. Merlin, J.P. Cornard, A Pictorial Representation of Normal Modes of Vibration Using Vibrational Symmetry Coordinates, J. Chem. Educ. 83 (2006) 1393. doi:10.1021/ed083p1393.

[57] Y. Sato, S. Ye, T. Haba, K. Uosaki, Potential Dependent Orientation and Oxidative Decomposition of Mercaptoalkanenitrile Monolayers on Gold. An in Situ Fourier Transform Infrared Spectroscopy Study , Langmuir. 12 (2002) 2726–2736. doi:10.1021/la950675t.

[58] B. Ren, R.A. Gu, J.L. Yao, X.M. Fan, Z.Q. Tian, Y.X. Yuan, The reorientation of benzonitrile on Platinum electrode probed by surface enhanced Raman spectroscopy, J. Electroanal. Chem. 624 (2008) 129–

133. doi:10.1016/j.jelechem.2008.08.004.

[59] A. Kawski, B. Kukliński, P. Bojarski, Dipole moment of benzonitrile in its excited S1 state from thermochromic shifts of fluorescence spectra, Chem. Phys. Lett. 419 (2006) 309–312. doi:10.1016/j.cplett.2005.12.007.

[60] A. Kawski, B. Kukliński, P. Bojarski, Excited S1 state dipole moments of nitrobenzene and p-nitroaniline from thermochromic effect on electronic absorption spectra, Chem. Phys. 330 (2006) 307–312. doi:10.1016/j.chemphys.2006.09.002.

[61] X. Gao, J.P. Davies, M.J. Weaver, Test of surface selection rules for surface-enhanced Raman scattering: the orientation of adsorbed benzene and monosubstituted benzenes on gold, J. Phys. Chem. 94 (1990) 6858–6864. doi:10.1021/j100380a059.

[62] M.L. Patterson, M.J. Weaver, Surface-Enhanced Raman Spectroscopy as a Probe of Adsorbate-Surface Bonding: Simple Alkenes and Alkynes Adsorbed at Gold Electrodes, J. Phys. Chem. 89 (1985) 5046–5051. doi:10.1021/j100269a032.

Chapter 5: The adsorption and orientation of thioamide molecular wires on gold

Molecular wires (MWs) are structures that facilitate electron transfer and have gained much research attention due to their applications in molecular electronic devices [1–3], with the eventual goal to substitute solid-state wires with molecules [4] and continue the atomic scale miniaturisation of electronics and furtherance of Moore's law [2]. MWs transport charge through a conjugated pathway between two terminal groups that attach to the electrode surface, with the linker group now understood to control the rate of electron transport across the MW. Therefore, designing a highly conductive junction that is stable and strongly couples to electrodes is vital in furthering MW design [5]. Traditional MWs use thiols as the contact group to Au electrodes because of its stable thiolate bonding and easy self-assembly into monolayers [6–8]. However, thiols readily form disulfides and are easily attacked in nucleophilic addition and substitution reactions [3]. Various other functional groups have been investigated, including amine and carboxyl [9–12], but thioamides are also a variable alternative. Thioamides are simply generated from cyanide groups, are easily handled species which are not prone to dimerization and their contact resistance should not suffer from the same sulphur hybridisation disadvantages observed for thiols [13]. Thioamide terminated monolayers have been previously studied using electrochemistry [14,15], x-ray photoelectron spectroscopy (XPS) and surface enhanced Raman spectroscopy (SERS) [16–18] and it has been demonstrated that heterocyclic thioamides bind covalently to gold surfaces by formation of Au-S bonds, in a similar manner to thiolates [16]. However, a proposed additional interaction between the amine group and the surface has not been proven. The MWs used in this study are were 1,4-benzenedicarbothioamide (BDTA) and 4,4'-(ethyne-1,2-diyl)dibenzodicarbothioamine (EDBDTA) and are shown in Figure 5.1. If a greater understanding of the thioamide-surface interaction can be developed, both species are good candidates as MWs due to the conjugation and rigidity provided by the single or linked benzene rings, providing fast charge transfer within the molecule and the conformational control required for electronic devices [19].

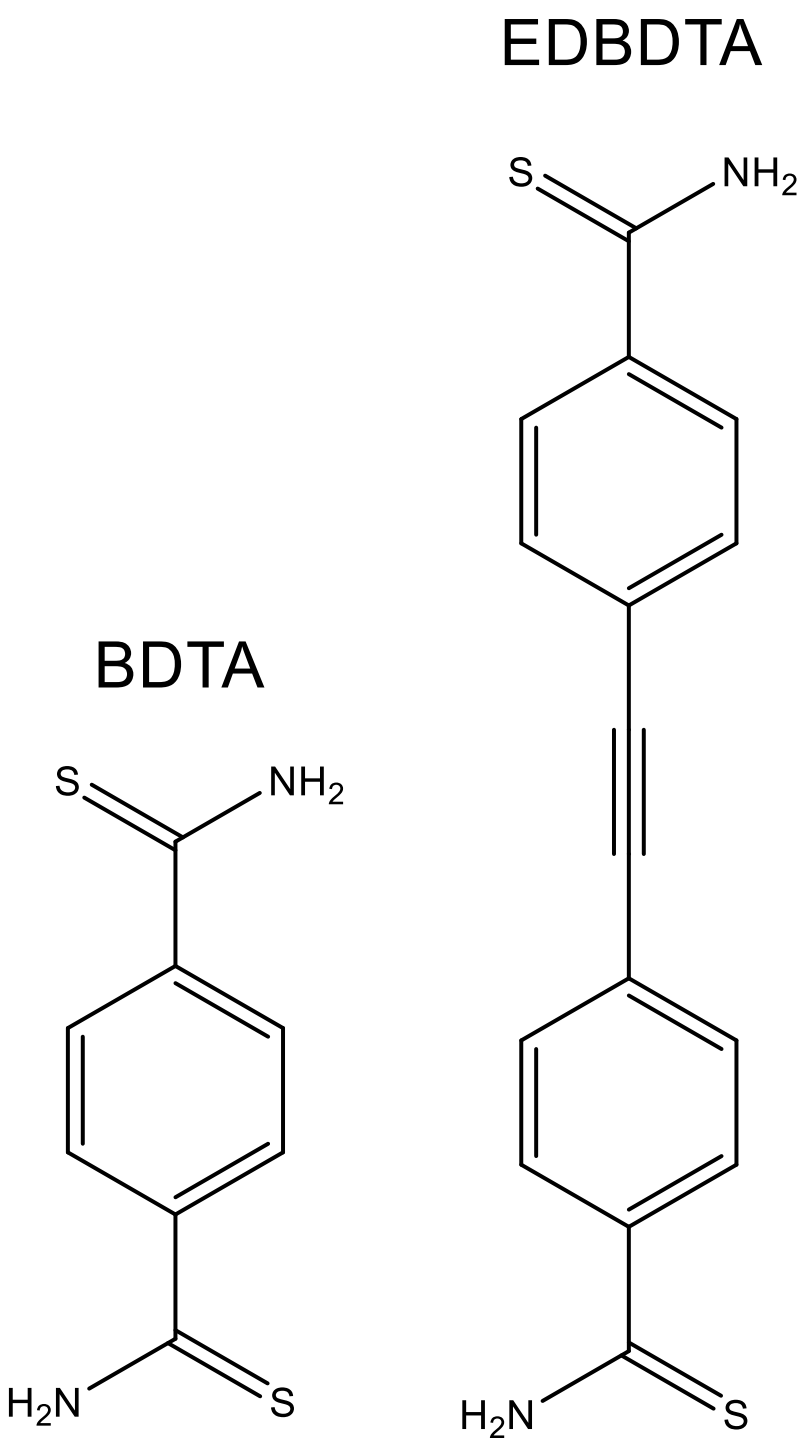

Figure 5.1: Thioamide molecular wires ,1-4-benzenedicarbothioamide (BDTA) and 4,4'-(ethyne-1,2-diyl)dibenzodicarbothioamine (EDBDTA).

In this chapter I present a combined SERS and density functional theory (DFT) study to determine the binding and orientation of BDTA and EDBTA MWs adsorbed on Au sphere segment void (SSV) substrate electrodes [20,21], including how even imperfect computational models can provide good insight into such details. The thioamide species were supplied and synthesised by Sally Dixon at the University of Southampton [13].

5.1 Thioamide adsorption on Au

The experimentally obtained SERS and DFT calculated spectra of BDTA are shown in Figure 5.2, with the molecule adsorbed on an Au_5 cluster via the S atom in the thioamide group. These show reasonable agreement in peak position, but there are significant differences in the intensities of the vibrational modes, especially in the 1250-1750 cm^{-1} window, indicating that the binding configuration chosen for the DFT model does not match that seen in the SERS spectrum. A full SERS and DFT vibrational assignment for BDTA is available in Appendix D.

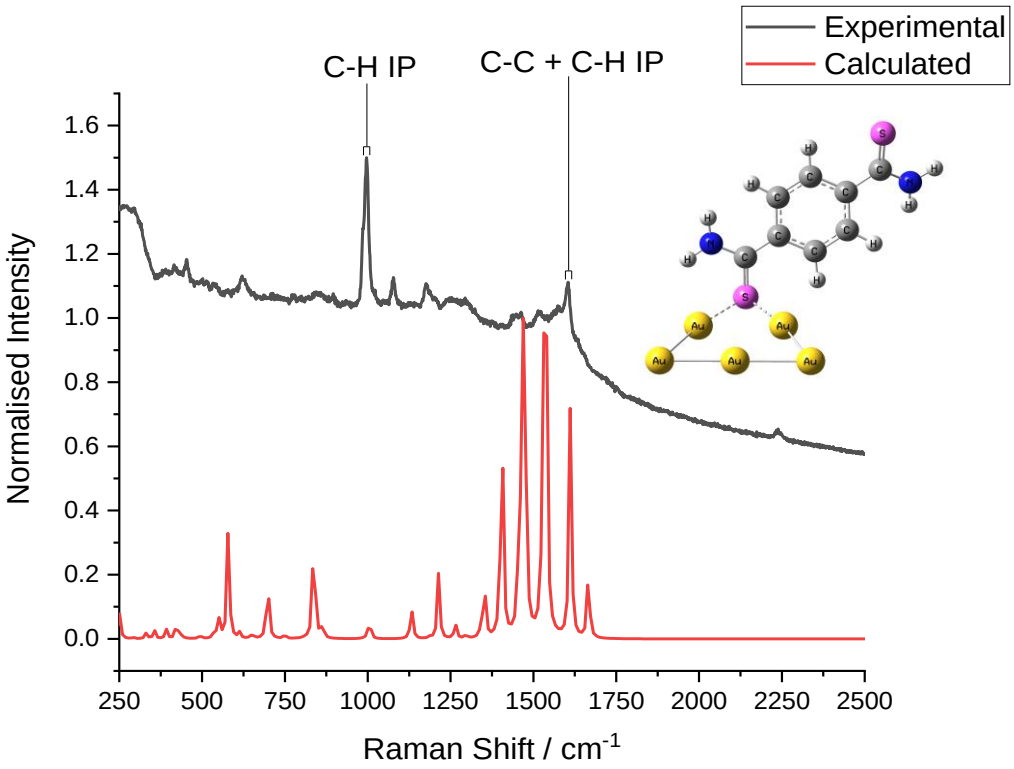

Figure 5.2: Experimental SERS and calculated DFT spectra of BDTA. The SERS spectrum is of a BDTA SAM adsorbed on an Au SSV substrate and the DFT spectrum is of the BDTA optimised structure as seen inset. The two peaks with the largest intensity in the SERS spectrum are marked. The spectra have been normalised to the largest peak in each spectrum and are offset for clarity.

The labelled peaks in Figure 5.2 correspond to the two most intense peaks in the SERS spectrum and can be assigned to a C-C bending vibration ($\delta_{C\text{-}C}$, Wilson number = 12) and C-C stretching and C-H bending vibration ($\nu_{C\text{-}C}$ + $\delta_{C\text{-}H}$, 8a + 9a) that both vibrate in the plane (IP) of the aromatic ring. No peaks for out of plane (OOP) aromatic ring vibrations were found in the experimental

SERS spectra. The dipole derivative unit vectors for the IP vibrations are shown in Figure 5.3 and are both almost directly aligned along the molecular axis. Therefore, these vibrations can provide a good indication of the orientation of the molecules adsorbed on the surface. Furthermore, the vibrational assignment of the 1604 cm^{-1} peak to a C-C stretching and C-H bending vibration at 1622 cm^{-1} in the DFT spectra could also feasibly be assigned to a C-C bending and C-H bending vibration (δ_{C-C} + δ_{C-H}, 19b + 18b) at 1546 cm^{-1}. However, they both have very similar dipole directions along the plane of the molecule so the analysis remains valid.

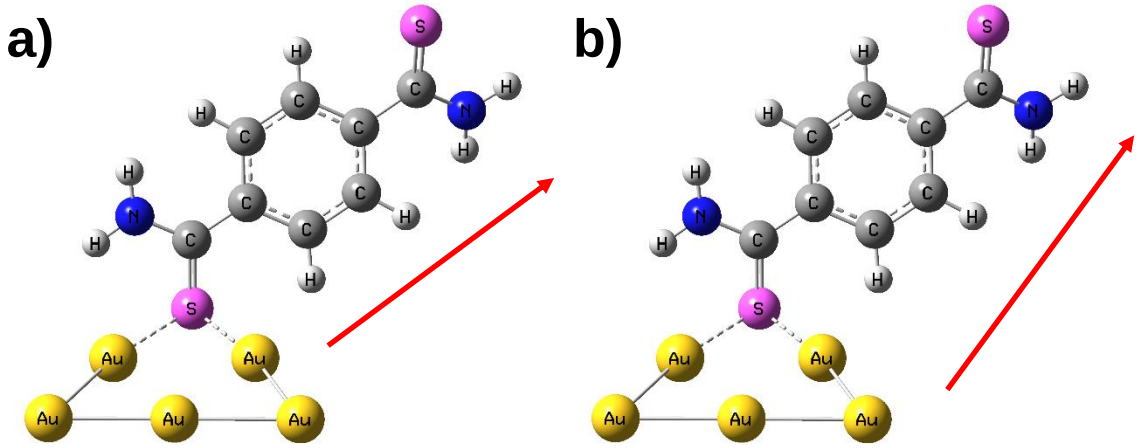

Figure 5.3: The dipole derivative unit vectors for the BDTA a) C-C bending vibration (δ_{C-C}, Wilson number = 12) at 996 cm^{-1} and b) the C-C stretching and C-H bending vibration (ν_{C-C} + δ_{C-H}, 8a + 9a) at 1605 cm^{-1}.

Similarly to Chapters 3 and 4, the orientation of BDTA can be defined by the tilt angle, θ, which is the angle between the aromatic ring and the surface normal. By consideration of the SERS surface selection rules (See Chapter 1), the lack of OOP vibrations and the high intensity of IP vibrations indicate that θ is very small and BDTA is in an almost perpendicular orientation to the surface. Therefore, the thioamide-surface interaction must be different to that proposed in the DFT model (Figure 5.2), where the intensities for these vibrations are much lower. In addition, further analysis of the DFT spectra reveals many peaks that correspond to N-H bending vibrations of the thioamide group closest to the surface (1-Thioamide: 332, 422, 579, 837 and 1667 cm^{-1}), which either have very low intensity in the experimental SERS spectrum or are not seen, contrary to the expected high intensities from modes that are so close to the surface. Thus, I propose their absence is due to an additional interaction of N with the surface. Such amine-Au interactions are common in the literature, with many

previous reported studies [9–12,22,23]. Furthermore, a combined S + N interaction with the metal surface would also result in BDTA sitting in a more perpendicular orientation with respect to the surface, giving a very small θ and matching the conclusion drawn from the aromatic ring vibrations described earlier.

This experiment was repeated with a monolayer of EDBDTA and the SERS and DFT calculated spectra are shown in Figure 5.4. A full SERS and DFT vibrational assignment for EDBDTA is available in Appendix D. The same conclusions from these spectra can be drawn as for BDTA; there is a clear discrepancy in the intensities. Excluding the mode at 2250 cm^{-1} for the C≡C stretching vibration, the two most intense peaks are at 1175 cm^{-1} and 1593 cm^{-1}, assigned to a C-H bending vibration (δ_{C-H}, 18b), and C-C stretching and C-H bending vibration (ν_{C-C} + δ_{C-H}, 8a + 9a) for the aromatic ring closest to the surface (Ring 1). These are both IP with respect to the aromatic ring and their dipole derivative unit vectors are shown in Figure 5.5.

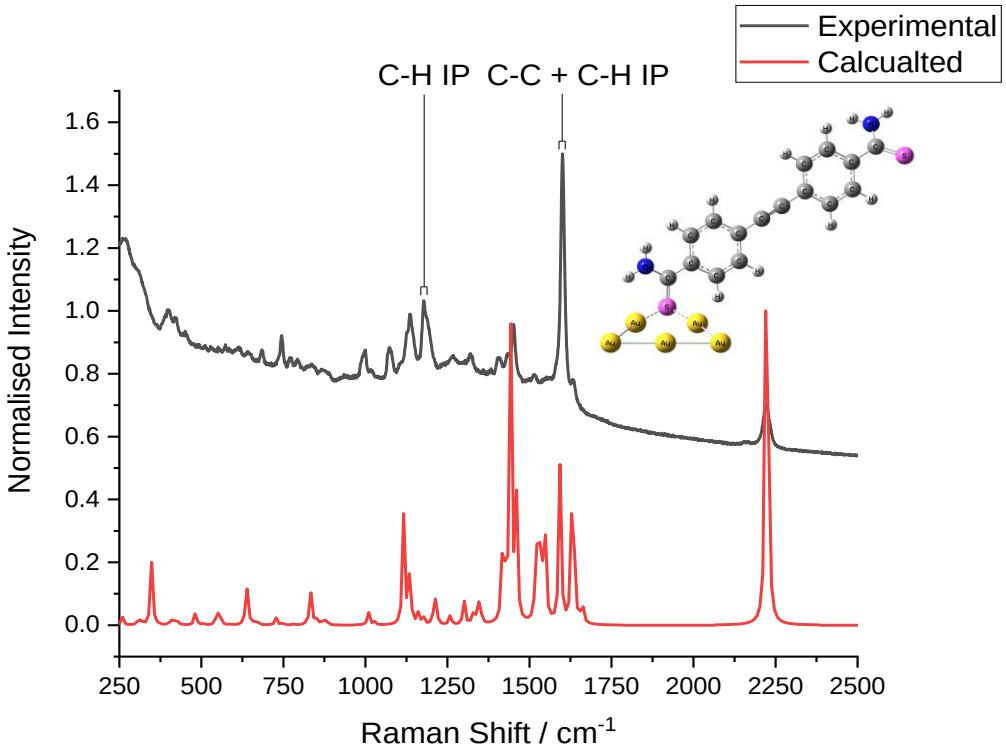

Figure 5.4: Experimental SERS and calculated DFT spectra of EDBDTA. The SERS spectrum is of a EDBDTA SAM adsorbed on an Au SSV substrate and the DFT spectrum is of the EDBDTA optimised structure as seen inset. The two peaks with the largest intensity in the SERS spectrum are marked. The spectra have been normalised to the largest peak in each spectrum and are offset for clarity.

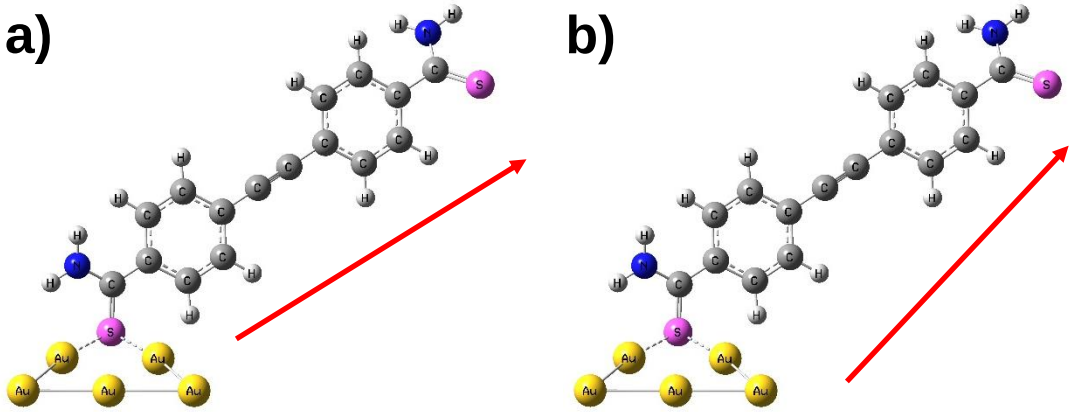

Figure 5.5: Dipole derivative unit vector for the C-H bending vibration (δ_{C-H}, 18b) and C-C stretching and C-H bending vibration (ν_{C-C} + δ_{C-H}, 8a + 9a) for the aromatic ring closest to the Au cluster.

Again, the high intensity of the IP peaks and the lack of OOP vibrations, indicates that EDBDTA, like BDTA, has a small θ and is in an almost perpendicular orientation with respect to the surface. Similarly, the thioamide N-H vibrations for the ring closest to the surface in EDBDTA (Ring 1: 348, 412, 748, 832, 1661 cm^{-1}) are very small; again suggesting thioamide adsorbs on the Au surface by both N and S.

5.2 SERS potential dependence

A cyclic voltammogram for EDBDTA adsorbed on an Au SSV substrate in 0.1 M $NaClO_4$ is presented in Figure 5.6. The lack of redox processes in this window indicates that the monolayer is electrochemically stable. Therefore, as per the work carried out in Chapter 3, any effects of applied potential on the monolayer can be attributed to changes in orientation.

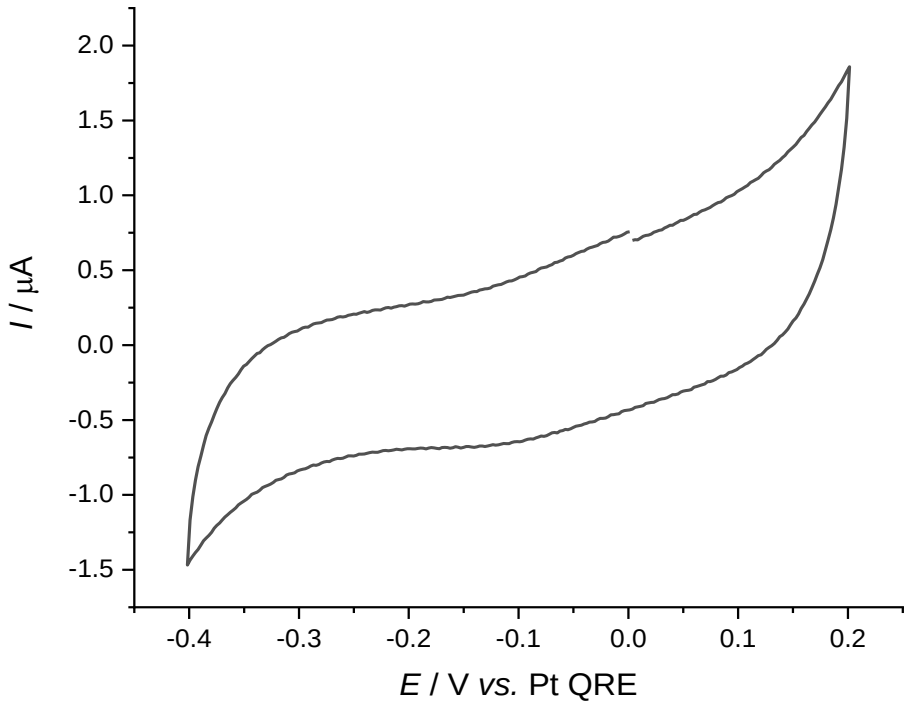

Figure 5.6: Cyclic voltammogram of an EDBTA SAM adsorbed on an Au SSV electrode in 0.1 M $NaClO_4$. Scan rate = 5 mV s^{-1}.

Variations in the EDBDTA IP vibrational intensities (Figure 5.4) are displayed in Figure 5.7. As can be seen, these both show very little potential dependence, indicating that θ does not change and EDBDTA remains in a perpendicular orientation across the potential window. This is in contrast to a previously reported EC-SERS study using thioamides, where de Tércio *et al.* found pyridylthioamides became more parallel to the surface at positive potentials. However, they proposed this was due to additional hydrogen bonding between the N atom in the pyridyl ring and NH_2 of the neighbouring thioamide [18]. In addition, this differs to the results of Chapters 3 and 4, where there are multiple adsorbate-surface interactions controlling the orientation. I propose this discrepancy is due to EDBDTA (and thioamide SAMs) having a smaller θ and being more perpendicular to the surface than thiols. Thus, any functional groups and aromatic π orbitals are too far from the surface to interact and there is no potential dependence.

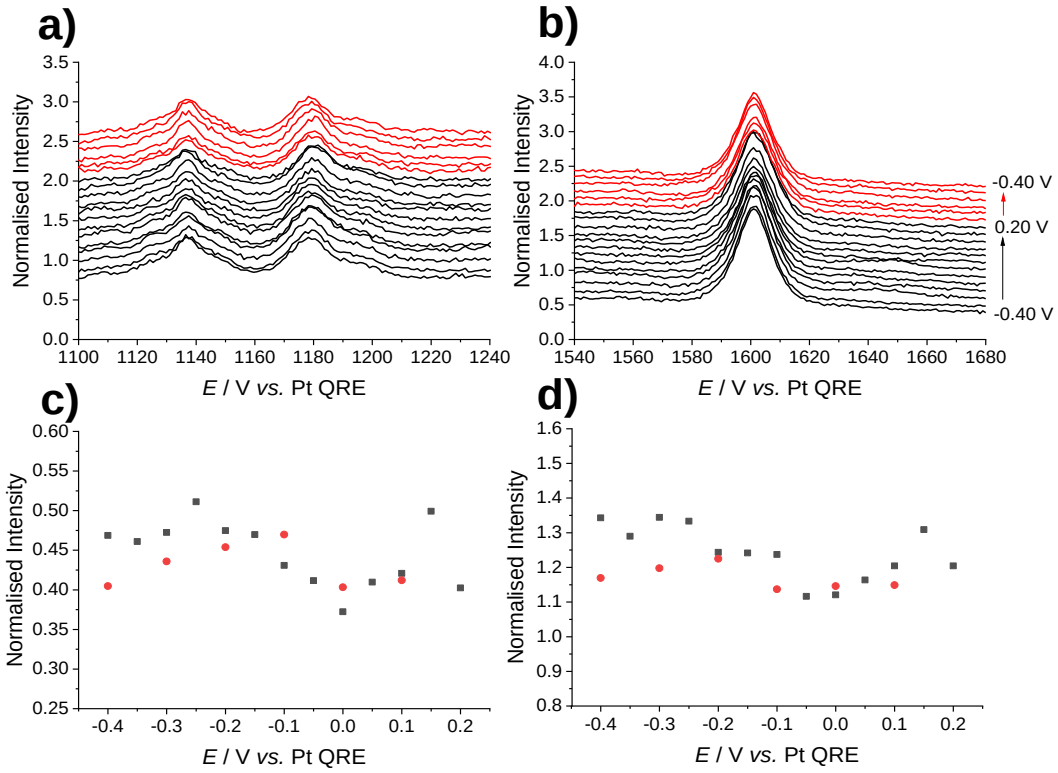

Figure 5.7: SERS spectra of the EDBDTA a) C-H bending vibration (δ_{C-H}, 18b) and b) C-C stretching and C-H bending vibration (ν_{C-C} + δ_{C-H}, 8a + 9a) for the aromatic ring closest to the Au cluster, alongside their normalised intensities, c) and d), with respect to potential.

5.3 Summary

In this chapter I have presented the SERS spectra of two thioamide terminated molecular wires, BDTA and EDBDTA. Initially, the adsorbate-surface binding was proposed to be via C=S of the thioamide group. However, there was poor agreement in the mode intensities when compared to DFT calculated spectra in this configuration. The highest intensity peaks in the SERS spectra were for vibrational modes in the plane of the aromatic ring, indicating that the molecules sat in an orientation closer to perpendicular. In addition, peaks assigned to N-H vibrations in the thioamide closest to the metal surface were not active. Therefore, It was determined that the thioamides were bound via both C=S and NH_2, pushing the MWs into more upright orientations to the surface. The potential dependence of EDBDTA was also investigated and only small changes in the intensities of the IP vibrations were observed, indicating the molecule remained in a stable orientation across the potential window and did not interact further with the charged electrode surface.

5.4 References

[1] D. Xiang, X. Wang, C. Jia, T. Lee, X. Guo, Molecular-Scale Electronics: From Concept to Function, Chem. Rev. 116 (2016) 4318–4440. doi:10.1021/acs.chemrev.5b00680.

[2] D.M. Guldi, H. Nishihara, L. Venkataraman, Molecular wires, Chem. Soc. Rev. 44 (2015) 842. doi:10.1039/c5cs90010g.

[3] T. Sagisaka, S. Kurokawa, A. Sakai, K. I. Yamashita, M. Taguchi, M.S. Asano, K. I. Sugiura, Conductance of Au/1,4-benzenedicarbothioamide/Au molecular junctions: A proposal for a potential linker, Chem. Phys. Lett. 595–596 (2014) 167–170. doi:10.1016/j.cplett.2014.01.054.

[4] J.M. Tour, Molecular Electronics. Synthesis and Testing of Components, (2000). doi:10.1021/AR0000612.

[5] L. Venkataraman, Y.S. Park, A.C. Whalley, C. Nuckolls, M.S. Hybertsen, M.L. Steigerwald, Electronics and chemistry: Varying single-molecule junction conductance using chemical substituents, Nano Lett. 7 (2007) 502–506. doi:10.1021/nl062923j.

[6] J.C. Love, L.A. Estroff, J.K. Kriebel, R.G. Nuzzo, G.M. Whitesides, Self-assembled monolayers of thiolates on metals as a form of nanotechnology, Chem. Rev. 105 (2005) 1103–1169. doi:10.1021/cr0300789.

[7] K. Stokbro, J. Taylor, M. Brandbyge, J.L. Mozos, P. Ordejón, Theoretical study of the nonlinear conductance of Di-thiol benzene coupled to Au(1 1 1) surfaces via thiol and thiolate bonds, Comput. Mater. Sci. 27 (2003) 151–160. doi:10.1016/S0927-0256(02)00439-1.

[8] C.H. Ko, M.J. Huang, M.D. Fu, C.H. Chen, Superior contact for single-molecule conductance: Electronic coupling of thiolate and isothiocyanate on Pt, Pd, and Au, J. Am. Chem. Soc. 132 (2010) 756–764. doi:10.1021/ja9084012.

[9] F. Chen, X. Li, J. Hihath, Z. Huang, N. Tao, Effect of anchoring groups on single-molecule conductance: Comparative study of thiol-, amine-, and

carboxylic-acid-terminated molecules, J. Am. Chem. Soc. 128 (2006) 15874–15881. doi:10.1021/ja065864k.

[10] W. Hong, D.Z. Manrique, P. Moreno-García, M. Gulcur, A. Mishchenko, C.J. Lambert, M.R. Bryce, T. Wandlowski, Single molecular conductance of tolanes: Experimental and theoretical study on the junction evolution dependent on the anchoring group, J. Am. Chem. Soc. 134 (2012) 2292–2304. doi:10.1021/ja209844r.

[11] C. Nuckolls, L. Venkataraman, J.E. Klare, M.L. Steigerwald, M.S. Hybertsen, I.W. Tam, Single-Molecule Circuits with Well-Defined Molecular Conductance, Nano Lett. 6 (2006) 458–462. doi:10.1021/nl052373+.

[12] J. Tobita, Y. Kato, M. Fujihira, Single molecular conductance measurements of molecular junction of Au/1,4-phenylenediamine/Au, Ultramicroscopy. 108 (2008) 1040–1044. doi:10.1016/j.ultramic.2008.04.033.

[13] S. Dixon, R.J. Whitby, Efficient synthesis of thioamide terminated molecular wires, Tetrahedron Lett. 47 (2006) 8147–8150. doi:10.1016/j.tetlet.2006.09.032.

[14] H. Aoki, P. Bühlmann, Y. Umezawa, Self-assembly of a tricarboxylate receptor through thioamide groups and its use for electrochemical detection of protonated amines, J. Electroanal. Chem. 473 (1999) 105–112. doi:10.1016/S0022-0728(99)00312-5.

[15] T. de F. Paulo, M.A.S. da Silva, S. de O. Pinheiro, E. Meyer, L.S. Pinheiro, J.A. Freire, A.A. Tanaka, P. de Lima Neto, Í. de S. Moreira, I.C.N. Diógenes, 5-(4-pyridinyl)-1,3,4-oxadiazole-2-thiol on gold: SAM Formation and electroactivity, J. Braz. Chem. Soc. 19 (2008) 711–719. doi:10.1590/S0103-50532008000400015.

[16] I. Haidar, S. Lau-Truong, J. Aubard, J.-P. Renault, N. Félidj, F. Maurel, L. Boubekeur-Lecaque, Oxadiazole-2-thiol Adsorption on Gold Nanorods: A Joint Theoretical and Experimental Study by Using SERS, XPS, and DFT, ChemPhysChem. 15 (2014) 3646–3654. doi:10.1002/cphc.201402197.

[17] T.D.F. Paulo, S.D.O. Pinheiro, M.A.S. Da Silva, L.G.D.F. Lopes, L.S.

Pinheiro, G.F.A. Aquino, M.L.A. Temperini, P.D.L. Neto, I.C.N. Diógenes, Thionicotinamide SAM on gold: Adsorption studies and electroactivity, Electroanalysis. 21 (2009) 1081–1089. doi:10.1002/elan.200804503.

[18] T.D.F. Paulo, R.A. Ando, I.C.N. Diógenes, M.L.A. Temperini, Understanding the equilibria of thio compounds adsorbed on gold by surface-enhanced raman scattering and density functional theory calculations, J. Phys. Chem. C. 117 (2013) 6275–6283. doi:10.1021/jp400235y.

[19] L.D.A. Siebbeles, F.C. Grozema, Charge and Exciton Transport through Molecular Wires, 2011. doi:10.1002/9783527633074.

[20] A.E. Russell, S.H. Pelfrey, J. Speed, S. Mahajan, P.N. Bartlett, J.J. Baumberg, Sphere Segment Void Structures: a Reproducible SERS Substrate for Electrochemical Studies, in: 41st Am. Chem. Soc. Cent. Reg. Meet., 2009.

[21] M.E. Abdelsalam, P.N. Bartlett, J.J. Baumberg, S. Cintra, T.A. Kelf, A.E. Russell, Electrochemical SERS at a structured gold surface, Electrochem. Commun. 7 (2005) 740–744. doi:10.1016/j.elecom.2005.04.028.

[22] R. Holze, The adsorption of aniline on gold: a SERS study, J. Electroanal. Chem. 250 (1988) 143–157. doi:10.1016/0022-0728(88)80199-2.

[23] L. Bin Zhao, R. Huang, M.X. Bai, D.Y. Wu, Z.Q. Tian, Effect of aromatic amine-metal interaction on surface vibrational Raman spectroscopy of adsorbed molecules investigated by density functional theory, J. Phys. Chem. C. 115 (2011) 4174–4183. doi:10.1021/jp1117135.

Chapter 6: The challenge of using SERS to understand a complex mechanism - the electrooxidation of glycerol

Further understanding of glycerol electrooxidation is vital in in the development of direct liquid fuel cells (DLFCs). DLFCs convert chemical energy into electrical energy by electrochemically reacting a fuel such as methanol, ethanol or glycerol with oxygen to produce water [1], and are thus a promising green energy alternative to fossil fuels [2]. DLFCs have many advantages over similar technologies, for example when compared to polymer electrolyte membrane fuel cells (PEMFCs), which use hydrogen as a fuel, there are fewer safety concerns around fuel handling, storage and transport. However, they also have a number of difficulties to be overcome before commercialisation is a reality. These include: sluggish reaction kinetics, incomplete fuel oxidation and high costs. Among the fuels for DLFCs, glycerol is a non-toxic, non-flammable, non-volatile biorenewable alcohol that is a coproduct in the production of biodiesel [3], and can also be used in producing high value oxygenated chemicals [4]. Therefore, due to the popularity of biodiesel there is an abundance of glycerol that it is relatively cheap when compared to other alcohol fuels [5], and thus it is considered a promising alternative fuel for DLFCs [6].

Several studies show Au-catalysed glycerol electrooxidation has a higher activity in alkaline media [7–12] than in acid [13–15]. Furthermore, Zhang *et al.* have shown a greater activity for glycerol oxidation when compared to methanol or ethylene glycol when using Au [16]. The mechanism of glycerol oxidation has been studied with a variety of catalysts [17–21]. However, its complexity has led to a multitude of intermediates and products being proposed that can be summarised into two possible routes, depending on the alcohol functional group that is oxidised first, as shown in Figure 6.1. In Route 1 the C2 secondary alcohol is initially oxidised, giving dihydroxyacetone, that with further oxidations leads to formic acid and glycolic acid as the final products. In Route 2 the C1 primary alcohol is initially oxidised, giving glyceraldehyde and eventually leading to formic acid and oxalic acid. Efforts made to identify these intermediates have been made using infrared (IR) spectroscopy [22–26], online high-

performance liquid chromatography (HPLC) [27,28] and mass spectrometry.[21,29,30], and when using Au-based catalysts glyceric, glycolic, formic and oxalic acids have all been previously identified [7,26,29].

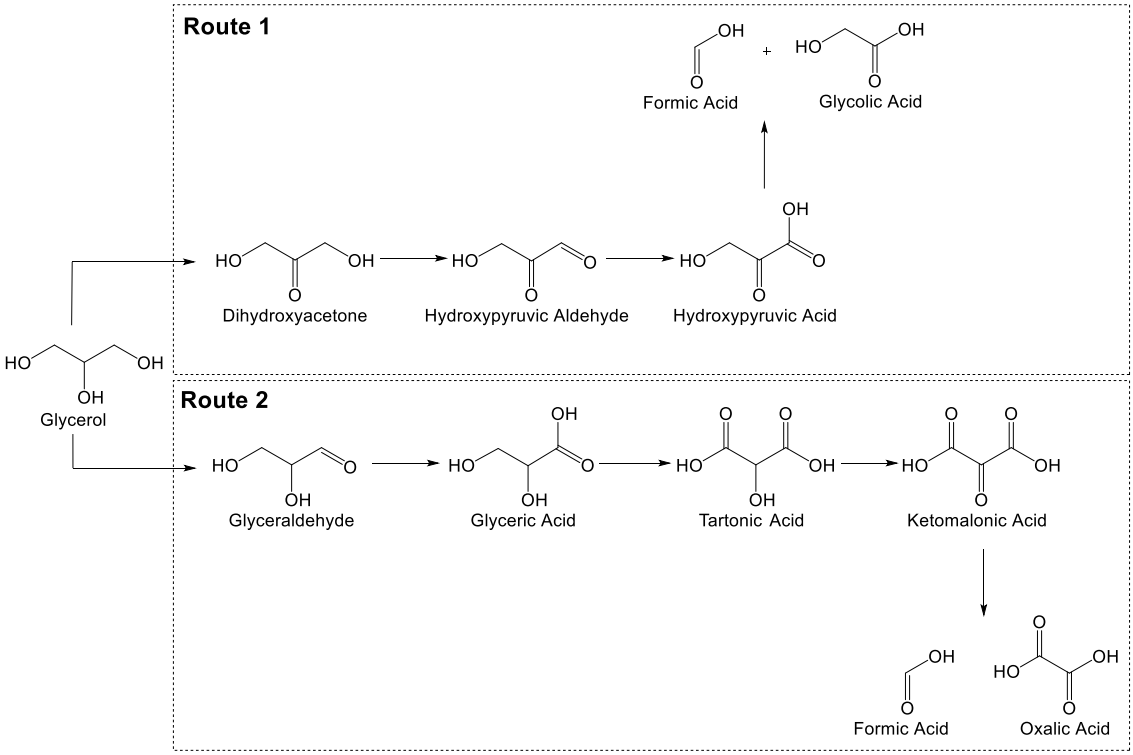

Figure 6.1: The two proposed oxidation pathways of Au catalysed glycerol oxidation

However, there are challenges associated with investigating the mechanism of glycerol electrooxidation due to the similarity in the intermediates. Comparable fragmentation resulting in the presence of similar species with the same mass leads to difficulty using mass spectrometry. IR spectroscopy is excellent at identifying functional groups such as C=O, but suffers from strong absorption of water based electrolytes and is poor at determining the differences in C-C chains. Also, X-ray absorption spectroscopy is limited to systems that contain heavier elements [20,31]. Surface enhanced Raman spectroscopy (SERS) can be used to overcome these issues as it can be used in aqueous systems and the low wavenumber region (0-1000 cm^{-1}) provides more detailed information regarding the carbon chain. Some electrochemical reactions which are important for fuel cell systems have been successfully studied using SERS on Au-based substrates, such as the oxidation of methanol, [32,33] ethanol [34], formic acid [33–36], and borohydride [37].

In this chapter I present density functional theory (DFT) Raman and SERS spectra to characterise the intermediates and products of glycerol electrooxidation on Au SSV substrate electrodes in alkaline media. In addition, I investigate the challenges these studies face when there are multiple, similar intermediate species with complex SERS spectra. This work was carried out in partnership with Giancarlo R. Salazar-Banda, a visiting academic from Tiradentes University in Aracaju, Brazil. Giancarlo carried out the electrochemistry and I performed the electrochemical SERS (EC-SERS) measurements, DFT calculations and subsequent analysis.

6.1 Identification of intermediates

A CV of an Au SSV electrode in 0.1 M glycerol in 0.1 M KOH is shown in Figure 6.2. This shows the characteristic behaviour seen for the electrooxidation of several alcohols, on the forward sweep, an oxidation peak increases in current with an onset potential of -0.30 V *vs.* Au/AuO, before decreasing down to zero current by 0.50 V, that is characteristic of glycerol electrooxidation. On the reverse scan a second oxidation peak increases in current with an onset potential of 0.25 V that is understood to correspond to the removal of incompletely oxidised species during the forward scan.

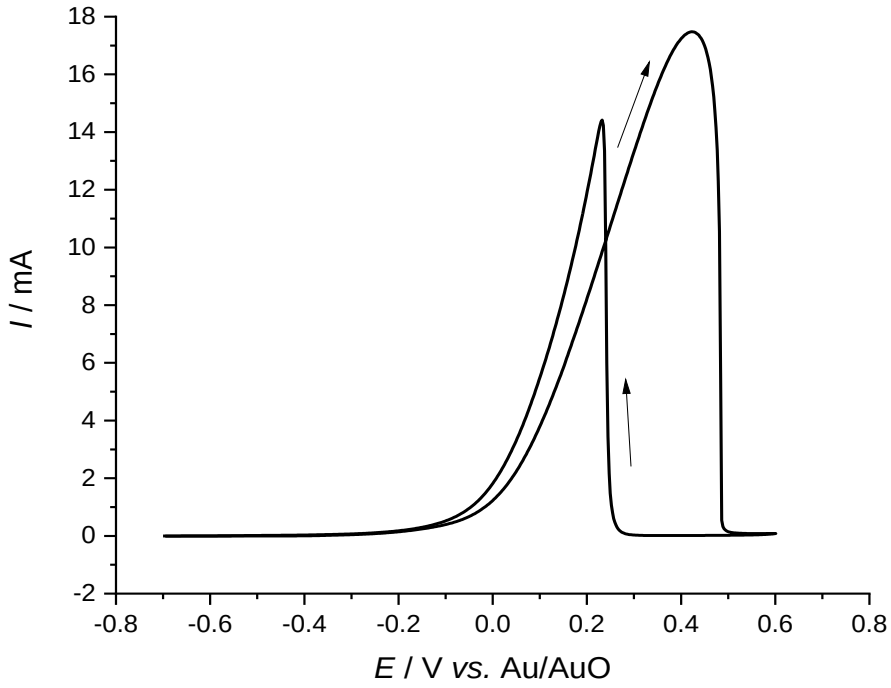

Figure 6.2. CV of an Au SSV electrode in 0.1 M glycerol in 0.1 M KOH solution. Scan rate = 10 mV s^{-1}. The sweep starts at -0.70 V and the arrows show the sweep direction.

The measured Raman spectra of glycerol and its commercially available proposed electrooxidation intermediates are presented in Figure 6.3, showing great similarity between the spectra and their mode assignments. Equally, the DFT calculated Raman spectra of these species and their corresponding optimised structures are shown in Figure 6.4 for Route 1 and Figure 6.5 for Route 2 and the same problem is apparent. Therefore, identifying individual peaks for each species will be very challenging and a different approach must be taken to differentiate between them. Thus, rather than focussing on individual vibrational modes (as has been done in previous chapters) a greater focus will be placed on the pattern of peaks to help identify intermediate species.

Furthermore, the binding of each intermediate species to the Au cluster in the DFT calculations was chosen to be consistent between each reaction pathway and each was optimised to ensure they were the lowest energy structures. However, as seen in the previous chapters of this thesis, the orientation of the species on the surface can have a significant impact on the frequency and intensity of the vibrational bands in the DFT spectra. If more time were available for this work additional binding of each species by a succession of their alcohol

and carbonyl groups would have been investigated. This would not only have helped in the identification of species in the SERS spectra, but would also have given an indication into the orientation on the electrode surface.

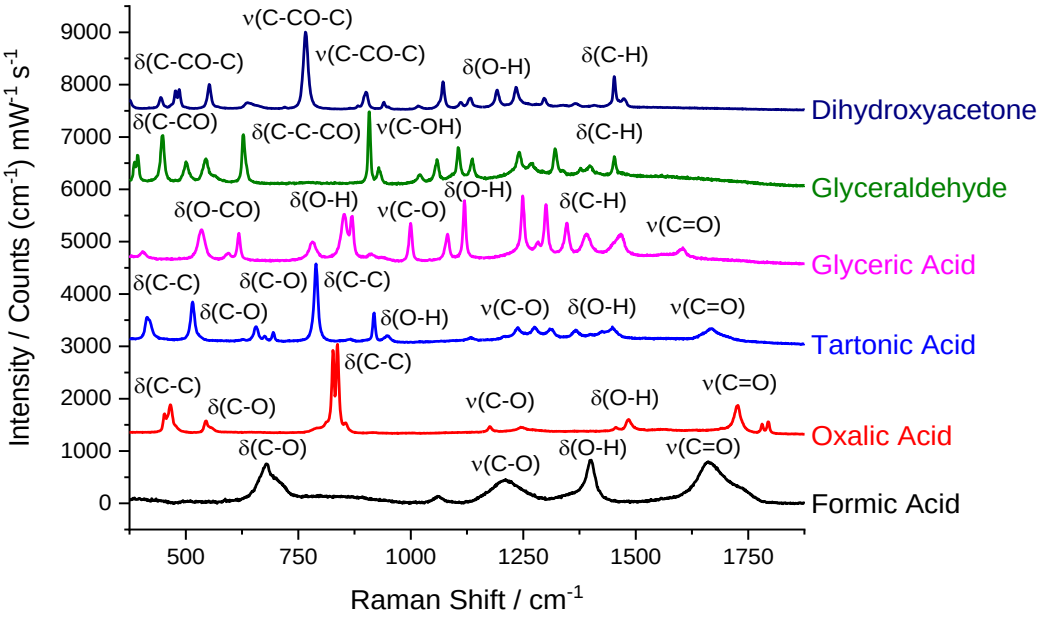

Figure 6.3.Raman spectra of a selection of commercially available solid glycerol electrooxidation intermediates. Mode assignments made using the work by Socrates [40]. ν = stretch, δ = bend and spectra offset for clarity.

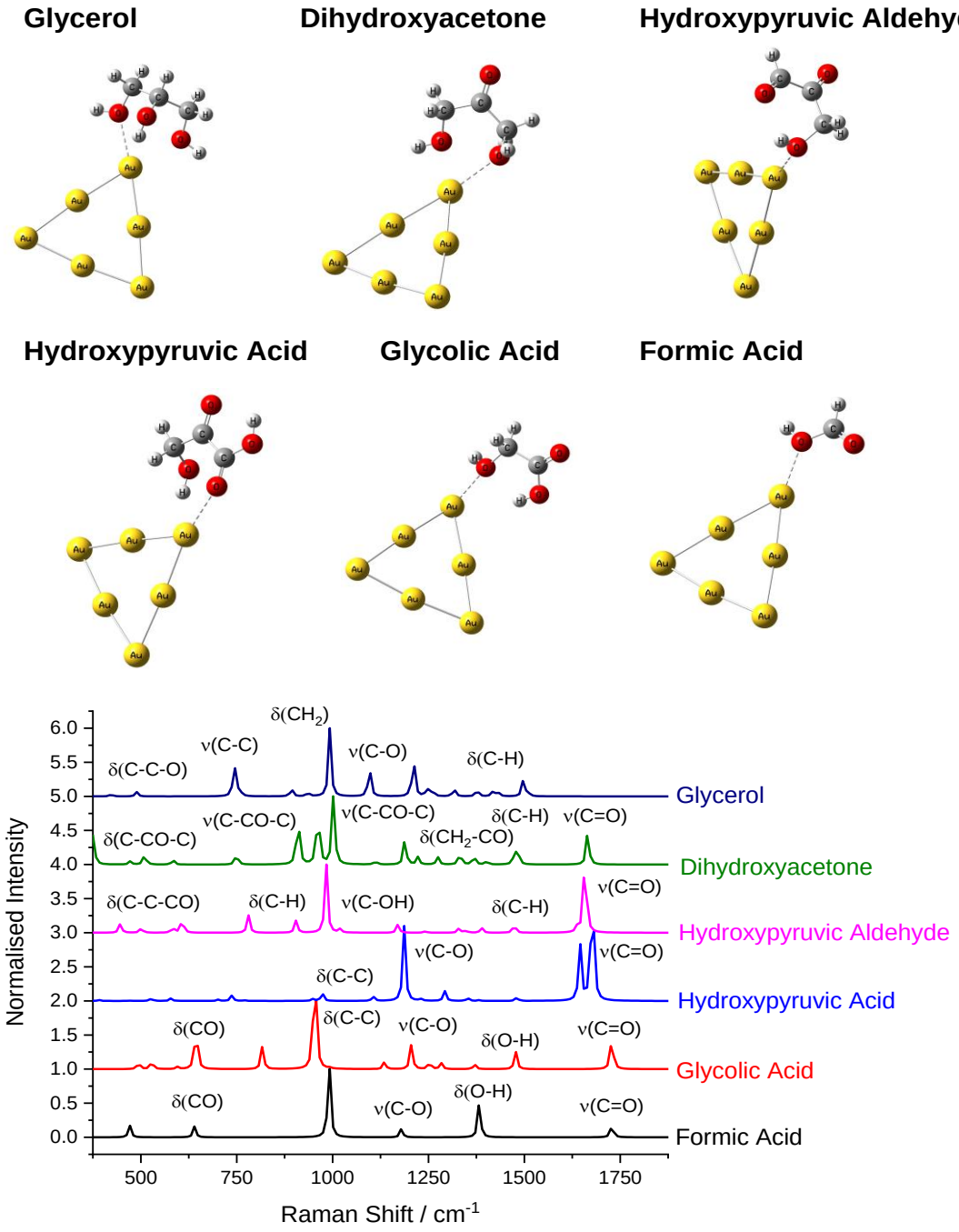

Figure 6.4: Optimised DFT structures of glycerol and its Route 1 electrooxidation products (Figure 6.1) adsorbed on Au_6 clusters and their DFT calculated Raman spectra. Mode assignments for glycerol made using the work of Mendelovici *et al.*[41] and for the intermediates from Socrates [40], ν = stretch, δ = bend. Spectra are normalised to the largest peak in each spectra and offset for clarity.

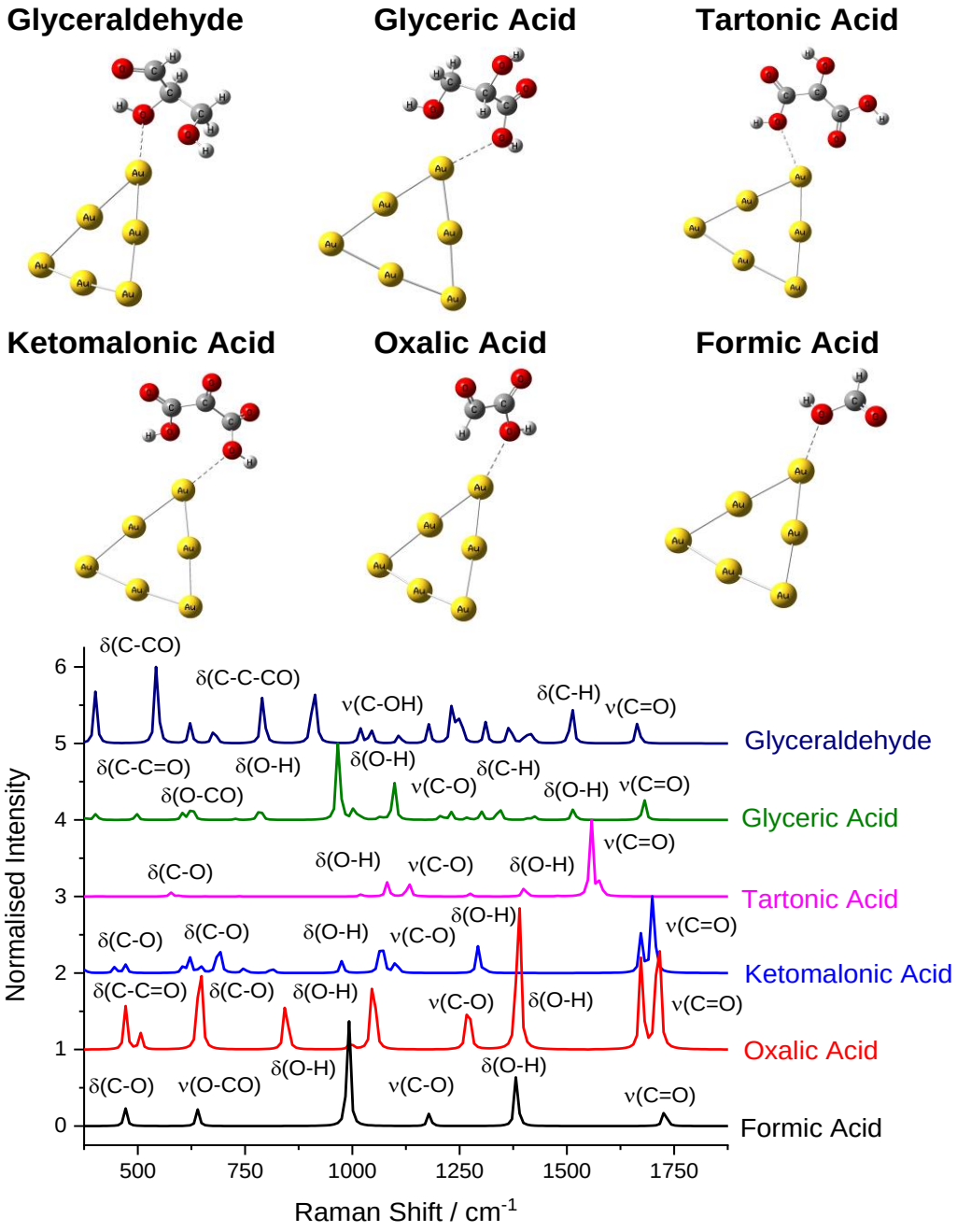

Figure 6.5: Optimised DFT structures of the Route 2 glycerol electrooxidation products (Figure 6.1) adsorbed on Au_6 clusters and their DFT Raman spectra. Mode assignments made using the work by Socrates [40], ν = stretch, δ = bend. Spectra are normalised to the largest peak in each spectra and offset for clarity.

Figure 6.6 shows the EC-SERS spectra of an Au SSV substrate in 0.1 M Glycerol in 0.1 M KOH as the potential is stepped from -0.40 V to 0.50 V vs. Au/AuO. At -0.40 V, three peaks appear at 1000, 1028 and 1085 cm^{-1} that increase to a maximum intensity at -0.10 V, then decrease to the level of the noise by 0.50 V. At 0.00 V peaks appear at 388, 800, 958 and 1461 cm^{-1} that are no longer visible as the potential is stepped to 0.10 V, and at 0.20 V a new

set of peaks appear at 407, 553, 788, 832, 981, 1015, 1171, 1390, 1558 and 1590 cm^{-1}, that also disappear the on the next positive potential step. When compared to the CV in Figure 6.2, the appearance of vibrational bands at potentials more negative of the oxidation peak's onset potential (-0.20 V) indicates there are significant adsorption of species pre-oxidation. However, as new bands appear when the potential is moved into the region of the oxidation peak (more positive of -0.20 V) there is clearly a change in species at the electrode surface caused by this oxidation.

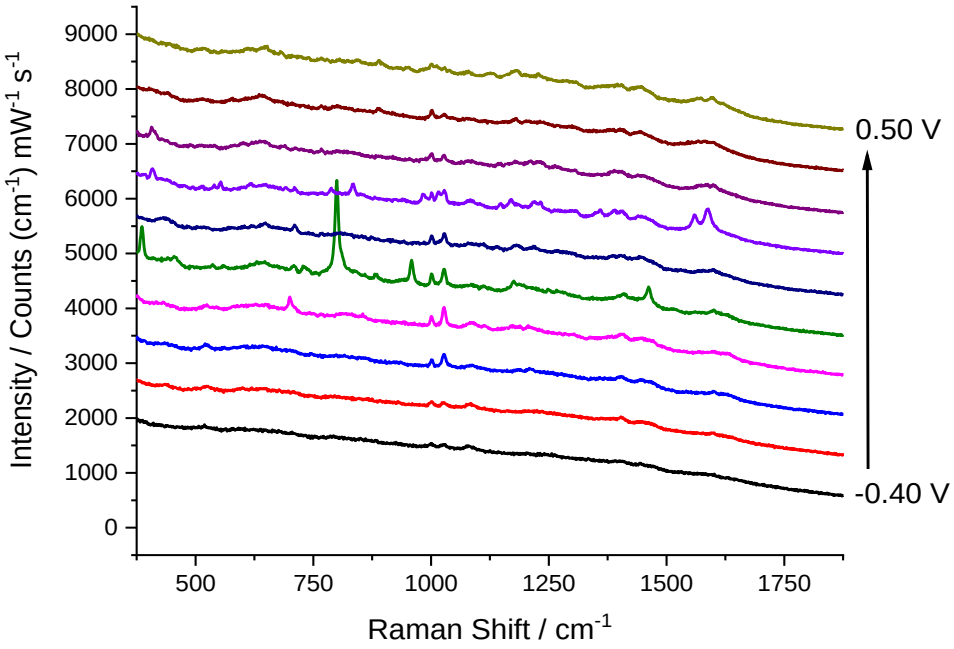

Figure 6.6: EC-SERS spectra of an Au SSV substrate in 0.1 M Glycerol in 0.1 M KOH. Spectra offset for clarity.

To be able to better compare the SERS spectra (Figure 6.6) to the calculated DFT spectra (Figures 6.4 and 6.5) they have been replotted together in Figures 6.7 and 6.8. Figure 6.7 shows the SERS spectra from -0.30 V to 0.00 V plotted with DFT spectra of glycerol and the initial oxidation products of Route 1 (Figure 6.7a) and Route 2 (Figure 6.7b). At -0.30 V there are peaks at 522, 1000, 1028, 1085 and 1403 cm^{-1} that all increase in intensity up to -0.10 V. By comparison to glycerol and dihydroxyacetone (Figure 6.7a) there is no distinctive match to this pattern of peaks. For example, it is possible to assign these to peaks to 992 (δ_{C-H}), 1098 (δ_{C-O}) and 1434 cm^{-1} (δ_{C-H}) for glycerol and 507 and 1002 cm^{-1} (both ν_{C-CO-C}) for dihydroxyacetone, but the peaks at 1028 and 1403 cm^{-1} remain unassigned. However, by comparison to Route 2 (Figure

6.7b) all the peaks can be assigned to those at 542 ($\delta_{C\text{-}CO}$), 1022 ($\nu_{C\text{-}OH}$), 1045 ($\nu_{C\text{-}OH}$), 1107 ($\delta_{C\text{-}O}$) and 1416 cm^{-1} ($\delta_{C\text{-}H}$) for glyceraldehyde. Furthermore, at -0.10 V an additional peak appears at 700 cm^{-1} that can only be assigned to the 674 cm^{-1} ($\delta_{C\text{-}C\text{-}CO}$) glyceraldehyde peak. At 0.00 V several new peaks appear at 388, 800, 958 and 1461 cm^{-1} and again, it is possible to assign these to 374 ($\delta_{C\text{-}CO\text{-}C}$) , 745 ($\nu_{C\text{-}CO\text{-}C}$) , 913($\nu_{C\text{-}CO\text{-}C}$) and 1478 cm^{-1} (δ_{CH2}) for dihydroxyacetone in Route 1 (Figure 6.7a). However, the peaks at 1000 and 1028 cm^{-1} are still present at this potential and remain unassigned when compared to the DFT spectra of this pathway. When compared to Route 2 (Figure 6.7b) the pattern of peaks is again a better match and they can be assigned to 966 ($\nu_{C\text{-}O}$) for glyceric acid and 401 ($\delta_{C\text{-}CO}$) 780 ($\delta_{C\text{-}C\text{-}CO}$), 913 ($\delta_{C\text{-}C\text{-}CO}$) and 1513 cm^{-1} ($\delta_{C\text{-}H}$) for both species.

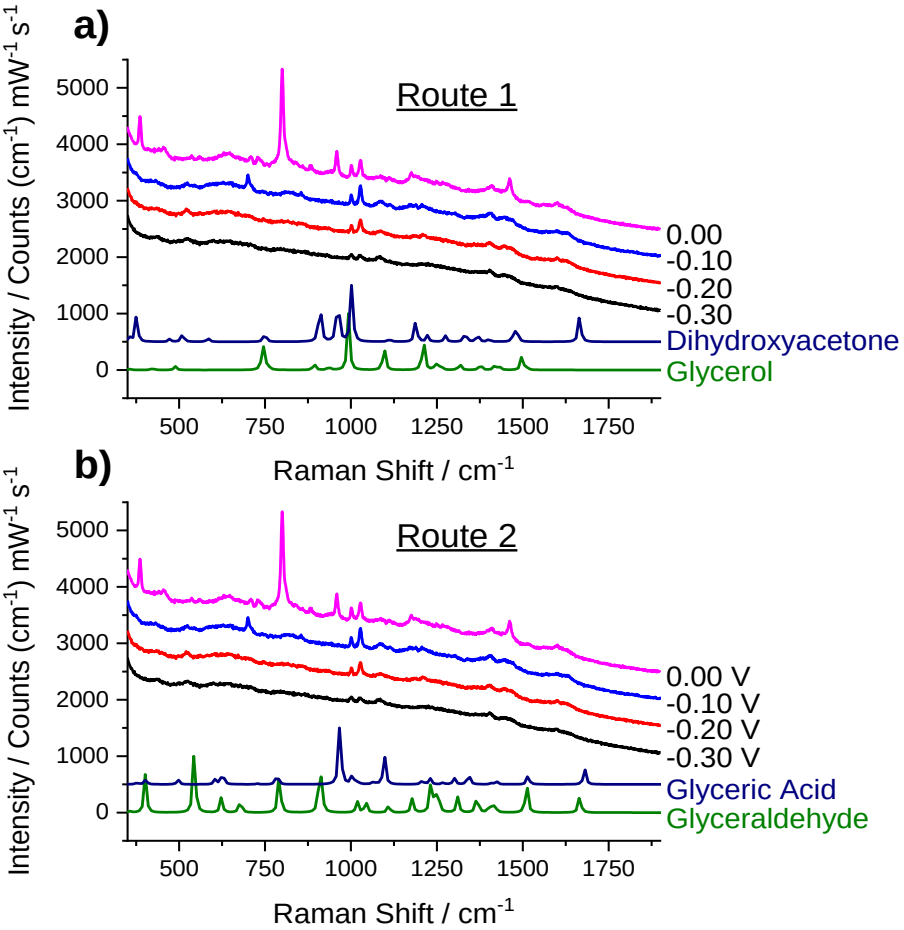

Figure 6.7: EC-SERS spectra of an Au SSV substrate in 0.1 M Glycerol in 0.1 M KOH from -0.30 V to 0.10 V *vs* Ag/AgO, plotted with DFT calculated Raman spectra of the initial species from a) Route 1 and b) Route 2 of the proposed glycerol oxidation mechanism.

Figure 6.8 shows the remainder of the EC-SERS spectra, from 0.10 V to the apex of the glycerol oxidation peak (Figure 6.2) at 0.40 V. At 0.20 V peaks at 407, 553, 788, 832, 981, 1015, 1171, 1390, 1558 and 1590 cm^{-1} all appear. When compared to the species of Route 1 (Figure 6.8a) these peaks can be assigned to hydroxypyruvic aldehyde at 445 (δ_{C-C-CO}), 486 (δ_{C-C-CO}), 780 (δ_{C-H}), 983 (δ_{C-H}), 1169 (ν_{C-OH}) and 1390 (δ_{C-H}), or to formic acid at 471 (δ_{C-O}), 992 (δ_{O-H}), 1178 (ν_{C-O}), and 1381 cm^{-1} (δ_{O-H}). However there is no assignment possible for the two large peaks at 1558 and 1590 cm^{-1}. In fact, the only possible assignment of these peaks when compared to all the species is to tartonic acid from Route 2 at 1557 and 1575 cm^{-1} (both $\nu_{C=O}$, Figure 6.8b). Further assignments to tartonic acid can be made at 577(δ_{C-O}), 1019 (δ_{O-H}), 1134 (ν_{C-O}), and 1398 cm^{-1} (δ_{O-H}), and the remaining peaks can be matched to those for ketomalonic acid at 445, 745, 816 (all δ_{C-O}), and 975 cm^{-1} (δ_{O-H}). By 0.40 V all these peaks were no longer present, but the 1000 and 1028 cm^{-1} peaks remained with a lower intensity, indicating there are still adsorbed species on the SSV surface, albeit at a lower concentration than at the more negative potentials. Therefore, it has been possible to assign vibrational modes of a variety of intermediates from both Route 1 and Route 2 of glycerol oxidation. However, the pattern of peaks in the SERS spectra provide a better match to the DFT spectra of species in Route 2, with glyceraldedhyde and tartonic acid the most obviously observed intermediates. However, the low intensity of the Raman bands in this study mean that no quantitative information can be elucidated. This is due to a combination of low Raman scattering cross section of the intermediate species and possibly different adsorbate-surface binding to that shown in Figures 6.4 and 6.5.

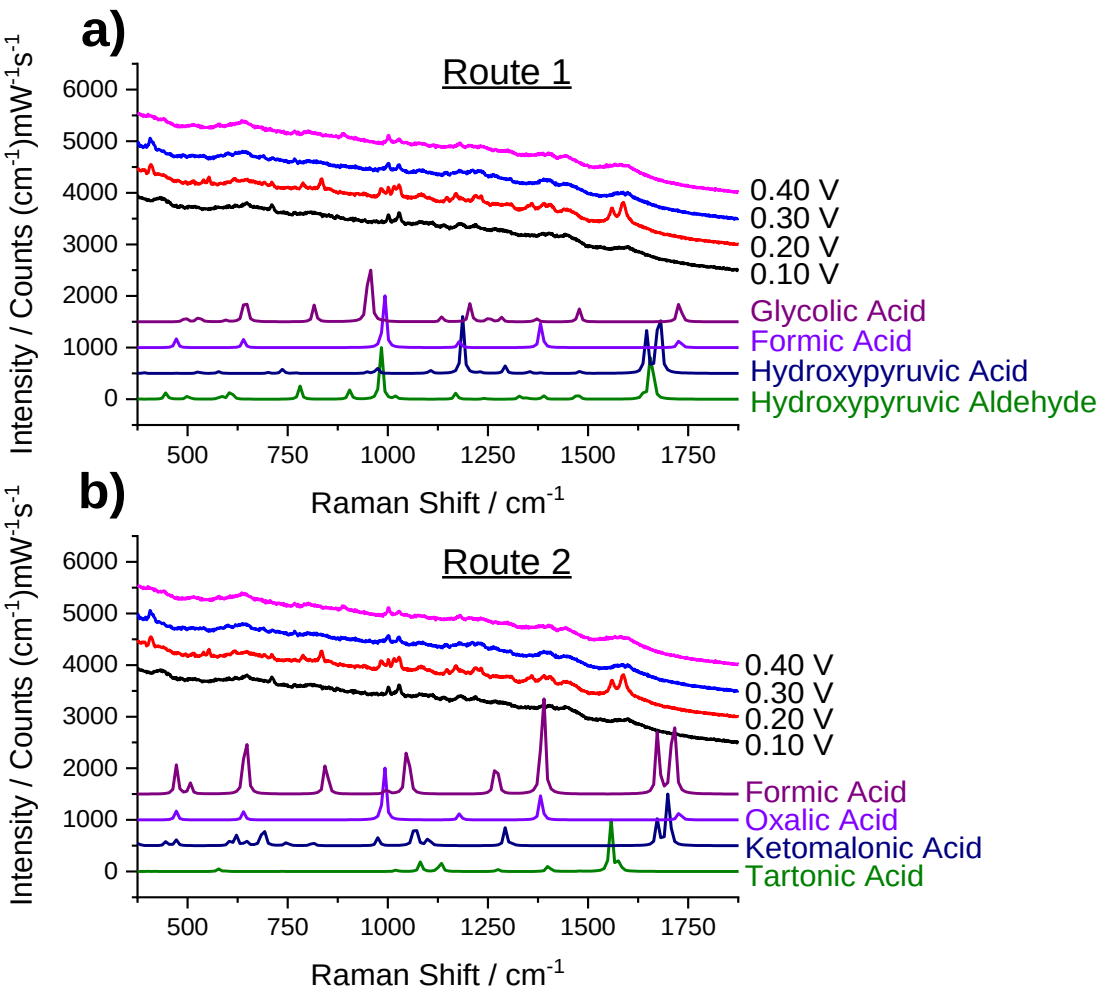

Figure 6.8: EC-SERS spectra of an Au SSV substrate in 0.1 M Glycerol in 0.1 M KOH from 0.10 V to 0.40 V *vs* Ag/AgO, plotted with DFT calculated Raman spectra of the initial species from a) Route 1 and b) Route 2 of the proposed glycerol oxidation mechanism.

6.2 Summary

In this chapter I have presented an *in situ* potential dependent SERS study into Au-catalysed glycerol electrooxidation in alkaline media. When investigating both Raman and calculated DFT spectra of the possible intermediates and products it was found that the spectra of these species contained many peaks with complex vibrational assignments. Therefore, identifying species by individual modes was very challenging and so more emphasis was made on the pattern of SERS peaks for identification. When doing so the intermediate species of glyceraldehyde and tartonic acid were distinguishable, providing evidence for the C1 oxidation pathway (Route 2).

6.3 References

[1] A.M. Bonastre, “Catalysts for Alcohol-Fuelled Direct Oxidation Fuel Cells,” Platin. Met. Rev. 57 (2013) 297–301. doi:10.1595/147106713X671871.

[2] B.C. Ong, S.K. Kamarudin, S. Basri, Direct liquid fuel cells: A review, Int. J. Hydrogen Energy. 42 (2017) 10142–10157. doi:10.1016/J.IJHYDENE.2017.01.117.

[3] C.-H. (Clayton) Zhou, J.N. Beltramini, Y.-X. Fan, G.Q. (Max) Lu, Chemoselective catalytic conversion of glycerol as a biorenewable source to valuable commodity chemicals, Chem. Soc. Rev. 37 (2008) 527–549. doi:10.1039/B707343G.

[4] Z. Gholami, A.Z. Abdullah, K.-T. Lee, Dealing with the surplus of glycerol production from biodiesel industry through catalytic upgrading to polyglycerols and other value-added products, Renew. Sustain. Energy Rev. 39 (2014) 327–341. doi:10.1016/J.RSER.2014.07.092.

[5] N. Benipal, J. Qi, Q. Liu, W. Li, Carbon nanotube supported PdAg nanoparticles for electrocatalytic oxidation of glycerol in anion exchange membrane fuel cells, Appl. Catal. B Environ. 210 (2017) 121–130. doi:10.1016/J.APCATB.2017.02.082.

[6] N. Benipal, J. Qi, J.C. Gentile, W. Li, Direct glycerol fuel cell with polytetrafluoroethylene (PTFE) thin film separator, Renew. Energy. 105 (2017) 647–655. doi:10.1016/J.RENENE.2016.12.028.

[7] S. Yongprapat, A. Therdthianwong, S. Therdthianwong, Au/C catalyst prepared by polyvinyl alcohol protection method for direct alcohol alkaline exchange membrane fuel cell application, J. Appl. Electrochem. 42 (2012) 483–490. doi:10.1007/s10800-012-0423-3.

[8] J.L. Bott-Neto, A.C. Garcia, V.L. Oliveira, N.E. de Souza, G. Tremiliosi-Filho, Au/C catalysts prepared by a green method towards C3 alcohol electrooxidation: A cyclic voltammetry and in situ FTIR spectroscopy study, J. Electroanal. Chem. 735 (2014) 57–62. doi:10.1016/J.JELECHEM.2014.10.010.

[9] K.X. Yao, X. Liu, Z. Li, C.C. Li, H.C. Zeng, Y. Han, Preparation of a Ru-

Nanoparticles/Defective-Graphene Composite as a Highly Efficient Arene-Hydrogenation Catalyst, ChemCatChem. 4 (2012) 1938–1942. doi:10.1002/cctc.201200354.

[10] J. Qi, L. Xin, D.J. Chadderdon, Y. Qiu, Y. Jiang, N. Benipal, C. Liang, W. Li, Electrocatalytic selective oxidation of glycerol to tartronate on Au/C anode catalysts in anion exchange membrane fuel cells with electricity cogeneration, Appl. Catal. B Environ. 154–155 (2014) 360–368. doi:10.1016/J.APCATB.2014.02.040.

[11] Y. Kwon, S.C.S. Lai, P. Rodriguez, M.T.M. Koper, Electrocatalytic Oxidation of Alcohols on Gold in Alkaline Media: Base or Gold Catalysis?, J. Am. Chem. Soc. 133 (2011) 6914–6917. doi:10.1021/ja200976j.

[12] J. Zhang, Y. Liang, N. Li, Z. Li, C. Xu, S.P. Jiang, A remarkable activity of glycerol electrooxidation on gold in alkaline medium, Electrochim. Acta. 59 (2012) 156–159. doi:10.1016/J.ELECTACTA.2011.10.048.

[13] J.F. Gomes, G. Tremiliosi-Filho, Spectroscopic Studies of the Glycerol Electro-Oxidation on Polycrystalline Au and Pt Surfaces in Acidic and Alkaline Media, Electrocatalysis. 2 (2011) 96–105. doi:10.1007/s12678-011-0039-0.

[14] Z. Zhang, L. Xin, J. Qi, D.J. Chadderdon, W. Li, Supported Pt, Pd and Au nanoparticle anode catalysts for anion-exchange membrane fuel cells with glycerol and crude glycerol fuels, Appl. Catal. B Environ. (2013) 29–39. doi:10.1016/j.apcatb.2013.01.045.

[15] E. Habibi, H. Razmi, Glycerol electrooxidation on Pd, Pt and Au nanoparticles supported on carbon ceramic electrode in alkaline media, Int. J. Hydrogen Energy. 37 (2012) 16800–16809. doi:10.1016/J.IJHYDENE.2012.08.127.

[16] Z. Zhang, L. Xin, W. Li, Supported gold nanoparticles as anode catalyst for anion-exchange membrane-direct glycerol fuel cell (AEM-DGFC), Int. J. Hydrogen Energy. 37 (2012) 9393–9401. doi:10.1016/J.IJHYDENE.2012.03.019.

[17] B. Katryniok, H. Kimura, E. Skrzyńska, J.S. Girardon, P. Fongarland, M. Capron, R. Ducoulombier, N. Mimura, S. Paul, F. Dumeignil, Selective

catalytic oxidation of glycerol: Perspectives for high value chemicals, Green Chem. 13 (2011) 1960–1979. doi:10.1039/c1gc15320j.

[18] G. Wu, X. Wang, T. Jiang, Q. Lin, Selective Oxidation of Glycerol with 3% H2O2 Catalyzed by LDH-Hosted Cr(III) Complex, Catalysts. 5 (2015) 2039–2051. doi:10.3390/catal5042039.

[19] I. Velázquez-Hernández, M.T. Oropeza-Guzmán, M. Guerra-Balcázar, L. Álvarez-Contreras, N. Arjona, Electrocatalytic Promotion of Pt Nanoparticles by Incorporation of Ni(OH)2 for Glycerol Electro-Oxidation: Analysis of Activity and Reaction Pathway, ChemNanoMat. 5 (2019) 68–78. doi:10.1002/cnma.201800317.

[20] N.I. Andersen, K. Artyushkova, I. Matanović, D.P. Hickey, S.D. Minteer, P. Atanassov, Spectro-Electrochemical Microfluidic Platform for Monitoring Multi-Step Cascade Reactions, ChemElectroChem. 6 (2019) 246–251. doi:10.1002/celc.201800578.

[21] Y. Kwon, K.J.P. Schouten, M.T.M. Koper, Mechanism of the Catalytic Oxidation of Glycerol on Polycrystalline Gold and Platinum Electrodes, ChemCatChem. 3 (2011) 1176–1185. doi:10.1002/cctc.201100023.

[22] A. Falase, K. Garcia, C. Lau, P. Atanassov, Electrochemical and in situ IR characterization of PtRu catalysts for complete oxidation of ethylene glycol and glycerol, Electrochem. Commun. 13 (2011) 1488–1491. doi:10.1016/J.ELECOM.2011.10.001.

[23] V.L. Oliveira, C. Morais, K. Servat, T.W. Napporn, G. Tremiliosi-Filho, K.B. Kokoh, Glycerol oxidation on nickel based nanocatalysts in alkaline medium – Identification of the reaction products, J. Electroanal. Chem. 703 (2013) 56–62. doi:10.1016/J.JELECHEM.2013.05.021.

[24] C.A. Ottoni, S.G. da Silva, R.F.B. De Souza, A.O. Neto, PtAu Electrocatalyst for Glycerol Oxidation Reaction Using a ATR-FTIR/Single Direct Alkaline Glycerol/Air Cell In Situ Study, Electrocatalysis. 7 (2016) 22–32. doi:10.1007/s12678-015-0277-7.

[25] A.C. Garcia, E.B. Ferreira, V. V. Silva de Barros, J.J. Linares, G. Tremiliosi-Filho, PtAg/MnOx/C as a promising electrocatalyst for glycerol electro-oxidation in alkaline medium, J. Electroanal. Chem. 793 (2017)

188–196. doi:10.1016/J.JELECHEM.2016.11.053.

[26] M. Simões, S. Baranton, C. Coutanceau, Electro-oxidation of glycerol at Pd based nano-catalysts for an application in alkaline fuel cells for chemicals and energy cogeneration, Appl. Catal. B Environ. 93 (2010) 354–362. doi:10.1016/J.APCATB.2009.10.008.

[27] Y. Holade, C. Morais, K. Servat, T.W. Napporn, K.B. Kokoh, Toward the Electrochemical Valorization of Glycerol: Fourier Transform Infrared Spectroscopic and Chromatographic Studies, ACS Catal. 3 (2013) 2403–2411. doi:10.1021/cs400559d.

[28] L. Prati, A. Villa, C.E. Chan-Thaw, R. Arrigo, D. Wang, D.S. Su, Gold catalyzed liquid phase oxidation of alcohol: the issue of selectivity, Faraday Discuss. 152 (2011) 353. doi:10.1039/c1fd00016k.

[29] Y. Kwon, M.T.M. Koper, Combining Voltammetry with HPLC: Application to Electro-Oxidation of Glycerol, Anal. Chem. 82 (2010) 5420–5424. doi:10.1021/ac101058t.

[30] Y. Kwon, Y. Birdja, I. Spanos, P. Rodriguez, M.T.M. Koper, Highly Selective Electro-Oxidation of Glycerol to Dihydroxyacetone on Platinum in the Presence of Bismuth, ACS Catal. 2 (2012) 759–764. doi:10.1021/cs200599g.

[31] N.E. de Souza, J.F. Gomes, G. Tremiliosi-Filho, Reactivity of 3-carbon-atom chain alcohols on gold electrode: A comparison to understand the glycerol electro-oxidation, J. Electroanal. Chem. 800 (2017) 106–113. doi:10.1016/J.JELECHEM.2016.08.019.

[32] Y. Zhang, M.J. Weaver, Application of surface-enhanced Raman spectroscopy to organic electrocatalytic systems: decomposition and electrooxidation of methanol and formic acid on gold and platinum-film electrodes, Langmuir. 9 (1993) 1397–1403. doi:10.1021/la00029a038.

[33] F.J.E. Scheijen, G.L. Beltramo, S. Hoeppener, T.H.M. Housmans, M.T.M. Koper, The electrooxidation of small organic molecules on platinum nanoparticles supported on gold: influence of platinum deposition procedure, J. Solid State Electrochem. 12 (2008) 483–495. doi:10.1007/s10008-007-0343-z.

[34] S.C.S. Lai, S.E.F. Kleijn, F.T.Z. Öztürk, V.C. van Rees Vellinga, J. Koning, P. Rodriguez, M.T.M. Koper, Effects of electrolyte pH and composition on the ethanol electro-oxidation reaction, Catal. Today. 154 (2010) 92–104. doi:10.1016/J.CATTOD.2010.01.060.

[35] R. Muralidharan, M. McIntosh, X. Li, In situ surface-enhanced Raman spectroscopic study of formic acid electrooxidation on spontaneously deposited platinum on gold, Phys. Chem. Chem. Phys. 15 (2013) 9716. doi:10.1039/c3cp51128f.

[36] H. Jeong, J. Kim, Insights into the Electrooxidation Mechanism of Formic Acid on Pt Layers on Au Examined by Electrochemical SERS, J. Phys. Chem. C. 120 (2016) 24271–24278. doi:10.1021/acs.jpcc.6b08611.

[37] G. Rostamikia, A.J. Mendoza, M.A. Hickner, M.J. Janik, First-principles based microkinetic modeling of borohydride oxidation on a Au(1 1 1) electrode, J. Power Sources. 196 (2011) 9228–9237. doi:10.1016/J.JPOWSOUR.2011.07.042.

[38] A.E. Russell, S.H. Pelfrey, J. Speed, S. Mahajan, P.N. Bartlett, J.J. Baumberg, Sphere Segment Void Structures: a Reproducible SERS Substrate for Electrochemical Studies, in: 41st Am. Chem. Soc. Cent. Reg. Meet., 2009.

[39] M.E. Abdelsalam, P.N. Bartlett, J.J. Baumberg, S. Cintra, T.A. Kelf, A.E. Russell, Electrochemical SERS at a structured gold surface, Electrochem. Commun. 7 (2005) 740–744. doi:10.1016/j.elecom.2005.04.028.

[40] G. Socrates, Infrared and Raman characteristic group frequencies, John Wiley & Sons, 2001. doi:10.1002/jrs.1238.

[41] E. Mendelovici, R.L. Frost, T. Kloprogge, Cryogenic Raman spectroscopy of glycerol, J. Raman Spectrosc. 31 (2000) 1121–1126. doi:10.1002/1097-4555(200012)31:12<1121::AID-JRS654>3.0.CO;2-G.

Chapter 7: Summary and future work

7.1 Overview

Surface enhanced Raman spectroscopy (SERS) is an powerful technique to study molecules at, or close to, metal surfaces [1]. When combined with electrochemical control, it can provide *in situ* analysis of electrode surfaces, allowing electrochemical reactions to be followed and the fundamental interactions between molecules and metal surfaces to be probed. The onset of modern computing and developments in the understanding of theoretical chemistry has allowed density functional theory (DFT) calculated Raman spectra to also be easily acquired, resulting in much more accurate and precise vibrational assignment. In this thesis, with the experimental control provided by electrochemistry and the analytical capabilities of SERS and calculated spectra, it has been possible to investigate adsorbate orientation, adsorbate-surface electrostatic interactions, intermediate formation, and mechanistic information for a variety of electrochemical reactions and systems.

In Chapter 3, the potential dependent orientation of 4-sulfanylbenzonitile (4-SBN), 3-SBN and 2-SBN monolayers was investigated. The SERS modes of all three monolayers were characterised by comparison to DFT calculated Raman spectra and by analysis of the band intensities, C≡N stretching vibration frequencies, and peak width of the ring breathing modes it was determined that they all underwent a change in orientation as the potential was increased. The nitrile group was found to be oriented closer to parallel to the surface with increasing potential via a variation in tilt (θ) and/or twist (χ) angle. Similarly, the orientation of the aromatic ring, defined by χ, was found to vary with potential, increasing slightly for 4-SBN and decreasing for 3-SBN and 2-SBN. These orientation changes were driven by the electrostatic interactions of the nitrile group and aromatic ring with the electrode surface.

In Chapter 4, the mechanisms of *p*-nitrothiophenol (PNTP) electroreduction and *p*-aminothiophenol (PATP) electrooxidation were investigated. When collecting SERS spectra for these species there was significant formation of the photocatalysed product p-p'-dimercaptoazobenzene (DMAB), therefore laser powers were kept at a minimum to eradicate that

pathway during PNTP reduction and minimise it during PATP oxidation, while maintaining high signal intensity. By comparison to DFT calculated Raman spectra the intermediates DMAB and p-nitrosothiophenol (PNSTP) were identified during PNTP electroreduction, indicating that both the unimolecular and dimerisation pathways were active. In addition, using the same analysis as in Chapter 3 it was determined PNTP underwent an orientation change at potentials above, and during, electroreduction. As the potential was moved negative the nitro group oriented to be closer to normal to the surface, via a decrease in θ and the plane of the aromatic ring also twisted with a reducing χ, both as a result of adsorbate-surface interactions previously described in Chapter 3. PATP electrooxidation was investigated in acidic and alkaline media. By comparison to DFT calculated Raman spectra, in acid 4'-mercapto-N-phenyl-1,4-quinone diimine (NPQDI), 4'-mercapto-N-phenyl-1,4-quinone diamine (NPQDA), 4'-mercapto-N-phenyl-1,4-quinone monoimine (NPQMI) and 4'-mercapto-N-phenyl-1,4-quinone monoamine (NPQMA) were identified, providing evidence of an N-C4 coupling pathway and additional hydrolysis reaction. In alkaline electrolyte, DMAB formation via an N-N coupling pathway and the corresponding reduction back to PATP via the intermediate p-p'-dimercaptohydrazobenzene (DMHAB) was observed.

In Chapter 5, the adsorption and orientation of two thioamide molecular wires (MWs), 1,4-benzenedicarbothioamide (BDTA) and 4,4'-(ethyne-1,2-diyl)dibenzodicarbothioamine (EDBTA), were investigated. It was initially proposed that the thioamide-surface bonding was via the C=S group, much like the thiol interaction of the monolayers in Chapters 3 and 4. However, when the DFT and SERS spectra of these MWs were compared there were clear discrepancies, with the highest intensity peaks being for vibrations in the plane of the aromatic ring. In addition, peaks assigned to N-H vibrations in the thioamide closest to the metal surface were not active. Therefore, It was determined that the MWs were bound via both C=S and NH_2 in a more perpendicular orientation to the surface. The potential dependence of EDBTA was also investigated and only small changes in the intensities of the IP vibrations were observed, indicating the molecule remained in a stable orientation across the potential window and did not interact further with the electrode surface.

In Chapter 6, the mechanism of Au-catalysed glycerol electrooxidation was investigated in alkaline media. The proposed intermediates of this reaction were many, and simple comparison of single peaks from the DFT calculated Raman spectra was insufficient to allow assignment. In addition, SERS intensities were low, and therefore, a different approach was required and the patterns of SERS peaks were used for species identification. By doing so, the intermediate species glyceraldehyde and tartonic acid were clearly identified, providing evidence for the C1 oxidation pathway.

7.2 Future Work

In Chapters 3 and 4, I have shown how nitrile and nitro functional groups can electrostatically interact with electrode surfaces. This could be extended to many additional molecules, such as chlorobenzenethiol, to further investigate the relative adsorbate-surface interactions between functional groups. In addition, it would be interesting to increase the length of these benzenethiol substituted molecules to allow probing of the adsorbate-surface interaction distance dependence. Furthermore, recent literature has suggested that variations in adsorbate orientation can influence additional reactions happening on the electrode surface, for example, how 4,4'-bipyridine accelerates the hydrogen evolution reaction on Au [2], or that 3-amino-1,2,3-triazole inhibits Cu corrosion [3], but imidazole has no such effect [4]. Therefore, by combining the greater understanding of potential-dependent orientation presented here, with these interesting initial studies in the literature, I believe a greater understanding of the effects of orientation on additional electrochemical reactions could be investigated in future work.

The plasmons generated at the surface of SERS active substrates have been recently found to promote catalysis [5]. The SSV substrates used in this thesis are highly tuneable and have been well characterised by Mahajan *et al.* including the how the void dimensions influence individual plasmon activity [6]. Therefore, it would be interesting to investigate the effect of individual plasmons on catalytic reactions by appropriately manufacturing a selection of SSV substrates with various void shapes and sizes. Furthermore, the adsorbates and redox systems in this thesis have been limited to those that bind to Au, as this metal is SERS active. However, it is possible to deposit a thin layer of

SERS inactive material onto the substrate surface, where the plasmons generated from the Au penetrate the additional material and still provide good signal enhancement. This technique is called borrowed SERS [1] and a recent study by Jeong and Kim has provided mechanistic insight of formic acid electrooxidation on Pt, with an underlying Au substrate [7]. Borrowed SERS would allow the redox processes and potential dependent orientation of adsorbates on a different metal surface to be investigated, such as expanding Chapter 7 to explore glycerol's electrooxidation mechanism on Pt or Pd using SERS.

7.3 References

[1] P.L. Stiles, J.A. Dieringer, N.C. Shah, R.P. Van Duyne, Surface-Enhanced Raman Spectroscopy, Annu. Rev. Anal. Chem. 1 (2008) 601–626. doi:10.1146/annurev.anchem.1.031207.112814.

[2] Y. Yonezawa, H. Minamimoto, F. Nagasawa, M. Takase, S. Yasuda, K. Murakoshi, In-situ electrochemical surface-enhanced Raman scattering observation of molecules accelerating the hydrogen evolution reaction, J. Electroanal. Chem. 800 (2017) 7–12. doi:10.1016/j.jelechem.2017.04.049.

[3] Y. Wan, Z. Qin, Q. Xu, M. Chen, Y.L. Min, M. Li, Corrosion inhibition activity and adsorption behavior of 3-amino-1, 2, 4-triazole on copper, Int. J. Electrochem. Sci. 12 (2017) 10701–10713. doi:10.20964/2017.11.68.

[4] E.F. Silva, M.C.E. Bandeira, W.A. Alves, O.R. Mattos, Surface-Enhanced Raman Scattering and Electrochemical Investigations on the Adsorption of Imidazole: Imidazolium Couple and Its Implications on Copper Corrosion Inhibition, J. Electrochem. Soc. 165 (2018) C375–C384. doi:10.1149/2.0841807jes.

[5] X.J. Chen, G. Cabello, D.Y. Wu, Z.Q. Tian, Surface-enhanced Raman spectroscopy toward application in plasmonic photocatalysis on metal nanostructures, J. Photochem. Photobiol. C Photochem. Rev. 21 (2014) 54–80. doi:10.1016/j.jphotochemrev.2014.10.003.

[6] S. Mahajan, R.M. Cole, B.F. Soares, S.H. Pelfrey, A.E. Russell, J.J.

Baumberg, P.N. Bartlett, Relating SERS intensity to specific plasmon modes on sphere segment void surfaces, J. Phys. Chem. C. 113 (2009) 9284–9289. doi:10.1021/jp900661u.

[7] H. Jeong, J. Kim, Insights into the Electrooxidation Mechanism of Formic Acid on Pt Layers on Au Examined by Electrochemical SERS, J. Phys. Chem. C. 120 (2016) 24271–24278. doi:10.1021/acs.jpcc.6b08611.

Appendix A

This is additional information for Chapter 2: Experimental and theoretical methods.

A.1 Macro Script

The following macro script was written using Pullover's Macro Creator and is the first in a set of 25 for a typical EC-SERS experiment. Here, the potential is held at -0.60 V *vs.* Pt QRE and a Raman spectrum is acquired and saved, before moving onto the next macro that acquires and saves a spectra at -0.55 V *vs.* Pt QRE. The rest of the macros take and save Raman spectra as the potential is moved from -0.55 V to -0.20 V in 50 mV increments and back down to -0.60 V in 100 mV increments.

```
WinActivate, NOVA  (1.10.1.9) ahk_class
WindowsForms10.Window.8.app.0.3ce0bb8_r11_ad1

# This command begins the NOVA script to control the electrochemistry for
the whole experiment – the timings of which are matched the macro
presented here.

Click, 84, 966 Left, Down

Click, 92, 974, 0

Sleep, 78

Click, 92, 974 Left, Up

Sleep, 716000

# This wait of 5 minutes allows the potential applied using nova to stabilise
and reach the 'actual' potential. This is only present in this macro, the
remaining 24 have a wait of only 100 seconds.

WinActivate, WiRE

Sleep, 100

Click, 111, 104 Left, 1
```

```
Sleep, 100

Sleep, 170000

WinActivate,  ahk_class tooltips_class32

# This set of commands acquires a Raman spectrum.

Sleep, 333

Sleep, 100

Click, 28, -1005, 0

Sleep, 100

Sleep, 296

Click, 29, -1005, 0

Sleep, 100

Click, 38, 45 Left, 1

Sleep, 1000

Click, 68, 193 Left, 1

Sleep, 1000

Send, {LControl Down}

Sleep, 1000

Sleep, 1000

Send, {a}

Sleep, 1000

Sleep, 1000

Send, {LControl Up}

Sleep, 1000

Sleep, 1000
```

SendRaw, C:\Users\Raman\Documents\Alex\Post 20-7-2016 - Mainly MBN stark effect SERS\Automated experiments\Raman\1 Automated experiment extended scan -0.60 V

Sleep, 1000

Send, {Enter}

This set of commands saves the data in a specified folder with a unique file name.

Sleep, 1793

Goto, negative550mV

This command moves onto the next macro in the sequence.

A.2 Spot Size Determination

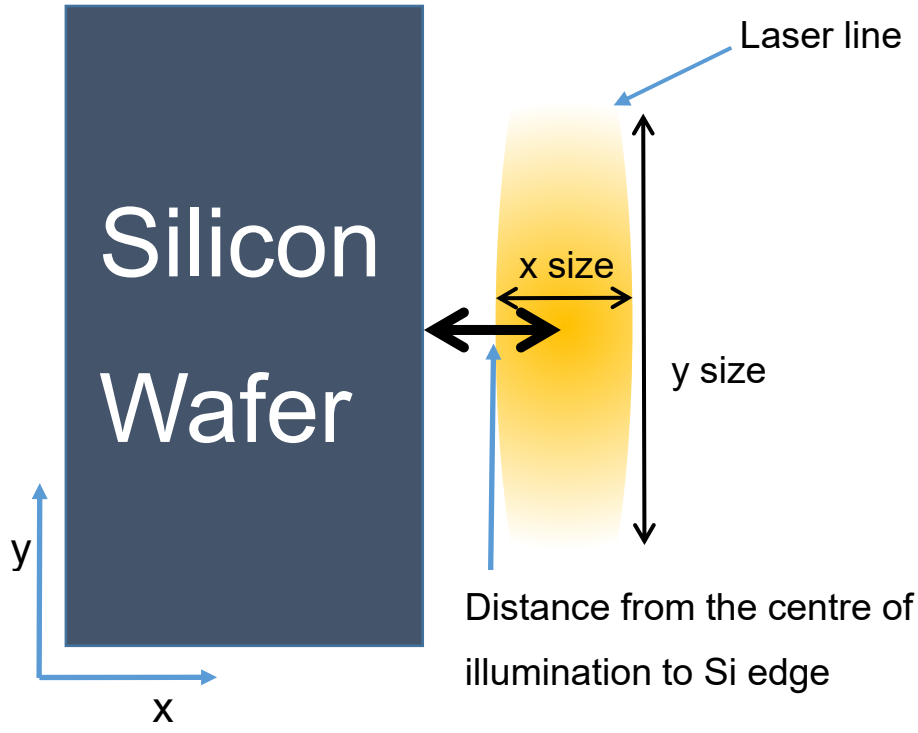

Figure A.1: Pictorial representation of measuring the laser line size.

Figure A.1 shows how the spot size was determined for the InVia Raman spectrometer used in all the experiments in this thesis. The spot's had line geometry and Raman spectra were taken at different distances away from the silicon wafer surface in both the x and y plane. The first spectrum was taken with the spot off set from the wafer and moved then sequentially onto the wafer itself. By examining how the intensity of the silicon Raman peak changed as the spot was moved onto the wafer the size of the spot in that plane can be determined.

Figure A.2 and A.3 shows Raman spectra at different distances from the edge of a silicon wafer in the y and x planes, alongside the intensity of the Si peak at 520 cm^{-1}. In the y plane it can be seen that as the laser line is moved closer to the edge of the silicon wafer the intensity of the silicon peak increased, beginning at 14 µm away up to a maximum intensity at -6 µm. In the x plane the intensity increased at 2 µm away up to a maximum intensity at -6 µm.

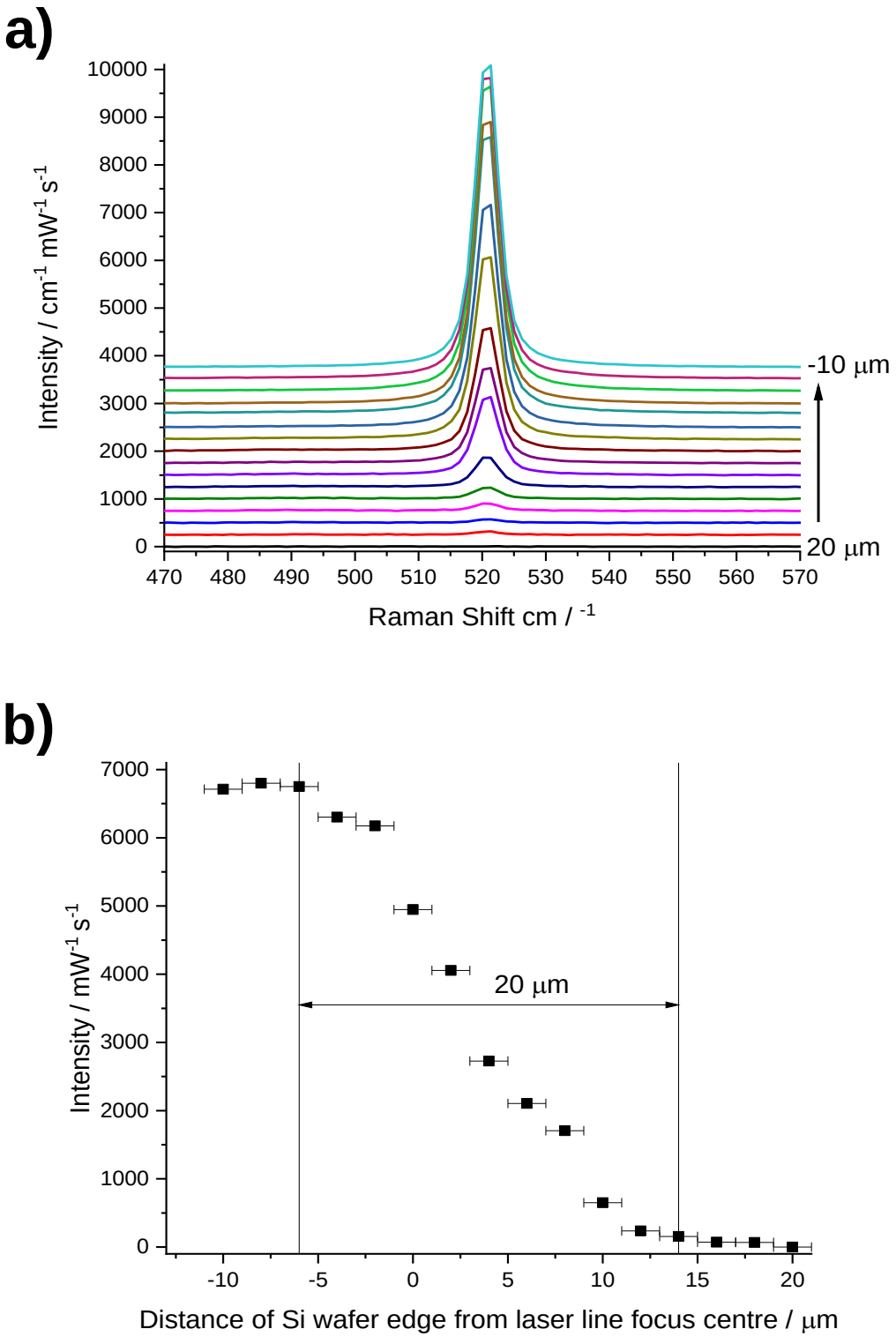

Figure A.2: a) Raman spectra at difference distances from the edge of a silicon wafer. The distance indicates how far away from the silicon edge the spectra is taken in the y-plane. Negative numbers indicate that the spectra is on the Si surface. Spectra acquired at 1 % power with an acquisition time of 10 s and area offset for clarity. b) the intensity of the 520 cm^{-1} Si peak plotted the differing distances from the Si wafer edge in the y plane. Error = ± 1 μm

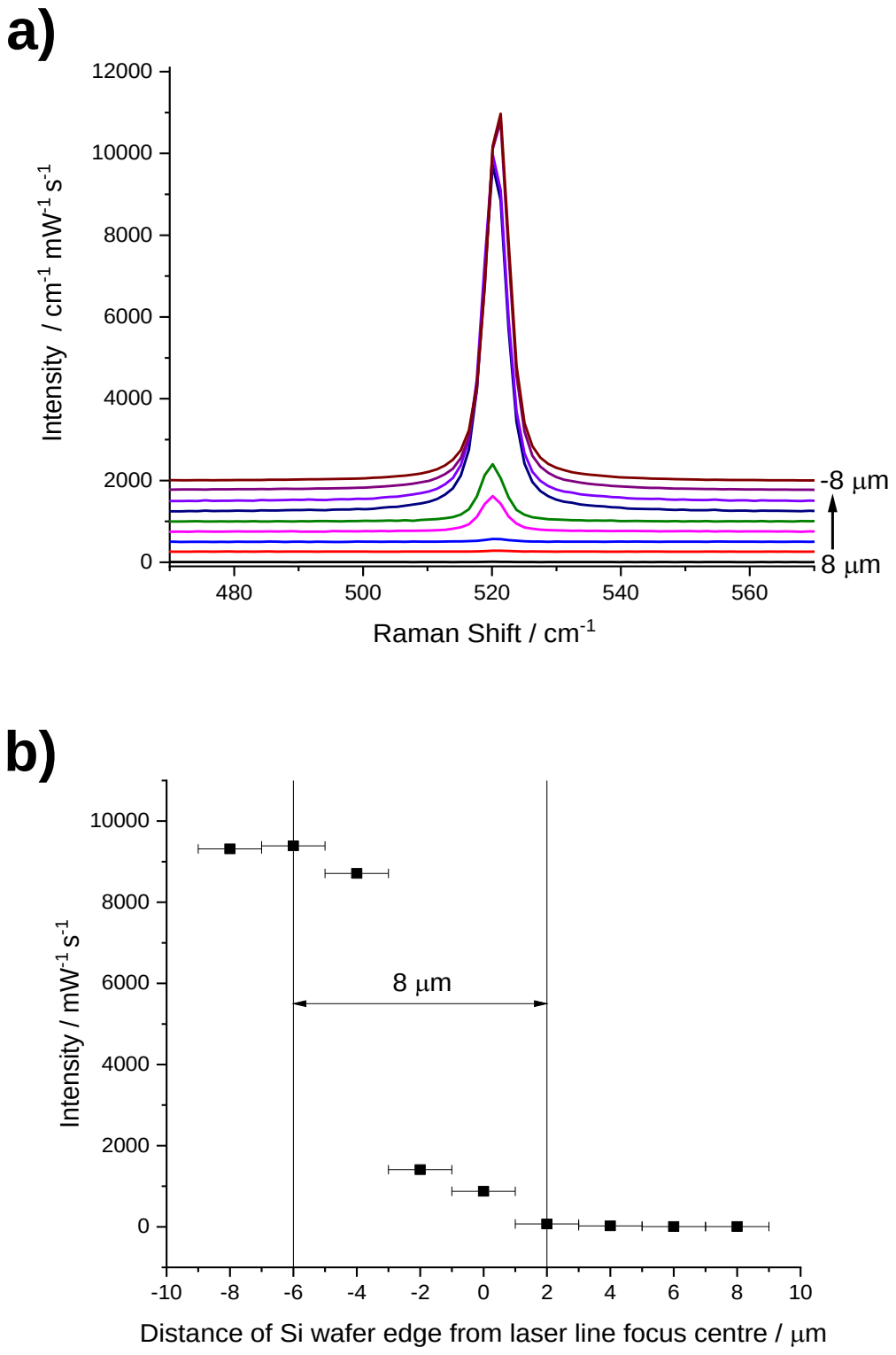

Figure A.3: a) Raman spectra at difference distance from the edge of a silicon wafer. The distance indicates how far away from the Si edge the spectra is taken in the x-plane. Negative numbers indicate that the spectra is on the Si surface. Spectra acquired at 1 % power with an acquisition time of 10 s and are offset for clarity. b) the intensity of the 520 cm^{-1} Si peak plotted at the differing distance from the SI wafer edge in the x plane. Error = ± 1 μm.

The distance over which the intensity of the Si peak increased gives an indication of the laser spot size in that direction. Therefore, the spot size was determined to be 20 ± 2 µm x 8 ± 2 µm, with an area of 160 µm^2 ± 60 µm^2, and is shown pictorially in Figure A.4.

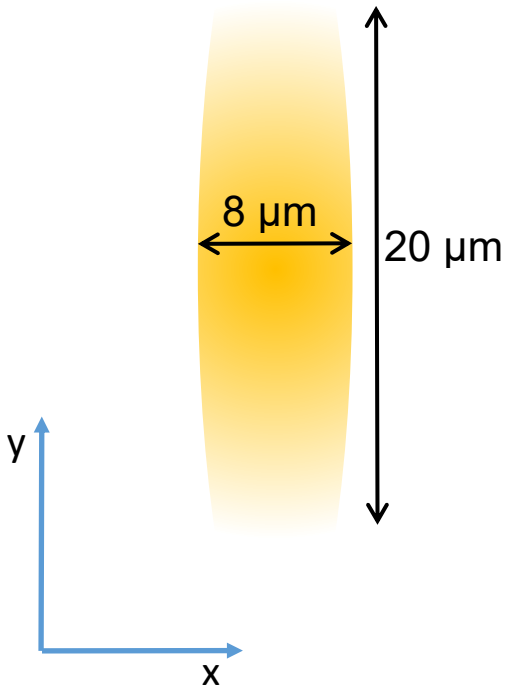

Figure A.4: The laser line size.

Appendix B

This appendix contains tables accompanying Chapter 3: Potential dependent orientation of sulfanylbenzonitrile monolayers monitored by SERS.

B.1 Sulfanylbenzonitrile vibrational assignment

The vibrational assignments of SAMs of 4-SBN, 3-SBN and 2-SBN are tabulated in Table B1, B2 and B3. Calculated DFT Raman spectra were generated with Gaussian 09W [1] and GaussView 5 [2], using each molecule adsorbed on a Au_5 cluster, a 6-311G+(d', p') basis set for the H, N, C and S atoms, a LANL2DZ for the Au valence electrons and LANL2DZ ECP for the Au core electrons In addition, the generalised gradient approximation functional B3LPY was used and the solvent interactions were modelled using the PCM model, with ethanol as the solvent ($\varepsilon = 24.5$), matching the experimental conditions.

Mode	Wilson Number	Calculated / cm^{-1}	SERS / cm^{-1}
δ_{C-C}	16a (OOP)*	413 (vw)	431 (vw)
δ_{C-N}	CN (OOP)*+	446 (w)	446 (vw)
δ_{C-H}	6a*	553 (m)	582 (m)
δ_{C-N}	CN (IP)*	564 (w, sh)	
δ_{C-C}	16a (OOP)*	571 (w, sh)	603 (vw, sh)
δ_{C-C}	6b (IP)*	658 (w)	642 (vw)
δ_{C-H}	10b (OOP)*	777 (m)	777 (vw)
δ_{C-H}	10a (IP)*	852 (vw, sh)	
δ_{C-H}	5 (IP)*	985 (vw)	
δ_{C-H}	17a (OOP)*	996 (vw)	999 (vw, sh)
δ_{C-C}	12 (IP)*	1024 (w)	
δ_{C-C}	1 (IP)*	1066 (s)	1077 (s)
δ_{C-H}	18b (IP)*+	1129 (w)	1131 (vw, sh)
δ_{C-H}	9a (IP)*+	1201 (s)	1177 (m)
δ_{C-H}	9b (IP)*	1212 (vw, sh)	1201 (w)
ν_{C-C}	14 (IP)*	1287 (vw)	
δ_{C-H}	3 (IP)*	1334 (vw)	
δ_{C-H} / δ_{C-C}	18b (IP)* / 19b (IP)*+	1407 (vw)	
δ_{C-H} / ν_{C-C}	18a (IP)* / 19a (IP)*	1504 (w)	
ν_{C-C}	8b (IP)*	1557 (vw, sh)	
ν_{C-C}	8a (IP)*	1598 (s)	1585 (s)
ν_{C-N}	CN (IP)*+	2223 (s)	2227 (m)

Table B1: Calculated and SERS vibrational assignment of 4-SBN. Assignments were based on the work of Holze [3], shown by $^{+}$, or via a DFT Raman spectra calculated 4-SBN molecule adsorbed onto an Au_5 cluster, shown by *. Wilson number and mode information taken from Merlin *et al.* [4]. *v* = stretch, *δ* = bend, IP = in plane of the benzene ring, OOP = out of plane of the benzene ring, s = strong, m = medium, w = weak, vw = very weak, sh = shoulder.

Mode	Wilson Number	Calculated / cm^{-1}	SERS / cm^{-1}
δ_{C-N}	C-N (OOP)$^{+*}$	387 (m)	416 (m)
δ_{C-C}	16a (OOP)*	465 (vw, sh)	454 (w)
δ_{C-H}	6a (IP)*	467 (w)	462 (w)
δ_{C-N}	CN (IP)*	557 (w)	585 (w)
δ_{C-C}	16a (OOP)*	615 (w)	679 (w)
δ_{C-C}	6b (IP)$^{+*}$	682 (w)	700 (vw)
δ_{C-C}	16a (OOP)*	703 (vw, sh)	718 (w)
δ_{C-H}	10b (OOP)$^{+*}$	813 (vw, sh)	766 (vw)
δ_{C-C}	6b (IP)*	817 (m)	838 (w)
δ_{C-H}	10a (IP)*	929 (vw, sh)	
δ_{C-H}	18a (IP)$^{+}$ / 5 (IP)*	941 (vw)	
δ_{C-H} / δ_{C-C}	18a (IP)$^{+}$ / 12 (IP)	1004 (s)	996 (s)
δ_{C-C}	1 (IP)*	1077 (s)	1078 (m)
δ_{C-H}	18b (IP)*	1108 (m)	1133 (w)
δ_{C-H}	9b (IP)*	1201 (w, sh)	1172 (vw)
δ_{C-H}	9a (IP)$^{+*}$	1205 (s)	1192 (m)
ν_{C-C}	14 (IP)*	1287 (m)	
δ_{C-H}	3 (IP)*	1338 (w)	
δ_{C-H} / δ_{C-C}	18b (IP)* / 19b (IP)$^{+*}$	1418 (m)	
δ_{C-H} / ν_{C-C}	18a (IP)* / 19a (IP)*	1489 (m)	
ν_{C-C}	8b (IP)*	1564 (s)	1559 (w, sh)
ν_{C-C}	8a (IP)* / 8b (IP)$^{+}$	1598 (s)	1578 (m)
ν_{C-N}	CN (IP)$^{+*}$	2225 (s)	2227 (w)

Table B2: Calculated and SERS vibrational assignment of 3-SBN. Assignments were based on the work of Holze [3], shown by $^{+}$, or via a DFT Raman spectra calculated 4-SBN molecule adsorbed onto an Au_5 cluster, shown by *. Wilson number and mode information taken from Merlin *et al*. [4]. *v* = stretch, δ = bend, IP = in plane of the benzene ring, OOP = out of plane of the benzene ring, s = strong, m = medium, w = weak, vw = very weak, sh = shoulder.

Mode	Wilson Number	Calculated / cm^{-1}	SERS / cm^{-1}
δ_{C-N}	C-N (OOP)$^{+*}$	387 (m)	397 (m)
δ_{C-C}	16a (OOP)*	481 (vw, sh)	
δ_{C-H}	6a*	499 (w)	506 (w)
δ_{C-N}	C-N (IP)*	586 (w)	577 (w)
δ_{C-C}	6b (IP)$^{+*}$	671 (w)	671 (vw)
δ_{C-C}	16a (OOP)*	751 (vw, sh)	767 (vw)
δ_{C-H}	10b (OOP)$^{+*}$	778 (vw, sh)	779 (w)
δ_{C-C}	6b (IP)*	781 (m)	
δ_{C-H}	10a (IP)*	895 (vw)	
δ_{C-H}	17a (OOP)*	977 (vw, sh)	
δ_{C-H}	5 (IP)*	1013 (vw, sh)	1024 (w, sh)
δ_{C-C}	1 (IP)*	1032 (s)	1035 (m)
δ_{C-C}	12 (IP)*	1058 (w)	
δ_{C-H}	18b (IP)$^{+*}$	1133 (m)	
δ_{C-H}	9b (IP)*	1195 (w, sh)	1168 (w)
δ_{C-H}	9a (IP)$^{+*}$	1204 (m)	1196 (w)
δ_{C-H}	3 (IP)*	1282 (w)	
ν_{C-C}	14 (IP)*	1295 (w)	
δ_{C-H} / δ_{C-C}	18b (IP)* / 19b (IP)$^{+*}$	1453 (m)	
δ_{C-H} / ν_{C-C}	18a (IP)* / 19a (IP)*	1478 (m)	
ν_{C-C}	8b (IP)*	1566 (s)	1557 (m)
ν_{C-C}	8a (IP)*	1595 (s)	1579 (m)
ν_{C-N}	C-N (IP)$^{+*}$	2218 (s)	2221 (w)

Table B3: Calculated and SERS vibrational assignment of 2-SBN. Assignments were based on the work of Holze [3], shown by $^{+}$, or via a DFT Raman spectra calculated 4-SBN molecule adsorbed onto an Au_5 cluster, shown by *. Wilson number and mode information taken from Merlin *et al.* [4]. *v* = stretch, *δ* = bend, IP = in plane of the benzene ring, OOP = out of plane of the benzene ring, s = strong, m = medium, w = weak, vw = very weak, sh = shoulder.

B.2 Error Calculation

The error in the Raman shift of spectra was calculated by measuring the change in shift of SERS peaks while the potential was held at -0.10 V, taking a spectrum every 5 minutes. Figure B.1 shows how the Raman shift of the 1075 cm^{-1} peak of a 4-SBN SAM adsorbed on Au SSV varies in this experiment. By calculating the standard deviation of these Raman shifts the error was determined to be 0.254 cm^{-1}.

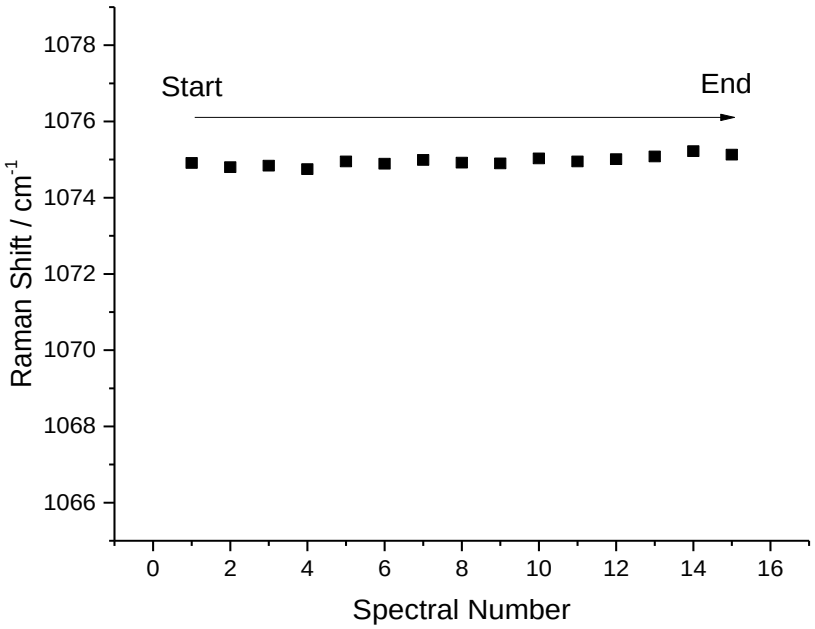

Figure B.1: Plot of the Raman shift of the SERS peak at 1075 cm^{-1} of a 4-SBN SAM. Spectra taken from a 4-SBN SAM on an Au SSV substrate submerged in a 0.1 M TBATFB/ethanol electrolyte held at -0.10 V *vs.* Pt QRE, with spectra taken every 5 minutes.

The error in peak intensity was measured in exactly the same way and calculated both for the raw intensity and the normalised intensity, as shown in Figure B.2. The resulting errors are 155 mW^{-1} s^{-1} and 0.0832 respectively.

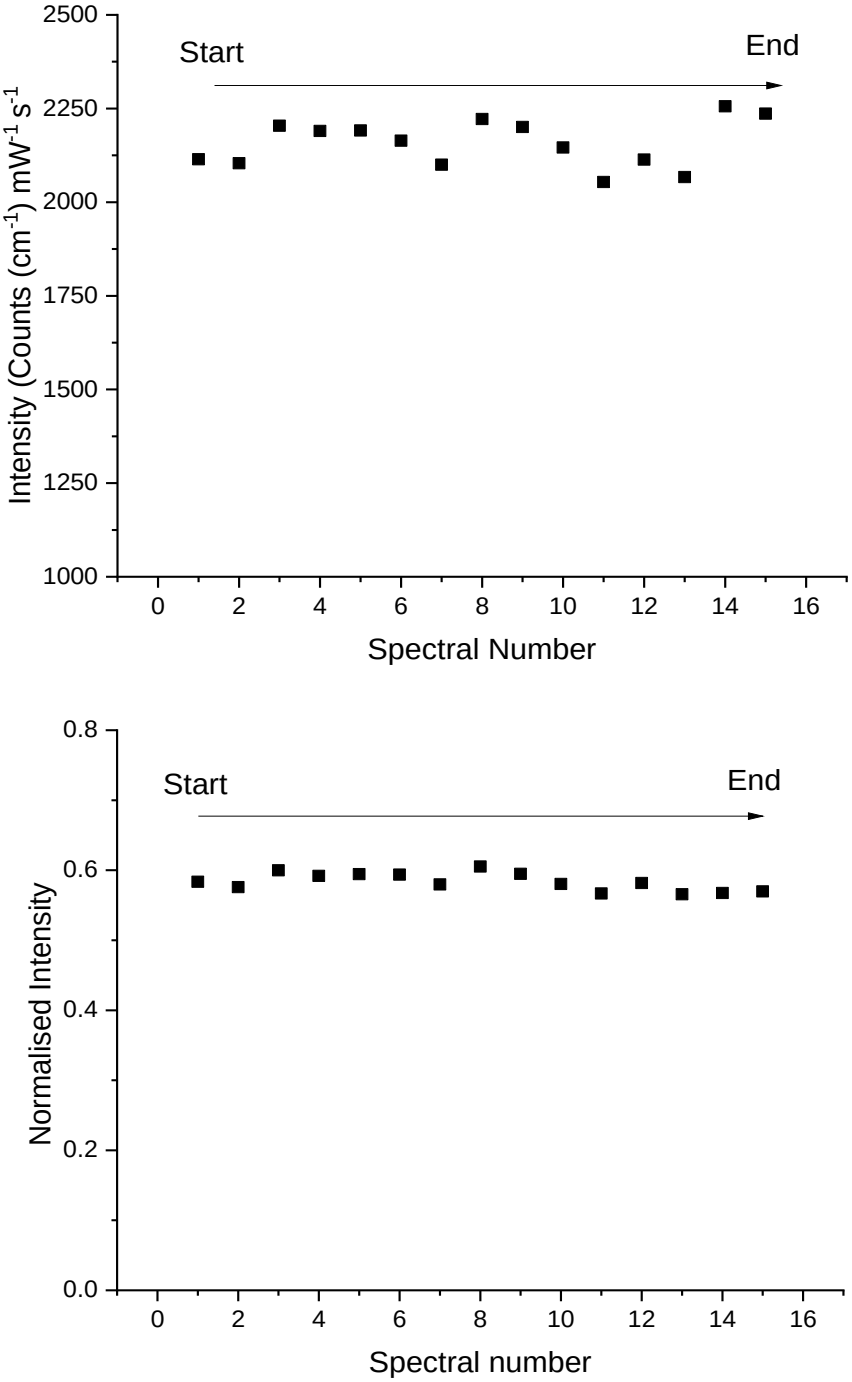

Figure B.2: Plot of the raw intensity and normalised intensity of the SERS peak at 1075 cm^{-1} of a 4-SBN SAM. Spectra taken from a 4-SBN SAM on an Au SSV substrate submerged in a 0.1 M TBATFB/ethanol electrolyte held at -0.10 V *vs.* Pt QRE, with spectra taken every 5 minutes.

B.3 References

[1] M.J. Frisch, G.W. Trucks, H.B. Schlegel, G.E. Scuseria, M.A. Robb, J.R. Cheeseman, G. Scalmani, V. Barone, G.A. Petersson, H. Nakatsuji, X. Li, M. Caricato, A. Marenich, J. Bloino, B.G. Janesko, R. Gomperts, B. Mennucci, H.P. Hratchian, J. V. Ortiz, A.F. Izmaylov, J.L. Sonnenberg, D. Williams-Young, F. Ding, F. Lipparini, F. Egidi, J. Goings, B. Peng, A. Petrone, T. Henderson, D. Ranasinghe, V.G. Zakrzewsk, J.G. I, N. Rega, G. Zheng, W. Liang, M. Hada, M. Ehara, K. Toyota, R. Fukuda, J. Hasegawa, M. Ishida, T. Nakajima, Y. Honda, O. Kitao, H. Nakai, T. Vreven, K. Throssell, J.A. Montgomery, J.E. Peralta, F. Ogliaro, M. Bearpark, J.J. Heyd, E. Brothers, K.N. Kudin, V.N. Staroverov, T. Keith, R. Kobayashi, J. Normand, K. Raghavachari, A. Rendell, J.C. Burant, S.S. Iyengar, J. Tomasi, M. Cossi, J.M. Millam, M. Klene, C. Adamo, R. Cammi, J.W. Ochterski, R.L. Martin, K. Morokuma, O. Farkas, J.B. Foresman, D.J. Fox, Gaussian, (2009). http://gaussian.com/.

[2] R. Dennington, T. Keith, J. Millam, GaussView, (2009). http://gaussian.com/.

[3] R. Holze, Competition of anchoring groups in adsorption on gold electrodes - A comparative spectroelectrochemical study of 4-mercaptobenzonitrile and aromatic nitriles, J. Solid State Electrochem. 17 (2013) 1869–1879. doi:10.1007/s10008-013-2076-5.

[4] J.C. Merlin, J.P. Cornard, A Pictorial Representation of Normal Modes of Vibration Using Vibrational Symmetry Coordinates, J. Chem. Educ. 83 (2006) 1393. doi:10.1021/ed083p1393.

Appendix C

This appendix contains tables accompanying Chapter 4: *p*-nitrothiophenol electroreduction and *p*-aminothiophenol electrooxidation

C.1 PNTP electroreduction and PATP electrooxidation intermediates and products vibrational assignment

The SERS and DFT calculated Raman vibrational assignments of PNTP and PATP (Table C.1) and the DFT vibrational assignments of PNSTP, PHATP (Table C.2), DMAOB, DMAB, DMHAB (Table C.3). The SERS and DFT vibrational assignments of NPQDI, NPQMA (Table C.4), NPQMI, NPQMA (Table B.5), DMAB and DMHAB (Table B.6) Calculated DFT Raman spectra were generated with Gaussian 09W [1] and GaussView 5 [2], using each molecule adsorbed on a Au_5 cluster, a 6-311G+(d', p') basis set for the H, N, O, C and S atoms, a LANL2DZ for the Au valence electrons and LANL2DZ ECP for the Au core electrons In addition, the generalised gradient approximation functional B3LYP was used and the solvent interactions were modelled using the PCM model, with water as the solvent (ε = 78.4), matching the experimental conditions. DFT frequencies scaled by 0.981 as per Zhao *et al.* [3].

PNTP				PATP			
Mode	**Wilson Number**	**Calculated / cm^{-1}**	**SERS / cm^{-1}**	**Mode**	**Wilson number**	**Calculated / cm^{-1}**	**SERS / cm^{-1}**
δ_{C-C}	6a	325	330	δ_{C-C}	6a	373	391
δ_{C-C}	16a	419	410	δ_{C-C}	16a	423	
ν_{Au-C} / δ_{C-N}		517	529	δ_{C-C} + δ_{C-H}	10b + 17b	520	544
δ_{C-C}	6b	644		δ_{C-C} + ν_{S-C}	6a	623	636
δ_{C-C}	6a	693	724	δ_{C-C}	6b	654	
δ_{C-H}	5	721	741	δ_{C-H}	16a	719	727
δ_{C-C} + ν_{C-N}	6a	830	855	δ_{C-C}	6a	836	817
				δ_{C-H}	10a	840	
δ_{C-C}	12	1026	1009	δ_{C-C}	12	1016	1006
ν_{C-C}	1	1084	1081	ν_{C-C}	1	1090	1075
δ_{C-H} + ν_{C-N}	18a	1110	1146	δ_{C-H}	9a	1210	1184
δ_{C-H}	9a	1202	1181				
δ_{C-H} + ν_{C-N}	9a	1296	1310	δ_{C-H} ν_{C-N}	18a	1338	1315
ν_{C-C} + δ_{C-H}	14 + 9b	1357		ν_{C-C} + δ_{C-H}	14 + 9b	1357	
ν_{C-C} + δ_{C-H}	19b + 18b	1416					
ν_{C-C} + δ_{C-H}	19a + 18a	1505		ν_{C-C} + δ_{C-H}	19a + 18a	1523	1578
ν_{C-C} + δ_{C-H}	8a + 9a	1607	1572	ν_{C-C} + δ_{C-H}	8a + 9a	1630	1581

Table C.1: Calculated and SERS vibrational assignment of PNTP and PATP from DFT Raman spectra, calculated from a geometry optimized PNTP or PATP molecule adsorbed on an Au_5 cluster. Wilson number and mode information taken from Merlin and Cornard [4]. ν = stretch, δ = bend.

PNSTP			PHATP		
Mode	**Wilson Number**	**Calculated / cm^{-1}**	**Mode**	**Wilson Number**	**Calculated / cm^{-1}**
δ_{Au-C}		346	δ_{O-H}		362
δ_{Au-C}		370	δ_{O-H}		372
			δ_{O-H} + δ_{N-H}		484
ν_{Au-C} / $\delta_{C=O}$		542	δ_{C-C} + δ_{C-H}	10b + 17b	532
			δ_{N-H}		595
δ_{C-C}	6b	641	δ_{C-C}	6b	650
δ_{C-C} / $\delta_{C=O}$	6a	701	δ_{C-C} / δ_{N-H}	6a	696
δ_{C-C} / ν_{C-N}	6a	838	δ_{C-H}	10a	837
δ_{C-H}	10a	863	δ_{C-C} + δ_{N-H}	6a	858
δ_{C-C}	12	1020	δ_{C-C} + ν_{N-O}	12	1013
			δ_{C-C} + ν_{N-O}	12	1020
ν_{C-C}	1	1077	ν_{C-C}	1	1090
δ_{C-H} + ν_{C-N}	9a	1161	δ_{C-H}	9a	1203
δ_{C-H} + ν_{C-N}	9a	1229	δ_{C-H} + ν_{C-N} + δ_{O-H}	9a	1281
δ_{C-H}	9b	1326	ν_{C-C} + δ_{C-H}	14 + 9b	1328
ν_{C-C}	14	1354	ν_{C-C} + δ_{C-H}	14 + 9b	1336
δ_{C-C} + δ_{C-H} + $\nu_{C=O}$	19b + 18b	1398			
δ_{C-C} + δ_{C-H} + $\nu_{C=O}$	19b + 18b	1440	δ_{O-H}		1385
ν_{C-C} + δ_{C-H}	19a + 18a	1503	ν_{C-C} + δ_{C-H}	19a + 18a	1518
ν_{C-C} + δ_{C-H}	8b + 9b	1592	ν_{C-C} + δ_{C-H} + δ_{N-H}	8b + 9b	1609
ν_{C-C} + δ_{C-H}	8a + 9a	1614	ν_{C-C} + δ_{C-H}	8a + 9a	1629

Table C.2: Calculated vibrational assignment of PNSTP and PHATP from DFT Raman spectra, calculated from a geometry optimized PNSTP or PHATP molecule adsorbed on an Au_5 cluster. Wilson number and mode information taken from Merlin and Cornard [4]. ν = stretch, δ = bend.

DMAOB			DMAB			DMHAB		
Mode	Wilson Number	Calculated / cm^{-1}	Mode	Wilson Number	Calculated / cm^{-1}	Mode	Wilson Number	Calculated / cm^{-1}
δ_{C-S}		365	δ_{C-S} (IP)		358	δ_{C-S}		377
δ_{C-C}	16a (Ring 1 + 2)	387	δ_{C-C}	16a	429	δ_{C-C}	16a	423
δ_{C-S}		409						
ν_{C-S}		466	ν_{C-S} (IP)		469	ν_{C-S}		452
ν_{C-S}		526				δ_{N-H}		473
δ_{C-C}	10b (Ring 1 + 2)	544	δ_{C-C}	10b	518	$\delta_{C-C} + \delta_{N-H}$	10b	538
δ_{C-C}	6b (Ring 2)	641	δ_{C-C}	6b	645	δ_{C-C}	6b	648
δ_{C-C}	6b (Ring 1)	647						
δ_{C-C}	6a (Ring 2)	657				δ_{C-C}	6a	670
δ_{C-C}	16a (Ring 1)	732	δ_{C-C}	6a	722	δ_{C-C}	16a	725
δ_{C-C}	6a (Ring 1)	734	δ_{C-C}	16a	734			
δ_{C-C}	16a (Ring 2)	737				δ_{C-H}	10a	834
δ_{C-C}	6a (Ring 1 + 2)	840	δ_{C-H}	10a	875	δ_{C-C}	6a	840
$\delta_{N=N} + \delta_{C-O}$		893	$\delta_{N=N}$		924			
δ_{C-C}	12 (Ring 2)	1020	δ_{C-C}	12	1023	δ_{C-C}	12	1014
δ_{C-C}	12 (Ring 1)	1025						
ν_{C-C}	1	1084	ν_{C-C}	1	1082	ν_{C-C}	1	1089
			δ_{C-H}	18b	1119	δ_{C-H}	18b	1124
δ_{C-H}	9a (Ring 1)	1189	δ_{C-H}	9a	1168	$\delta_{C-H} + \nu_{N-N}$	9a	1187
δ_{C-H}	9a (Ring 2)	1201	δ_{C-H}	9a	1214	δ_{C-H}	9a	1201
$\delta_{C-H} + \nu_{C-N}$	18a (Ring 2)	1247	δ_{C-H}	9b	1324	ν_{C-N}		1277
$\delta_{C-H} + \nu_{C-N}$	18a (Ring 1)	1263						
$\nu_{C-C} + \delta_{C-H}$	14 + 9b (Ring 2)	1340	$\nu_{C-C} + \delta_{C-H}$	14 + 9b	1349	ν_{C-C}	14	1327
$\nu_{C-C} + \delta_{C-H}$	14 + 9b (Ring 1)	1358				δ_{C-H}	9b	1337
$\delta_{C-C} + \delta_{C-H}$	19b + 18b (Ring 1)	1417	$\delta_{C-C} + \delta_{C-H}$	19b + 18b	1415	ν_{N-N}		1389
$\delta_{C-C} + \delta_{C-H}$	19b + 18b (Ring 2)	1422				$\delta_{C-C} + \delta_{C-H}$	19b + 18b	1423
$\nu_{N=N}$		1480	$\nu_{N=N}$		1472			
δ_{C-H}	18a (Ring 1)	1503	δ_{C-H}	18a		$\delta_{C-H} + \delta_{N-H}$	18a	1508
δ_{C-H}	18a (Ring 2)	1511				δ_{C-H}	18a	1523
$\nu_{C-C} + \delta_{C-H}$	8b + 9b (Ring 2)	1572	ν_{C-C}	8b	1597	$\nu_{C-C} + \delta_{C-H} + \delta_{N-H}$	8b + 9b	1610
$\nu_{C-C} + \delta_{C-H}$	8a + 9a (Ring 1 +2)	1612	ν_{C-C}	8a	1618	$\nu_{C-C} + \delta_{C-H} + \delta_{N-H}$	8a + 9a	1630
$\nu_{C-C} + \delta_{C-H}$	8b + 9b (Ring 1)	1617						

Table C.3: Calculated vibrational assignment of DMAOB, DMAB and DMHAB from DFT Raman spectra, calculated from a geometry optimized DMAOB, DMAB or DMHAB molecule adsorbed on an Au_5 cluster. Wilson number and mode information taken from Merlin and Cornard [4]. v = stretch, δ = bend, Ring 1 and Ring 2 correspond to the different aromatic rings in the structure of DMOAB.

NPQDI				NPQDA			
Mode	**Wilson Number**	**SERS / cm^{-1}**	**Calculated / cm^{-1}**	**Mode**	**Wilson Number**	**SERS / cm^{-1}**	**Calculated / cm^{-1}**
δ_{C-C}	16a (Ring 2)		379	δ_{N-H}			403
δ_{C-C}	16a (Ring 1)	407	416	$\delta_{C-C} + \delta_{N-H}$	16a (Ring 1)	411	424
$\delta_{C=N}$		431	450	$\delta_{C-C} + \delta_{N-H}$	16a (Ring 2)	439	453
δ_{C-H}	17b (Ring 2)		508	δ_{C-H}	17b (Ring 1 + 2)		517
δ_{C-H}	17b (Ring 1 + 2)		543	δ_{C-C}	6a (Ring 2)		569
δ_{C-H}	17b (Ring 1)	511	563				
δ_{C-C}	6b (Ring 2)	584	608	δ_{C-C}	6b (Ring 1 + 2)	607	646
δ_{C-C}	6b (Ring 1)	639	647	δ_{C-C}	6b (Ring 1 + 2)		652
$\delta_{C-C} + \delta_{N-H}$	16a (Ring 2)	751	757	δ_{C-C}	6a (Ring 1)		678
$\delta_{C-H} + \delta_{N-H}$	10a (Ring 2)		772	δ_{C-C}	16a (Ring 1)		718
$\delta_{C-H} + \delta_{N-H}$	10a (Ring 2)		781	δ_{C-C}	16a (Ring 2)		730
ν_{C-C}	19a (Ring 2)		797				
δ_{C-H}	10a (Ring 1)		852	δ_{C-H}	11 (Ring 1)		798
δ_{C-H}	11 (Ring 1)		860	δ_{C-H}	11 (Ring 2)		839
δ_{C-H}	11 (Ring 1)		870	δ_{C-H}	17a (Ring 1)		960
δ_{C-H}	17a (Ring 1)		997				
δ_{C-C}	12 (Ring 1)	1007	1024	δ_{C-C}	12 (Ring 1)	1010	1014
				δ_{C-C}	12 (Ring 2)		1025
ν_{C-C}	1 (Ring 1)	1076	1087	ν_{C-C}	1 (Ring 1)	1081	1090
δ_{C-H}	18b (Ring 1)		1126				
δ_{C-H}	9a (Ring 1 + 2)	1151	1196	δ_{C-H}	9a (Ring 1 + 2)		1204
$\delta_{C-H} + \nu_{C-N}$	18a (Ring 1 + 2)	1176	1239	$\delta_{C-H} + \nu_{C-N-C}$	18a (Ring 1 + 2)	1181	1248
δ_{C-H}	9b (Ring 2)	1235	1304				
$\nu_{C-C} + \delta_{C-H}$	14 (Ring 1 + 2) + 6b (Ring 2)		1320				
δ_{C-H}	6b (Ring 2)	1321	1330	$\delta_{C-H} + \nu_{C-N}$	18a (Ring 2)		1330
$\nu_{C-C} + \delta_{C-H} + \delta_{N-H}$	14 (Ring 2) + 9b (Ring 2)	1361	1386	$\nu_{C-C} + \delta_{C-H}$	14 (Ring 1 + 2) + 9b (Ring 1 + 2)		1343
δ_{C-H}	18a (Ring 2)	1396	1409	$\nu_{C-C} + \delta_{C-H}$	14 (Ring 1 + 2) + 9b (Ring 1 + 2)	1347	1392
$\delta_{C-C} + \delta_{C-H}$	19a (Ring 1) + 18b (Ring 1)		1420	$\delta_{C-C} + \delta_{C-H} + \delta_{N-H}$	19b (Ring 1) + 18b (Ring 1)	1391	1419
				$\nu_{C-C} + \delta_{C-H} + \delta_{N-H}$	19a (Ring 1) + 18a (Ring 1)		1511
$\nu_{C-C} + \delta_{C-H} + \delta_{N-H}$	8b (Ring 2) + 9b (Ring 2)		1451	$\nu_{C-C} + \delta_{C-H} + \delta_{N-H}$	19a (Ring 1) + 18a (Ring 1)		1530
δ_{C-H}	18a (Ring 1)		1504	$\nu_{C-C} + \delta_{C-H}$	19a (Ring 2) + 18a (Ring 2)		1547
$\nu_{C=N}$		1484	1565				
$\nu_{C-C} + \delta_{C-H}$	8a (Ring 1) + 9a (Ring 2)	1581	1605	$\nu_{C-C} + \delta_{C-H}$	8a (Ring 1) + 9a (Ring 1)	1573	1624
$\nu_{C-C} + \delta_{C-H}$	8a (Ring 1) + 9a (Ring 2)	1626	1681	$\nu_{C-C} + \delta_{C-H}$	8a (Ring 2) + 9a (Ring 2)	1587	1655

Table C.4: SERS and calculated vibrational assignment of NPQDI and NPQDA from DFT Raman spectra of the gerometry opmised molecule adsorbed on an Au_5 cluister. Wilson number and mode information taken from Merlin and Cornard [4]. v = stretch, δ = bend. Ring 1 and Ring 2 correspond to the aromatic rings closest or furthest away from the gold surface.

NPQMI				NPQMA			
Mode	**Wilson Number**	**SERS / cm^{-1}**	**Calculated / cm^{-1}**	**Mode**	**Wilson Number**	**SERS / cm^{-1}**	**Calculated / cm^{-1}**
δ_{C-C}	16a (Ring 2)		375	$\delta_{C-C} + \delta_{N-H}$	16a (Ring 1)	406	405
δ_{C-C}	16a (Ring 1)	407	413	$\delta_{C-C} + \delta_{N-H}$	16a (Ring 2)	435	435
$\delta_{C=O}$		433	455	δ_{N-H}			460
δ_{C-H}	17b (Ring 2)	514	541	δ_{C-H}	17b (Ring 1 + 2)		531
δ_{C-H}	17b (Ring 1)		566	δ_{C-C}	6a (Ring 2)		565
δ_{C-C}	6b (Ring 2)		601	δ_{C-C}	6b (Ring 2)	608	643
δ_{C-C}	6b (Ring 1)	638	645	δ_{C-C}	6b (Ring 1)		651
δ_{C-C}	6a (Ring 1)		674	δ_{C-C}	6a (Ring 1)		681
δ_{C-C}	16a (Ring 1 + 2)	751	764	δ_{C-C}	16a (Ring 2)		718
				δ_{C-C}	16a (Ring 1)		723
δ_{C-H}	10a (Ring 2)		792	δ_{C-H}	10a (Ring 1)		784
δ_{C-H}	10a (Ring 1)		850	δ_{C-H}	10a (Ring 2)		829
δ_{C-H}	11 (Ring 1)		862	δ_{C-H}	11 (Ring 2)		843
ν_{C-C}	19a (Ring 1 + 2)		871	δ_{C-H}	11 (Ring 1)		862
δ_{C-H}	11 (Ring 2)		889	ν_{C-C}	19a (Ring 1 + 2)		889
δ_{C-H}	5 (Ring 1)		981	δ_{C-H}	17a (Ring 2)		945
δ_{C-H}	17a (Ring 1)		988	δ_{C-H}	17a (Ring 1)		965
δ_{C-C}	12 (Ring 1)	1007	1021	δ_{C-C}	12 (Ring 1)	1012	1017
				δ_{C-C}	12 (Ring 2)		1026
ν_{C-C}	1 (Ring 1)	1076	1086	ν_{C-C}	1 (Ring 1)	1080	1090
δ_{C-H}	18b (Ring 2)		1106				
δ_{C-H}	18b (Ring 1)		1129				
				δ_{O-H}			1168
δ_{C-H}	9a (Ring 2)	1150	1183	δ_{C-H}	9a (Ring 2)		1197
δ_{C-H}	9a (Ring 1)	1172	1197	δ_{C-H}	9a (Ring 1)	1183	1211
$\delta_{C-H} + \nu_{C-N}$	18a (Ring 1 + 2)	1235	1241	$\delta_{C-H} + \nu_{C-N-C}$	18a (Ring 1 + 2)		1248
δ_{C-H}	9b (Ring 2)	1321	1278	ν_{C-O}		1267	1273
$\nu_{C-C} + \delta_{C-H}$	14 (Ring 1) + 9b (Ring 2)		1319	$\nu_{C-C} + \delta_{C-H}$	9b (Ring 1) + 14 (Ring 1)		1330
δ_{C-H}	9b (Ring 1)		1327	δ_{C-H}	9b (Ring 1 + 2)		1347
$\nu_{C-C} + \delta_{C-H}$	14 (Ring 2) + 9b (Ring 1)		1340	$\delta_{C-H} + \nu_{C-N-C} + \delta_{O-H}$	9b (Ring 1 + 2)	1349	1357
δ_{C-H}	18a (Ring 2)	1361	1401	$\nu_{C-C} + \delta_{C-H} + \delta_{O-H}$	14 (Ring 2) + 9b (Ring 2)		1374
$\delta_{C-C} + \delta_{C-H}$	19b (Ring 1) + 18b (Ring 1)	1396	1423	$\delta_{C-C} + \delta_{C-H} + \delta_{N-H}$	19b (Ring 1) + 18b (Ring 1)	1392	1428
$\nu_{C-C} + \delta_{C-H}$	8b (Ring 2) + 9b (Ring 2)		1430	$\delta_{C-C} + \delta_{C-H} + \delta_{O-H}$	19b (Ring 2) + 18b (Ring 2)	1448	1459
δ_{C-H}	18a (Ring 1)		1503	$\delta_{C-H} + \delta_{N-H}$	18a (Ring 1)		1516
				$\delta_{C-H} + \delta_{N-H}$	18a (Ring 1 + 2)		1534
$\nu_{C=O} + \nu_{C=N}$		1485	1551	$\delta_{C-H} + \delta_{N-H}$	18a (Ring 2)		1548
$\nu_{C-C} + \delta_{C-H} + \nu_{C=O}$	8a (Ring 1) + 9a (Ring 1)	1575	1600	$\nu_{C-C} + \delta_{C-H}$	8a (Ring 2) + 9a (Ring 2)	157	1628
$\nu_{C-C} + \delta_{C-H}$	8a (Ring 2) + 9a (Ring 2)	1625	1671	$\nu_{C-C} + \delta_{C-H}$	8a (Ring 1) + 9a (Ring 1)	1588	1654

Table C.5: SERS and calculated vibrational assignment of NPQMI and NPQMA from DFT Raman spectra of the geometry optimised molecule adsorbed on an Au_5 cluister. Wilson number and mode information taken from Merlin and Cornard [4]. v = stretch, δ = bend. Ring 1 and Ring 2 correspond to the aromatic rings closest or furthest away from the gold surface.

DMAB				DMHAB			
Mode	**Wilson Number**	**SERS / cm^{-1}**	**Calculated / cm^{-1}**	**Mode**	**Wilson Number**	**SERS / cm^{-1}**	**Calculated / cm^{-1}**
δ_{C-S}			358	δ_{C-S}			377
δ_{C-C}	16a	407	429	δ_{C-C}	16a		423
ν_{C-S}		441	469	ν_{C-S}			452
δ_{C-C}	10b	529	518	δ_{N-H}		494	473
δ_{C-C}	6b	641	645	$\delta_{C-C} + \delta_{N-H}$	10b		538
δ_{C-C}	6a	718	722	δ_{C-C}	6b		648
δ_{C-C}	16a	750	734	δ_{C-C}	6a	669	670
				δ_{C-C}	16a		725
δ_{C-H}	10a		875	δ_{C-H}	10a		834
$\delta_{N=N}$			924	δ_{C-C}	6a		840
δ_{C-C}	12		1023	δ_{C-C}	12		1014
ν_{C-C}	1	1078	1082	ν_{C-C}	1		1089
δ_{C-H}	18b	1142	1119	δ_{C-H}	18b		1124
δ_{C-H}	9a	1173	1168	$\delta_{C-H} + \nu_{N-N}$	9a	1190	1187
δ_{C-H}	9a	1191	1214	δ_{C-H}	9a		1201
δ_{C-H}	9b	1305	1324	ν_{C-N}			1277
$\nu_{C-C} + \delta_{C-H}$	14 + 9b		1349	ν_{C-C}	14		1327
				δ_{C-H}	9b		1337
				ν_{N-N}			1389
$\delta_{C-C} + \delta_{C-H}$	19b + 18b	1390	1415	$\delta_{C-C} + \delta_{C-H}$	19b + 18b		1423
$\nu_{N=N}$		1420	1472	$\delta_{C-H} + \delta_{N-H}$	18a		1508
δ_{C-H}	18a	1436		δ_{C-H}	18a		1523
ν_{C-C}	8b	1574	1597	$\nu_{C-C} + \delta_{C-H} + \delta_{N-H}$	8b + 9b		1610
ν_{C-C}	8a	1589	1618	$\nu_{C-C} + \delta_{C-H} + \delta_{N-H}$	8a + 9a		1630

Table C.6: SERS and calculated vibrational assignment of DMAB and DMHAB from DFT Raman spectra of the geometry optimised molecule adsorbed on an Au_5 cluister. Wilson number and mode information taken from Merlin and Cornard [4]. ν = stretch, δ = bend. Ring 1 and Ring 2 correspond to the aromatic rings closest or furthest away from the gold surface.

C.2 References

[1] M.J. Frisch, G.W. Trucks, H.B. Schlegel, G.E. Scuseria, M.A. Robb, J.R. Cheeseman, G. Scalmani, V. Barone, G.A. Petersson, H. Nakatsuji, X. Li, M. Caricato, A. Marenich, J. Bloino, B.G. Janesko, R. Gomperts, B. Mennucci, H.P. Hratchian, J. V. Ortiz, A.F. Izmaylov, J.L. Sonnenberg, D. Williams-Young, F. Ding, F. Lipparini, F. Egidi, J. Goings, B. Peng, A. Petrone, T. Henderson, D. Ranasinghe, V.G. Zakrzewsk, J.G. I, N. Rega, G. Zheng, W. Liang, M. Hada, M. Ehara, K. Toyota, R. Fukuda, J. Hasegawa, M. Ishida, T. Nakajima, Y. Honda, O. Kitao, H. Nakai, T. Vreven, K. Throssell, J.A. Montgomery, J.E. Peralta, F. Ogliaro, M. Bearpark, J.J. Heyd, E. Brothers, K.N. Kudin, V.N. Staroverov, T. Keith, R. Kobayashi, J. Normand, K. Raghavachari, A. Rendell, J.C. Burant, S.S. Iyengar, J. Tomasi, M. Cossi, J.M. Millam, M. Klene, C. Adamo, R. Cammi, J.W. Ochterski, R.L. Martin, K. Morokuma, O. Farkas, J.B. Foresman, D.J. Fox, Gaussian, (2009). http://gaussian.com/.

[2] R. Dennington, T. Keith, J. Millam, GaussView, (2009). http://gaussian.com/.

[3] L. Bin Zhao, J.L. Chen, M. Zhang, D.Y. Wu, Z.Q. Tian, Theoretical study on electroreduction of p-nitrothiophenol on silver and gold electrode surfaces, J. Phys. Chem. C. 119 (2015) 4949–4958. doi:10.1021/jp512957c.

[4] J.C. Merlin, J.P. Cornard, A Pictorial Representation of Normal Modes of Vibration Using Vibrational Symmetry Coordinates, J. Chem. Educ. 83 (2006) 1393. doi:10.1021/ed083p1393.

Appendix D

This appendix contains tables accompanying Chapter 5: The adsorption and orientation of thioamide molecular wires on gold.

D.1 BDTA and EDBDTA vibrational assignment

The SERS and DFT calculated Raman vibrational assignments of BDTA and EDBDTA are displayed in Table D1 and D2. Calculated DFT Raman spectra were generated with Gaussian 09W [1] and GaussView 5 [2], using each molecule adsorbed on a Au_5 cluster, a 6-311G+(d', p') basis set for the H, N, O, C and S atoms, a LANL2DZ for the Au valence electrons and LANL2DZ ECP for the Au core electrons. In addition, the generalised gradient approximation functional B3LPY was used and DFT frequencies were scaled by 0.981 as per Zhao *et al.* [3].

Mode	Wilson number	Calculated / cm^{-1}	SERS / cm^{-1}
δ_{N-H} (Thioamide-1)		332	
δ_{C-S} (Thioamide-1+4)		356	
δ_{C-C}	10b	392	415
δ_{N-H} (Thioamide-1)		422	454
δ_{N-H} (Thioamide-4)		552	
δ_{C-S} (Thioamide-1+4)		579	
δ_{N-H} (Thioamide-4)		613	620
δ_{C-C}	6a	697	
$\nu_{C-S} + \delta_{N-H}$ (Thioamide-1+4)		837	
δ_{C-C}	12	1005	996
ν_{C-C}	1	1131	1176
δ_{C-H}	18b	1213	1205
$\delta_{C-H} + \delta_{C-N}$ (Thioamide-1)	9a	1265	
$\nu_{C-C} + \delta_{C-H}$	8b + 9b	1354	
$\delta_{C-H} + \nu_{C-N}$ (Thioamide-4)	18a	1405	1423
$\delta_{C-C} + \delta_{C-H} + \nu_{C-N}$ (Thioamide-1)	19b + 18b	1456	1463
$\nu_{C-C} + \delta_{C-H}$	19a + 18a	1536	1516
$\nu_{C-C} + \delta_{C-H}$	8a + 9a	1622	1604
δ_{N-H} (Thioamide-1)		1667	

Table D1: Calculated and SERS vibrational assignment of BDTA. Wilson number and mode information taken from Merlin and Cornard [4]. ν = stretch, δ = bend. Thioamide 1 indicates the thioamide group closest to the surface. Thioamide-4 indicates the group furthest away.

Mode	Wilson number	Calculated / cm^{-1}	SERS cm^{-1}
δ_{N-H} (Ring 1)		348	401
δ_{N-H} (Ring 1)		412	
δ_{C-C}	10b	419	422
$\delta_{C\equiv C}$		482	466
δ_{C-H} (Ring 1)	11	548	
δ_{C-C} (Ring 1)	6b	640	
δ_{C-C} (Ring 2)	6b	671	684
δ_{C-C} (Ring 1 + 2)	6a	728	
$\nu_{C-S} + \delta_{N-H}$ (Ring 1)		748	744
$\nu_{C-S} + \delta_{N-H}$ (Ring 2)		780	776
δ_{N-H} (Ring 1)		832	
δ_{C-H} (Ring 2)	10a	852	
$\delta_{C-H} + \delta_{N-H}$ (Ring 2)	17b	872	
$\delta_{C-H} + \delta_{N-H}$ (Ring 2)	17b	881	
δ_{C-C} (Ring 1)	12	1009	1000
δ_{C-C} (Ring 2)	12	1029	
ν_{C-C} (Ring 1 + 2)	1	1117	1071
δ_{C-H} (Ring 1 + 2)	15	1133	1137
δ_{C-H} (Ring 2)	18b	1161	
δ_{C-H} (Ring 1)	18b	1176	1178
δ_{C-H} (Ring 1 + 2)	9a	1210	1195
$\delta_{C-H} + \delta_{C-N}$ (Ring 1)	9a	1259	
δ_{N-H} (Ring 2)		1300	
$\nu_{C-C} + \delta_{C-H}$ (Ring 2)	8b + 9b	1328	
$\nu_{C-C} + \delta_{C-H}$ (Ring 2)	8b + 9b	1348	
$\delta_{C-C} + \delta_{C-H} + \nu_{C-N}$ (Ring 2)	19b + 18b	1420	1416
$\delta_{C-C} + \delta_{C-H} + \nu_{C-N}$ (Ring 1)	19b + 18b	1443	1451
$\delta_{C-C} + \delta_{C-H} + \nu_{C-N}$ (Ring 1)	19b + 18b	1460	
$\nu_{C-C} + \delta_{C-H}$ (Ring 1)	19a + 18a	1527	1516
$\nu_{C-C} + \delta_{C-H}$ (Ring 2)	19a + 18a	1546	
$\nu_{C-C} + \delta_{C-H}$ (Ring 1)	8a + 9a	1593	1601
$\nu_{C-C} + \delta_{C-H}$ (Ring 2)	8a + 9a	1632	1636
δ_{N-H}		1661	
$\nu_{C\equiv C}$		2223	2222

Table D2: Calculated and SERS vibrational assignment of EDBDTA. Wilson number and mode information taken from Merlin and Cornard [4]. v = stretch, δ = bend. Ring 1 indicates the ring closest to the surface, and Ring 2 indicates the one furthest away.

D.2 References

[1] M.J. Frisch, G.W. Trucks, H.B. Schlegel, G.E. Scuseria, M.A. Robb, J.R. Cheeseman, G. Scalmani, V. Barone, G.A. Petersson, H. Nakatsuji, X. Li, M. Caricato, A. Marenich, J. Bloino, B.G. Janesko, R. Gomperts, B. Mennucci, H.P. Hratchian, J. V. Ortiz, A.F. Izmaylov, J.L. Sonnenberg, D. Williams-Young, F. Ding, F. Lipparini, F. Egidi, J. Goings, B. Peng, A. Petrone, T. Henderson, D. Ranasinghe, V.G. Zakrzewsk, J.G. I, N. Rega, G. Zheng, W. Liang, M. Hada, M. Ehara, K. Toyota, R. Fukuda, J. Hasegawa, M. Ishida, T. Nakajima, Y. Honda, O. Kitao, H. Nakai, T. Vreven, K. Throssell, J.A. Montgomery, J.E. Peralta, F. Ogliaro, M. Bearpark, J.J. Heyd, E. Brothers, K.N. Kudin, V.N. Staroverov, T. Keith, R. Kobayashi, J. Normand, K. Raghavachari, A. Rendell, J.C. Burant, S.S. Iyengar, J. Tomasi, M. Cossi, J.M. Millam, M. Klene, C. Adamo, R. Cammi, J.W. Ochterski, R.L. Martin, K. Morokuma, O. Farkas, J.B. Foresman, D.J. Fox, Gaussian, (2009). http://gaussian.com/.

[2] R. Dennington, T. Keith, J. Millam, GaussView, (2009). http://gaussian.com/.

[3] L. Bin Zhao, J.L. Chen, M. Zhang, D.Y. Wu, Z.Q. Tian, Theoretical study on electroreduction of p-nitrothiophenol on silver and gold electrode surfaces, J. Phys. Chem. C. 119 (2015) 4949–4958. doi:10.1021/jp512957c.

[4] J.C. Merlin, J.P. Cornard, A Pictorial Representation of Normal Modes of Vibration Using Vibrational Symmetry Coordinates, J. Chem. Educ. 83 (2006) 1393. doi:10.1021/ed083p1393.